

**Development of energy storage systems capable of Cu extraction from
CuFeS₂**

by

Kashif Mairaj Deen

B.Sc. (Engineering), University of the Punjab, 2007

M.Sc. (Engineering), University of the Punjab, 2012

A THESIS SUBMITTED IN PARTIAL FULFILLMENT OF
THE REQUIREMENTS FOR THE DEGREE OF

Doctor of Philosophy

in

THE FACULTY OF GRADUATE AND POSTDOCTORAL STUDIES

(Materials Engineering)

THE UNIVERSITY OF BRITISH COLUMBIA

(Vancouver)

April 2019

© Kashif Mairaj Deen, 2019

The following individuals certify that they have read, and recommend to the Faculty of Graduate and Postdoctoral Studies for acceptance, the dissertation entitled:

Development of energy storage systems capable of Cu extraction from CuFeS_2

submitted by Kashif Mairaj Deen in partial fulfillment of the requirements for

the degree of Doctor of Philosophy

in Materials Engineering

Examining Committee:

Edouard Asselin, Materials Engineering

Supervisor

David Dixon, Materials Engineering

Supervisory Committee Member

Wenyong Liu, Materials Engineering

Supervisory Committee Member

David Dreisinger

University Examiner

Dan Bizzotto

University Examiner

Additional Supervisory Committee Members:

Supervisory Committee Member

Supervisory Committee Member

Abstract

Two hybrid energy storage systems, i.e., a fixed bed flow cell (FBFC) and a tri-functional battery (TFB) are introduced, which use either synthetic CuFeS_2 or a mineral concentrate (MC) as electrode materials and a source of Cu. In the FBFC, the composite negative electrode is CuFeS_2 or MC sandwiched in graphite felt (GF). The $\text{Fe}^{\text{II}}/\text{Fe}^{\text{III}}$ redox reaction (in the presence of Cu^{II}) occurs on a GF positive electrode. Under optimized conditions, the presence of CuFeS_2 resulted in a continuous increase in the specific capacity of the FBFC from 9 to 48 mAh g^{-1} and in the specific energy from 2 to 6.3 Wh kg^{-1} in 500 galvanostatic charge/discharge (GCD) cycles. However, in the same setup, the MC had an increase in the specific energy from 3.5 to 8.5 Wh kg^{-1} in 400 GCD cycles. Advantageously, 10.3 and 12.7% Cu is extracted from the synthetic CuFeS_2 and MC, respectively.

In the TFB, two energy intensive processes, Cu extraction from CuFeS_2 and Zn electrowinning, are integrated for energy storage. In this setup, the positive slurry electrode (PSE) composed of CuFeS_2 or MC mixed with activated carbon (AC) in H_2SO_4 was separated by a membrane from the circulating Zn^{2+} solution in the negative compartment. The Zn deposition/re-dissolution and commencement of reversible reactions in the PSE during GCD cycles are responsible for energy storage akin to a battery. The maximum 388 Wh kg^{-1} specific energy (1.13 Wh l^{-1}) during the 1st discharge cycle decreased to $\approx 50 \text{ Wh kg}^{-1}$ over the subsequent 14 GCD cycles. The low coulombic ($\approx 50\%$) and energy ($\sim 40\%$) efficiencies are offset by $\sim 23\%$ Cu extraction from CuFeS_2 in 100 GCD cycles. The cell potential of $\sim 0.95 \text{ V}$ and potential efficiency ($>70\%$) imply that the TFB can be used as a hybrid energy storage device.

Using MC in the TFB-M, a monotonic increase in energy density from 2.6 to 36.2 mWh l⁻¹ at low energy efficiency (between 14–43%) was obtained for the initial 14 GCD cycles. On the other hand, in 100 GCD cycles, ~16.1% Cu was also extracted from the MC.

Lay Summary

Due to rapid industrial growth and high demand for energy, the use of renewable sources has compelled researchers to develop efficient energy storage devices. On the other hand, ores with a high concentration of Cu are being rapidly depleted and those that remain consist largely of CuFeS_2 —a mineral that is hard to decompose for Cu extraction. Here we combine both energy storage and extraction processes into hybrid batteries. These batteries serve to extract Cu for its eventual recovery and sale. Two types of hybrid mineral batteries, which use synthetic and naturally sourced CuFeS_2 , are introduced. For example, a trifunctional battery is developed in which both Cu extraction from CuFeS_2 and Zn deposition are possible in addition to energy storage. It is expected that coupling of these energy storage devices with wind turbines or solar cells at remote mining sites might be an attractive option.

Preface

The object of this research work was to investigate the possible use of CuFeS_2 as an electrode material in a battery-like setup. This setup would also be capable of extracting Cu. Unlike most battery systems, in which undesirable irreversible reactions are always responsible for capacity fade and deterioration of the electrodes, we are using this deterioration as a beneficial feature in this research. This research work is the first of its kind. The development and performance of two systems, a *fixed bed flow cell* (FBFC) and a *tri-functional battery* (TFB) is discussed. Initially, the core idea around the development of a system capable of leaching Cu from CuFeS_2 through the use of the $\text{Fe}^{\text{II}}/\text{Fe}^{\text{III}}$ couple was introduced by Dr. Asselin and myself. Next, the FBFC design, characterization and analysis of the experimental results was conducted by myself as presented in chapters 5 to 7. The integration of two energy-intensive hydrometallurgical processes in one setup was proposed by myself. Briefly, in this setup, Zn electrowinning is coupled with CuFeS_2 (or mineral concentrate) oxidation in the negative and positive compartments, respectively. Quantitative analyses of Cu extraction and energy storage capabilities of these systems are discussed in chapter(s) 8 and 9. The journal articles and conference presentations produced from this dissertation are listed as follows. I designed and executed the experiments. Dr. Asselin and I analyzed the data and equally contributed in the writing of these publications.

Journal Articles

1. **K. M. Deen**, E. Asselin, “Differentiation of the non-faradaic and pseudocapacitive electrochemical response of graphite felt/ CuFeS_2 composite electrodes”, *Electrochimica Acta*, 212 (2016), 979–991.
2. **K. M. Deen**, E. Asselin, “A hybrid mineral battery: Energy storage and dissolution behavior of CuFeS_2 in a fixed bed flow cell”, *ChemSusChem*, 11 (2018), 1533–1548.

3. **K. M. Deen**, E. Asselin, “On the use of a naturally-sourced CuFeS₂ mineral concentrate for energy storage”, *Electrochimica Acta* 297 (2019) 1079–1093.
4. **K. M. Deen**, E. Asselin, “A trifunctional battery setup that integrates Cu extraction and Zn electrowinning processes”, (Submitted for consideration)

Conference Presentations

5. **K. M. Deen**, E. Asselin, “A hybrid system for energy storage which integrates Zn deposition and Cu leaching processes”, *Resources for Future Generations* (RFG 2018), June 16–21, 2018, Vancouver, BC, Canada
6. **K. M. Deen**, E. Asselin, “A Hybrid Energy Storage System Combining Zn Deposition and Cu Leaching in One Setup”, *Extraction 2018*, August 26–29, 2018, Ottawa, Canada
7. **K. M. Deen**, E. Asselin, “Cu extraction from naturally-sourced CuFeS₂ coupled to Zn electrowinning in a battery-like setup”, *COM-2019*, (Accepted)

The following table indicates the specific publications corresponding to the chapters provided in this dissertation:

Chapter #	Publication # (as listed above)
5	1
6	2
7	3
8	4, 5 and 6
9	7

Table of Contents

Abstract.....	iii
Lay Summary	v
Preface.....	vi
Table of Contents	viii
List of Tables	xiii
List of Figures.....	xv
List of Symbols	xxvi
List of Abbreviations	xxix
Glossary	xxxi
Acknowledgments	xxxii
Dedication	xxxiii
Chapter 1: Introduction	1
1.1 Research goals	3
1.2 Thesis outline	4
Chapter 2: Literature Review	6
2.1 Structure of CuFeS ₂	7
2.2 Eh-pH diagram of CuFeS ₂ and discrepancies	9
2.3 Passivation of CuFeS ₂	11
2.4 Leaching of CuFeS ₂	14
2.4.1 Leaching in sulfate media	15
2.4.2 Factors influencing CuFeS ₂ leaching.....	20
2.4.3 Reduction of CuFeS ₂	22

2.5	Zn electrowinning and its use in energy storage.....	24
2.5.1	Solution purity and its importance.....	26
2.5.2	Optimum conditions for Zn deposition.....	28
2.5.3	Use of Zn as an electrode material in batteries.....	29
2.6	Energy storage and its importance.....	30
2.6.1	Electrochemical energy storage.....	30
2.6.2	Current state of battery research.....	35
2.6.3	Use of CuFeS ₂ as battery electrode material.....	38
2.6.4	Electrochemical capacitors or supercapacitors.....	42
Chapter 3: Objectives.....		46
3.1	Setup 1: Fixed bed flow cell (FBFC).....	47
3.2	Setup 2: (TFB).....	47
Chapter 4: Approach and Methodology.....		49
4.1	Materials.....	49
4.2	Experimental methods.....	50
4.2.1	Synthesis of CuFeS ₂ and pretreatment of mineral concentrate.....	50
4.2.2	Schematic of the systems under investigation.....	51
4.2.3	Preparation of the electrodes for electrochemical study.....	52
4.2.4	Construction of fixed bed flow cell (FBFC).....	54
4.2.5	Construction and design of the tri-functional battery setup (TFB).....	56
4.3	Physical characterization of electrode materials.....	57
4.4	Electrochemical Testing.....	60
4.4.1	Characterization of the composite electrode(s).....	60

4.4.2	Electrochemical characterization of electrode(s) for FBFC setup	62
4.4.3	Comparing the performance of as-synthesized CuFeS ₂ and MC in FBFC.....	64
4.4.4	Electrochemical behavior of electrode(s) used in the TFB.....	65
4.4.5	Performance evaluation of the TFB	67
4.5	The reaction sequence for Cu extraction and system mass balance	68
Chapter 5: Electrochemical behavior of CuFeS₂/GF composite electrodes		70
5.1	Characterization of the synthetic CuFeS ₂	71
5.2	Cyclic Voltammetry.....	74
5.3	Galvanostatic cyclic charging and discharging profiles of electrode systems.....	84
5.4	Mechanistic study of charge distribution on CF and Composite electrode	87
5.5	Summary	98
Chapter 6: The hybrid mineral battery: energy storage and dissolution behavior of		
CuFeS₂ in an FBFC.....		100
6.1	Physical characterization of as-synthesized CuFeS ₂	100
6.2	Electrochemical behavior of individual electrode systems.....	104
6.3	Estimating the charge storage capability by the FBFC system.....	120
6.4	Ex-Situ characterization of CuFeS ₂	130
6.5	Proposed reaction sequence during GCD process	135
6.6	Summary.....	140
Chapter 7: Use of a CuFeS₂ mineral concentrate in the FBFC		142
7.1	Characterization of synthetic and CuFeS ₂ mineral concentrate.....	142
7.2	Electrode Kinetics.....	146
7.3	Estimating the energy storage capability of CuFeS ₂ and MS in the FBFC	156

7.4	Ex-situ characterizations of the retrieved CuFeS ₂ from the C-1 system	168
7.5	Summary	174
Chapter 8: Integrating the Cu extraction and Zn electrowinning processes for energy storage		177
8.1	Physical characterization of the electrode materials	177
8.2	Reaction sequence and optimization of the process conditions	182
8.3	Estimation of energy and Cu extraction capabilities of the TFB	194
8.4	Cause of capacity fade and mass balance in TFB	209
8.4.1	Diagnosing possible reactions in TFB	209
8.4.2	SO ₄ ²⁻ transport and mass balance	212
8.5	Polarization behavior of TFB	218
8.6	Energy storage by TFB equivalent to energy produced by a diesel generator	220
8.7	Summary	221
Chapter 9: Using a CuFeS₂ mineral concentrate in the TFB-M		224
9.1	Difference between TFB and TFB-M	224
9.2	Energetics of the TFB-M	225
9.3	Energy storage and Cu extraction capabilities	229
9.4	Energy storage equivalent to energy produced by a diesel generator	235
9.5	Summary	237
Chapter 10: Conclusion		238
10.1	Remarks on the important findings	238
10.2	The practical implications of the current research work	240
10.3	Future perspectives and recommendations	241

References	245
Appendices	264
Appendix A	264

List of Tables

Table 2-1 Oxidative acidic sulfate leaching of CuFeS_2 , the reaction chemistry [48].....	19
Table 2-2 Sulfate based Cu extraction processes from ore or mineral concentrate commercialized and/or studied at pilot plant scale [7, 60]	19
Table 2-3 Formation of possible species during electrochemical reduction of CuFeS_2 in 1.7 M H_2SO_4 [32].....	23
Table 2-4 Existing commercialized and developing battery technologies, their performance, and comparison [121, 157]	37
Table 2-5 Performance metrics of EDLCs and recently reported asymmetrical supercapacitors.....	45
Table 4-1 The designation and composition of electrode and electrolyte systems used in the FBFC.....	63
Table 4-2 The electrode systems and composition of the electrolytes used in the TFB setups	66
Table 5-1 Quantitative measurement of parameters from Multipoint BET surface area analysis.....	71
Table 6-1 Impedance parameters evaluated after fitting the spectra by using the EEC model	119
Table 7-1 Parameters calculated from the CV scans obtained at various sweep rates at 25 °C (Note: Geometrical surface area of the GF (14.4 cm^2) was used in the calculation).....	155
Table 8-1 Quantitative determination of the extent of reaction from GCD and ICP-OES analysis.....	212
Table 8-2 Parameters used to determine the mass transport across the AEM	214

Table 8-3 Estimation of energy storage by a TFB, which has the capacity to accommodate 1 tonne of CuFeS_2 in PSE and comparison with the energy generated by a diesel generator . 221

Table 9-1 Energy storage capability of TFB-M, which can process 1 tonne of MC in one batch and estimation of MC to diesel ratio for the supply of same amount of energy 236

List of Figures

Figure 2-1 (a) Unit cell of CuFeS_2 in which each Cu atoms are shown in black spheres, Fe and S atoms are represented as small and large grey spheres, respectively [24]. (b) Schematic of CuFeS_2 band structure [10].....	8
Figure 2-2 Potential–pH diagram of Cu–Fe–S– H_2O (activity of solute = 0.1 M, except $a_{\text{Cu}^{2+}} = 0.01$ M) at 25 °C [30]	10
Figure 2-3 Polarization trend of CuFeS_2 in 0.5 M H_2SO_4 developed from the steady-state current values obtained potentiostically [11].....	14
Figure 2-4 (a) Effect of H_2SO_4 concentration and temperature on the passivation potential of CuFeS_2 [56](b) % Cu recovery from the Kristineberg concentrate at 80 °C. The redox potentials were adjusted by the addition of dilute H_2O_2 in H_2SO_4 solution (pH =1.5) containing initial Fe^{2+} (1 g l^{-1}) [57]	17
Figure 2-5 Strategies applied to enhance Cu extraction form CuFeS_2 . (Note: ORP was controlled by applying DC potential of 0.4–0.45 V vs. Ag/AgCl electrode, bacterial controlled process was carried out at 50 °C) [60, 61]	18
Figure 2-6 Percentage Cu and Fe extraction at various temperatures, 100 g solids in 1 liter of 1 M H_2SO_4 solution containing initial $10 \text{ g l}^{-1} \text{ Cu}^{2+}$ and $5 \text{ g l}^{-1} \text{ Fe}^{3+}$ was used [48]	18
Figure 2-7 General Zn metal production process flow sheet via roasting, leaching, and electrowinning.....	25
Figure 2-8 Effect of metallic impurities concentration on the current efficiency of Zn deposition process in industrial acid sulfate solution at 430 A m^{-2} (a) IV A and VI-A (b) III-A and V-A group metals including Sn [97].....	27

Figure 2-9 Types of reactions that may occur on the electrode materials of an electrochemical energy storage system	33
Figure 2-10 Charge storage mechanism in batteries and supercapacitors, formation of double layer (A) at the surface (B) within the bulk of porous carbon. Pseudocapacitive behavior (C) due to surface redox reaction onto a hydrous RuO ₂ electrode (D) due to intercalation of Li ⁺ ions within the bulk of host material. Cyclic voltammograms of (E) supercapacitor and (F) battery electrode. Pseudocapacitive discharge curve (G) of MnO ₂ capacitor and (H) LiCoO ₂ battery electrode materials [130].	33
Figure 2-11 Morphologies of the as-synthesized CuFeS ₂ reported in the literature (a) pyramidal [165], (b) nanowires [166], (c) plates/sheets [167], and (d) spikelike nanorods [129, 168].....	39
Figure 2-12 Morphology of synthetic CuFeS ₂ (a) without and (b) in the presence of PVP. Charge/discharge profiles (at various specific currents), cyclic voltammograms and specific capacity of as-synthesized CuFeS ₂ (c, e & g) without and (d, f & h) in the presence of PVP [162].....	41
Figure 4-1 Schematic diagram of the electrode systems used in each battery setup. The combination of positive (red lines) and negative (black lines) connect the two electrodes into a cell assembly.	52
Figure 4-2 Assembly of three electrodes cell in which each electrode i.e., CF electrode, comp electrode, GF-CuFeS ₂ , GF-MC and GF-Fe/Cu was tested in its respective electrolyte.....	54
Figure 4-3 Schematic diagram of the FBFC, the original setup demonstrates the overall assembly.....	55

Figure 4-4 (a) Schematic diagram of the TFB (cross-sectional view), (b) assembled cell, the high-density polyethylene end plates in which (c) components of the cell were tightened with screws. (1; GP is the flexible graphite sheet (FGS), 2; pure Al sheet, 3; Si rubber gaskets, 3a; AEM sandwiched in Si rubber gaskets and 4 represents the flow channels in PTFE plates for PSE and anolyte flow through nozzles 57

Figure 5-1(a) Morphology and (b) particle size distribution curve of as-synthesized CuFeS₂. (c) Multipoint BET analysis. (d) XRD pattern of CuFeS₂. (e) The XPS survey scan of the CuFeS₂ powder sample. (f) Deconvoluted high-resolution spectra of 'S 2p_{3/2}' 73

Figure 5-2 CV scans (at 5–100 mV s⁻¹) of (a) CF and (b) Composite (CF+CuFeS₂) electrode. (c) Trends of current vs. sweep at various potentials. (d) b–values as a function of charge and discharge potential (For comparison, the current is normalized by the mass of GF) 78

Figure 5-3 CV of (a) CF and (b) Composite electrodes at 20 mV s⁻¹, showing the current distribution. (c) Comparison of the total current contributed to the non-faradaic and faradaic processes leading to diffusion controlled processes as revealed from C_{sp} plots of (d) CF and (e) composite electrodes. ('ch' and 'dis' represent the start and end of discharge, respectively). 79

Figure 5-4 FTIR spectra of unexposed (as received) and exposed (after GCD in de-aerated 0.2 mol dm⁻³ H₂SO₄ at 25°C) graphite felt (CF)..... 82

Figure 5-5 GCD cycling at 0.02 A g⁻¹ (a) of the CF and (b) the composite electrodes. (Note: arrows down and up represent the charging and discharging, respectively, the E_{OC} of composite electrode = 0.470 ± 0.005 V_{SHE} at pH = 0.702 ± 0.005). (c) The discharge-specific capacitance at various currents. (d) Columbic efficiency of the CF and composite electrodes 87

Figure 5-6 The Nyquist plots of (a) CF electrode (from $E_{OC} = 0.683 V_{SHE}$ to $E_{max} -0.216 V_{SHE}$ ($\eta = -0.9 V$) in the cathodic (charge) direction). (b) The impedance behavior at $\omega \rightarrow \infty$ for CF electrode. (c) The Nyquist plots of the composite electrode at various potentials starting from 0.470 to $-0.429 V_{SHE}$ ($\eta = -0.9 V$) (d) high-frequency impedance behavior of composite electrode 90

Figure 5-7 Schematic of (a) CF electrode and morphology of graphite fibers in the GF. The inset shows the EEC. (b) Composite electrode and EEC used to simulate impedance spectra for analysis 91

Figure 5-8 Variation in Φ_{dl} and Φ_p of CF and composite electrode. (b) The extent of current leakage through faradaic processes ($\eta = 0$ corresponds to the E_{OCP} ($0.683 V_{SHE}$) and mixed potential ($0.470 V_{SHE}$) for the CF and composite electrodes, respectively) 93

Figure 5-9 Cathodic polarization trends of (a) CF and composite electrodes starting from their respective OCP to $-0.9 V$ vs. OCP, low field ($\eta \rightarrow 0$) polarization trends showing the convergence potential. (b) The proposed mechanism of the overall charge distribution in the composite electrode 97

Figure 6-1 N_2 adsorption/desorption isotherm of as-synthesized $CuFeS_2$ particles (77 K).. 102

Figure 6-2 ToF-SIMS analysis of as-synthesized $CuFeS_2$ (a) 3D surface distribution of Fe and Cu (b) positive ion spectrum (c) 3D mapping for sulfur (S) (d) negative ion spectrum 103

Figure 6-3 Potentiodynamic polarization scans of composite electrode (GF- $CuFeS_2$ +CB) in 0.2 M H_2SO_4 solution; the current is normalized by the mass of $CuFeS_2$ 106

Figure 6-4 CV scans of (a) the composite electrode in 0.2 M H_2SO_4 (the current is normalized by the mass of composite electrode) and (b) GF electrode in 0.5 M Fe^{2+} + 0.2 M

H₂SO₄ solution. (c) GF in solution as in (b) with 0.1 M Cu²⁺ (the current is normalized by the wt. of GF) (d) peak current vs. (sweep rate)^{1/2}..... 110

Figure 6-5 Stability analyses of Fe^{III} species in Cu²⁺ containing solution at a GF electrode. (a) Schematic of sequential protocol applied for the charging (Fe^{II} → Fe^{III}) and discharging (Fe^{III} → Fe^{II}). (b) The discharge current profiles of GF after sequential delay (0 to 60 min) in 0.5 M Fe²⁺ solution and in (c) 0.1 M Cu²⁺ ions containing electrolyte. (d) Discharge peak current profiles as a function of delay time (Note: mass (187 mg) and geometrical surface area (14.4 cm²) of GF electrode were same for each test). 114

Figure 6-6 Impedance spectra of composite (GF – CuFeS₂ + CB), GF–Fe and GF–Fe/Cu electrodes (at 0 V vs. OCP). The EEC is shown in the inset in which Y_x is the admittance for the diffusion parameter and x=B, (for finite diffusion) and x=w (for semi-infinite diffusion), similarly σ_B = Warburg constant for GF–CuFeS₂, and σ_w = Warburg constant for GF–Fe and GF–Fe/Cu electrodes. In addition, the geometrical area of the GF in all electrodes was the same (14.4 cm²). 116

Figure 6-7 (a) Bode plots (b) Phase angle (c) Residual error plots obtained after fitting of impedance spectra with EEC. (Echem® Analyst 6.25 software; Gamry Instruments Inc.). 117

Figure 6-8 SEM images and EDX analyses of the (a) as received and (b) treated GF (in 0.5M Fe²⁺/0.2M H₂SO₄) (c) GF treated in 0.5M Fe²⁺/0.1M Cu²⁺/0.2M H₂SO₄..... 120

Figure 6-9 CV scans of (a) CFe and (b) CFeCu systems. (c) Trends showing the variation in the specific capacitance as a function of (sweep rate)^{-0.5} (at 1 V cell potential), (d) comparison of CFe and CFeCu system (voltammograms at 1 mV s⁻¹)..... 123

Figure 6-10 GCD cyclic trends of (a) CFe and (b) CFeCu systems (c) the specific capacity behavior of both systems (d) Trends of coulombic (η_c) and energy (η_E) efficiencies for both systems	126
Figure 6-11 Specific energy trends of CFe and CFeCu system (Note: Charging and discharging was carried out at 200 mA g^{-1} and 150 mA g^{-1} , respectively)	129
Figure 6-12 Morphological, compositional and structural changes in the CuFeS_2 before and after 500 GCD cycles in CFeCu system, SEM and EDX spectra of (a) as-synthesized, (b) and retrieved CuFeS_2 (c) XRD patterns comparison	131
Figure 6-13 Fe and Cu species concentration in the anolyte after 500 GCD cycles (ICP-OES analysis), the % Cu extraction and retrieved anolyte and catholyte from CFeCu cell system after 500 cycles are shown as an inset.	132
Figure 6-14 Deconvoluted X-ray photoelectron spectra of S 2p depicting the split of peaks associated with mono, di, and polysulfide species on the surface of (a) as-synthesized (b) retrieved CuFeS_2 samples (CFeCu cell system) (c) doublet peaks of Cu associated with Cu 2p _{3/2} and Cu 2p _{1/2} orbital	133
Figure 6-15 Schematic diagram showing the proposed reactions sequence on the negative electrode in the FBFC system during (a) charging and (b) discharging process	136
Figure 6-16 Potentiostatic polarization of CuFeS_2 + CB slurry (a) Variation in pH during charge (cell potential = -1.0 V) and discharge cycles (cell potential = 1.0), (b) Change in current profile (Note: only CuFeS_2 slurry in $0.2 \text{ M H}_2\text{SO}_4$ was used for pH measurements)	140
Figure 7-1 The EDX spectrum of the synthetic CuFeS_2	144
Figure 7-2 Particle size distribution histograms of (a) synthetic CuFeS_2 and (b) MC	144

Figure 7-3 XRD pattern of the mineral concentrate (MC), the inset shows an SEM image of the MC particles 146

Figure 7-4 Cyclic voltammograms of composite (a) GF–CuFeS₂, (b) GF–MC electrodes obtained at various sweep rates. (c) log (v) vs. ΔE_{1,2} (peak separation) trends for the composite electrodes. (d) CV of GF–Fe/Cu electrode at different sweep rates (For composite electrodes, the current is normalized by the weight of GF + CuFeS₂ / MC, whereas for the GF–Fe/Cu electrode, the weight of GF was used to calculate the specific current). 150

Figure 7-5 Peak current (for P_{a1} and P_{c1} only) variation vs. sweep rate (v) (0.04 ≥ v < 0.1 V s⁻¹) 151

Figure 7-6 From the CV scans (0.001 ≤ v ≤ 0.02 V s⁻¹) and Equation 6.2, i_p vs. v^{1/2} of (a) GF–CuFeS₂ (b) E_p vs. log (v) of GF–CuFeS₂ electrode (c) i_p vs. v^{1/2} and (d) E_p vs. log (v) trends for the GF–MC electrode used to calculate charge transfer coefficient, α, values 151

Figure 7-7 The E_p – E_{px} vs. log (i_p) trends for the calculation of k_h (Equation 7.4) from the peak shift and peak current variation in the CV scans of (a) GF–CuFeS₂ and GF–MC (b) GF–Fe/Cu electrodes, where I represents the intercept on the y-axis after linear fitting of data. 156

Figure 7-8 CV scans obtained for FBFC at various sweep rates when the negative electrode is (a) GF–CuFeS₂ (C–1) and (b) GF–MC (C–2), whereas the positive electrode used was GF. 0.5 M Fe²⁺ + 0.1 M Cu²⁺ in 0.2 M H₂SO₄ was circulated from the external thermostatic reservoirs. (Note: The current is normalized by the weight of either synthetic CuFeS₂ or MC) (c) The i_p vs. v^{1/2} trends of the C–1 and C–2 cells (d) variation of i_{pa}/i_{pc} and peak separation due to change in sweep rate 159

Figure 7-9 GCD tests showing the (a) 1st, 250th and 500th charge / discharge cycles and (b) discharge curves of C-1 (c) 1st, 250th and 400th charge/discharge cycles of C-2 (d) discharge profiles of C-2. 163

Figure 7-10 (a) Variation in discharge specific capacity and coulombic efficiency of C - 1 and C - 2 cells (b) the maximum specific energy that can be stored by C-1 and C-2 FBFC setups. The inset shows the % Cu extraction calculated based on the weight of CuFeS₂ in the C-1 and C-2 cells 166

Figure 7-11 (a) SEM image of retrieved CuFeS₂ from C-1 after GCD cycling, the inset shows the lattice structure of CuFeS₂ and CuS (b) EDX spectrum shows the elemental composition (c) XRD pattern of CuFeS₂ after 500 GCD cycles 169

Figure 7-12 XPS core Cu 2p peaks of (a) as-synthesized and (b) retrieved CuFeS₂ particles (from the C-1 cell) show the presence of 2p_{3/2} and 2p_{1/2} spin orbitals (c) high-resolution S 2p_{3/2} peak of the as-synthesized and (d) retrieved CuFeS₂ 171

Figure 7-13 Potentiodynamic cathodic polarization of the GF-CuFeS₂ electrode in 0.2 M H₂SO₄ (anolyte) containing various amounts of Cu²⁺. The inset shows the cathodic Tafel slope (β_c) as a function of Cu²⁺ concentration. 174

Figure 8-1 (a) SEM image showing the morphology and (b) Deconvoluted S 2p_{3/2} high-resolution spectra of synthetic CuFeS₂. (c) N₂ adsorption/desorption isotherm for surface analysis and (d) multi-pore size/volume analysis curve of CuFeS₂ particles 178

Figure 8-2 (a) XRD pattern (b) XPS survey scan and (c) the deconvoluted high-resolution spectra of Cu 2p_{1/2} and Cu 2p_{3/2} bands of as-synthesized CuFeS₂ 179

Figure 8-3 (a) A three-electrode setup for measurement of electrochemical behavior of the PSE containing (80 wt. % CuFeS₂ + 20 wt. % AC in 0.2 M H₂SO₄. (b) SEM image of AC (c) Multipoint BET surface area and pore size distribution curve for AC 184

Figure 8-4 (a) CV (4th cycle) of positive electrode components; GP, GP-AC and GP-AC-CuFeS₂. (Note: exposed area of GP = 6.28 cm², 20 wt. % total solids in the slurry) (b) CV curves of negative electrode (Al strip ≈ 2 cm²). (c) Chronopotentiometry scans (30 mA cm⁻²) depicting the effect of CTAB concentration in the anolyte (vs. MSE = 0.62 V_{SHE}) (d) a potential/concentration (PC) diagram developed from the CV and chronopotentiometry results. 185

Figure 8-5 The CV of the PSE (5mV s⁻¹ sweep rate). (a) The cyclic performance of the positive electrode (5 cycles). (b) The 1st and 5th cycles show the current peaks (as labeled) used to predict the reactions sequence during actual charge/discharge process in the TFB. 188

Figure 8-6 SEM images of Zn deposit on Al substrate obtained in the base solution containing, (a) 0.1 M Na₂SO₄, (b) a + 1 ppm CTAB, (c) a + 2 ppm CTAB, (d) a + 4 ppm CTAB (e) a + 8 ppm CTAB (f) XRD patterns of Zn deposits formed in a – e 193

Figure 8-7 TFB showing the assembly of a cell connected to a potentiostat 196

Figure 8-8 Performance evaluation of TFB (a) CV curves of negative and positive electrode, (5 mV s⁻¹). (b) Equilibrium cell potential (EC) and schematic of potential drop within the TFB. (c) CV scans of TFB at various sweep rates and (d) the trends of peak current vs. (sweep rate)^{0.5} 197

Figure 8-9 (a) CV curves of TFB as shown in Figure 8-8c indicating peak P2 (b) shift in peak potentials (P1 and P3) vs. sweep rate (c) variation in peak current and potential vs. sweep rate for peak P2 200

Figure 8-10 The 10 GCD cycles (a) charge and (b) discharge cycles. (c) 20 to 100 GCD cycles; the specific capacity is calculated based on the mass of Zn deposit during the first charge cycle. (d) Repetitive CV scans of TFB obtained at 0.002 V s^{-1} 203

Figure 8-11 Quantitative assessment of (a) Specific capacity (discharge), coulombic, energy and Voltage efficiencies of the TFB. (b) Energy storage capability and % Cu extraction as a function of GCD cycles (Note: The % Cu extraction was calculated from the ICP-OES analysis). (c) The filtrate retrieved from the PSE. (d) Instantaneous % Cu extraction from CuFeS_2 in the TFB during 100 GCD cycles 205

Figure 8-12 (a) Discharge profiles of the TFB obtained at various C-rates, (charged at the 1C rate) (b) Ragone plots developed based on the first GCD cycle (c) Cell potential variation of fully charged TFB under an applied load of single LED (d) Illuminated LED when connected to fully charged TFB 208

Figure 8-13 (a) Schematic diagram of ionic species transport across AEM. (b) The molar fraction of ionic species in the anolyte at 25°C (c) The transient electric field and (d) the molar flux of SO_4^{2-} across AEM 216

Figure 8-14 I-V curve of the fully charged TFB (at 1C) showing the polarization trend and variation in specific power at various discharge currents. 219

Figure 9-1 (a) OCV of the TFB-M and (b) CV scans of the TFB-M at various sweep rates. 226

Figure 9-2 CV curves of TFB-M (at 25 mV s^{-1}) showing the variation in current response during repetitive cycling 229

Figure 9-3 The galvanostatic (a) charge and (b) discharge profiles of TFB-M (initial 3 cycles). 231

Figure 9-4 The performance of TFB-M setup (a) energy density vs. no. of cycles, (b) coulombic efficiency, (c) potential efficiency and (d) rate of Cu extraction measured from ICP–OES analysis of the PSE-M filtrate after various GCD cycles. (Note: the specific energy is calculated based on the volume of slurry in the PSE-M)..... 232

List of Symbols

Symbol	Meaning	Common Units
a & b	Adjustable parameters	–
A_m	Membrane area	m^2
av	Applied potential	V
B	Time Constant	$s^{1/2}$
C	BET constant	–
C_s^a	Bulk SO_4^{2-} concentration in anolyte	$mol\ l^{-1}$
C_s^c	Bulk SO_4^{2-} concentration in catholyte	$mol\ l^{-1}$
C_{nc}	Charge capacity	$mAh\ g^{-1}$
C_o^*	Bulk ionic concentration	$mol\ l^{-1}$
C_{sp}	Specific capacitance	$F\ g^{-1}$
D	Diffusion coefficient	$cm^2\ s^{-1}$
D_s	Diffusion coefficient of SO_4^{2-}	$cm^2\ s^{-1}$
\bar{D}_s	SO_4^{2-} diffusion coefficient within membrane	$cm^2\ s^{-1}$
dt	Change in time	s
dV	Change in potential	V
dV/dt	Shift in potential	$V\ s^{-1}$
E	Potential	V
E_{app}	Applied potential	V
E_{NOC}^N	OCP of negative electrode	V (vs. ref)
E^o	Potential	V (vs. SHE)
E_{OCP}^P	OCP of positive electrode	V (vs. ref)
E_{px}	Redox potential	V (vs. ref)
E_{pxa}	Anodic peak potential (x=1, 2, ...)	V (vs. ref)
E_{pxc}	Cathodic peak potential (x=1, 2...)	V (vs. ref)
ΔE_p	Peak separation potential	V
F	Faraday's constant	$C\ mol^{-1}$
i	Intercept	–
I(V)	Sweep rate dependant current	A
i_c	Charging current	$mA\ g^{-1}$
i_d	Discharging current	$mA\ g^{-1}$
i_dR	Potential drop at the start of discharge	V
i_o	Exchange current density	$A\ cm^{-2}$
I_{p1}	Peak current	A
i_{pa}	Anodic peak current	A
i_{pc}	Cathodic peak current	A
i_{peak}	Max. peak current	A
IR	Potential drop	V
J	Instantaneous molar flux	$mol\ m^{-2}s^{-1}$
k₁ & k₂	Differential capacitance coefficients	$A\ (V\ s^{-1})^{-1}$ & $A\ (V\ s^{-1})^{-0.5}$
k_h	Heterogeneous rate constant	$cm\ s^{-1}$
k_m	Membrane constant	–
m	Mass	gm
M	Molecular mass	gm
m/z	Mass to charge ratio	–

Symbol	Meaning	Common Units
ROMAN		
m_{GF}	Mass of the graphite felt	gm
m_{nc}	Amount of SO_4^{2-} transferred to catholyte	mol l ⁻¹
m_{Zn}	Mass of deposited Zn	gm
n	No. of electrons	–
n	Number of cycles	–
η	Overpotential	V
n_1 & n_2	Phase angle coefficient	–
N_A	Avogadro's number	–
η_C	Coulombic efficiency	%
η_E	Energy efficiency	%
η_V	Potential efficiency	%
OCP/E_{OCP}	Open circuit potential	V (vs. ref)
P	Equilibrium pressure	mbar
P1 & P2	Potential plateaux	–
P_{ax}	Anodic peak (x=1, 2...)	–
P_{cx}	Cathodic peak (x=1, 2...)	–
P^o	Saturation potential	mbar
Q_{ad}	Constant phase element (for adsorption)	mS s ⁿ²
Q_c	Specific capacity	mAh g ⁻¹
Q_{charge}	Total charge from charging cycle	C
$Q_{discharge}$	Total charge from discharging cycle	C
Q_g	Total charge (from gravimetric analysis)	C
Q_{gs}	Total charge (from galvanostatic)	C
Q_{irr}	Irreversible charge	C
R	Universal gas constant	J mole ⁻¹ K ⁻¹
R	Total resistance	Ω
R_{ad}	Resistance (for adsorption)	Ω
R_{ct}	Charge transfer resistance	Ω
R_p	Parallel resistance	k Ω
R_s	Solution resistance	Ω
S	Slope	–
s	Sweep rate	mV s ⁻¹
S_{BET}	BET surface area	m ² g ⁻¹
t	Time	s
T	Temperature	K
t_1	Initial time	s
t_2	Final time	s
V	Volume of gas adsorbed	cm ³
V	Potential window	V
v	Sweep rate	mV s ⁻¹
$V(t)$	Decay in cell potential with time	V
V_1 & V_2	Initial and final potential	V
V_A	Volume of anolyte	ml
V_C	Volume of catholyte	ml
v_p	Membrane pore volume	cm ³
V_S	Volume of slurry	ml

Symbol	Meaning	Common Units
ΔV	Potential difference	V
ΔV_{CF}	Potential delay (CF electrode)	V
ΔV_{comp}	Potential delay (composite electrode)	V
W	Weight of adsorbed N_2	gm
W_{CuFeS_2}	Initial weight of $CuFeS_2$	gm
W_m	Adsorbed N_2 monolayer capacity	gm cm ⁻²
x	Extent of reaction	–
x_m	Membrane thickness	m
Y_s	Warburg diffusion coefficient	S s
z	Charge number of SO_4^{2-}	–
Z_{img}	Impedance (Imaginary)	Ω
Z_{Re}	Impedance (Real)	Ω
GREEK		
α_a	Charge transfer coefficient (anodic)	–
α_c	Charge transfer coefficient (Cathodic)	–
β_a	Anodic Tafel slope	mV decade ⁻¹
β_c	Cathodic Tafel slope	mV decade ⁻¹
Γ_T	Surface concentration	moles cm ⁻²
θ	Membrane Tortuosity	–
Λ	Dimensionless rate constant	–
$\pi^{1/2}x(bt)$	Current function	–
σ_B	Finite diffusion coefficient	$\Omega s^{-1/2}$
σ_w	Infinite diffusion coefficient	$\Omega s^{-1/2}$
Φ_{dl}	Constant phase element (double layer)	mS s ⁿ¹
Φ_p	Constant phase element (pseudocapacitance)	S s ⁿ²
ω	Frequency	Hz
$d\Psi$	Electric field	V m ⁻¹

List of Abbreviations

AC	Activated Carbon
AEM	Anion exchange membrane
ATR	Attenuated total reflection
BET	Brunauer-Emmet-Teller
C-2	FBFC: GF-MC (Negative) & GF-Fe/Cu (Positive)
CB	Carbon black
CD	Charge/discharge
CF	An electrode assembly (GF connected to graphite rod)
CFe	FBFC: GF-CuFeS ₂ (Negative) & GF-Fe (Positive)
CFeCu or C-1	FBFC: GF-CuFeS ₂ (Negative) & GF-Fe/Cu (Positive)
Composite	Composite electrode (CuFeS ₂ encapsulated in GF)
CPE	Carbon paste electrode
CTAB	Cetyltrimethylammonium bromide
CV	Cyclic voltammetry
DC	Direct current
DFT	Density functional theory
DI	Deionized water
DMC	Dimethyl carbonate
EC	Ethylene carbonate
EDLC	Electrochemical double layer capacitor
EDX	Energy dispersive x-ray spectroscopy
EEC	Equivalent electrical circuit
EFC	Electrochemical flow cell
EIS	Electrochemical impedance spectroscopy
FBFC	Fixed bed flow cell
FGP/GP	Flexible graphite plate/Graphite plate
FTIR	Fourier-transform infrared
FWHM	Full width at half maximum
GCD	Galvanostatic charging/discharging
GF	Graphite felt
GF-CuFeS₂	Composite electrode (GF + synthetic CuFeS ₂)
GF-Fe	CF electrode immersed in Fe(II) containing electrolyte
GF-Fe/Cu	CF electrode immersed in Fe(II)+Cu(II) containing electrode
GF-MC	Composite electrode (GF + CuFeS ₂ mineral concentrate)
GHG	Greenhouse gases
GS	Galvanostatic polarization
HDPE	High density polyethylene
ICP-OES	Inductively coupled plasma-optical emission spectroscopy
I-V	Current potential curve
LED	Light emitting diode
LiBs	Lithium ions batteries
LSV	Linear scan voltammetry
MC	Mineral concentrate
MRI	Magnetic resonance imaging
OCP	Open circuit potential
OCV	Open circuit voltage
ORP	Oxidation/reduction potential

PC	Potential-concentration diagram
PCP	Potentiodynamic cathodic polarization
PD	Potentiodynamic polarization
PEM	Proton exchange membrane
PSE	Positive slurry electrode (synthetic CuFeS ₂ +AC in 0.2M H ₂ SO ₄)
PSE-M	Positive slurry electrode (MC + AC in 0.2M H ₂ SO ₄)
PTFE	Polytetrafluoroethylene
PVDF	Polyvinylidene fluoride
PVP	Polyvinyl pyrrolidone
QXRD	Quantitative x-ray diffraction
SCs	Supercapacitors
SEM	Scanning electron microscopy
SHE	Standard hydrogen electrode
SSFC	Semisolid flow cell
SX/EW	Solvent Extraction/Electrowinning
TFB	Tri-functional battery
TFB-M	Tri-functional battery setup with MC
ToF-SIMS	Time of flight secondary ion mass spectroscopy
UPD	Under potential deposition
XPS	X-ray photoelectron spectroscopy
XRD	X-ray diffraction

Glossary

Capacitive (non-faradaic)	Charge stored in the electrical double layer
Capacity	Reversible charge storage; mAh
Energy density	Energy normalized by the volume of PSE; Wh l ⁻¹
Internal charge mediator	Facilitating the charge transfer within the composite electrode i.e. formation and transportation of intermediate H ⁰ from GF to CuFeS ₂
Non-Capacitive (irreversible)	Irreversible faradaic reactions or conversion reactions
Pseudocapacitive	Charge storage due to reversible faradaic processes on the surface
Specific capacity	Charge normalized by the mass of electrode material; mAh g ⁻¹
Specific energy	Energy normalized by the mass of electrode material; Wh kg ⁻¹
Specific Power	Power normalized by the mass of electrode material; W kg ⁻¹

Acknowledgments

I express my deepest appreciation to the administrative and technical staff at the Department of Materials Engineering for their kind support during the course of my Ph.D. studies. My gratitude goes to my supervisory committee, Professor D. Dixon and Dr. W. Liu whose valuable suggestions helped me to improve my work. I also acknowledge the very useful discussions with Dr. Zih Ren about the synthesis of chalcopyrite. In particular, I am extremely grateful to my supervisor Professor Edouard Asselin, whose consistent moral and technical support and critical reviews on this research work encouraged me to do my best. Thanks to his extended compassion, professionalism, and enchanting personality, which taught me a lesson to convert my deficiencies into perfection and skills into strengths.

The financial support from *Natural Science & Engineering Research Council of Canada* (NSERC), the Four-Year Fellowship (FYF) from the *University of British Columbia* and partial funding from the *University of the Punjab* are highly acknowledged.

I am indebted to all my fellow graduate students and friends, especially Tasawar Javed, Yu Liu and M. Haziq, whose social, moral and competitive support helped me to tune my personality and technical skills. I never felt loneliness even staying thousands of miles away from my hometown in their company.

Special thanks to my daughters and son, who remained desperate for my time and company during my Ph.D. studies. My sincere gratitude to my lovely wife Uzma, whose continuous support, patience and great endurance in every hardship are incomparable. Finally, yet importantly, I do not have qualified words to tribute my father (Mairaj Deen) and mother (Ruqaya Mairaj), who's unconditional and untiring efforts from my birthday until today are incalculable and inimitable.

Dedicated to my teachers, parents,
daughters (Ulaika, Tasmia, and Fatima),
son (M. Ali Murtza), my wife Uzma and to
all my well-wishers

Chapter 1: Introduction

Cu is an essential ingredient of many technologies in our modern society including solar systems, electronics, construction, and other industrial equipment. Due to its excellent electrical and thermal conductivity, Cu is the conductor of choice for most applications. In nature, Cu largely exists in the form of oxide and/or sulfides ores (elemental or “native” Cu is also possible though rare). To produce Cu from oxide minerals via hydrometallurgical processes, the heap leach–solvent extraction-electrowinning (HL–SX–EW) sequence is adopted. On the other hand, depending on the ore grades; the sulfidic ores from mines are processed and concentrated to 25 – 35 % Cu through froth floatation. The mineral concentrate (MC) is then smelted and electro–refined to produce pure 99.99 % Cu metal [1]. At present, globally about 80 % of the total Cu production is via the pyro–metallurgical route by the use of existing smelting processes. To produce 1 tonne of refined Cu, the global GHG emission is equivalent to ~3.3 tonnes of CO₂ [2-5]. The energy requirements for Cu production and GHG emission directly relate to the grade of Cu ores. From the previous 100-year history of existing Cu mines, a continuous decline in ore grades has been evident. From 1900 to 2010, on average, global Cu grades have been substantially decreased from 1.5 – 4.0 % to 0.62 %. It is also forecasted that with an annual decline of 1.5 to 3.7 %, Cu grades may further drop to ~0.49 % in 2050 [6].

Chalcopyrite (CuFeS₂) is the main economic copper bearing mineral, which is, as discussed above, generally processed through pyro-metallurgical methods to extract the Cu. However, serious environmental issues with smelting, depletion of high-grade ores and a large number of impurities (some toxic) have resulted in continued research aimed at the development of hydrometallurgical technologies to process CuFeS₂. There are a number of

different proposed routes in the literature to treat CuFeS_2 concentrates, but only a few of them have attained commercial acceptance [7].

The literature provides good insight about the possible leaching of CuFeS_2 under oxidizing conditions or by the reductive conversion of CuFeS_2 into Cu_2S , which could in turn be more easily oxidized to Cu^{2+} . The use of Fe^{III} ions in the presence of oxygen to leach Cu^{2+} from CuFeS_2 has been rigorously studied in the past [8-11]. The energy generated during oxidation of CuFeS_2 by Fe^{III} ions in the presence of oxygen is lost as heat. In contrast to the direct reduction of Fe^{III} on CuFeS_2 , we propose that the $\text{Fe}^{\text{II}}/\text{Fe}^{\text{III}}$ redox reaction could proceed on a separate electrode in a battery like a cell setup. Thus, the amount of useful energy, which may be retrieved and stored for further use, can be quantified.

Zn is another commercially important metal that is mainly produced via acid leaching of roasted sphalerite (ZnS). The pregnant leach solution is rigorously purified to remove all the soluble metal impurities, particularly those that are electrochemically more noble than Zn and present large kinetic activity towards H_2 evolution [12-15]. Metal impurities such as Cu, Co, Ni, Cd, Pb, Sb, As, Ge and Fe etc., if they exist in the leach liquor beyond the tolerance limits, can decrease the current efficiency during electrowinning and deteriorate the deposit quality [16]. A complete flow sheet, describing the process steps of Zn metal production from mine site to pure metal is presented in section 2.5 as given elsewhere [17].

Based on the reactions that occur during the electrowinning process, Zn deposition should take place at ~ 2.0 V and the theoretical energy required for this process would be 1.63 kWh kg^{-1} . But due to large overpotentials at the electrodes (particularly on the anode, ~ 0.6 V) and a potential drop in the leach liquor, an actual cell potential of ~ 3.2 V is required for Zn electrowinning, which corresponds to an energy consumption of $\sim 2.8 \text{ kWh kg}^{-1}$ [16-18].

With a lens on energy storage and/or sustainable Cu and Zn production, the tri-functional battery (TFB) proposed here could cumulatively save an enormous amount of energy, which is otherwise individually required for both of these hydrometallurgical processes. On the other hand, the aqueous-based chemistry in this setup innately suppresses the fire hazards and other safety concerns that are specifically associated with the scale-up of Li-ions batteries for stationary applications. The cyclic charge/discharge performance and the Cu extraction is another compelling feature of this setup in contrast to the existing Ag-Zn and Zn-air primary batteries [19-21].

1.1 Research goals

To date, the extractive industries have used minerals mainly for producing metals. However, many minerals possess intrinsic characteristics that could be used for purposes other than metal production e.g. for energy storage. There exists, then, a dichotomy between the current widespread use of these minerals for metal production and their potential application as energy materials. This research work is something radically different: to leverage existing mining infrastructure to rationalize the construction of battery systems and in turn encourage remote locations to build and use renewable energies.

The main goals of this work were to develop hybrid battery like setups that can be used as energy storage devices and as units for Cu extraction mainly from CuFeS_2 . The energy storage and % Cu extraction capabilities of both synthetic CuFeS_2 and MC have been measured by using two different setups. In the first, we used as-synthesized CuFeS_2/MC as a negative electrode material in a fixed bed flow cell (FBFC). In this hybrid battery like setup, the $\text{Fe}^{\text{II}}/\text{Fe}^{\text{III}}$ redox couple in the positive compartment promoted the reduction and oxidation reactions in the negative electrode during repetitive charging and discharging cycles, respectively.

Secondly, considering the highly energy intensive nature of hydrometallurgical processes, i.e. the oxidative leaching of CuFeS_2 and electrowinning of Zn, a radically novel concept of coupling these two processes in one setup is presented. This TFB setup is capable of electrodepositing Zn in synergy with Cu dissolution from CuFeS_2 during the charging cycle in the negative and positive compartments, respectively. In addition, this setup can supply back a portion of the energy in the discharge cycle but at the expense of deposited Zn, like a battery. It is speculated that by coupling this setup with a renewable energy generating facility, i.e. wind turbines and/or solar cells, this could be an attractive technology for the remote mining locations.

1.2 Thesis outline

Chapter 2 provides a brief literature review on the hydrometallurgical processes mainly focusing on Cu extraction from CuFeS_2 in H_2SO_4 lixiviant. The leaching chemistry and possible Cu extraction mechanisms are explained. In addition, the importance of energy storage, and in particular electrochemical energy storage systems, their functionality and factors influencing their performance are also discussed in this chapter.

Chapter 3 states the motivation and key objectives of this research work. The design of the hybrid battery setups, experimental procedures, characterization of electrode materials, and performance evaluation methods are discussed in Chapter 4.

Electrochemical characterization of the composite electrode and its use as the anode (negative electrode) in the final FBFC are summarized in Chapter 5. Also, the possible reactions and charge storage mechanism by the composite electrode is rigorously investigated using electrochemical techniques. Chapter 6 describes the design and performance of the hybrid mineral battery (FBFC) in which synthetic CuFeS_2 and the $\text{Fe}^{\text{II}}/\text{Fe}^{\text{III}}$ couple were used

as negative and positive electrodes, respectively. In addition, the electrochemical behavior of the individual electrodes, the cyclic energy storage capability, and % Cu extraction capability of the FBFC is quantified.

The use of a mineral concentrate as a negative electrode and its comparison with synthetic CuFeS_2 in the FBFC is explained in Chapter 7. This chapter also describes the electrochemical reactions that occur on the various electrodes and how these relate to the performance of the FBFC during the charge/discharge process.

The construction and analytical description of the TFB, which integrates two hydrometallurgical processes, i.e., Zn electrowinning and Cu extraction from CuFeS_2 are discussed in Chapter 8. In this chapter, the operating conditions for each electrode process are optimized. In addition, the energy storage and Cu extraction capabilities of the TFB using synthetic CuFeS_2 (as a positive slurry electrode; PSE) are quantified. Chapter 9 explains some preliminary results on the use of a CuFeS_2 mineral concentrate (PSE-M) in the TFB-M.

Finally, a summary of key findings, practical implications and opportunities for future work are described in Chapter 10.

Chapter 2: Literature Review

The demand for Cu metal is rapidly growing due to ever increasing population and industrial growth. Mainly, Cu exists either in the form of oxide or sulfide minerals in the earth crust. It is estimated that total Cu reserves in the earth's crust are 2100 Mt of which approximately 1470 Mt exists in the form of CuFeS_2 . This sulfide mineral represents about 70–80% of the total world copper resource [10, 22, 23]. Generally, Cu sulfide ores containing more than 0.4 % Cu are mined, processed and concentrated to increase Cu contents to 25 – 35 %. Conventionally, Cu extraction from this mineral concentrate is achieved via smelting and electro-refining processes, which account for about 80 % of the total Cu metal production [1]. The large amount of GHG emissions (3.3 kg of CO_2 /kg of refined Cu) associated with the mineral processing and pyrometallurgical processes is another big global challenge [2].

The hydrometallurgical treatment of low-grade sulfidic minerals is considered more economical and environmentally friendly compared to pyrometallurgical processes. Currently, approximately 20 % of world Cu production occurs via a hydrometallurgical route but this is largely directed at oxide minerals and secondary sulfide minerals, such as chalcocite and covellite. The hydrometallurgical processes use acidic lixiviants and Fe^{III} to leach Cu from the secondary sulfides but the processing of CuFeS_2 is not currently viable using this technology.

With the gradual decline in Cu ore grades over the past century, the economic and environmental feasibility of existing mineral processing technologies are threatened. One of the major issues is the high energy demand for such processes, which is mostly met by the burning of fossil fuels. At remote mine sites, renewable energy sources could be an acceptable alternative to fossil fuels. The major drawback of these energy generating units is their intermittent and unpredictable energy supply due to geological conditions, weather, time

and/or location etc. However, from such sources, the continuous supply of energy could be ensured by coupling with smart grid systems integrated with efficient energy storage systems i.e. batteries.

Given the above, the focus of this research is the use of CuFeS_2 as an electrode material in battery-like setups, in which the possibility of both energy storage and Cu extraction are explored. In this Chapter, our discussion is constrained to the hydrometallurgical treatment of CuFeS_2 and the Zn electrowinning process - concepts that are used in these battery setups. Finally, a brief literature review on existing electrochemical energy storage systems e.g. batteries and supercapacitors is provided.

2.1 Structure of CuFeS_2

The crystal structure of CuFeS_2 is similar to sphalerite (ZnS) in which the tetragonal unit cell contains four Cu, four Fe and eight S atoms representing the $I\bar{4}2d$ space group as shown in Figure 2-1a. The c-length is almost twice the length of 'a = 0.5289 nm' in a unit cell and two atoms of each Cu and Fe occupy tetrahedral interstitial sites of S atoms framework at the half of c-axis [24]. Each Fe and Cu atom is coordinated with the S atoms as a tetrahedron. The S atoms in the tetrahedron are slightly shifted from the center towards the Fe-Fe edge resulting in an Fe-S bond length of 0.2257 nm and Cu-S bond length of 0.2302 nm. On the other hand, each S atom in the unit cell is bonded with two atoms of Cu and two atoms of Fe [23].

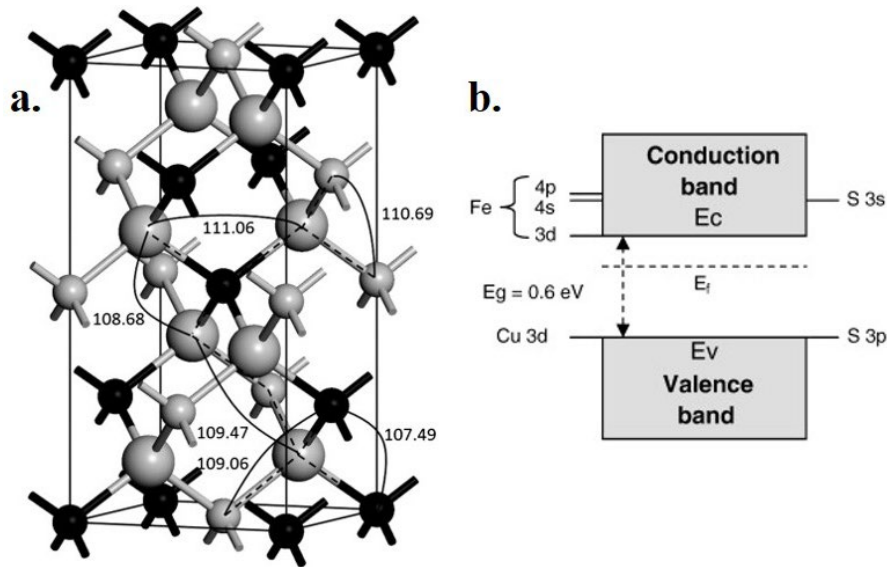


Figure 2-1 (a) Unit cell of CuFeS₂ in which each Cu atoms are shown in black spheres, Fe and S atoms are represented as small and large grey spheres, respectively [24]. (b) Schematic of CuFeS₂ band structure [10]

Neutron diffraction studies have shown that CuFeS₂ is antiferromagnetic at room temperature and the bond angles of Fe–S and Cu–S are 109.47° and 108.68–111.06°, respectively [25, 26]. Based on the neutron diffraction results, the zero magnetic moment of Cu, and filled 3d shell corresponds to the oxidation states of +1 and +3 for Cu and Fe, respectively. However, S atom in the chemical formula have the oxidation state of –2, hence suggesting a chemical formula for CuFeS₂ of Cu⁺Fe³⁺(S²⁻)₂ [24-27]. CuFeS₂ is a degenerate semiconductor having a band gap in the range of 0.53–0.6 eV and it behaves like a metal as confirmed from its optical, magnetic and electrical properties [27-29]. As shown in Figure 2-1b, the band gap of CuFeS₂ depends on the spin of Fe in the lattice structure and near the Fermi level the individual contribution of Fe(3d) at the bottom of conduction orbitals and Cu(3d)/S(3p) orbitals at the top of valence band decides its value [27].

2.2 Eh-pH diagram of CuFeS₂ and discrepancies

The stability of CuFeS₂ in aqueous solutions and its tendency to form other phases in oxidizing, reducing, acidic and basic conditions can be explained with the help of potential-pH diagram as shown in Figure 2-2. In this diagram, several discrepancies related to the difference between theoretical thermodynamic aspects and experimental evidence have been explained [30]. Thermodynamically, at low pH, the oxidation of CuFeS₂ should form bornite (Cu₅FeS₄), pyrite (FeS₂), chalcocite (Cu₂S) and covellite (CuS) as a product but all of these reactions would proceed in the presence of H₂S as a reactant. None of these products has been reported to form under laboratory conditions even in the presence of H₂S. For example, the nucleation and growth of Cu₂S and FeS₂ would require an extended period and severe geological conditions. On the other hand, the oxidation of CuFeS₂ into Cu²⁺ is possible with the formation of elemental S⁰, which occurs under aggressive oxidizing conditions and is one of the main possible reactions. Also, the formation of Cu²⁺ species should further promote the oxidation of S⁰ into sulfate (SO₄²⁻). But under laboratory conditions, it has been reported that due to the extended stability of sulfide sulfur, experimentally its oxidation into sulfate would require highly aggressive oxidizing conditions contrary to the observations in the potential-pH diagram at ambient conditions shown in Figure 2-2 [30, 31].

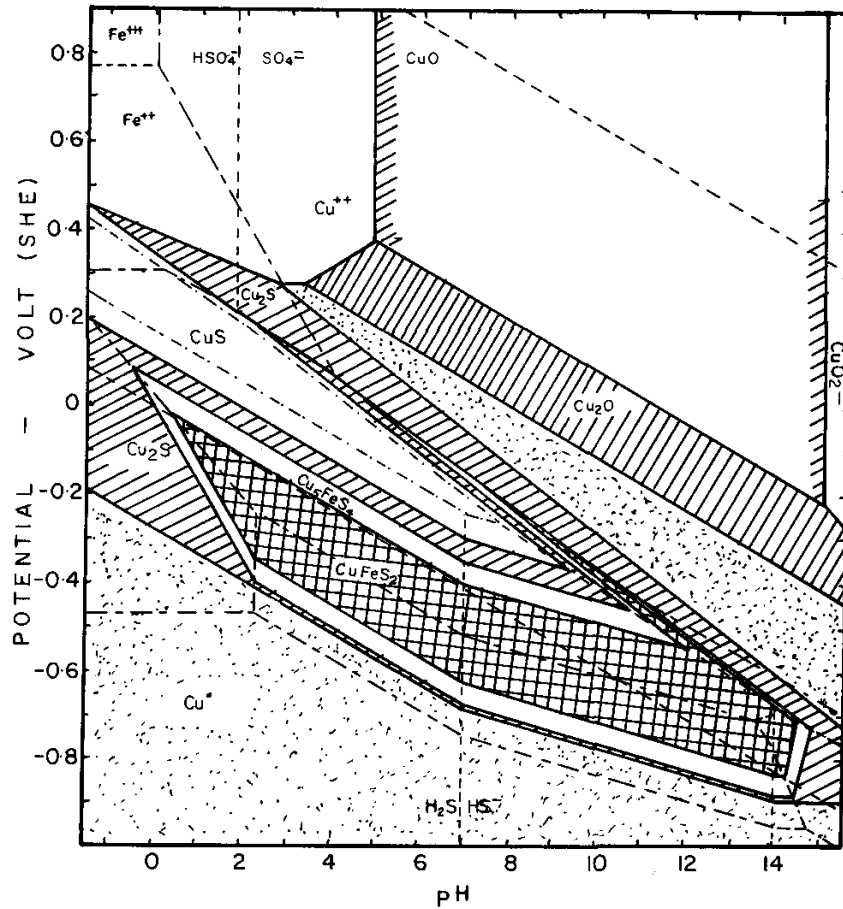


Figure 2-2 Potential-pH diagram of Cu-Fe-S-H₂O (activity of solute = 0.1 M, except $a_{\text{Cu}^{2+}} = 0.01$ M) at 25 °C [30]

From Figure 2-2, it may be predicted that CuFeS_2 can be reduced to Cu_2S and eventually Cu. These reactions have been experimental confirmed by Nava et al. [32], who suggested the reduction of CuFeS_2 into intermediate species i.e. talnakhite ($\text{Cu}_9\text{Fe}_8\text{S}_{16}$) and Cu_5FeS_4 prior to conversion into Cu_2S at potential < -0.385 V vs. SHE. Under alkaline conditions, the formation of Fe, and Cu oxides as predominant species have been reported in the literature. For instance, Todd et al. [33] examined the nature of surface species formed in air saturated aqueous solutions and suggested the formation of Fe_2O_3 and Fe-O-OH dominant species at high pH (between 3.28 – 10.67). Yin et al. [34] reported the formation of a Fe_2O_3

and CuS_2 surface layer at potential < 0.54 V vs. SHE in an alkaline solution of pH 9.2. With an increase in pH from zero to 13, the sulfur to sulfate ratio decreased to 3.2:1 from 6:1 and very little passivation effect was evident in weakly acid and in strongly alkaline solutions.

2.3 Passivation of CuFeS_2

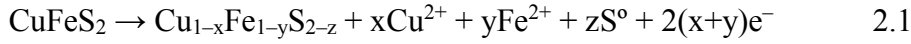
The slow dissolution of CuFeS_2 under most hydrometallurgical conditions has been reported to be due to the formation of a passive film on its surface. The extended sulfide sulfur stability and the existence of metal-deficient sulfide sulfur species of descending coordination states i.e. monosulfide (S^{2-}), disulfide (S_2^{2-}) and polysulfide (S_n^{2-}) due to physical relocation of atoms at the cleaved surface of CuFeS_2 have been experimentally confirmed [35]. The surface oxidation of CuFeS_2 in air has been reported in various studies. The formation of a thin surface layer (3 – 4 nm) containing CuS , S , Fe_2O_3 , Cu(II)O , Cu(II)S , Fe-O-OH and/or Cu(II)/Fe(III) sulfate species on the surface of CuFeS_2 is possible when exposed to air and/or water under ambient conditions [33, 36-38]. An increase in the concentration of Fe as oxide and hydroxide at the surface would lead to the enrichment of Cu^+ species bonded with S in the form of CuS_2 during the initial stage of oxidation based on the XPS analysis of the S 2p spectrum [39-41].

During acidic oxidative leaching processes, CuFeS_2 dissolution is inhibited and formation of the passive film is believed to be one of the main reasons for its slow kinetic response. The nature of this inhibition (and the passive film that may be responsible) is still controversial and a number of studies describe it as elemental S^0 [42, 43], S_2^{2-} [34, 44, 45], S_n^{2-} and/or Fe hydroxy-oxide [46, 47]. However, the S^{2-} , S_2^{2-} , S_n^{2-} , $\text{Cu}_{1-x}\text{Fe}_{1-y}\text{S}_2$ ($x + y \approx 1$ and $y \gg x$), iron deficient sulfide and CuS_n ($n > 2$) species are detected within the surface film and well documented in the literature [48]. Also, another possible reason for slow CuFeS_2

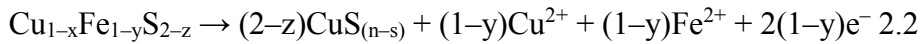
dissolution could be its n-type semiconductive behavior as reported by Crundwell and coauthors [49]. They proposed that the slow anodic dissolution of CuFeS_2 is due to the formation of an electron depleted region at the surface and is exhibited by the decrease in current due to application of potential in the reverse bias. However, recently, Nicol *et al.* [50] questioned the relevance of the semi-conductive behavior of sulfide minerals i.e. CuFeS_2 and FeS_2 during anodic dissolution. They proposed that at potentials < 1.0 V, the rate-determining step for the dissolution of CuFeS_2 was associated with the solid-state diffusion of Fe or possibly Cu from the passive film. In direct contradiction to the theory proposed by Crundwell *et al.* [51], the photocurrent generation during oxidation of these minerals in acidic sulfate solutions was shown by Nicol *et al.* [50, 52]. They proposed that current generation was related to thermal effects in the semiconductive surface film and not to the bulk CuFeS_2 . Despite these contradictions about the mechanism of anodic dissolution of transition metal sulfide minerals, there exists a large consensus on the formation of a metal-deficient sulfide sulfur enriched layer at the surface, which likely restricts mineral dissolution [52].

The polarization curve of polycrystalline natural CuFeS_2 (98.1 wt. %) in 0.5 M H_2SO_4 is shown in Figure 2-3 [11]. The curve was obtained by polarizing the electrode in both anodic and cathodic regions potentiostatically, the steady state current vs. potential values are plotted. In the anodic polarization curve, the limiting current within the 0.6 – 0.9 V vs. SHE potential region suggests the passivation of CuFeS_2 followed by transpassive behavior depicting the breakdown of the passive film. The continuous increase in current in the transpassive region corresponds to the active dissolution of CuFeS_2 . In the passive region, at low potential (< 0.9 V vs. SHE), the preferential dissolution of Fe from the surface would lead to the formation of

a metal deficient polysulfide film ($\text{Cu}_{1-x}\text{Fe}_{1-y}\text{S}_{2-z} + z\text{S}^0$, where $y > x$) according to reaction 2.1 as suggested by many authors [11, 48, 53].



The formed polysulfide film has semiconductive properties [46] and it has been shown that ferric reduction on the surface of passivated CuFeS_2 is faster than the oxidation of chalcopyrite itself [11]. This polysulfide film is further decomposed into another intermediate $\text{CuS}_{(n-s)}$ product at about 0.7 V vs. SHE according to reaction 2.2 [48, 53].



The formation of these intermediate polysulfide products i.e. bornite type $\text{Cu}_{1-x}\text{Fe}_{1-y}\text{S}_{2-z}$ ($y > x$) and covellite type CuS_n during CuFeS_2 oxidation were found to be thermodynamically stable products as suggested in the potential-pH diagram [30, 48]. This demonstrates that Fe deficient but Cu enriched polysulfide film provides a barrier to electron and ion transport. Recently, Ghahremaninezhad et al. [11] proposed that during the leaching process, the electron transport through this passive film is controlled by the diffusion of Fe atoms.

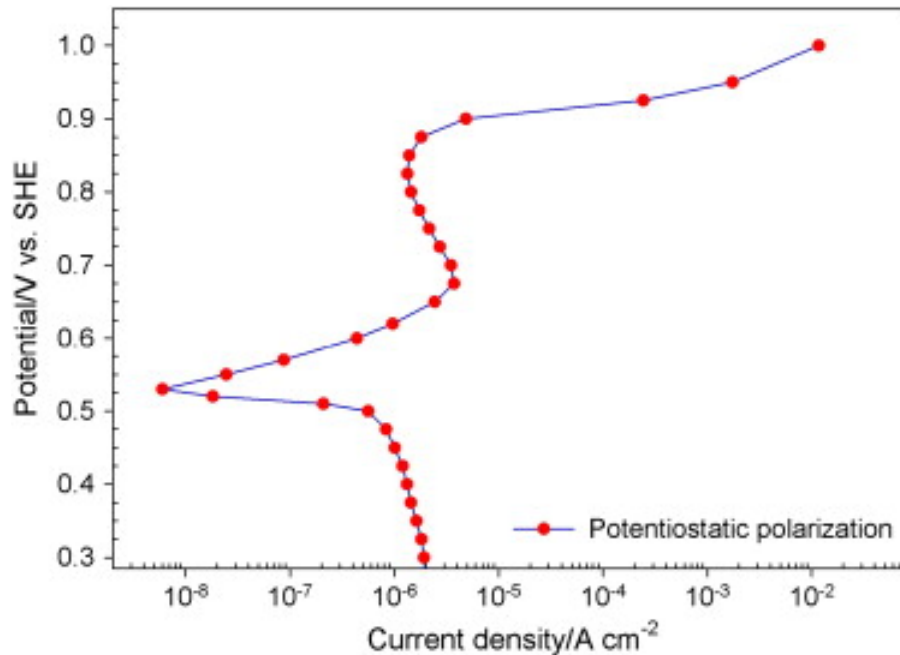


Figure 2-3 Polarization trend of CuFeS₂ in 0.5 M H₂SO₄ developed from the steady-state current values obtained potentiostatically [11]

2.4 Leaching of CuFeS₂

As given in the literature, various leaching approaches have been adopted to increase the Cu dissolution rate under oxidizing conditions, but few of these processes has gained commercial acceptance [7]. The reason for the low Cu extraction rate from CuFeS₂ has been widely investigated in the past and there exists a general agreement about the formation of a surface layer, which impedes this process, as discussed above. Nevertheless, the extent of the dissolution reaction and the nature of the surface film remains controversial. Many studies have shown that with an increase in temperature, acid or oxidant concentration, the dissolution of CuFeS₂ can be enhanced. Other factors i.e. acidic type of lixiviant, particle size, agitation speed, mechanical activation, redox potential, and pulp density etc. also influence the dissolution kinetics as discussed in the following sections.

2.4.1 Leaching in sulfate media

Leaching of CuFeS_2 in sulfate media is preferred due to the compatibility of this process with the established heap leaching processes for Cu_2S and CuS . Also, conventional solvent extraction and electrowinning technologies developed for the SX-EW process can be adopted without significant modification [54]. However, at ambient temperature and pressure, during the leaching process, the formation of a passive film on the surface of CuFeS_2 in the sulfate media hinders the dissolution of Cu, which makes this process industrially unfeasible. Sulfate-based (in H_2SO_4) leaching processes typically use ferric sulfate and oxygen as oxidants. However, to enhance Cu dissolution and to aid in the re-oxidation of ferrous to ferric, leaching is carried out at various temperatures and in the presence of bacteria. The reaction chemistry of CuFeS_2 in the acidic sulfate medium and favorable conditions for Cu extraction are summarized in Table 2-1 [48]. Generally, the sulfide sulfur of CuFeS_2 oxidizes to either elemental S^0 or SO_4^{2-} in the presence of oxidants e.g. Fe^{3+} and O_2 . In ferric sulfate solution, the leaching rate of chalcopyrite is slow due to the formation of the secondary reaction products discussed above.

At atmospheric pressure, the conditions for the leaching of Cu from CuFeS_2 in sulfuric acid solution depend on the solution potential. Increased Cu dissolution has been reported up to approximately 0.6 V vs. SHE (referred to as the passivation potential) [10, 11, 55]. Beyond this potential, the observed decrease in dissolution is attributed to the passivation of CuFeS_2 . The effect of H_2SO_4 concentration and temperature on the passivation potential of CuFeS_2 is shown in Figure 2-4a. The passivation potential at low (25 – 40 °C) and at moderately high temperature (60 – 80 °C) is found to be independent to the acid concentration. However, the low passivation potential (~0.44 V vs. SCE) at low temperature and relatively high passivation

potential (~ 0.52 V vs. SCE) at high temperature indicate the CuFeS_2 transition from active to passive. It can be observed that the active to passive transition at 50°C is sensitive to the H_2SO_4 concentration and the passivation potential decreased from 0.5 V to 0.44 V vs. SCE with an increase in acid concentration from 2 to 70 g l^{-1} [56]. In agreement with Viramontes et al. [56] and results reported in the following discussion, batch leaching tests conducted at 80°C by Khoshkhoo et al. [57] yielded a Cu extraction of $\sim 80\%$ in 24 h at low redox potential (0.42 V vs. Ag/AgCl), as shown in Figure 2-4b. These results are consistent with the active dissolution of Cu from the mineral concentrate compared to results obtained at high redox potential (0.62 V vs Ag/AgCl), where the formation of the passive film restricted the leaching process.

Increasing the Cu extraction from CuFeS_2 is possible either by adjusting the oxidation-reduction potential (ORP) of the solution with the addition of oxidants, bacteria or by applying an external potential. The accelerated Cu leaching under an applied potential of $0.4 - 0.45$ V (vs. Ag/AgCl) and in the presence of moderate thermophilic bacteria at 50°C , $\sim 90\%$ Cu extraction was achieved in 20 days as depicted in Figure 2-5.

In comparison, in only the bioleaching process, and under ORP controlled processes by either chemically or via electrochemically, the copper extraction was $\sim 65\%$ and $< 30\%$, respectively.

In another study, the ORP was controlled at 0.635 V vs. SHE by the addition of KMnO_4 in the suspension containing 1 M H_2SO_4 and FeSO_4 at 50°C [55]. The leaching reaction was found to be surface controlled and related to the formation of elemental sulfur on the surface of CuFeS_2 . As reported by Sandstrom et al. [58], the Cu extraction was enhanced in the presence of thermophilic bacteria (*Sulfolobus metallicus*) and constant redox potential of 0.6 V vs. Ag/AgCl was maintained by sparging CO_2 enriched air in the bioreactor. The complete

oxidation of sulfide sulfur to sulfate was possible under these conditions but the limited Cu extraction was related to the passivation of CuFeS_2 and precipitation of Jarosite.

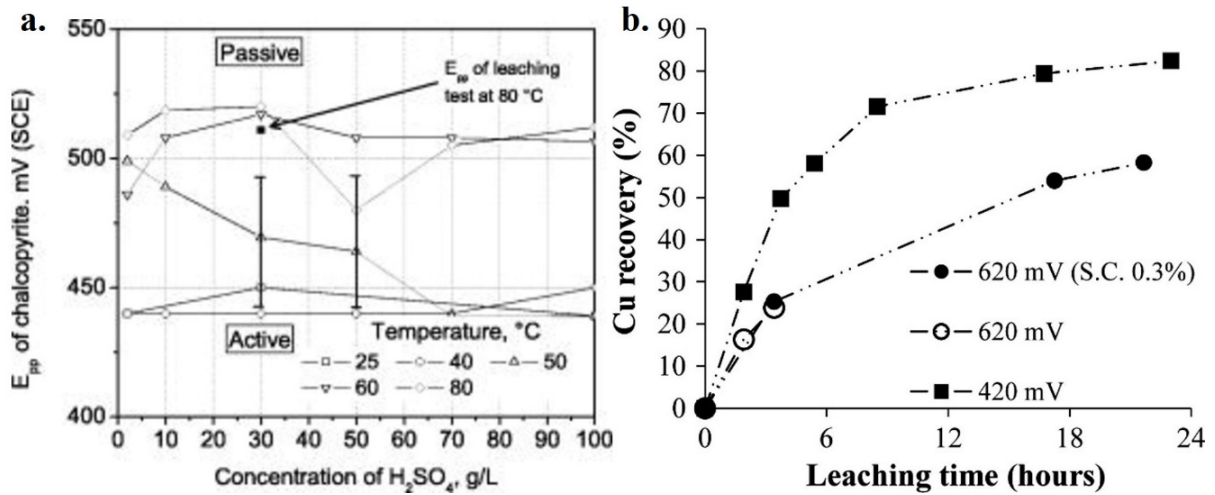


Figure 2-4 (a) Effect of H_2SO_4 concentration and temperature on the passivation potential of CuFeS_2 [56](b) % Cu recovery from the Kristineberg concentrate at 80 °C. The redox potentials were adjusted by the addition of dilute H_2O_2 in H_2SO_4 solution (pH =1.5) containing initial Fe^{2+} (1 g l^{-1}) [57]

Hackl et al. [48] described the effect of temperature (between 110 – 220°C) on Cu and Fe extraction from chalcopyrite, as shown in Figure 2-6. The relatively low copper extraction of 45 – 50 % in the range of 130 – 170 °C was thought to be due to molten sulfur encapsulation of the mineral particles, which is known to restrict metal extraction by blocking solution access to the mineral surface. The rapid increase in the Cu extraction and a sharp decrease in Fe contents beyond this temperature to 220 °C were attributed to complete S^0 oxidation to SO_4^{2-} and Fe precipitation in the form of Jarosite, respectively.

Various sulfate-based processes have been patented in the recent past, very few of these have been commercialized and only a handful of others have achieved pilot plant or demonstration status [7, 59]. The medium (150°C) and high-temperature (>200°C) processes are out of the

scope of this work (Table 2-2). Further details about these processes and operating conditions may be found in the paper by Dreisinger [7] and references cited therein.

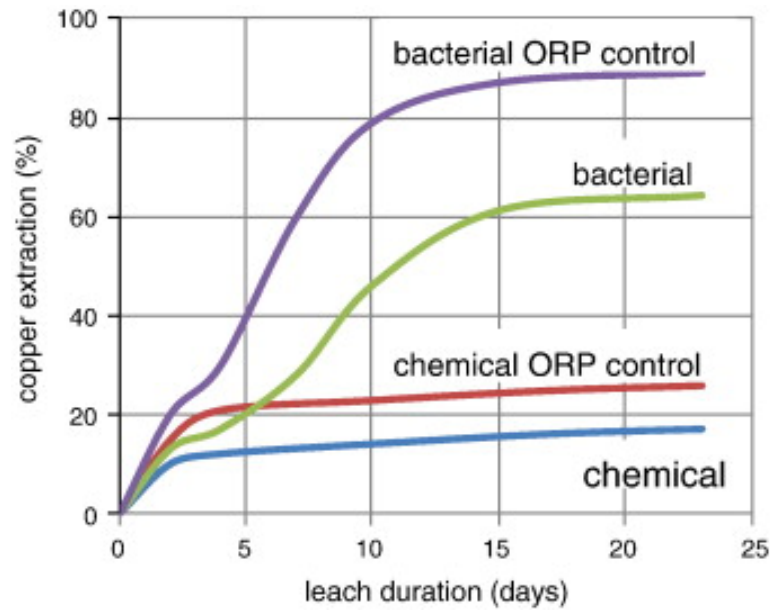


Figure 2-5 Strategies applied to enhance Cu extraction form CuFeS_2 . (Note: ORP was controlled by applying DC potential of 0.4–0.45 V vs. Ag/AgCl electrode, bacterial controlled process was carried out at 50 °C) [60, 61]

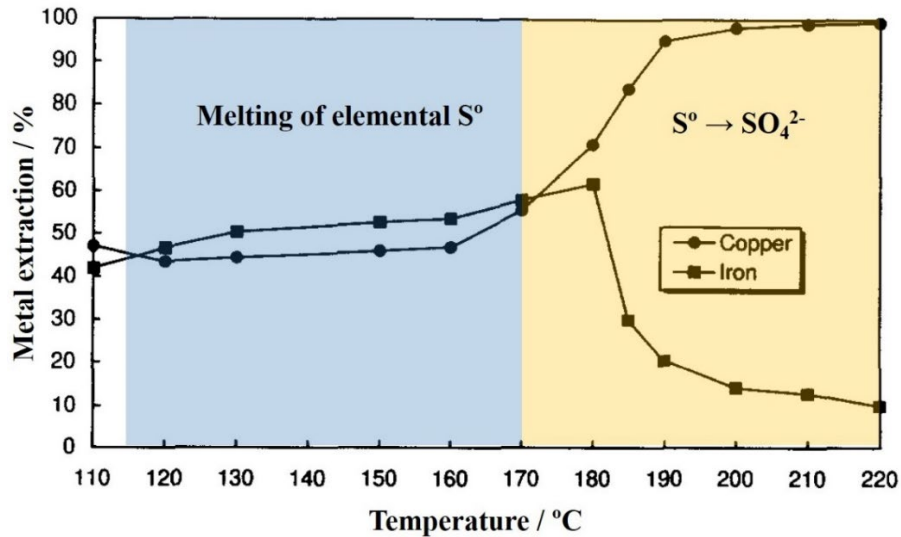


Figure 2-6 Percentage Cu and Fe extraction at various temperatures, 100 g solids in 1 liter of 1 M H_2SO_4 solution containing initial $10 \text{ g l}^{-1} \text{ Cu}^{2+}$ and $5 \text{ g l}^{-1} \text{ Fe}^{3+}$ was used [48]

Table 2-1 Oxidative acidic sulfate leaching of CuFeS₂, the reaction chemistry [48]

Leaching Process	Temperature (°C)	Possible Reactions	Ref.
Bacterial leaching	20 – 40	$\text{CuFeS}_2 + 4\text{O}_2 \rightarrow \text{Cu}^{2+} + \text{Fe}^{2+} + 2\text{SO}_4^{2-}$ $2\text{Fe}^{2+} + 0.5\text{O}_2 + 2\text{H}^+ \rightarrow 2\text{Fe}^{3+} + \text{H}_2\text{O}$ $\text{CuFeS}_2 + 4\text{Fe}^{3+} \rightarrow \text{Cu}^{2+} + 5\text{Fe}^{2+} + 2\text{S}^{\circ}$ $\text{S}^{\circ} + 1.5\text{O}_2 + \text{H}_2\text{O} \rightarrow \text{H}_2\text{SO}_4$	[62-64]
Ferric sulfate leaching	20 – 100	$\text{CuFeS}_2 + 4\text{Fe}^{3+} \rightarrow \text{Cu}^{2+} + 5\text{Fe}^{2+} + 2\text{S}^{\circ}$ $\text{CuFeS}_2 + 16\text{Fe}^{3+} + 8\text{H}_2\text{O} \rightarrow \text{Cu}^{2+} + 17\text{Fe}^{2+} + 2\text{SO}_4^{2-} + 16\text{H}^+$	[65, 66]
Pressure oxidation (O ₂)	100 – 220	$\text{CuFeS}_2 + 4\text{H}^+ + \text{O}_2 \rightarrow \text{Cu}^{2+} + \text{Fe}^{2+} + 2\text{S}^{\circ} + 2\text{H}_2\text{O}$ $\text{CuFeS}_2 + 4\text{O}_2 \rightarrow \text{Cu}^{2+} + \text{Fe}^{2+} + 2\text{SO}_4^{2-}$ $2\text{Fe}^{2+} + 0.5\text{O}_2 + 2\text{H}^+ \rightarrow 2\text{Fe}^{3+} + \text{H}_2\text{O}$	[59, 67]

Table 2-2 Sulfate based Cu extraction processes from ore or mineral concentrate commercialized and/or studied at pilot plant scale [7, 60]

Process	Temperature (°C)	Pressure (atm)	Particle Size, D80 (µm)	Special Requirements	Ref.
BioCOP™	65 – 80	1	37	Use of thermophilic bacteria	[68]
TPOX	200 – 230	30 – 40	37	High temperature and pressure is required	[69]
Mt. Gordon	90	8	100	Pressure oxidation of Cu ₂ S/FeS ₂ or concentrate in Fe sulfate solution	[70]
Activox	90 – 110	10 – 12	5 – 10	Very fine grinding and high O ₂ overpressure	[71]
Albion	85	1	5 – 10	Very fine grinding of concentrate and Fe ³⁺ species	[72]
Anglo American–UBC	150	10 – 12	10 – 15	Use of surfactant with moderate grinding for CuFeS ₂ leaching	[73]
Galvanox™	80	1	53 – 75	Addition of Pyrite (FeS ₂ :CuFeS ₂ = 2:1)	[74]

2.4.2 Factors influencing CuFeS₂ leaching

There are many factors i.e. type and concentration of lixiviant, oxidant, and temperature which significantly affect the leaching kinetics of CuFeS₂. In addition, particle size, pulp density, and agitation speed are also found to be important considerations to evaluate the leaching behavior [24]. Both from an economic point of view and from a process optimization perspective, a rigorous analysis of the effect of acid concentration (pH control) is always necessary. The use of H₂SO₄ is very common for CuFeS₂ leaching as explained above and many processes use this lixiviant due to its compatibility with the well-established downstream processes, i.e. solvent extraction (SX) and electrowinning (EW). High concentrations of acid (pH < 0.5) may promote the formation of the Fe deficient surface layer leading to passivation of CuFeS₂ and therefore, 0.1 – 1 M concentration is suggested to be optimal for most processes [75]. Among various oxidants, e.g. Cu²⁺, Cr₂O₇²⁻, O₂, H₂O₂, ClO₃⁻, O₃, MnO₄⁻, HNO₃, NaNO₃ and S₂O₈²⁻, Fe³⁺ is the most inexpensive reagent, which has been widely utilized for the oxidative leaching of CuFeS₂ (and other sulfide minerals) and it may be regenerated during the leaching process [24, 60]. The addition of Cu²⁺ species in H₂SO₄ solution containing ferrous ions can reduce CuFeS₂ to Cu₂S at low potential (0.56 V vs SHE) via metathesis, the Cu₂S can then be further, and more readily, oxidized by dissolved O₂ [76].

H₂O₂ is another strong oxidant in dilute acidic solution and in the presence of Fe²⁺: it dissociates into OH[°] and OH⁻ with the generation of Fe³⁺ [77]. These species may further oxidize the sulfide sulfur species into more porous elemental S[°] and/or SO₄²⁻ [78]. In other studies, an improvement in the Cu extraction (from 20 to 60 %) was achieved by the addition of ethylene glycol in the H₂SO₄-H₂O₂ media at 65 °C due to the restricted decomposition of H₂O₂ at such high temperature [79, 80]. However, permanganate ions (MnO₄⁻) are not used as

a direct oxidant for the leaching of CuFeS_2 but these species have been used as surrogate oxidants, i.e. to oxidize ferrous ions to ferric and therefore maintain the high ORP of the solution [58]. The rate laws, kinetic behavior and the use of other oxidants (e.g. $\text{Cr}_2\text{O}_7^{2-}$ and ClO_3^-) are not discussed here but for detailed information it is recommended to consult the reviews by Watling [60] and Li et al. [24] in addition to the references cited therein.

Independent to the impurity contents in the mineral concentrate, pH and temperature, the active dissolution of CuFeS_2 takes place below 0.68 V vs. SHE. Careful control of the ORP by the addition of oxidants and/or by the adjustment of temperature have always been important considerations to avoid passivation of CuFeS_2 as discussed above.

Many authors reported no positive effect of mixing or agitation on CuFeS_2 dissolution even in the presences of various oxidants. For instance, Dutrizac [81] reported that mixing has a very negligible effect on CuFeS_2 dissolution in both ferric chloride and ferric sulfate solution. However, in the presence of $\text{K}_2\text{Cr}_2\text{O}_7 + \text{H}_2\text{SO}_4$ [82] and HClO_4 (without Fe^{3+} addition) [35], the highest dissolution rate was achieved with an increase in mixing rate up to 400 and 500 rpm, respectively. At high mixing rate, a significant decrease in dissolution rate was observed and thought to be controlled by bulk diffusion processes which were associated with the depletion of reacting species on the surface of CuFeS_2 . The benefit of magnetic agitation over mechanical stirring and its positive effect on the increase in abrasion of CuFeS_2 particles improved the Cu dissolution rate as highlighted by Nicol et al [83]. In contrast, other work by Sokic et al. [84] and Adebayo et al. [77] showed a decrease in leaching rate with increase in stirring speed in an H_2SO_4 solution containing NaNO_3 and H_2O_2 oxidants, respectively. These authors found that little particle to oxidant contact and/or H_2O_2 dissociation at large stirring speed would limit the dissolution tendency of CuFeS_2 .

Recently, mechanical activation of CuFeS_2 by grinding in the presence of Fe^{3+} has been carried out, which resulted in the formation of a very soluble copper sulfate layer on the particles. During successive activation and leaching steps (leaching in H_2SO_4 , pH 1 and at $50\text{ }^\circ\text{C}$), about 98 % Cu extraction was possible in 1.5 h [85, 86].

The particle size and/or surface area of CuFeS_2 particles is very critical in term of dissolution kinetics, as it would directly affect the reactor design and operating cost. During the leaching process, diffusion-controlled processes such as the development of a product layer (passive film) on the CuFeS_2 would always require smaller particle sizes to achieve effective dissolution, as discussed in many studies [75, 77, 81-84].

2.4.3 Reduction of CuFeS_2

As learned from the previous discussion, the leaching of Cu from CuFeS_2 is usually carried out under oxidative conditions. Despite the significant advances in the oxidative hydrometallurgical processes in the past decades, still there exists the controversial passivation issue, which has forced researchers to investigate alternative strategies for efficient Cu extraction from CuFeS_2 . This has led to the development of various processes including, high temperature/pressure treatment, use of oxidants, fine grinding etc. and has introduced complex downstream steps for the efficient recovery of Cu and other precious metals.

As depicted in Figure 2-2, thermodynamically, at low pH < 2 , CuFeS_2 may reduce into Cu_2S with the formation of some intermediate products i.e. bornite and elemental Cu. However, it is noticed that the stability lines for these phases are below the H_2 evolution line and conversion of CuFeS_2 into these species depends, of course, on its kinetic response in a given system. In a detailed study by Warren et al. [87], electrochemical investigation revealed

the formation of Cu₂S or djurleite (Cu_{1.96}S) during cathodic polarization in H₂SO₄ containing Cu²⁺ and Fe²⁺ species.

The reductive decomposition of CuFeS₂ is carried out to generate an intermediate Cu₂S product, which is more reactive and may be more easily oxidized. Many approaches in the past have been adopted to improve Cu leaching from CuFeS₂ via reduction processes, which have included the use of reducing agents i.e. metallic Fe [75], Cu [88], Al [89], and Pb [90] and/or nascent hydrogen (H⁰) in an electro-assisted reduction process [91].

A detailed electrochemical analysis of CuFeS₂ reduction (carbon paste electrode) in 1.7 M H₂SO₄ suggested the formation of intermediate products i.e. talnakhite (Cu₉Fe₈S₁₆), bornite (Cu₅FeS₄) before conversion into Cu₂S and Cu [32] within various potential ranges as given in Table 2-3. These results support to the electrochemical results discussed by Elsherief [92], who also claimed the formation of Cu₂S and metallic Cu at extremely negative potentials. During cathodic polarization, Fe³⁺ atoms in the crystal lattice of CuFeS₂ at the surface accept electrons and preferentially dissolve in the solution by leaving behind Cu and S species. These reorganize themselves to form an Fe deficient structure at the surface as discussed above [93].

Table 2-3 Formation of possible species during electrochemical reduction of CuFeS₂ in 1.7 M H₂SO₄ [32]

Potential (E vs. SHE)	Possible reactions
0.115 ≥ E > -0.085	9CuFeS ₂ + 4H ⁺ + 2e ⁻ ⇌ Cu ₉ Fe ₈ S ₁₆ + Fe ²⁺ + 2H ₂ S
-0.085 ≥ E > -0.285	5CuFeS ₂ + 12H ⁺ + 4e ⁻ ⇌ Cu ₅ FeS ₄ + 6H ₂ S + 4Fe ²⁺
-0.285 ≥ E > -0.385	2CuFeS ₂ + 6H ⁺ + 2e ⁻ ⇌ Cu ₂ S + 2Fe ²⁺ + 3H ₂ S
-0.385 ≥ E	Cu ₂ S + 2H ⁺ + 2e ⁻ ⇌ 2Cu + H ₂ S CuFeS ₂ + 4H ⁺ + 2e ⁻ ⇌ Cu + Fe ²⁺ + 2H ₂ S

2.5 Zn electrowinning and its use in energy storage

Zn is another important metal and ~7 million tonne of Zn is produced annually, mainly by acid leaching of roasted sphalerite (ZnS). This is followed by rigorous purification of leach solution to remove all soluble impurities i.e. Cu, Co, Ni, Cd, Pb, Sb, As, Ge and Fe etc. The complete removal of impurities, particularly those that are more electropositive than Zn and have low overpotential for H₂ evolution is essential [12-14, 94]. These impurities in the leach liquor may decrease the current efficiency, deteriorate deposit quality and may increase the energy requirements during electrowinning [16]. The flow sheet, describing the process steps of Zn metal production from Zn concentrate to pure metal is shown in Figure 2-7 as reported elsewhere [17, 95]. During roasting, ZnS concentrate is oxidized to ZnO and SO₂. The gas is further processed to produce sulfuric acid which can be reused in the following leach process of the solid residue. Leaching of ZnO is carried out in spent electrolyte generated in the electrowinning step. Initially, leaching is conducted in continuous stirred tanks containing an almost neutral solution of pH ~5 at 60 °C. The unreacted solids in the concentrate are further classified and leached in H₂SO₄ (5–10 g l⁻¹) solution before leaching in hot (90 °C) strong acidic solution (containing 30 –100 g l⁻¹ H₂SO₄). Iron and other impurity removal is essential prior to the electrowinning. The ferrous species produced during the leaching process are oxidized to ferric which are precipitated as either jarosite, goethite and/or hematite depending on the process conditions applied [96].

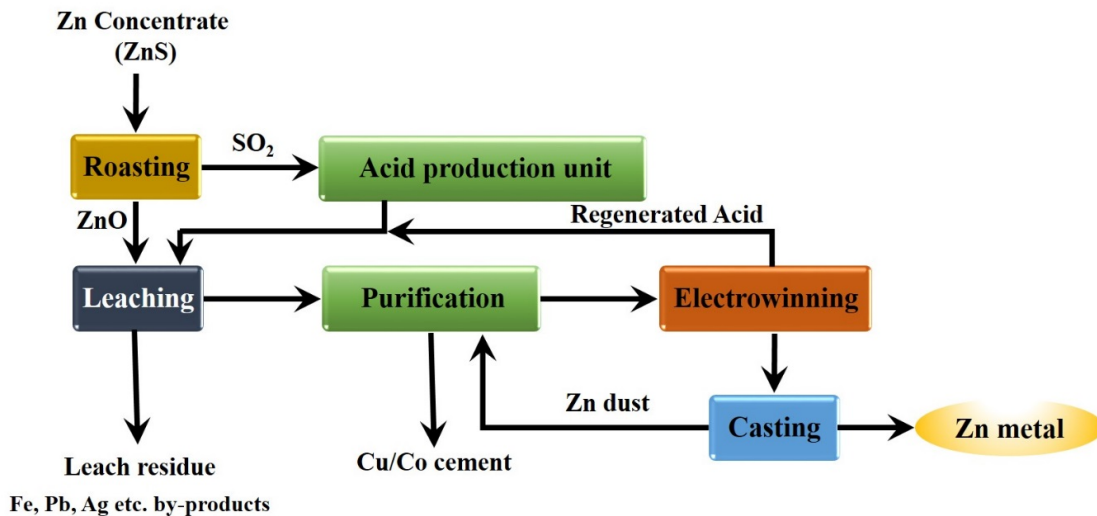
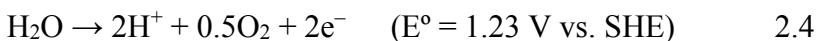


Figure 2-7 General Zn metal production process flow sheet via roasting, leaching, and electrowinning

Following Fe removal, the Zn leach solution is purified via cementation process prior to electrowinning step. In this process, any soluble metal impurities are precipitated out, particularly those which are more electropositive than Zn. These are removed by the addition of Zn dust, which is oxidized in the leach solution and is recovered in the electrowinning stage. However, the metal impurities, i.e. Ni, Cd, and Co that have a standard potential close to the Zn/Zn²⁺ redox potential are difficult to remove. A large number of other impurities such as Cu, As, Sb, Fe, and Ge are removed from the Zn leach solution to less than 1-ppm level.

In this study, the Zn/Zn²⁺ redox reaction, akin to the electrowinning process, is used in the battery setup. Some other issues, which may restrict efficient Zn electrowinning, are also discussed here. The Zn electrowinning process accounts ~30 % of the total energy required to produce Zn metal from as mined ore. On an industrial scale, Zn is electrodeposited (reaction 2.3) on aluminum cathodes while H₂O oxidation (reaction 2.4) occurs on Pb–Ag (0.5 – 0.75 %) alloy anodes in an electrolytic cell. The anode material is of significant importance because

a relatively large overpotential for oxygen evolution (reaction 2.4) appreciably increases the overall cell potential.



Based on these reactions, Zn deposition should proceed at ~ 2.0 V and the theoretical energy required for this process is 1.63 kWh kg^{-1} . But due to a large overpotential on the electrodes (particularly on the anode, ~ 0.6 V) and a potential drop in the leach liquor, an actual cell potential of ~ 3.2 V is required for Zn electrowinning, which corresponds to $\sim 2.8 \text{ kWh kg}^{-1}$ of energy consumption [16-18].

2.5.1 Solution purity and its importance

Owing to the negative reduction potential of Zn, electrolyte purification is very necessary. Otherwise, the preferential deposition of more noble metal impurities, i.e. Cu, Ni, etc. on the cathode would impair the purity of the Zn deposit in addition with accelerated H_2 evolution over these catalytic micro-cathodes. These impurities consequently decrease the current efficiency during the electrowinning process. Mackinnon et al. [97] rigorously studied the effect of metal impurities in industrial zinc sulfate solution and found a variable influence on the deposit morphology, orientation and current efficiency. The critical limits of impurity contents were investigated and their effect on the current efficiency is shown in Figure 2-8a and Figure 2-8b.

The tolerable concentration of Cu and Cd in the Zn electrolyte containing 9 mg l^{-1} Pb is found to be less than 50 mg l^{-1} in zinc sulfate solution. However, a further increase in concentration beyond this level could significantly influence the deposit morphology and current efficiency [98, 99]. Ni and Co are more deleterious owing to their small overpotential

for H₂ evolution and low concentrations (> 5 mg l⁻¹) could greatly decrease the current efficiency. The preferential deposition of these more noble impurities results in the catalysis of H₂ evolution and the enhanced localized re-dissolution of Zn by galvanic corrosion [12]. Figure 2-8a shows that current efficiency is very sensitive to the presence of Sb, Ge, Te, Se and Sn (< 2 g l⁻¹) in the electrolyte. Surprisingly, the presence of As(III), In and Tl has a negligible effect on the current efficiency as shown in Figure 2-8b [97].

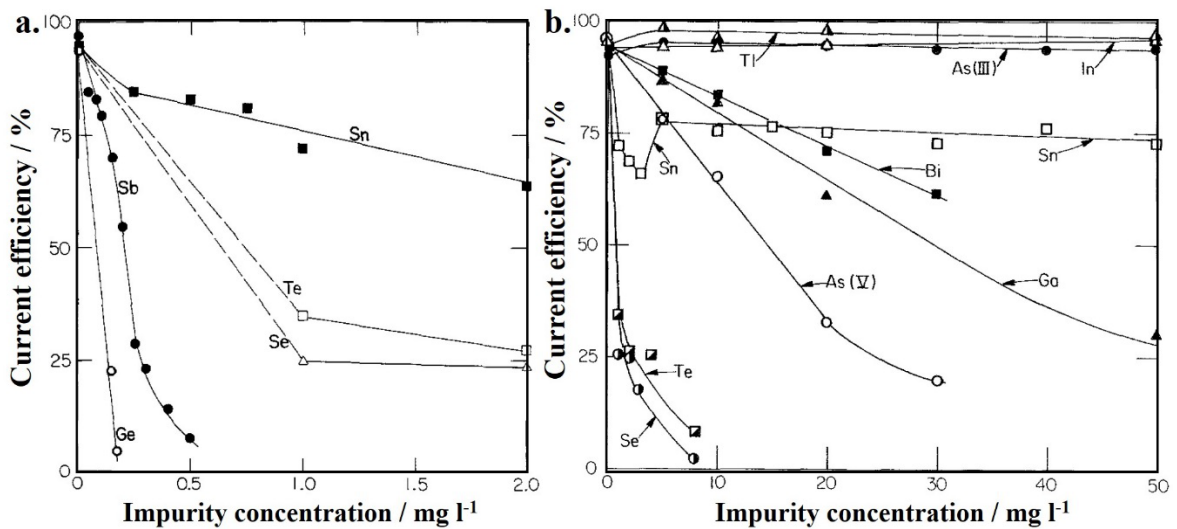


Figure 2-8 Effect of metallic impurities concentration on the current efficiency of Zn deposition process in industrial acid sulfate solution at 430 A m⁻² (a) IV A and VI-A (b) III-A and V-A group metals including Sn [97].

In order to decrease the power consumption, to improve the current efficiency and to refine the grain morphology, several organic additives are introduced to the Zn electrolyte in small quantities. These additives induce positive effects on the morphology of deposited crystals and promote the development of a bright and homogenous Zn deposit at high current efficiency by restricting the localized growth of the deposit (dendrite formation). The use of gelatin, glue, gum Arabic, organic surfactants (triethyl-benzyl ammonium chloride [100]), sodium lauryl sulfate [101], quaternary ammonium bromides [102], perfluorocarboxylic acids

[103], acid–mist suppressants (Tennafroth 250 (T), saponin, Dowfroth 250 (D) [104]) and flocculants have been found effective to enhance the current efficiency and deposit morphology as reported in the literature [105].

2.5.2 Optimum conditions for Zn deposition

Many variables i.e. electrolyte composition, temperature, current density, electrolyte circulation, Zn and acid concentration greatly influence the overall performance of the electrowinning process and may increase the energy requirements. For instance, Frazer et al. [106] investigated the effect of temperature, current density and electrode rotation on the current efficiency of Zn electrowinning in 0.8 M ZnSO₄ + 1.07 M H₂SO₄ in the presence of 1.2 ppm Pb and 0.2 ppm Ni. Using statistical analysis (2³ factorial design), a maximum current efficiency of 98.8 % was achieved by adjusting the electrolyte temperature to 50 °C, fixing the current density as 50 mA cm⁻² and by applying the electrode rotation speed of 35 s⁻¹. In another study, a maximum 95 % current efficiency was obtained in synthetic solution containing 160–65 g l⁻¹ Zn²⁺ in 40–90 g l⁻¹ acid concentration (25 °C) and by applying 35–60 mA cm⁻² current density. The addition of 50 g l⁻¹ gelatin + 10 ppm thiourea significantly improved the grain structure and prevented the nodular growth of the electrodeposit. It is also found that current efficiency decreased to 88 % from 96 % with the increase in Cu concentration from 6.2 to 20 ppm in 120 g l⁻¹ Zn and 50 g l⁻¹ H₂SO₄ solution [107]. The addition of Mn in the range of 1.5 – 3.0 g l⁻¹ is always recommended to avoid the corrosion of Pb anodes but higher concentration may produce negative effects on the current efficiency and grain size in the Zn deposit [108].

The effect of Zn and acid concentration variation at fixed sulfate concentration in Kidd Creek Zn electrolyte was determined by Alfantazi et al. [16]. They noticed that input energy required for effective Zn deposition decreased from 3.05 to 2.85 kWh kg⁻¹ when the

concentration of Zn in the solution was increased from 42 to 50 g l⁻¹ and became constant at high Zn concentrations. In addition, the current efficiency improved significantly to 95 % from 83 %, when the Zn concentration increased from 42 g l⁻¹ Zn to 107.5 g l⁻¹ in 95 g l⁻¹ H₂SO₄ solution. Similarly, the large deposition efficiency at high Zn concentration (1.4 M ZnSO₄) was achieved in 0.1 to 0.7 M H₂SO₄ solution. But the decrease in current efficiency at much high acid concentrations was attributed to the increase in H₂ evolution exchange current density [109].

2.5.3 Use of Zn as an electrode material in batteries

Zn and its alloys have great potential for use as anode materials in many aqueous-based energy storage systems owing to their low cost and high theoretical specific capacity of 820 mAh g⁻¹ [20]. However, the Zn based batteries exhibit poor cyclic charge/discharge performance and small cyclic life which restrict their use as secondary batteries [21]. Various battery setups i.e. Zn–C, Ni–Zn, Zn–Ag, Zn–MnO₂ and Zn–Air have been introduced that utilize alkaline electrolytes. Among these, only Ni–Zn and Zn–air batteries are rechargeable (secondary batteries) but there are several issues related with the electrochemical performance of Zn anodes. The shape change, formation of dendrites, non–uniform dissolution and limited solubility of Zn anode in the alkaline electrolytes are the main limitations to the design of rechargeable batteries [110]. Dendrite formation on Zn anodes during the charge cycle may rupture the membrane and short-circuiting of the electrodes may lead to failure of the battery. Modifications in the Zn anode design, separators, the addition of inhibiting agents in the electrolyte or alloying additions in the electrode and/or pulsed charging strategies have therefore been devised [21, 111-116].

Another issue is the simultaneous parasitic H₂ evolution during the charge cycle (Zn deposition), which ultimately decreases the coulombic efficiency and cyclic life of the batteries. To avoid this issue, many alloying additions which have large overpotential for H₂ evolution are introduced in the Zn anode i.e. Bi, In, and Ca [117, 118]. The major challenges that remain for existing commercialized Zn–Ni rechargeable batteries are related to the Zn based anode materials. For Zn–air batteries, the fade in capacity, self–discharge and low cyclic stability of these systems are the key issues that require further attention [116, 119]. More detail on these issues and remedies are available in the literature [20, 110, 113] and not discussed in this work.

2.6 Energy storage and its importance

The ever-increasing energy demand due to rapidly increasing population and industrial growth has spurred interest in the invention of new renewable energy technologies and in the improvement of the performance of existing systems [120, 121]. The energy supply from renewable sources is always intermittent because of their dependence on geological conditions e.g., weather, time of day or year and location. Therefore, efficient energy storage systems are always required for peak shaving during day and night shifts and to ensure continuous supply on demand [122-128].

2.6.1 Electrochemical energy storage

Among many other energy storage systems, e.g, mechanical and thermal, electrochemical energy storage devices such as batteries and supercapacitors (SCs) are flexible for use in both mobile and stationary applications. Figure 2-9 shows the general type of reactions that may occur on, or in, electrode materials and defines the mechanism of charge storage. In batteries, chemical energy is stored during the charge cycle and retrieved as

electrical energy during the discharge cycle. The charge is stored reversibly by the occurrence of faradaic reactions at or within the bulk of the electrode material. This is referred to as pseudocapacitive behavior. For example, in a lead acid battery, the oxidation reaction at the negative Pb electrode (anode) is supported by the reduction of the positive PbO₂ (cathode) to PbSO₄ (*conversion reaction*) and the attendant release of electrical energy during the discharge cycle. However, irreversible reactions, such as electrolyte dissociation and reactions with the electrode material, can deteriorate a battery's charge storage capability and decrease its cyclic life during repetitive charge/discharge. On the other hand, in supercapacitors (also referred to as *electrochemical capacitors*), the formation of the electrical double layer (*capacitive behavior*) or adsorption/desorption processes (*pseudocapacitive process*) are limited to the surface and/or near surface regions of the electrode materials. Therefore, supercapacitors can endure a large number of charge/discharge cycles.

Thus, both pseudocapacitive faradaic (reversible electron transfer reactions) and pseudocapacitive reactions are desirable in a charge storage device, whereas the occurrence of unwanted parasitic reactions (*electrochemically irreversible reactions*) deteriorate their cyclic performance.

Electrochemical characterization of battery electrode materials reveals the charge storage mechanism, as shown in Figure 2-10. In batteries, redox reactions (i.e. conversion reactions) and intercalation processes are responsible for charge storage. These processes are diffusion controlled and depend on the transport of ionic species to or from the electrode materials. Thus, batteries require extended time for charging. The slow release of electrical energy during discharge from these mass transfer-controlled redox reactions also appear as current peaks and potential plateaux in the CV and discharge curves, respectively (Figure

2-10F and H). On the other hand, SCs can be charged and discharged rapidly due to the storage of charge on the surface or within the near surface regions of porous electrode materials. These surface reactions are not dependent on mass transfer processes and, therefore, SCs present rapid current response upon change in potential during charge/discharge (Figure 2-10E and G) [129-131]. Based on these charge storage characteristics, batteries can store and supply a large amount of energy (high energy density), whereas, SCs can be charged rapidly and are discharged by providing high power density to overcome intermittent and momentary power outages.

The key issues with existing battery technologies are their limited cyclic stability, relatively lower energy density and inferior-than-expected rate capability. These issues are mainly related to the electrochemical properties of the battery electrode materials and their interaction with the electrolytes during charge/discharge operation. SCs have a long cyclic life, high power density and high charge/discharge rate capabilities [128]. Nevertheless, the low energy density of SCs and limited power density of batteries are the two extremes, which impede their individual performances.

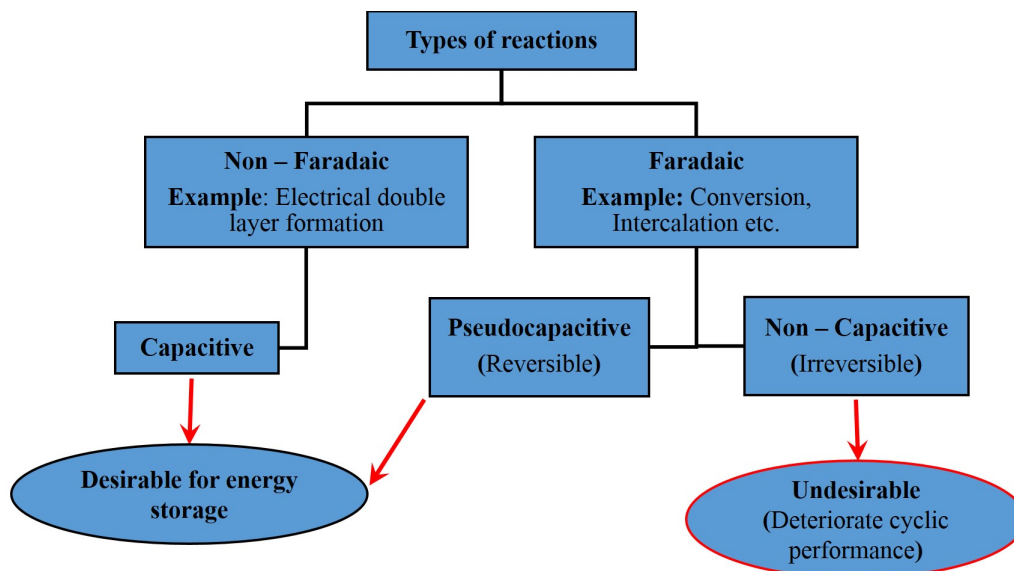


Figure 2-9 Types of reactions that may occur on the electrode materials of an electrochemical energy storage system

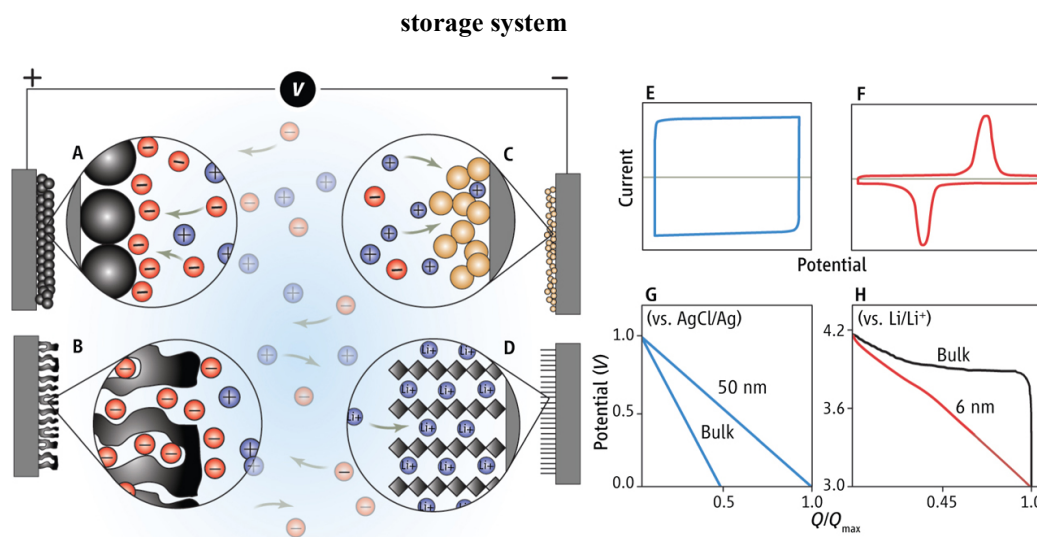


Figure 2-10 Charge storage mechanism in batteries and supercapacitors, formation of double layer (A) at the surface (B) within the bulk of porous carbon. Pseudocapacitive behavior (C) due to surface redox reaction onto a hydrous RuO_2 electrode (D) due to intercalation of Li^+ ions within the bulk of host material. Cyclic voltammograms of (E) supercapacitor and (F) battery electrode. Pseudocapacitive discharge curve (G) of MnO_2 capacitor and (H) LiCoO_2 battery electrode materials [130].

Therefore, the hybridization of batteries and SCs is an attractive way of achieving both higher energy and power densities from a single system with improved cyclic life, good safety, and good efficiency at low cost. In a hybrid system, the contribution of each component - battery or SC - depends on the configuration [132]. The key goal of hybrid battery/SCs is a rapid electrochemical response of the electrode materials at large applied potential and rapid charging/discharging response without significant polarization and stability loss [133]. These hybrid systems could economically store an enormous amount of energy and could fulfill energy storage and supply requirements for future hybrid vehicles and grid systems.

Research on the development of new hybrid systems has accelerated in recent years. As noted above, high energy and power density are the two characteristics belonging to batteries and SCs, respectively. To achieve both from a single or a pair of materials is still under intense investigation. But currently, these technologies are immature and widespread commercialization is limited because of the various materials' intrinsic behavior, bulk vs. surface faradaic/non-faradaic and diffusion controlled reactions [132, 134]. The diffusion-controlled processes limit rapid charging/discharging of LiBs due to local overpotential built up across the electrode surface [135]. To enhance ion and electron transport kinetics, various approaches such as modification of the electrode materials [136], application of conductive coatings over electroactive electrode materials [128, 137] and size reduction to nanoscale [122, 131, 138] have been adopted. To achieve ultra-high charging/discharging rates, a decrease in ion diffusion time and a short electron transport path length are always required. The time constant for diffusion is decreased significantly ($t \sim L^2/D$) by reducing electroactive material dimensions [136, 139].

2.6.2 Current state of battery research

Batteries are considered to be the most reliable and attractive technologies for the storage and continuous supply of energy. Many battery systems have been developed and much information about the recent advances in lead-acid batteries [140], Li-ion batteries [141], Li-S batteries [142, 143], Na-ion batteries [144, 145], Na-S [146], vanadium redox flow batteries [147, 148] and Zn-air batteries [149] etc. is readily available in the literature. Table 2-4 summarizes the performance characteristics of some well-established battery technologies for comparison. A detailed discussion about these battery technologies is beyond the scope of this work. However, the types of electrode materials and the use of CuFeS_2 as an electrode material in the batteries is discussed here.

Among all other battery systems at present, the Li-Ion batteries (LiBs) have been widely researched and account for a major share in the market in almost every application e.g. cell phones, laptops, electric vehicles, and energy storage systems at grid level etc. Nevertheless, the key issue with the LiBs is their limited charging rate due to potential build up (polarization) across the electrode/electrolyte interface. These polarization effects could increase the local temperature during charging/discharging leading to explosion or fire hazards [150].

The selection of electrode materials for LiBs depends on particle size, morphology, electron transport properties, functionalization, crystal structure, electrolyte type, chemical stability, and charge storage mechanism. In the past two decades, the development of highly energetic cathode materials for LiBs has been greatly focused on achieving high energy storage capabilities and electrochemical stability in both organic and aqueous electrolytes [143, 151].

Generally, the cathode materials are categorized into '*intercalation*' and '*conversion*' types and are selected based on design criteria such as specific capacity and operating potential.

Intercalation is defined as reversible insertion and removal of guest species i.e. Li^+ , Na^+ etc. into the host material having a layer type lattice structure. For example, in LiBs, the intercalating cathode host lattice structure can accept and release guest ions (Li^+ , Na^+) in a reversible manner during charge/discharge cycles. The commonly used cathode (host) materials are transition metal oxides i.e. LiCoO_2 [152], LiNiO_2 [153], $\text{LiNi}_{0.8}\text{Co}_{0.15}\text{Al}_{0.05}\text{O}_2$ [154], LiMnO_2 [155], $\text{Li}(\text{Ni}_{0.5}\text{Mn}_{0.5})\text{O}_2$, $\text{Li}(\text{Ni}_{1/3}\text{Co}_{1/3}\text{Mn}_{1/3})\text{O}_2$ [156], and LiFePO_4 [151], which display a wide variety of crystal structures i.e. layered, spinel, olivine, and tavorite.

Table 2-4 Existing commercialized and developing battery technologies, their performance, and comparison [121, 157]

Battery Type	OCV (V)	Specific Energy (Wh kg⁻¹)	Temperature (°C)	Cyclic life	Energy efficiency (%)	Discharge Time (h)
Pb acid battery	2.1	25–40	–40 to 60	1000	50 –75	8
Pb–C battery	2.1	25–40	–40 to 60	3000	–	4
Ni–Cd battery	1.3	30–45	–10 to 45	2000	55–70	4
V–redox flow battery	1.4	10–20	10 to 40	5000	65–80	4 to 12
Na–S battery	2.1	150–240	300–350	4000	75–90	4 to 8
Zeolite Battery Research Africa (ZEBRA)	2.6	95–120	300–350	3000	75–90	4 to 8
Li–ion battery with C anode	3 to 4	150	–25 to 40	1000	94–99	4
Li–ion battery with LiFePO ₄ cathode and Li ₄ Ti ₅ O ₁₂ anode	1.7	50–70	–25 to 40	4000	94–99	4

On the other hand, *Chalcogenides* are other promising conversion cathode materials, which are used in LiBs due to their higher thermal stability, electrical conductivity, and good electrochemical properties than metal oxides. The metal sulfides present high specific capacity but Li⁺ insertion/de-insertion is the diffusion-controlled process in these electrode materials. For instance, low surface area (large particle size) of electrode material could increase the electronic and ionic path length for Li⁺ ion diffusion and hence may reduce the energy and power densities [158]. The formation of intermediate polysulfide film could also form on the surface of the electrode (via reaction 2.5), which may dissolve in the organic electrolyte and may lead to irreversible capacity fade.



The soluble polysulfides are transported to the anode surface during the charging process and decrease the coulombic efficiency of the cell. This issue is overcome by decreasing the size and/or by modifying the morphology of sulfide-based electrode materials. Also, mixing with other graphitic materials (hybridization) may enhance both the energy and power efficiencies without compromising cyclic performance [142, 159].

2.6.3 Use of CuFeS₂ as battery electrode material

Recently, CuFeS₂ has been studied as a promising material for many applications including solar energy generation [160], energy storage [161, 162], electrochemical sensors [163] and as a thermoelectric material [164]. Many researchers in the past have adopted different procedures to synthesize various morphologies of CuFeS₂ such as *spherical* and *pyramidal* nanocrystallites [165], *nanowires* [166], hexagonal '*plate*' [167] and '*spike like nanorods*' [168] as shown in Figure 2-11a-d. Wu et al. [162] described the solvothermal synthesis of sheet-like nanocrystals of CuFeS₂ (Figure 2-12a) and converted them to rod shape

particles by adding '*polyvinyl pyrrolidone*' (PVP) surfactant during synthesis, as shown in Figure 2-12b. The PVP macromolecules significantly reduced the crystallite size by their ability to interact selectively with crystal facets while promoting anisotropic growth in other directions. The XRD patterns of crystallites synthesized with and without PVP suggested that PVP has no influence on the crystal structure but significantly affected the morphology.

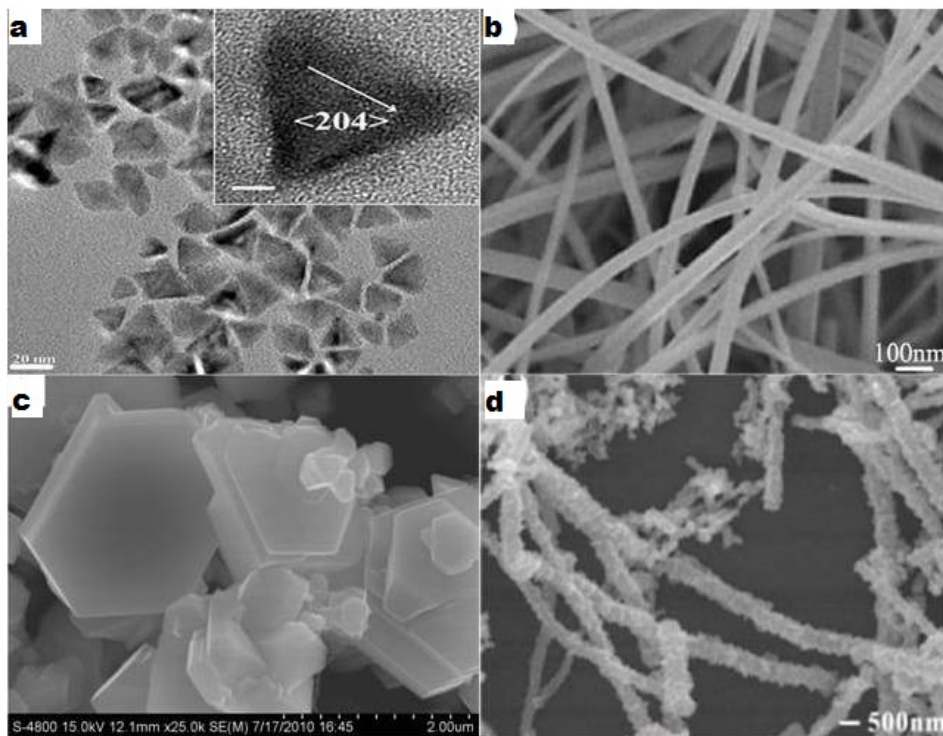
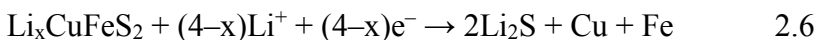


Figure 2-11 Morphologies of the as-synthesized CuFeS₂ reported in the literature (a) pyramidal [165], (b) nanowires [166], (c) plates/sheets [167], and (d) spikelike nanorods [129, 168]

The charge/discharge cycles (first 3 cycles) of the sheet and rod-like nano-crystallites of CuFeS₂ were conducted at 100 mA g⁻¹ within 0.001 – 3.0 V (vs. Li/Li⁺) potential as shown in Figure 2-12c and Figure 2-12d, respectively. The two potential plateaus at 0.8 and 1.5 V during discharge process (1st cycle) can be clearly observed, corresponding to conversion type reaction (reaction 2.6) and Li⁺ insertion into the crystal lattice of CuFeS₂, respectively [162, 167, 169]. The formation of metallic Cu and Fe was more pronounced than Cu²⁺ and Fe³⁺ (few

ppm) in the ethylene carbonate (EC)/dimethyl carbonate (DMC) (1:1 by volume) electrolyte containing 1M LiPF₆.



Similarly, two obvious potential plateaus at ~1.75 and 2.25 V were observed during charging. These were related with the oxidation of Li₂S (Li₂S → 2Li⁺ + S + 2e⁻) and S (S²⁻/S⁰ and or S²⁻/S₂²⁻), respectively [162]. The second and third charge/discharge plateaux were shifted slightly to lower capacity values but remained mirror images of the first scan profile. It was observed that the initial discharge capacity of CuFeS₂ without PVP was about 780 mA g⁻¹ in contrast to the much higher capacity (1020 mAh g⁻¹) exhibited by PVP-assisted CuFeS₂.

The cyclic voltammograms of both CuFeS₂ also validated the appearance of two reduction peaks at about 1.3 and 0.5 V (vs Li/Li⁺), which were assigned to Li⁺ intercalation and conversion reaction (reaction 2.6), respectively as shown in Figure 2-12e and Figure 2-12f. During anodic polarization, the two prominent peaks at 1.9 and 2.3 V were related to the oxidation reactions and deintercalation of Li⁺ ions in agreement with the charge/discharge behavior. The rate capability of CuFeS₂ at various current densities is shown in Figure 2-12g. The CuFeS₂ nanorods exhibited higher capacity than sheet-like CuFeS₂ nanoparticles even at higher C-rates. With an increase in charge/discharge specific current, the capacity was decreased from 700 mAh g⁻¹ at 100 mA g⁻¹ to 380 mAh g⁻¹ at 1000 mA g⁻¹ but it rebound back again to 620 mAh g⁻¹ when the discharge specific current of 100 mA g⁻¹ was selected. The better rate capability by rod-shaped CuFeS₂ nanocrystallite is correlated with the nanofeatures of chalcopyrite obtained through surfactant-assisted growth. The reduction in size and change in morphology promoted the electrolyte/active material interaction and reduced the diffusion path length for Li⁺ intercalation/de-intercalation reactions [167, 170, 171].

Furthermore, the cyclic stability test at 100 mA g⁻¹ showed a decrease in specific capacity from 700 mA g⁻¹ to 580 mA g⁻¹ after 50 charge-discharge cycles (Figure 2-12h).

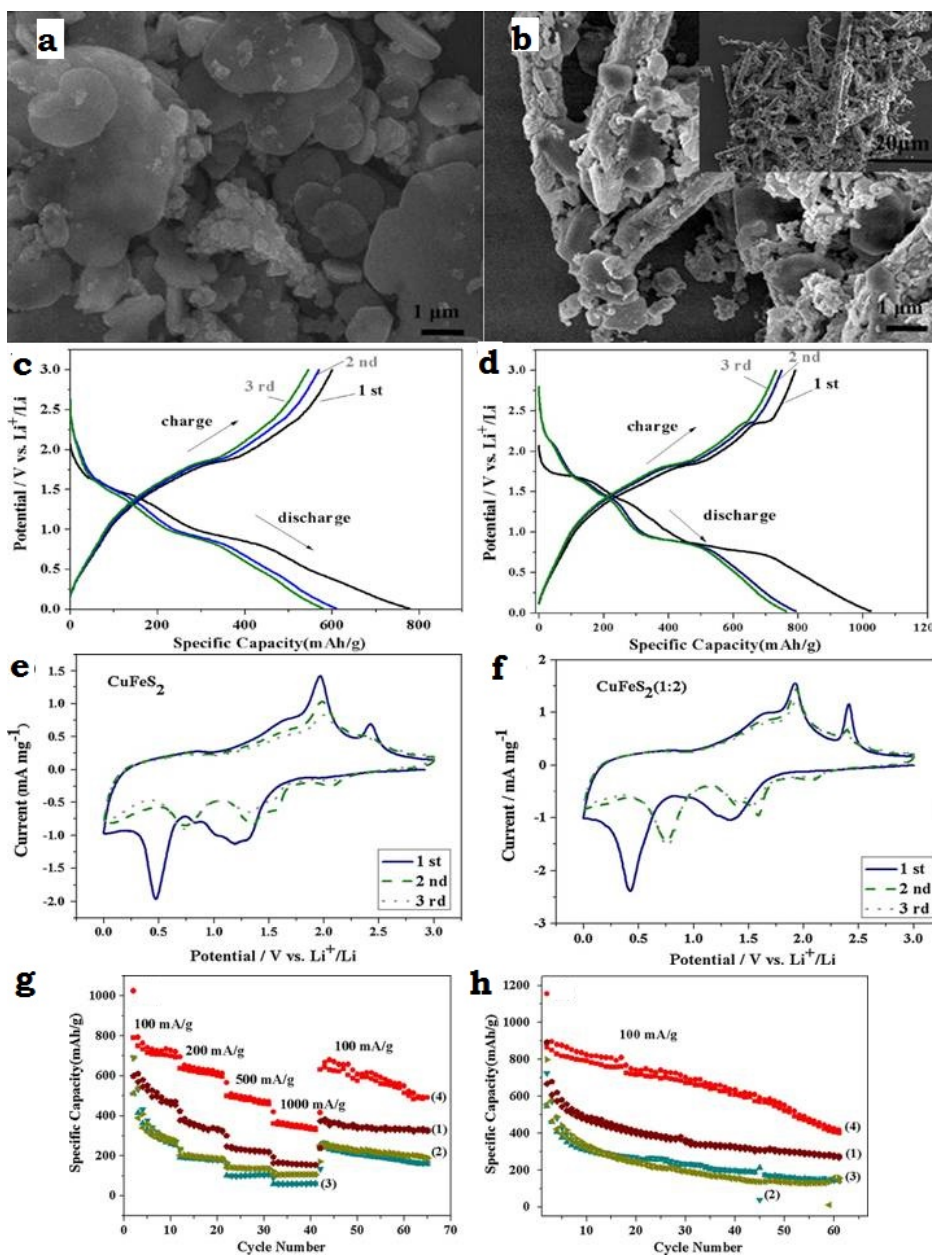


Figure 2-12 Morphology of synthetic CuFeS₂ (a) without and (b) in the presence of PVP.

Charge/discharge profiles (at various specific currents), cyclic voltammograms and specific capacity of as-synthesized CuFeS₂ (c, e & g) without and (d, f & h) in the presence of PVP [162]

2.6.4 Electrochemical capacitors or supercapacitors

The electrochemical capacitors are divided into two types (1) electrochemical double layer capacitor (EDLC) in which charge is stored within a few nanometers of the electrode surface by reversible adsorption/desorption of ions (non-faradaic) at the electrode/electrolyte interface. (2) Pseudo-capacitors involve surface or subsurface redox reactions (faradaic) at the electrode surface by the electrochemical species in the electrolyte [172, 173]. In recent years, the electrode in SC is generally composed of carbon-based materials, transition metal oxides or conductive polymers. The relatively lower power density of pseudocapacitors than EDLC is due to bulk electrochemical reactions dependent on ionic diffusion path length [174, 175]. The use of nano-sized electrode materials provides a large surface area ($\sim 1000\text{m}^2\text{ g}^{-1}$) and charge separation across a few nanometers. The diffusion time of an ion is proportional to the square of the diffusion length ($t \sim L^2/D$), thus for high rate capability high power could be realized by decreasing particle size of the active electrode material [131, 139]. The major concerns related to the nano-sizing of electroactive materials are agglomeration, electrical resistivity, cost and electrochemical stability for high rate applications.

Unlike Li-ions batteries, the electrolyte contribution to charge storage and supply is negligible in EDLCs and, therefore, the electrolyte remains stable after a large number of repetitive charging/discharging cycles. Activated carbon and graphitic carbon template and carbide-derived carbon [176], nanotubes [177], onions [178], nano-horns [179] have been investigated for EDLCs. The variety of carbonaceous materials having various shapes, structures, surface functionalities, porosity, and sizes are ideally considered the best electrode material for an EDLC. In terms of energy density, the EDLC cannot replace batteries but these can complement them in many applications for instance in welding, as an initial power source

for starting large electric motors, actuators, X-ray, MRI (magnetic resonance imaging) machines etc.

Similar electrode materials (both anode and cathode) are usually used in the development of EDLC, termed as symmetrical capacitors. Due to their low potential window, ‘small cell potential’, these devices present low specific energy and power, which is the main hindrance to their commercialization. On the other hand, asymmetrical supercapacitors utilize two different electrodes of large potential difference, which may consequently supply a relatively large amount of specific energy and power compared to EDLC. However, symmetrical capacitors have large cyclic life compared to asymmetrical supercapacitors due to the high stability of the electrode materials. Because of the large cell potential, the asymmetrical supercapacitor devices have relatively smaller specific energy than the battery setups but better than the EDLC. The aqueous electrolyte-based supercapacitors have shown less specific energy than organic based supercapacitor, mostly associated with their stability at large potentials (large potential window). In other words, the small potential window and dissociation of the aqueous electrolyte would limit the specific energy, but these devices could provide relatively high specific power than organic based electrolytes, attributing to the large ionic mobility in H₂O. The comparison of EDLC with recently reported asymmetrical supercapacitors is given in Table 2-5, which clearly illustrates the performance metrics of these devices in various electrolytes. However, due to the limited cyclic stability of electrode materials in the asymmetrical supercapacitor setups, and their relatively low specific power compared to EDLC, there is a demand for more research in this area. The development of new efficient electrode materials which can withstand large potential window without degradation during continuous charge/discharge cycles is essential [180].

In the past two decades, many flowable electrochemical energy storage systems such as redox flow batteries [181], Na-S molten batteries [182], semisolid 'Li' flow batteries (SSFC) and electrochemical flow capacitors (EFC) [183] have also been introduced. The key feature of these systems is their flexibility to decouple energy and power ratings since energy storage capacity is regulated by the size of electrolyte reservoir and power density could be tuned by controlling the size of the cell stack (size/volume of each cell) and/or by modifying electroactive materials. The EFC systems are highly efficient for rapid charge and discharge for energy storage at grid level due to their excellent cyclic stability. The charge is stored through non-faradaic adsorption phenomena and, therefore, these systems have a high-power rating but suffer from low energy density. Compared to LiBs, the SC can provide 10 times higher power density, 100 times faster charge/discharge rate and exhibit 1000 times longer cyclic life but deliver 20 times lower energy density. On the other hand, the slow charging response (several hours) under applied potential and capacity fade upon repeated cycles are the major issues associated with the LiBs [183, 184].

For hybrid electric vehicles and grid level power storage, researchers are most interested in the development of high surface area carbon-based, metal oxide or hybridized electrode materials which could give high capacitance ($\sim 1000 \text{ F g}^{-1}$) in synergy with high energy density at a high rate [123, 183, 185, 186].

Table 2-5 Performance metrics of EDLCs and recently reported asymmetrical supercapacitors

Electrodes (Positive/Negative)	Surface area (m ² g ⁻¹)	Cell Voltage (V)	Specific capacitance (F g ⁻¹)	Specific Energy (Wh kg ⁻¹)	Specific Power (kW kg ⁻¹)	Cyclic stability (%) / # of Cycles	Electrolyte	Measurement @	Ref.
Symmetrical or electrochemical double layer capacitors (EDLC)									
Carbon nano-spheres	791	1.0	551	20	2.5	97 /1.0k	1.0M HCl	1 A g ⁻¹	[187]
Carbon nano mesh	1198	3.5	194	56.1	61.25	90.6/100k	Ionic liquid	1 A g ⁻¹	[188]
Activated carbon	2731	1.0	311	8.3	18.75	96.4/5.0k	6.0M KOH	0.5 A g ⁻¹	[189]
Asymmetrical supercapacitors									
Activated carbon*/Zn	2000*	1.4	120	24.0	62.8	70.0/0.3k	7.3M KOH	0.005 A cm ⁻²	[190]
Ni(OH) ₂ /graphite	–	1.2	153	35.7	0.49	97.0/5.0k	1.0M KOH	0.05 V s ⁻¹	[191]
Carbon nanotubes + NiO / defect induced graphene*	456*	1.6	108	38.1	0.5	93.5/10k	1.0M KOH	0.5 A g ⁻¹	[192]
Co ₂ AlO ₄ +MnO ₂ /Fe ₃ O ₄	205.9/137.8	1.6	99.1	35.3	0.8	92.4/5.0k	2.0M KOH	5.0 A g ⁻¹	[193]
MnO ₂ +nano-porous gold/polypyrrole+ nano-porous gold	–	1.8	193	86	25	85.0/2.0k	1.0M LiClO ₄	0.1 V s ⁻¹	[194]
MnO ₂ /Fe ₃ O ₄	–	1.8	20	7.0	0.82	67.0/5.0k	0.1M K ₂ SO ₄	0.27 A g ⁻¹	[195]

Chapter 3: Objectives

Based on the literature review, it is determined that hydrometallurgical processing of CuFeS_2 is still a challenge owing to its refractory nature and passivation tendency in acidic media. On the other hand, CuFeS_2 may be reduced into the less refractory Cu_2S species in acidic media, which may in turn be oxidized to dissolve Cu. $\text{Fe}^{\text{II}}/\text{Fe}^{\text{III}}$ are common species used to control the solution potential and to enhance CuFeS_2 oxidation in acidic sulfate media. During this process, the reduction of $\text{Fe}(\text{III})$ at the surface and oxidation of CuFeS_2 consume energy to produce conversion products. Some fraction of this energy is lost as heat, the recovery of which is possible. However, these two processes could occur separately, in a battery like setup. In the first part of this work, a FBFC is introduced, which utilizes CuFeS_2 as a negative electrode. During the charge cycle, CuFeS_2 reduces into intermediate products which oxidize to produce Cu in the following discharge cycle. The $\text{Fe}^{\text{II}}/\text{Fe}^{\text{III}}$ redox couple is used as a supportive electrode reaction in the positive half of this FBFC.

In the second part of this work, two high energy demand hydrometallurgical processes, i.e., CuFeS_2 oxidation and Zn electrowinning are coupled in a tri-functional battery setup (TFB) to produce Cu and to store energy simultaneously. The Zn will deposit on a negative electrode material via the oxidation of CuFeS_2 in the positive compartment of the battery setup during the charging step. In this setup, the CuFeS_2 slurry is injected intermittently in the positive compartment and zinc solution is continuously circulated in the negative electrode compartment. During the charging cycle, the oxidation of CuFeS_2 and deposition of Zn take place simultaneously on the positive and negative electrodes, respectively. The unique feature of this TFB is the simultaneous extraction of Cu and energy storage that can be reused for other purposes but at the expense of deposited Zn.

The main objective of this work is to develop hybrid battery like setups in which CuFeS_2 can be used as an electrode material for energy storage and as source for Cu extraction. To quantify the energy storage and Cu extraction capabilities of these hybrid systems, the following sub-objectives were set.

3.1 Setup 1: Fixed bed flow cell (FBFC)

1. To establish a battery like hybrid system i.e. FBFC in which CuFeS_2 can be reduced in the negative composite electrode (CuFeS_2 mixed with carbon black and encapsulated in graphite felt) during the charge cycle with the help of Fe^{II} oxidation to Fe^{III} on the positive electrode.
2. To investigate the electrochemical behavior of the negative composite electrode to estimate its cyclic performance and establish the charge storage mechanism in the final FBFC (Chapter 5).
3. To study the effect of Cu^{II} addition in the catholyte to evaluate the electrochemical behavior of the positive electrode and to compare the cyclic charge/discharge performance of the FBFC with and without Cu^{II} . Quantify the specific energy, coulombic and energy efficiencies of this system (Chapter 6).
4. Compare the energy storage and Cu extraction capabilities of the FBFC when either synthetic CuFeS_2 or a naturally sourced mineral concentrate are used (Chapter 7).

3.2 Setup 2: (TFB)

5. Introduce a hybrid battery-like hydrometallurgical system in which both Cu extraction from CuFeS_2 and Zn deposition are simultaneously possible during the charge cycle.
6. Determine the reaction sequence at both electrodes in the TFB (Chapter 8).

7. Examine the cyclic charge/discharge performance of the TFB and quantify its energy storage and Cu extraction (Chapter 8).
8. Use a CuFeS_2 mineral concentrate as a positive slurry electrode in the TFB and determine its performance (Chapter 9).

Chapter 4: Approach and Methodology

4.1 Materials

The lab grade chemicals i.e., ferrous sulfate tetrahydrate ($\text{FeCl}_2 \cdot 4\text{H}_2\text{O}$; 99.95 %) from Fisher–Scientific, thiourea ($\text{CS}(\text{NH}_2)_2$; 99.98 %) from Alfa–Aesar and cupric chloride dehydrate ($\text{CuCl}_2 \cdot 2\text{H}_2\text{O}$; 99.5 %) from Sigma–Aldrich were used as received to synthesize CuFeS_2 hydrothermally. Other chemicals i.e. 1 M sulfuric acid (H_2SO_4) solution (Fisher–Scientific), sodium sulfate (Na_2SO_4), zinc sulfate ($\text{ZnSO}_4 \cdot 7\text{H}_2\text{O}$; 99.95 %) Sigma–Aldrich were obtained as used without further purification. Graphite felt (GFE-1, CeraMaterials) used in a Fixed Bed Flow Cell (FBFC) was purchased having a thickness of ~ 0.8 cm. The resistance of the GF was found to be $\sim 1.7 \Omega$ in the uncompressed state as measured by a conductivity meter in the laboratory. For the preparation of carbon paste Acetylene black, poly(vinyl difluoride) (PVDF) and 1-methyl-2-pyrrolidone ($\text{C}_5\text{H}_9\text{NO}$) as a curing agent were used. The high surface area activated carbon (AC) (EQ-AB-520Y) purchased from MTI Corporation is used as a component to prepare slurry, which was used as positive electrode in the tri-functional flow battery setups i.e. TFB and TFB-M. Pure Al sheets (1.27 mm thick) conforming to ASTM B209 were purchased from onlinemetals.com for use as current collector and substrate for Zn deposition in the negative half of the TFB. The 3.2 mm thick flexible graphite sheet was purchased from equalseal.com and was cut (L100 x W50 mm) to use as a positive current collector plate in the TFB. The 10 mm thick molded polytetrafluoroethylene (PTFE), the UHMW (ultra–high molecular weight) polyethylene sheets (25 mm) and silicone rubber for sealing (Silicone CG White) were purchased from onlinemetals.com and Rubber-Cal, respectively. The AAS grade Fe and Cu standards solutions (TraceCERT) for inductively

coupled plasma optical emission spectroscopy (ICP–OES) analysis were obtained from Sigma Aldrich, Canada.

4.2 Experimental methods

4.2.1 Synthesis of CuFeS₂ and pretreatment of mineral concentrate

The CuFeS₂ was synthesized hydrothermally in the laboratory to use as an electrode material in the proposed battery setups. Synthetic CuFeS₂ was used to explore its intrinsic electrochemical behavior and to avoid the complexities of associated with the impurities that exist in the natural mineral concentrates. To synthesize CuFeS₂, initially, the stoichiometric amounts of CuCl₂·2H₂O, FeCl₂·4H₂O, and thiourea were mixed in 150 ml deionized water (DI) for 2 h for homogenization. The mixture was transferred to a Teflon lined stainless steel vessel and the tightly closed vessel was then placed for 12h in a programmable furnace (VF1200D8) with a heating rate of 3.33 °C min⁻¹ and stabilized at 200°C. The reaction vessel was then furnace cooled to room temperature and the resultant product was washed with DI water 3 times followed by stirring in (2% v/v) sulfuric H₂SO₄ solution for 30 minutes to remove any impurity. The filtered mass was washed with excess of DI water until the filtrate solution pH became equal to the pH of DI water. The filtered particles dried at 50°C for 24h were then stored in an airtight glass bottle for further use. The synthesis process was devised by the authors in the laboratory after rigorous experimentation.

The CuFeS₂ mineral concentrate (MC) used in Chapter 7 and 9 was obtained from a mine and concentrator operation in British Columbia. The composition of the MC was determined via QXRD analysis and is reported in section 7.1. Prior to use, this MC was washed in DI water several times, filtered, mixed with dilute sulfuric acid (0.02 M solution) and stirred for 3 h to remove any air formed oxides or other air-related oxidation products. After acid

washing, the thoroughly washed MC with DI water ($\text{pH } 4.7 \pm 0.1$ at 25°C) was dried at room temperature (24 h) prior to storage in a glass bottle for further use.

4.2.2 Schematic of the systems under investigation

Two types of battery setups, i.e., FBFC and TFB are introduced in this work. Each positive and negative electrode and their components were rigorously characterized to identify the reaction sequence and to optimize the operating conditions for the operation of these battery setups. Figure 4-1 shows the scheme of the individual electrode system and components used in the battery setups. The combination of each positive and negative electrode for the FBFC (i.e., CFe, CFeCu or C-1, C-2) and TFB (i.e., TFB and TFB-M) were studied individually in their respective electrolytes (the final battery setups are presented as oval shape icons in this figure). In the following chapters, the detailed discussion on these electrode systems and battery setups is given.

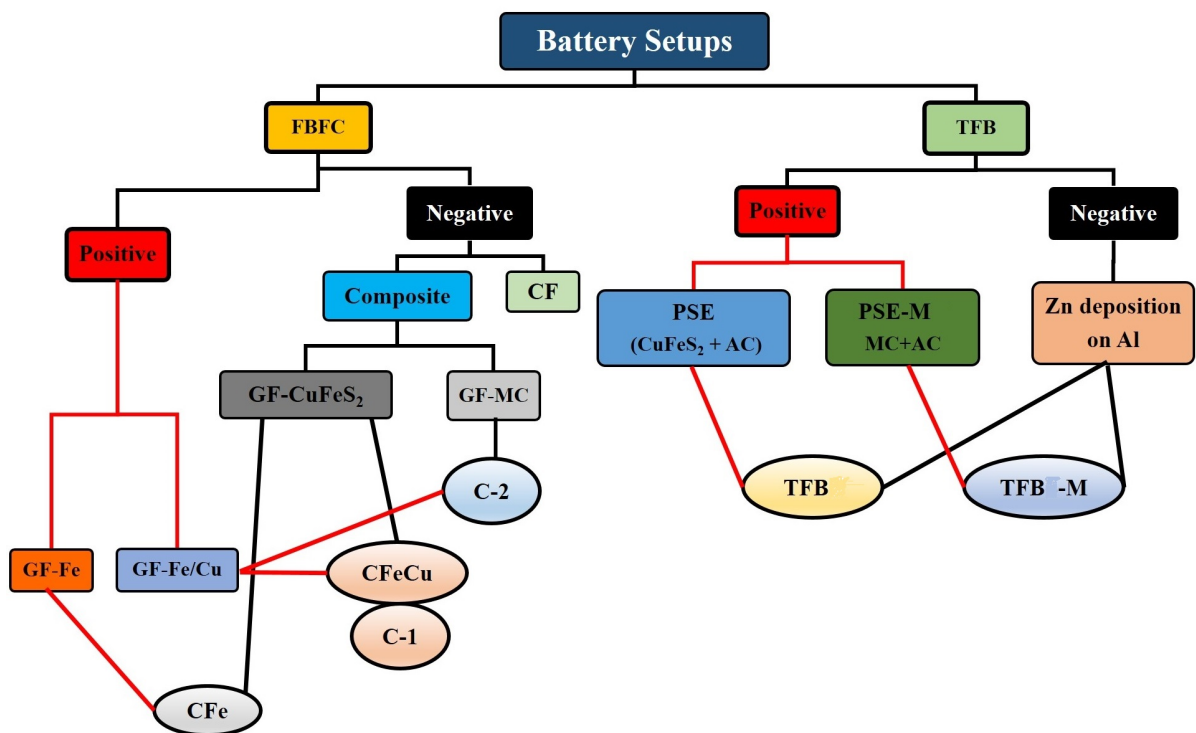


Figure 4-1 Schematic diagram of the electrode systems used in each battery setup. The combination of positive (red lines) and negative (black lines) connect the two electrodes into a cell assembly.

4.2.3 Preparation of the electrodes for electrochemical study

GF cut into 2.0×2.0 cm square was connected to a graphite rod by carbon paste. Herein, this assembly is referred to as the 'CF electrode'. The carbon paste was prepared by homogeneously mixing 80 wt. % acetylene black, 20 wt. % PVDF and 1-methyl-2-pyrrolidone (C_5H_9NO) as a curing agent. The composite electrodes (used in Chapter 5) were prepared by encapsulating 0.1 g of as-synthesized $CuFeS_2$ powder in the GF (without adding CB), by cutting the GF in half along its thickness and manually placing a layer of synthetic $CuFeS_2$ between the resultant halves. After incorporating the $CuFeS_2$ in the GF, the edges were sealed with carbon paste and this was then connected to a graphite rod by using the same procedure

as used for the CF electrode preparation. These electrodes were left to cure for 12 h at room temperature before use.

Similarly, in Chapter 6 the electrochemical kinetics study of both negative and positive electrodes (as used in the FBFC) was carried out separately in a three-electrode cell setup as shown in Figure 4-2. The composite (negative) electrodes were prepared using the same procedures as stated above. Briefly, as-synthesized CuFeS_2 or MC powder samples homogeneously mixed with carbon black (4:1) were manually sandwiched between two halves of GF (2 x 2 x 0.8 cm). The edges of the GF were sealed with carbon paste and connected to a graphite rod by carbon paste (Figure 4-2). These composite electrodes are designated as GF- CuFeS_2 and GF-MC. Similarly, GF (the positive electrode in the FBFC) connected to a graphite rod with carbon paste are referred to as GF-Fe/Cu electrodes in Chapter 6.

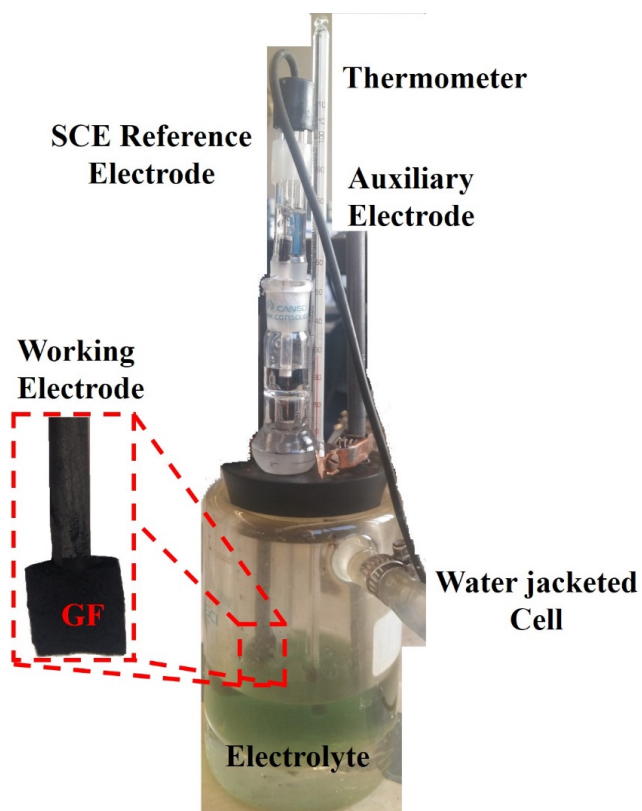


Figure 4-2 Assembly of three electrodes cell in which each electrode i.e., CF electrode, comp electrode, GF-CuFeS₂, GF-MC and GF-Fe/Cu was tested in its respective electrolyte.

4.2.4 Construction of fixed bed flow cell (FBFC)¹

The two-electrode FBFC was used to estimate the charge storage capability of the synthetic CuFeS₂ and MC as shown in Figure 4-3 and discussed elsewhere [196]. Briefly, the two compartments of the FBFC were constructed by drilling 10 mm deep circular cavities ($\varnothing = 10$ mm) in 30 mm long graphite cylinders. The inlet and outlet channels were made in the side of these cylinders by fitting Teflon nozzles, which opened in the cavities for electrolyte circulation. In one compartment (positive), disk shape GF was inserted whereas, the composite negative electrodes (made by sandwiching the mixture of either as-synthesized CuFeS₂ or MC

¹ From the published work, K.M. Deen, E. Asselin, *ChemSusChem*, 11 (2018), 1533–1548.

(80 wt. %) and carbon black (20 wt. %) were manually compressed into the other cavity. These two electrodes were compressed (up to ~ 30 % of the original thickness of the GF) against each other and were physically separated by a preconditioned proton exchange membrane (PEM). The anolyte (0.5M Fe^{2+} + 0.1M Cu^{2+} dissolved in 0.2M H_2SO_4) was circulated in the positive compartment via peristaltic pump. In the negative electrode compartment, the 0.2M H_2SO_4 solution was circulated. As shown in schematic diagram (Figure 4-3), both electrolytes were pumped in a closed loop configuration from the external water jacketed (for temperature control) reservoirs maintained at 25 °C.

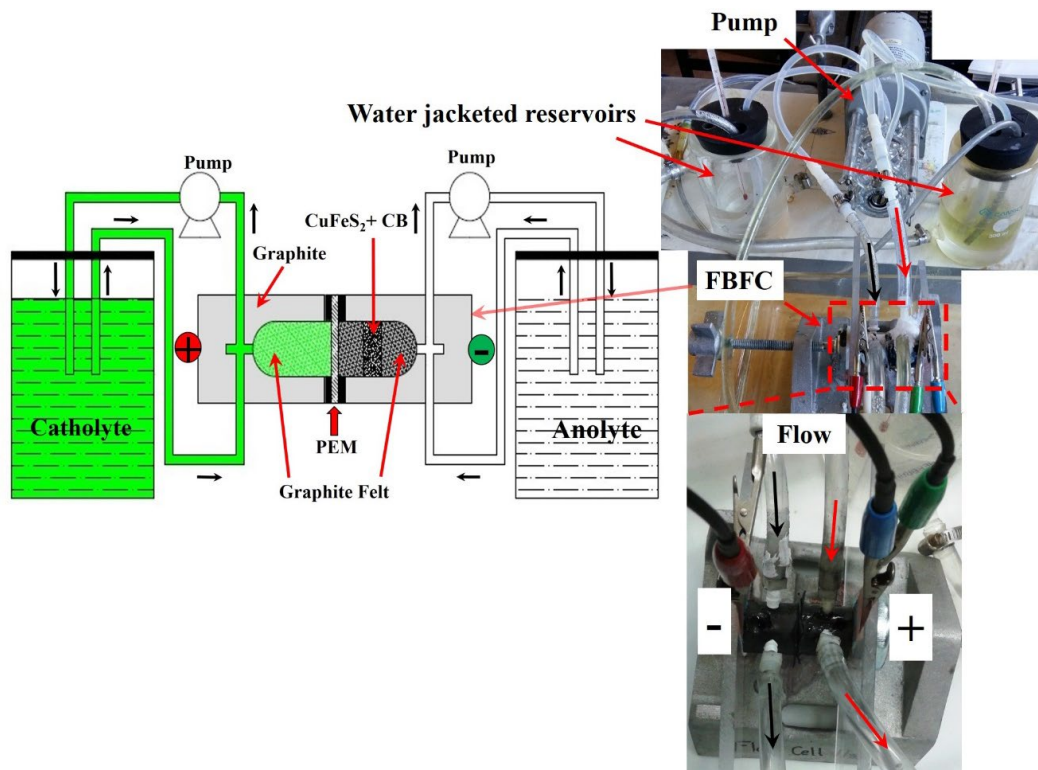


Figure 4-3 Schematic diagram of the FBFC, the original setup demonstrates the overall assembly

For electrochemical testing of the FBFC, the GF and composite electrodes (GF– CuFeS_2 or GF–MC) in the positive and negative compartments, respectively, were connected to the working/working sense and counter/reference leads of the potentiostat, respectively. Both

anolyte and catholyte were circulated separately in the FBFC at a constant flow rate (7.5 ml min^{-1}).

4.2.5 Construction and design of the tri-functional battery setup (TFB)²

The schematic of the two-electrode cell system designated as TFB is shown in Figure 4-4a. This TFB was designed and constructed in the laboratory. Briefly, two PTFE plates having rectangular flow channels (3 cm^2) were attached together by inserting the preconditioned anion exchange membrane (AEM) between them. The AEM was sandwiched in silicone gaskets prior to insertion between PTFE plates. On each side of the PTFE plates, the flexible graphite plate (GP) FGS and Al sheet as positive and negative current collectors, respectively were affixed. To avoid any leakage silicone gaskets were inserted between the current collectors and PTFE plates. This whole assembly (as shown schematically in Figure 4-4a) was tightened with screws through the holes made in HDPE end plates as shown in Figure 4-4b. Detailed information for each component of TFB is presented in Figure 4-4c.

The *catholyte* in the form of slurry and composed of 80 wt. % CuFeS_2 + 20 wt. % AC in 0.2 M H_2SO_4 solution was first injected from one end in the positive compartment to fill the flow cavity and to remove air. The other end was then closed with a graphite plug and connected electrically to the positive plate through a conductive copper tape. The initial total solid content in the slurry was (20 wt. %) and this value was retained for all experiments. The amount of slurry injected into the cavity was calculated to ensure that at least 65 % of the volume was filled with solid particles in the form of slurry once these are settled as shown schematically in Figure 4-4a. On the other side of the cell, the anolyte ($100 \text{ g l}^{-1} \text{ Zn}^{2+}$ dissolved

² This work is 'under consideration' for publication

in 0.2 M H_2SO_4) containing 0.1 M Na_2SO_4 and 2ppm cetyl-trimethylammonium bromide (CTAB) (optimized concentration) was circulated in a closed loop by a peristaltic pump at $10 \pm 0.5 \text{ ml min}^{-1}$ flow rate. The temperature of the anolyte solution was maintained constant at 25°C in an external water jacketed cell connected to a circulating thermostatic water bath.

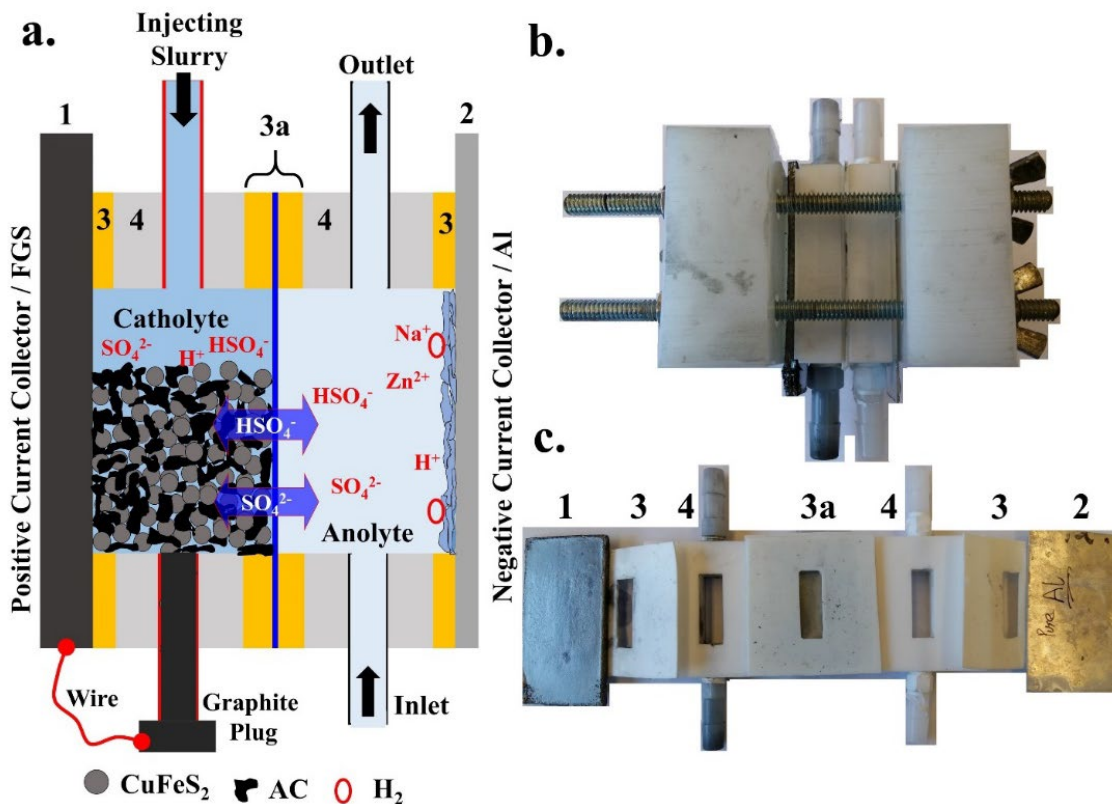


Figure 4-4 (a) Schematic diagram of the TFB (cross-sectional view), (b) assembled cell, the high-density polyethylene end plates in which (c) components of the cell were tightened with screws. (1; GP is the flexible graphite sheet (FGS), 2; pure Al sheet, 3; Si rubber gaskets, 3a; AEM sandwiched in Si rubber gaskets and 4 represents the flow channels in PTFE plates for PSE and anolyte flow through nozzles

4.3 Physical characterization of electrode materials

The morphology of the as synthesized CuFeS_2 particles and Zn deposit on the Al sheet sample was examined in scanning electron microscope (Hitachi S300N VP-SEM). Energy dispersive X-ray (EDX) analysis was carried out to evaluate any variation in the elemental

composition of CuFeS₂ particles before and after GCD in the FBFC and/or TFB. A Rigaku MultiFlex X-ray diffractometer was used to determine the crystal structure of the synthetic CuFeS₂ as well as the deposited Zn on Al under various conditions, as described below. The Cu K α 1 radiation source ($\lambda = 1.5405 \text{ \AA}$) was accelerated at 40 kV and 20 mA in a vacuum tube used to generate the X-rays. The CuFeS₂ powder sample was compressed in the cavity that was produced in a zero-diffraction quartz crystal and installed in the sample holder. A 1° min⁻¹ step size and 0.01° sampling width were selected to obtain diffraction patterns within the range of $2\theta = 10 - 90^\circ$. The K α 2 signals and background noise was subtracted from the diffraction patterns by using Jade 6 (Material Data Inc.) software.

The particle size of the as-synthesized CuFeS₂ and MC powder samples was determined by using a laser diffraction method in Malvern Mastersizer Hydro 2000S. Briefly, 3g of powder sample added in 100 ml of DI water was mixed on a magnetic stirrer to form a uniform dispersion. A representative sample was injected into the sample holder of Mastersizer and the ultrasound mode was turned on for 30 seconds to de-agglomerate and detach any physically interlocked particles.

For surface area measurement and to determine the pore size and distribution in the as-synthesized CuFeS₂ and AC, nitrogen (N₂) adsorption/desorption isotherms (at 77 K) were recorded with a Quantachrome Autosorb-1 machine. A known mass of synthetic CuFeS₂ and/or AC was added in a 6 mm glass bulb and degassed for 92 h at 25 °C prior to N₂ adsorption. The specific surface area and pore size distribution of the synthetic CuFeS₂ and AC were calculated by using the Brunauer–Emmet–Teller (BET) relation and density functional theory (DFT) methods, respectively. The multipoint BET surface area was

determined from the isotherms over the 0.025–0.3 relative pressure (P/P_0) range by following the procedure explained elsewhere [2].

Time of Flight Secondary Ion Mass Spectroscopy (ToF-SIMS) (TRIFT V nano TOF; Physical Electronics) was used to determine the surface characteristics of as-synthesized CuFeS_2 particles. Briefly, the sample powder was mounted on a commercially available (1 cm^2) silicon wafer by using double-sided adhesive tape. Both positive and negative mass spectra were collected by pulsing a 30 keV Au^+ primary ion beam over a $400 \mu\text{m} \times 400 \mu\text{m}$ raster area with a total ion dose $< 10^{12}$ ions/ cm^2 . In the acquisition of spectral data and images, high mass and spatial resolution were achieved by applying the bunched and un-bunched mode, respectively³.

To investigate the variation in the surface composition of CuFeS_2 particles before and after GCD cycling, X-ray photoelectron spectroscopy analyses of as synthesized and retrieved CuFeS_2 from FBFC and/or TFB were carried out by using Leybold Max2000 spectrometer. The X-rays generated from the $\text{Mg K}\alpha$ (1253.6 eV) radiation source were incident on the powder sample placed in the high vacuum chamber. The intensity of the emitted photoelectrons at 90° take-off angle was analyzed as a function of their binding energy in a hemispherical photoelectron analyzer. The survey and high-resolution spectra of Cu, Fe, and S were processed in the XPS peak 4.1 software to examine any change in the surface speciation. The deconvolution of the high-resolution spectra was performed by applying the Gaussian (80 %) + Lorentzian (20 %) function after background subtraction (Shirley method). Any peak shifting in the XPS spectra calibrated with respect to C 1s adventitious peak was analyzed.

³ From the published work, K.M. Deen, E. Asselin, *ChemSusChem*, 11 (2018), 1533–1548.

4.4 Electrochemical Testing

4.4.1 Characterization of the composite electrode(s)⁴

The electrochemical testing of an individual electrode (used in either FBFC or in TFB) was carried out in a water-jacketed three-electrode cell as shown in Figure 4-2. The intrinsic electrochemical behavior of the CF electrode (GF connected to the graphite rod) was initially determined and compared with the composite electrode under the same conditions and in 0.2 M H₂SO₄. Each experiment was repeated more than three times to verify the reproducibility of the results. It is important to note that no CB was added to CuFeS₂ to make the composite electrode analyzed in Chapter 5. However, the composite electrodes prepared for Chapter 6 and 7 contained 20 wt. % CB to enhance the inter-particulate conductivity. A graphite rod and a saturated mercury/mercury (I) sulfate (Hg/Hg₂SO₄) (0.620V_{SHE}) electrode were installed in the cell as auxiliary and reference electrodes, respectively. A Gamry Reference-600 Potentiostat and Echem Analyst (Software ver. 5.30) were used for all the electrochemical experiments and analyses. All potential values reported in this work were converted to the standard hydrogen electrode (SHE) scale unless otherwise stated. Before every electrochemical test, N₂ gas (99.95 %) was sparged for 30 min to eliminate any dissolved oxygen. A constant temperature of 25 ± 1.0 °C was maintained for all the experiments.

The cyclic voltammograms were obtained at various sweep rates (100, 80, 60, 40, 20, 10 and 5 mV s⁻¹) and potential was kept well within the thermodynamic water stability potential window (~1.23 V). Scans were initiated from the OCP to 0.020 V_{SHE} (segment referred to as 'charging') followed by a reverse scan to a maximum 1.020 V_{SHE} (discharging)

⁴ As reported in the published work by K.M. Deen, E. Asselin, *Electrochimica Acta*, 212 (2016), 979–991.

and proceeding to OCP to complete the cycle (see Figure 5-2a and b). Four cyclic scans at each sweep rate were obtained for identification of any variation in the behavior. The scans were reproducible, and data presented in this work is from the third cycle. The charge distribution and transport of ionic species was evaluated from the quantitative analysis of these cyclic voltammograms.

The galvanostatic charging/discharging cycling tests for the CF and composite electrodes were conducted at various constant specific current densities (based only on the weight of the GF) ranging from 0.01 to 0.1 A g⁻¹. The charging and discharging profiles were obtained within a 1.0 V potential range ($-0.6 \leq E_{OC} \leq 0.4$ V). The potential range was selected based on the measured OCP of the GF in 0.2 M H₂SO₄ electrolyte. The same potential range for both electrodes was selected (even if they had different OCP) to investigate any difference achieved with the composite electrode. At each current density, 20 charge/discharge cycles were performed to evaluate reversibility and any potential change due to electrochemical reactions. The columbic efficiency ((discharge/charge) x 100) of both electrodes was measured based on the individual charge/discharge specific capacity at each cycle. The procedure to calculate specific capacity is described in section 5.3.

In order to fully understand the current distribution and charge transport mechanism during the 'charging' process on both the CF and composite electrodes, the potentiostatic electrochemical impedance spectroscopy (EIS) and potentiodynamic cathodic polarization (PCP) tests were conducted. Within the charging regime, the impedance spectra were taken at constant potentials from the OCP of each electrode to -0.9 V (vs. OCP) with a step of -0.1 V. The constant potential was initially maintained for 3 h before each impedance measurement. At every static potential, a 5 mV alternating potential amplitude was applied through a

sequential variation of frequency from 100 kHz to 10mHz. The experimental spectra simulated with equivalent electrical circuits (EEC) were fitted to obtain quantitative information of the physical elements. The proposed model and quantification was validated by potentiodynamic cathodic polarization (PCP) curves obtained at a sweep rate of 5 mV s^{-1} . The final potential of -1.0 V (vs. OCP) below the H^+/H_2 stability line was intentionally selected to study the adsorption of intermediate species (H°) and any redox reactions on CuFeS_2 microspheres. The mechanism of charge transport and possible reactions at the surface of both electrodes is proposed based on these findings.

4.4.2 Electrochemical characterization of electrode(s) for FBFC setup

The electrochemical behavior of a given electrode used in the final FBFC was investigated in a three-electrode cell (Figure 4-2). The electrodes designation and composition of each electrolyte is given in Table 4-1. It is also important to note that electrolyte and electrode systems are designated based on the polarity of electrodes in the FBFC during the discharge cycle. The anode (negative) was a composite of GF and as-synthesized CuFeS_2 particles (80 wt. %) mixed with carbon black (CB) (20 wt. %). The composite electrode was prepared by sandwiching CuFeS_2 particles manually within the two halves of the GF. The edges of the GF were sealed with carbon paste (CB + poly (vinyl di-fluoride); PVDF (4:1)). This composite electrode was then connected to a solid graphite rod with the same carbon paste to complete the working electrode assembly as shown in Figure 4-2. The cathode (positive electrode) was made of only GF and connected similarly with a graphite rod. Potentiodynamic polarization (PD) scans, linear scan voltammetry, cyclic voltammetry (CV) and electrochemical impedance spectroscopy (EIS) analyses were carried out to analyze the

electrochemical response of the electrode materials and to estimate their performance in the actual FBFC system.

The potentiodynamic scans (PD) were obtained by applying a potential ($-1.5 \text{ V} \leq E_{\text{app}} \leq 1.2 \text{ V}$) vs. OCP with a sweep rate of 2 mV s^{-1} . The geometrical surface area of each (GF and composite) electrode was 14.4 cm^2 . However, to compare the results, the current was normalized with the weight of the GF. A total of 25 mg of the $\text{CuFeS}_2 + \text{CB}$ (4:1) mixture was used in the composite electrode.

Table 4-1 The designation and composition of electrode and electrolyte systems used in the FBFC⁵

Type	Composition of the electrode(s)	Electrolyte(s)
Anode (Negative)	GF / $\text{CuFeS}_2 + \text{CB}$ (synthetic)	(Anolyte) 0.2 M H_2SO_4
Cathode (Positive)	GF	(Catholyte) 0.5 M Fe^{2+} in 0.2 M H_2SO_4
		0.5 M $\text{Fe}^{2+} + 0.1 \text{ M Cu}^{2+}$ in 0.2 M H_2SO_4

The impedance spectra were obtained by imposing a 5 mV AC potential amplitude over OCP of each electrode in their respective electrolytes (Table 4-1) and 100 kHz – 0.01 Hz frequency range was selected. Similarly, the cyclic voltammetry scans were obtained at various sweep rates (100, 80, 60, 40, 20, 15, 10, 5, 2 and 1 mV s^{-1}) to evaluate the kinetic response of the individual electrodes in their respective electrolytes – the combination of which we refer to as electrode systems.

⁵ The electrode and electrolytes are designated based on the electrochemical process during the discharge cycle

After optimizing the conditions, the performance of the final FBFC system was evaluated by cyclic voltammetry (CV) and cyclic GCD tests. In order to identify the electrochemical behavior and maximum current response of the FBFC system, the CV scans were obtained at various sweep rates ($0.1 \text{ V s}^{-1} - 0.001 \text{ V s}^{-1}$). The specific capacity, energy density, coulombic efficiency, energy efficiency and cyclic performance of the FBFC system was calculated from the cyclic GCD profile as detailed in section 6.3.

The reaction sequence during GCD performance was also evaluated by post-experimental analyses of the CuFeS_2 retrieved from the composite electrode (negative electrode of the FBFC) after 500 GCD cycles. The surface morphology, phase transformation and any change in the surface composition of the retrieved samples were analyzed and compared via SEM, EDS, XRD and XPS analyses (section 6.4).

4.4.3 Comparing the performance of as-synthesized CuFeS_2 and MC in FBFC⁶

For electrochemical characterization and to compare the energy storage and Cu extraction capabilities in the FBFC system, the GF and composite electrodes (GF- CuFeS_2 or GF-MC) in the positive and negative compartments, respectively, were connected to the working/working sense and counter/reference leads of the potentiostat, respectively. Both anolyte and catholyte were circulated separately in the FBFC in a closed-loop and at a constant flow rate (7.5 ml min^{-1}).

To investigate the electrochemical response of both the synthetic CuFeS_2 and MC in the FBFC, CV scans were obtained at various sweep rates (from 0.1 V s^{-1} to 0.001 V s^{-1}) within a 1.0 V cell potential. The charge storage capability of the FBFC was evaluated from the cyclic

⁶ As reported in the published work by K.M. Deen, E. Asselin, *Electrochimica Acta* 297 (2019) 1079–1093.

GCD test. The charging was carried out at 200 mA g^{-1} and the FBFC was discharged at 150 mA g^{-1} . The specific capacity of the FBFC system (using both synthetic CuFeS_2 and MC) was calculated from the continuous GCD cycles. XRD and XPS analyses of the synthetic CuFeS_2 after GCD cycling was also carried out to evaluate any structural or compositional changes in the negative electrode. During GCD cycling Cu^{2+} released from the CuFeS_2 in the anolyte and/or migrating from the catholyte could affect the charge storage capacity of FBFC. Therefore, to support the experimental results, potentiodynamic cathodic polarization scans of GF- CuFeS_2 electrodes (separately in a three-electrode cell setup) were also obtained in a $0.2 \text{ M H}_2\text{SO}_4$ solution containing various amounts of Cu^{2+} species. For detail analysis and result please see section 7.3.

4.4.4 Electrochemical behavior of electrode(s) used in the TFB

The electrochemical behavior of the positive and negative electrodes in their respective electrolytes was measured individually in a standard three electrode setup. The electrodes were designated as positive (cathode) and negative (anode) in the TFB and TFB-M based on the electrochemical reactions during the discharge cycle as detailed in Table 4-2. For example, CuFeS_2 mixed with AC (20 wt. %) and $0.2 \text{ M H}_2\text{SO}_4$ in the form of slurry was used as a positive electrode in the TFB. Thus, the electrochemical response of each positive slurry electrode (PSE) component, i.e. GP (positive current collector in the TFB), AC and CuFeS_2 in $0.2 \text{ M H}_2\text{SO}_4$ solution was measured via CV scans obtained at a 5 mV s^{-1} sweep rate.

Table 4-2 The electrode systems and composition of the electrolytes used in the TFB setups⁷

Type	Electrode(s)/Current collector(s)	Electrolyte(s)
Anode (Negative)	Pure Aluminum sheet	(Anolyte) 100 g Zn ²⁺ +0.1 M Na ₂ SO ₄ +0.2 M H ₂ SO ₄
Cathode (Positive)	Flexible graphite sheet	(Catholyte; PSE) 20% solids (CuFeS ₂ +AC) in 0.2 M H ₂ SO ₄
		(Catholyte; PSE-M) 20% solids (MC+AC) in 0.2 M H ₂ SO ₄

Similarly, at the negative electrode side, it is important to optimize the conditions for efficient Zn²⁺ deposition on the Al substrate. For this reason, the effect of CTAB addition on the Zn deposition was investigated by galvanostatic polarization (GS), and CV scans. Based on these results, a potential – concentration (PC) diagram was developed to estimate the nucleation/deposition overvoltage as a function of CTAB concentration. The CTAB concentration was varied from 1 ppm to 8 ppm and coulombic efficiency of Zn deposition was determined from gravimetric analysis. By using Equation 4.1 below, the total charge consumed during GS polarization was calculated to evaluate the coulombic efficiency (η_c).

$$\eta_c = \left(\frac{Q_g}{Q_{gs}} \right) \times 100 = \left(\frac{\frac{mnF}{M}}{i_c t} \right) \times 100 \quad \text{Equation 4-1}$$

Where, Q_g and Q_{gs} are the total charges calculated from the gravimetric analysis by using Faraday's law and from GS tests, respectively. m , n , F and M are the mass of Zn deposit, a number of electrons, the Faraday constant (96485 C mole⁻¹) and the atomic mass of Zn,

⁷ The electrode and electrolytes are designated based on the electrochemical process during the discharge cycle

respectively. The i_c and t are the charging current and time, respectively, applied in the GS testing. The CV and GS tests were performed to determine the nucleation and steady-state potential values for Zn deposition. The potential/concentration (PC) diagram was developed to evaluate the overvoltage for nucleation and uniform deposition of Zn on Al as a function of CTAB concentration. The morphology of the Zn deposit obtained in the anolyte solution containing various amounts of CTAB after GS testing was examined by SEM. The influence of CTAB concentration on the crystallographic orientations of Zn deposits developed after GS testing was evaluated from XRD patterns. Based on these observations, the solution of 100 g Zn^{2+} + 0.1 M Na_2SO_4 dissolved in 0.2 M H_2SO_4 and containing 2 ppm CTAB was selected as anolyte in the TFB.

4.4.5 Performance evaluation of the TFB

The positive and negative current collector plates of the TFB were connected to the working and counter/reference leads of the cell cable attached to a potentiostat (Reference 600, Gamry®). The open circuit voltage (OCV) was determined, and anolyte was set to circulate continuously in a closed loop during the test. CV scans were obtained at various sweep rates ($1 - 25 \text{ mV s}^{-1}$) to identify the reaction sequence and to evaluate the system kinetics. Cyclic performance, specific capacity, and specific energy were measured from cyclic galvanostatic charge/discharge (GCD) tests. The charging and discharging were conducted at 1C and 0.5C rates, respectively (where 1C = 4.65 mAh, determined from the mass of Zn deposit during the charging process in a separate experiment). The coulombic (η_C), energy (η_E) and voltage (η_V) efficiencies were also calculated from individual GCD cycles. The rate performance of the TFB was also probed by charging at 1C but discharging at various rates (0.5C, 1C, 1.5C, 2C, and 2.5C). The cell polarization (I–V curve) behavior was estimated from the galvanodynamic

polarization curve. The cell was initially charged from OCV to 1.8 V at 1C, and the variation in cell voltage during discharge was observed (up to 0.6 V) by varying the load from 0 to 0.025 A at a 0.1 mA s⁻¹ scan rate.

To demonstrate the use of the TFB as an energy storage unit, the setup was initially charged to 1.8 V and a light emitting diode (LED) mounted on a pre-built microcontroller was connected with the current collector plates. The internal circuit of the microcontroller was designed to visually display the cell operation by turning on the LED at potential ≥ 1.0 V. In this test a constant LED load (~ 0.5 mA) would consume the stored charge, and under an applied load, the change in the cell potential as a function of time was measured.

4.5 The reaction sequence for Cu extraction and system mass balance

During repetitive charge/discharge cycles, the occurrence of irreversible faradaic processes i.e. oxidation/reduction of CuFeS₂ in the positive slurry electrode could significantly affect the reversible performance of the TFB. Based on GCD cycling, the total irreversible charge ($Q_{irr} = Q_{charge} - Q_{discharge}$) was calculated and the % Cu extraction was determined from ICP-OES (Varian 725-ES) analysis of both retrieved catholyte and anolyte after 20, 40, 60, 80 and 100 GCD cycles. For these analyses, standard solutions of various concentrations were prepared as background solution (2 % HNO₃ and 0.2 M H₂SO₄ (1:1)) for dilution. Based on Q_{irr} and Cu extraction (from ICP-OES analysis) as a function of a number of GCD cycles, the reaction sequence has been investigated (see section 8.4). During the charging cycle, the transport of anionic species (specifically SO₄²⁻ species) from anolyte to catholyte, and vice versa during discharge process, was calculated from the instantaneous electric field across the AEM. During Zn deposition on the negative electrode (charging step), the transport (diffusion + migration) of SO₄²⁻ toward the catholyte and reverse (only migration) was calculated using

the extended Nernst–Planck equation and compared with the Cu + Fe contents (extracted from CuFeS_2) for mass balance.

Chapter 5: Electrochemical behavior of CuFeS₂/GF composite electrodes⁸

In this Chapter, detailed electrochemical analyses of synthetic CuFeS₂ in a composite electrode were carried out. The motivation to conduct these analyses was to separate out the current distribution on the composite electrode and to predict its cyclic performance as a negative electrode in the FBFC. GF possesses relatively large surface area and high electrical conductivity compared to CuFeS₂. Therefore, the effect of GF in this composite electrode and its contribution to charge storage was also determined to predict the reaction sequence during reversible charge (reduction) and discharge (oxidation) cycles in the anolyte (0.2 M H₂SO₄). Synthetic CuFeS₂ was used in this study to avoid the complexities associated with the many impurities in natural mineral concentrates, and to avoid the variability in particle size and shape that could mask the actual electrochemical response of CuFeS₂.

It is proposed that in an acidic electrolyte the double layer can form quickly on the GF during charging and an intermediate species (H[°]) can adsorb by the interaction of H⁺ ions with surface functional groups without further reaction to H₂ evolution. This charge transfer process and formation of the intermediate H[°] species is referred to as underpotential deposition (UPD). Based on the literature, and experimental results described in this Chapter, the increase in the charge storage capacity of the composite electrode was attributed to the reversible transformation of the sulfide sulfur species on the surface of CuFeS₂, and to the formation and transportation of intermediate species (H[°]) to the CuFeS₂ crystallites.

⁸ From published work, by K.M. Deen, E. Asselin, *Electrochimica Acta*, 212 (2016), 979–991.

5.1 Characterization of the synthetic CuFeS₂

The as-synthesized CuFeS₂ particles presented spherical morphology in which a platelet-like open structure was attached to the core similar to pompom dahlia flowers as shown in Figure 5-1a. The average particle size (D80) of these microspheres was $23.48 \pm 2.00 \mu\text{m}$. A wide range of particles having variable size and morphology were formed during the hydrothermal synthesis process as depicted in the particle size distribution profile (Figure 5-1b). The micro-spherical morphology of these particles was similar to the results described elsewhere [145, 162, 167] in the literature. The surface area of the GF and synthetic CuFeS₂ microspheres were 4.201 and 3.511 m² g⁻¹, respectively, as determined from the N₂ adsorption/desorption isotherm and multipoint BET surface area analysis (Figure 5-1c). The relatively large surface area of the CuFeS₂ microspheres attributed to the open platelet-like structure. Table 5-1 provides the quantitative information about the multipoint BET surface area analyses.

Table 5-1 Quantitative measurement of parameters from Multipoint BET surface area analysis

Parameters	GF	Chalcopyrite (CuFeS ₂)
BET constant; <i>C</i>	6.71	59.25
Slope; <i>s</i>	704.9	975.2
Intercept; <i>i</i>	123.3	16.74
Surface Area; <i>S</i> _{BET} (m ² g ⁻¹)	4.205	3.511

The XRD pattern of the synthetic CuFeS₂ perfectly matched to the JCPDS 37-0471, reference pattern for pure CuFeS₂ (Figure 5-1d). This validated the formation of pure crystalline phase having a tetragonal crystal structure with lattice parameters (a, b = 5.2893; c = 10.423), belonging to the I-42d (122) space group. The sharp diffraction peaks at 2θ i.e.,

29.4°, 48.65°, 49.04°, 57.85°, and 79.48° were attributed to single phase CuFeS₂ originating from the (112), (220), (204), (312) and (316) lattice planes, respectively.

Figure 5-1e shows the full range XPS survey scan of as synthesized CuFeS₂, which confirmed the presence of copper, iron and sulfur core peaks. The 'C1s peak' commonly referred to as 'adventitious peak' originated at (284.87 eV) also confirmed no charging effects on the powder sample. This peak appeared possibly due to the presence of unreacted organic species left in the product or this may also arise due to the contamination of the specimen holder in the vacuum chamber. The origin of the peak for 'O 1s' at 531.7 eV was possible due to air oxidation of the as synthesized CuFeS₂ crystallites. The spin-orbital splitting of S 2p_{3/2} and S 2p_{1/2} in the XPS spectrum occur as doublets of the 'S 2p' peak. The high-resolution spectra of sulfur species (S 2p_{3/2}) core peaks were fitted by using XPS peak 4.1 software and by applying a Gaussian-Lorentzian function (weighing; 80% Gaussian + 20% Lorentzian). In addition, the Shirley method was used for background subtraction as shown in Figure 5-1f [197]. This function resolved the spectra and clearly fractionated the doublet peaks of S 2p_{3/2} at 161.42 and 162.45 eV corresponding to the S²⁻ and S₂²⁻ in the bulk phase, respectively. The 1.03 eV shift in the binding energy of the S 2p_{3/2} doublet peaks was slightly lower than the reported value (1.1 eV) for fully coordinated sulfur in the CuFeS₂ lattice structure [47, 198, 199]. Klauber et al. [45] reported the S₂²⁻ species S 2p_{3/2} peak position at 162.48 eV, which agreed well with our experimental value (162.45 eV). The broad collar peak at 163.73 eV (FWHM=2.044 eV) is due to the presence of S_n²⁻ species with (n > 2) at the crystallite surface [48]. In addition, the core level Fe 2p signatures (i.e., Fe 2p_{3/2}, Fe 2p_{1/2} peaks at 711.45 and 725.45 eV, respectively) were very weak and the dominant doublet peaks of copper (Cu 2p_{3/2}, 2p_{1/2}) at the crystallite surface corresponded to the association of copper with disulfide in the

form of CuS_n . The very low-intensity satellite peak at 942 eV was observed for the divalent Cu^{2+} species and dominant Cu 2p_{3/2}, 2p_{1/2} peaks at 932.48 and 952.53 eV, respectively, were attributed to mono-valent copper (Cu^+) species which are characteristic of CuFeS_2 .

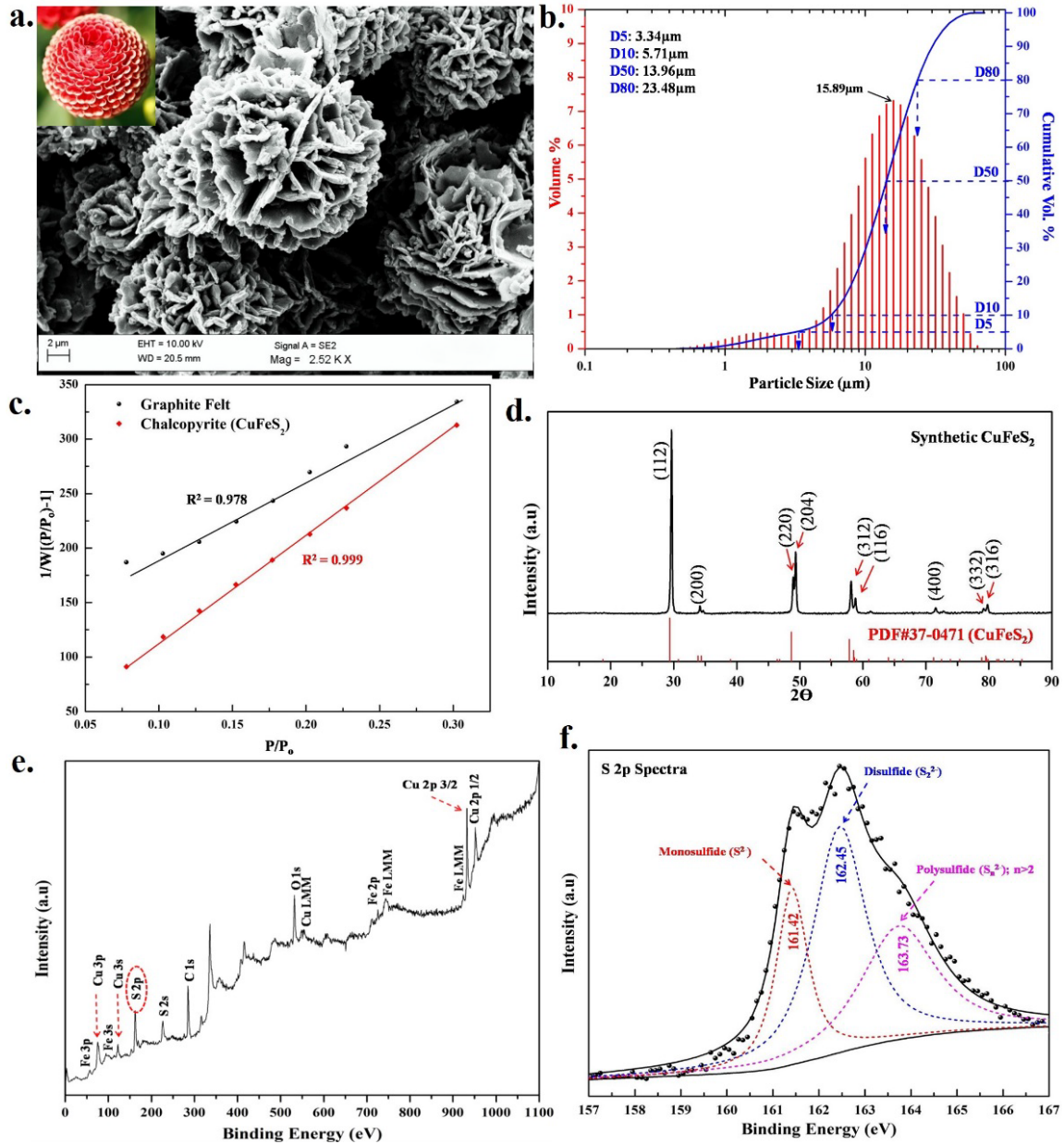


Figure 5-1(a) Morphology and (b) particle size distribution curve of as-synthesized CuFeS_2 . (c) Multipoint BET analysis. (d) XRD pattern of CuFeS_2 . (e) The XPS survey scan of the CuFeS_2 powder sample. (f) Deconvoluted high-resolution spectra of 'S 2p'

5.2 Cyclic Voltammetry

Within 1.0 V potential range (well within the thermodynamic stability of H₂O), the total current response was the sum of charge involved in the double layer charging and faradaic UPD of H⁺. In addition to these components, the faradaic current may also result from possible redox reactions occurring at the surface of the CF or on the CuFeS₂ microspheres in the composite electrode. Figure 5-2 shows the cyclic voltammograms of CF and composite electrode (GF+CuFeS₂), in 0.2 M H₂SO₄ (pH = 0.702±0.005). The sulfuric acid is dissociated into H⁺ and HSO₄⁻ ionic species (reaction 5.1) and were the dominant ionic species depending on their thermodynamic stability at 25 °C and the pH of the electrolyte [200].



The polarization effects possibly associated with the potential drop due to high resistivity of CuFeS₂ or due to diffusion controlled processed within the porous GF are pointed out in Figure 5-2a, b, where delay in current response upon potential sweep reversal is shown as 'V_{CF}' and 'V_{comp}' for the CF and the composite electrode, respectively. During charging (reverse scan), the total negative charge at the electrode surface is the sum of the charge in the electrical double layer and charge involved in the faradaic reactions across the electrode/electrolyte interface. These additional faradaic reactions (pseudocapacitive behavior) could further increase the overall capacitance [183]. In this case, these pseudocapacitive effects may either emerge due to (i) charge transfer through UPD of H₃O⁺ (adsorption) reaction 5.2, or via (ii) ionic transport through the porous structure of GF and within the platelet structure of the micro-spherical CuFeS₂ particles. The pseudocapacitive response may also originate due to the occurrence of (iii) reversible redox reactions at the electrode/electrolyte interface [129, 131].



Where C_x is the number of available sites on the graphite surface, ' H_n ' is the number of adsorbed H^0 species at the surface of GF during charging. For the CF electrode, the charge in the electrical double layer is distributed within the porous structure of GF and therefore the polarization effects due to the electrolyte resistance down the pore during charge/discharge could influence charge storage capacity [201]. The internal charge distribution within the pores (adsorption leading to depletion of H^+ species within the porous structure) is controlled by diffusion and therefore, the current response in cyclic voltammetry depends on the sweep rate as shown in Figure 5-2a and b.

The relatively large potential delay ($\Delta V_{comp} > \Delta V_{CF}$) observed for the composite electrode (Figure 5-2b) was possibly related to the slow kinetic reactions during charging/discharging cycles [202]. The potential dependent but relatively higher specific current density of the composite electrode was attributed to double layer charging complimented with pseudocapacitive reversible redox reactions.

The open porous platelet structure of the synthetic $CuFeS_2$ microspheres (surface area; $3.51 \text{ m}^2 \text{ g}^{-1}$) may enhance the overall current response due to the high interaction of cationic species (H_3O^+) at the interface. The transport of ionic species within the porous structure of the microspheres and reversible surface limited adsorption/desorption reactions may occur in addition to the electrostatic charge built up in the double layer. This is referred to as pseudocapacitive behavior and is considered to be one of the reasons for the higher specific current density registered by the composite electrode compared to the CF electrode (Figure 5-2a and b). The fractional contribution of surface limited current due to charge in the double layer and due to specifically adsorbed species from the CV analysis can be separated from the

current associated with the faradaic (diffusion controlled processes) by employing the power law (Equation 5.1) [129, 131].

$$I(V) = as^b$$

Equation 5-1

Where ' $I(V)$ ' is the current response at specific potential and 'a' and 'b' are adjustable parameters.

During charging/discharging scans of CF and composite electrodes, the total current at each potential presented a linear relation with the sweep rate (s) for both electrodes (as shown in Figure 5-2c; the trends for the composite electrode are provided as an example). The 'b-value' is the slope of the linear trends, which depends on the applied potential. $b = 1$ corresponds to pure double layer charge. $b = 0.5$ corresponds to faradaic adsorption and/or semi-infinite diffusion processes [131, 138]. The b-values calculated for the CF electrode ranged between ($0.68 \leq b \leq 1$) (as shown in Figure 5-2d), which can be related to mixed double layer charging and pseudocapacitive behavior i.e. by interaction of ionic species with the surface functional groups on GF (reaction 5.2) [131]. After an initial delay ($\Delta V_{CF} = \sim 0.20$ V), during the discharge scan, the pseudocapacitive (desorption) reactions were followed by the non-faradaic double layer transformation ($b \rightarrow \sim 1$). In the case of the composite electrode, during charging, within the 0.4 to 1.0 V potential range, the occurrence of faradaic reactions was predicted from the current response controlled by diffusion processes ($b \sim 0.5$). 'b' values below 0.4 V indicate the progress of irreversible reduction reactions at the surface of CuFeS_2 platelets. The b-value < 1.0 observed for the composite electrode can be assigned to surface limited faradaic reactions leading to a diffusion-controlled process. This behavior could also be related to the partial reduction of the ionic and surface species present on the CuFeS_2 particles during the charging cycle. The hybridized electrochemical response and relatively large specific current density presented by the composite electrode compared to the CF

confirmed the occurrence of such additional pseudocapacitive reactions on the surface of CuFeS₂ microspheres.

In order to quantify and separate the current contributions of non-faradaic and faradaic reactions leading to diffusion-controlled processes, many authors [131, 138, 183] have used the approach adopted here. As discussed above the total current output at various sweep rates as a function of potential is composed of non-faradaic capacitive (k_1s) and diffusion controlled (faradaic) processes ($k_2s^{1/2}$) according to the current partitioning Equation 5.2.

$$I(V) = k_1s + k_2s^{1/2} \quad \text{Equation 5-2}$$

The manipulation of the above equation to determine ' k_1 ' and ' k_2 ' may be used to calculate the fraction of each current contribution Equation 5.3.

$$I(V)/s^{1/2} = k_1s^{1/2} + k_2 \quad \text{Equation 5-3}$$

The sweep rate dependent ' $I(V)$ ' for both electrodes is plotted according to Equation 5.3 at each potential (V) and the linearly fitted curves provided the values of ' k_1 ' and ' k_2 '. In Figure 5-3a and b, the respective voltammograms of both 'CF' and composite electrodes at 20 mV s⁻¹ are presented in which the total specific current density was partitioned into non-faradaic (shaded area) and faradaic contributions. It is shown that the major current response (~93 %) from the composite electrode was controlled by diffusion controlled faradaic electrochemical reactions (pseudocapacitive current), whereas, the CF electrode provided a far greater amount of electrostatic current density (~52.5 %) attributed to the double layer charge as shown in Figure 5-3c. The differential specific capacitance (C_{sp}) involved during charging and discharging was measured by integrating the total current within the applied potential and normalizing with sweep rates according to the following Equation 5.4 [203].

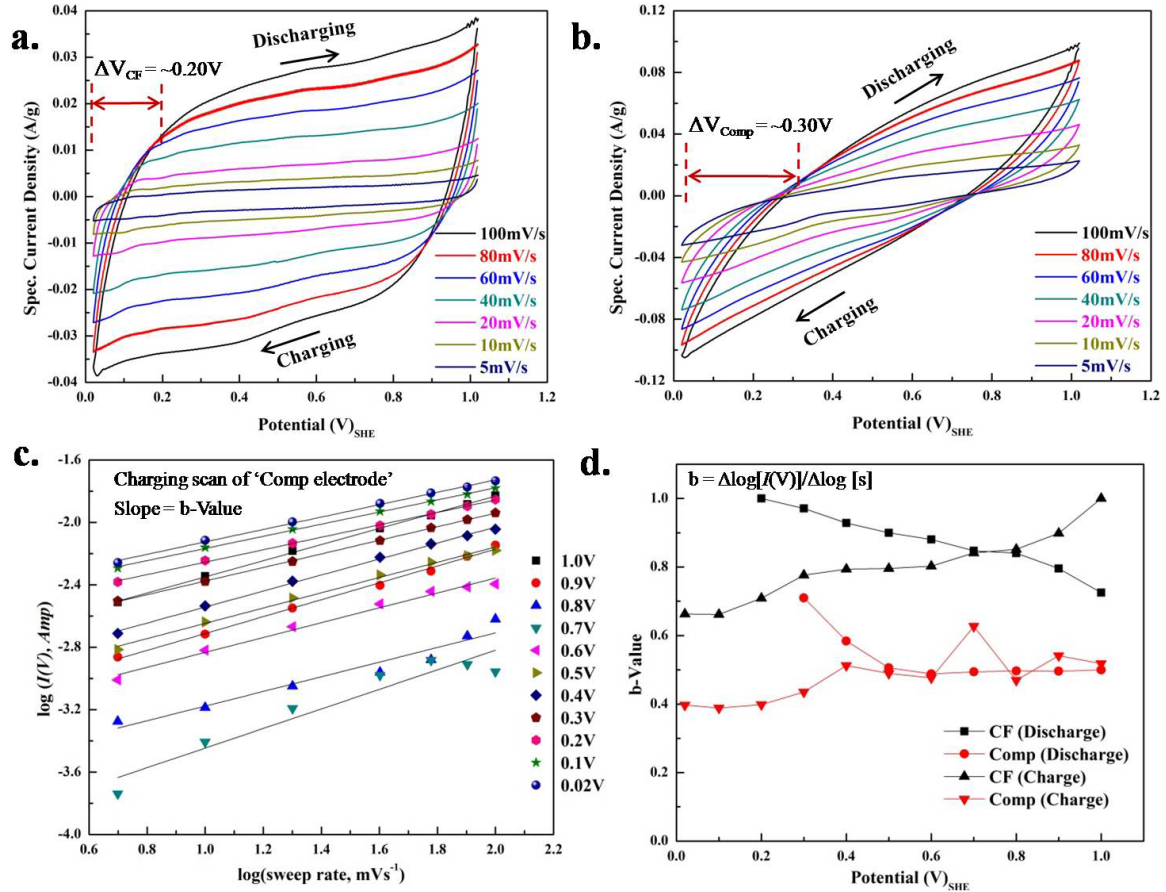


Figure 5-2 CV scans (at 5–100 mV s⁻¹) of (a) CF and (b) Composite (CF+CuFeS₂) electrode. (c) Trends of current vs. sweep at various potentials. (d) b–values as a function of charge and discharge potential (For comparison, the current is normalized by the mass of GF)

$$C_{sp} = \frac{I(V,t)}{sm_{GF}}$$

Equation 5-4

Where 's' is the *sweep rate*, 'dV/dt' (V s⁻¹), m_{GF} is the weight of the GF in the CF electrode; V₁ and V₂ are the potential extremes of 0.02 and 1.02 V_{SHE}, respectively. The increase in differential capacitance with a decrease in sweep rate (from 100 to 5 mV s⁻¹) confirmed the delay in the ionic charge redistribution within the porous structure of the CF electrode (Figure 5-3d) and growth of the diffusion layer at the electrode/electrolyte interface due to the progress of faradaic (pseudocapacitive) processes. Similarly, in the case of the composite electrode, reversible charging/discharging and highly distorted differential capacitance at low sweep rate

(compared to GF) also indicate the progress of pseudocapacitive faradaic reactions preferentially on the surface of CuFeS₂ crystallites as depicted in Figure 5-3e.

One can expect that the substantial amount of pseudocapacitive behavior of the composite electrode was affiliated with the morphology of the CuFeS₂ crystallites and/or to the occurrence of reversible reactions at the surface of these particles.

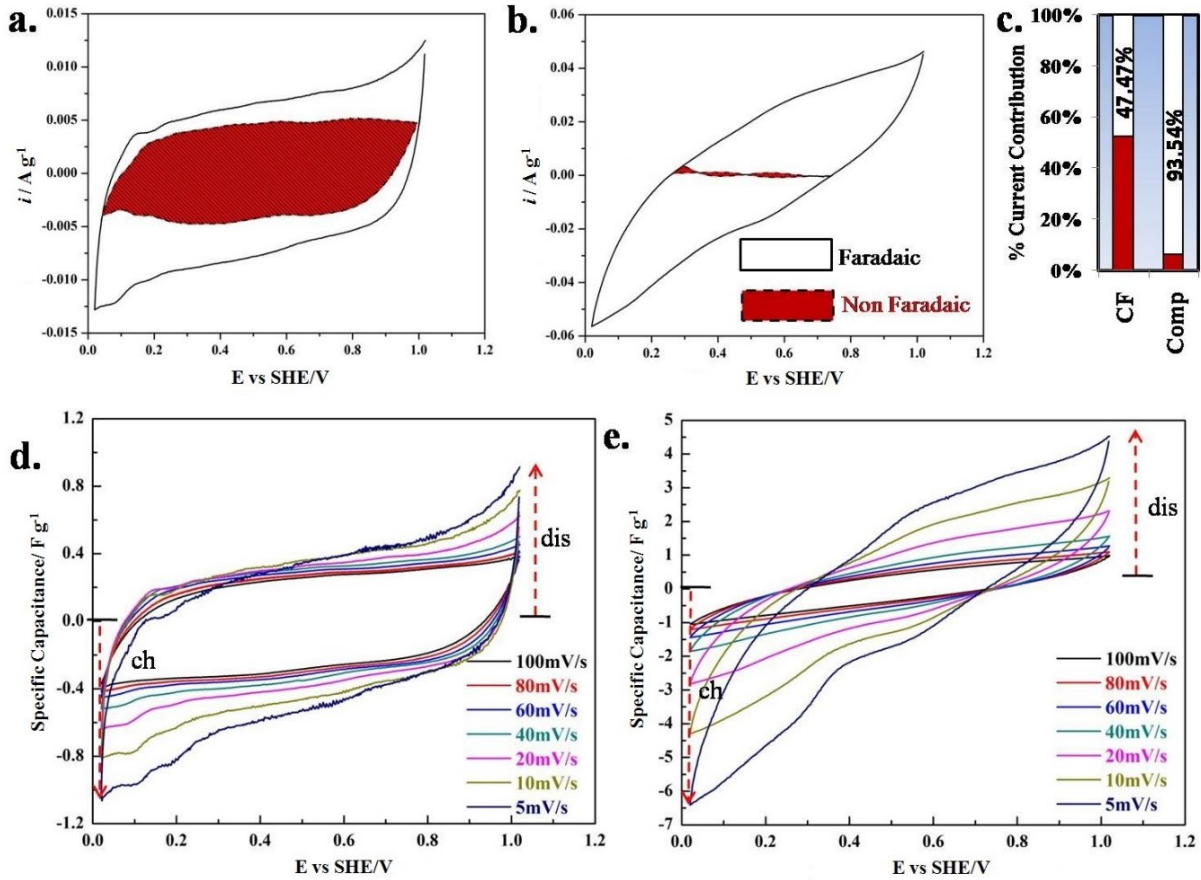


Figure 5-3 CV of (a) CF and (b) Composite electrodes at 20 mV s⁻¹, showing the current distribution. (c)

Comparison of the total current contributed to the non-faradaic and faradaic processes leading to diffusion controlled processes as revealed from C_{sp} plots of (d) CF and (e) composite electrodes. ('ch' and 'dis' represent the start and end of discharge, respectively).

The large surface area (3.51 m² g⁻¹) and porous structure of the microspheres also provided a shorter path length for H⁺ ion diffusion and therefore registered high current density

in the cyclic voltammetry scans. Furthermore, a significant amount of pseudocapacitive current contribution presented by the CF electrode was due to the reversible reactions of H^+ and quinone/pyrone type functional groups present at the surface of GF. This could be predicted from the broad anodic and cathodic peaks (centered at $\sim 0.6 V_{SHE}$) as evident in Figure 5-2a. From the cyclic voltammograms, it was evaluated that the overall faradaic contribution ($\sim 47\%$) included reversible redox reactions associated with these functional groups and formation of transient intermediate species (H°) (adsorption) at the surface of the graphite fibers during the UPD process [173, 202, 204]. In Figure 5-3a and c, about 47.47% of the total charge associated with the GF in the CF electrode was faradaic in nature.

To further confirm the cause of this significant amount of pseudocapacitive (faradaic) behavior affiliated with the surface functional groups, the FTIR spectra of '*un-exposed*' GF and '*exposed*' (after charge/discharge) were obtained as shown in Figure 5-4. The IR spectra of both samples were found to be similar to each other and no change in the band vibrations was observed. This behavior also shows the reversible electrochemical character of surface functional groups which remain stable even after exposure to the acidic solution. The spectra showed broad hydroxyl ($-OH$) stretching bands at $3500-3250\text{ cm}^{-1}$ and at 2670 cm^{-1} , indicated the strong hydrogen bonding in the structure and signatures of carboxylic groups on the GF. The free water ($-OH$) bands ($3600 - 3200\text{ cm}^{-1}$) were neglected in the analysis and are not shown in the spectra [205]. The stretching bands within $3000 - 2830\text{ cm}^{-1}$ and small bending bands at 1380 cm^{-1} and 875 cm^{-1} correspond to the alkane ($-C-H$) group. The sharp background signatures at $2550 - 2000\text{ cm}^{-1}$ were also prominent in the spectra and may originate due to the air and CO_2 present within the porous structure of the GF and from the ATR diamond crystal used during analysis. These bands were consistent with the spectra of

the air background taken before experiments (not shown here). The strong stretching vibrations within 1850 – 1600 cm^{-1} consisted of multiple bands mostly associated with the carbonyl ($=\text{C}=\text{O}$) group. These bands reflected the existence of the carbonyl group attached to aldehyde (1740 – 1720 cm^{-1}), ester (1750 – 1735 cm^{-1}) and multi-membered cyclic ketonic structures as reported by Fuente et al. [206]. The small but sharp bending vibrations at 1570 cm^{-1} and 1460 cm^{-1} represent the presence of aromatic ($-\text{C}=\text{C}-$) groups in the structure of GF [206, 207]. The strong vibration detected in the IR spectra of both samples within 1850 – 1600 cm^{-1} and bands at 1570 cm^{-1} and 1460 cm^{-1} are well documented in the literature and supported to the presence of quinone/pyrone (poly-aromatic and cyclic ketone) type functional groups at the surface of carbon-based materials [206, 208, 209].

The pseudocapacitive behavior of carbon-based materials is also well known due to reversible redox reactions of H^+ ions in acidic solutions with the functional groups (i.e. quinone/hydroquinone/pyrone) present at the edges of graphene layers as given in reaction 5.3 below [210, 211].



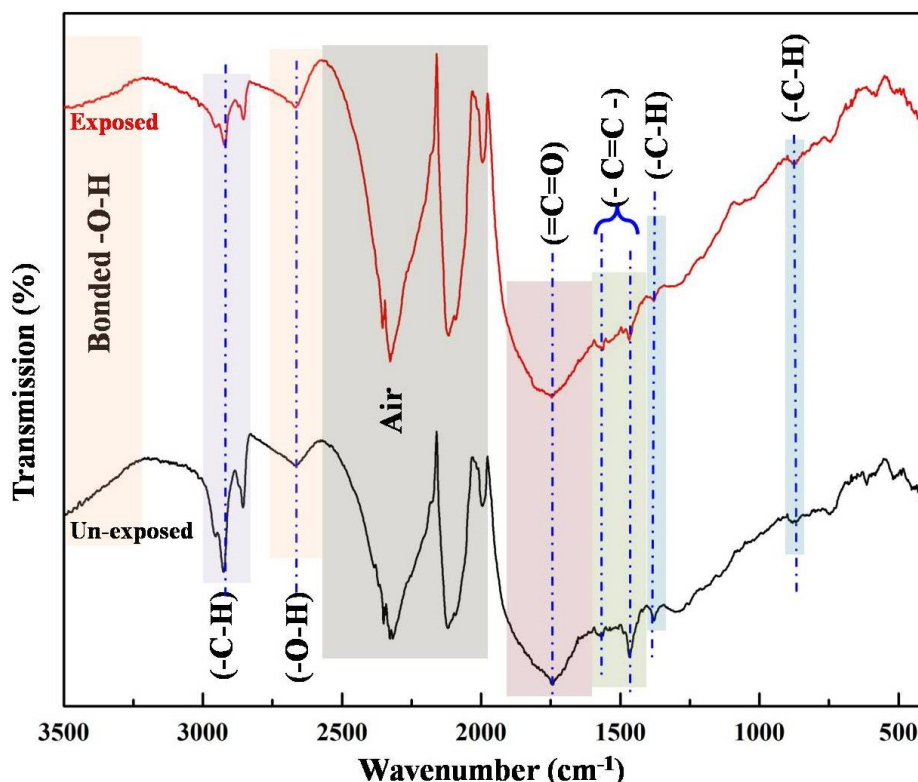


Figure 5-4 FTIR spectra of unexposed (as received) and exposed (after GCD in de-aerated 0.2 mol dm^{-3} H_2SO_4 at 25°C) graphite felt (CF)

In this study, the OCP of the CF electrode in $0.2 \text{ M H}_2\text{SO}_4$ was about $0.683 \pm 0.01 \text{ V}_{\text{SHE}}$ which also strengthens this feature of the quinone/hydroquinone/pyrone (E° range between $0.5\text{--}0.7 \text{ V}$) reversible redox activity in the GF [208, 210]. The current peaks centered at $\sim 0.6 \text{ V}_{\text{SHE}}$ in the CV scans (Figure 5-2a and b) of CF and composite electrodes validate this reversible behavior. Andreas et al. [211] also conducted a detailed study to investigate the pseudocapacitive behavior of carbon cloth in both acidic and basic electrolytes. They concluded that a significant amount of total capacitance in the acidic electrolyte was associated with the reversible redox reactions of quinone/pyrone type functional groups at the GF surface. These results were in support of the pseudocapacitive behavior of the GF (CF electrode) in our case.

XPS analysis of as synthesized CuFeS₂ confirmed the existence of sulfur enriched species (S₂²⁻, S²⁻ and S_n²⁻) at the crystallite surface as shown in Figure 5-1f. Conway et al. [173, 212] discovered the reversible pseudocapacitive behavior of disulfide (S₂²⁻) species present at the surface of pyrite (FeS₂) as follows (reactions 5.4 & 5.5).



The S₂²⁻ may reversibly transform to S²⁻ at the particle/electrolyte interface and, during the reduction of the S²⁻ species, may be protonated to form SH⁻. The repetitive CV scans of the composite electrode demonstrate the reversibility of the charge/discharge process which is attributed to the overall current response of both GF and CuFeS₂. However, under similar conditions, compared to the GF only, the large faradaic current response of the composite electrode also indicates the reversible character of sulfide sulfur species (i.e. S₂²⁻, S²⁻), which are present on the surface of CuFeS₂ as confirmed from the XPS analysis (Figure 5-1f). At low sweep rate (5 mV s⁻¹), the small current peaks at ~0.3 V_{SHE}, as shown in Figure 5-2, may be associated with the reversible S₂²⁻/S²⁻ redox reaction.

Based on the above, the reversible charging/discharging behavior of the composite electrode is related to the reversible adsorption/desorption of H⁺ on the surface functional groups of GF and the reversible transformation of S₂²⁻ into S²⁻ (reaction 5.4) on the polysulfide surface film. The increase in differential specific capacitance during charging (reduction of H⁺) was due to its the specific adsorption at potentials that are more negative but above the H⁺/H₂ couple potential under applied conditions. The occurrence of irreversible reactions on the composite electrode cannot be neglected during cycling and these were attributed to the reaction of H⁺ ions with the surface species and to the formation of conversion products on the

surface of CuFeS₂. The irreversible behavior was found to be more pronounced for the composite electrode where maximum differential capacitance during discharge at all scan rates was lower than the extreme capacitance obtained during charging sweeps (ch > dis) as shown in Figure 5-3d and e. This behavior may also arise due to potential drop across the interface by the accelerated ingress of cations inside the electrode or due to temporary depletion of H⁺ ions during charge cycle. For the composite electrode (Figure 5-3e), the increase in differential capacitance with decrease in sweep rate is attributed to the effective penetration of the electrochemical signal down the porous GF structure and the occurrence of quasi-reversible reactions (as identified and discussed in Chapter 7) on the polysulfide film that was developed on the surface CuFeS₂. In other words, the electrochemical response of CuFeS₂ was sluggish at high sweep rate but improved significantly at low sweep rate. This behavior suggests that to achieve maximum specific capacity from this type of electrode material would require a slow charge/discharge rate similar to many existing battery electrode materials [203, 212, 213].

5.3 Galvanostatic cyclic charging and discharging profiles of electrode systems

The galvanostatic charging (GC) and discharging (GD) profiles of both the CF and composite electrodes were obtained to support cyclic voltammetry analysis. The quantitative estimation of the total charge stored and released by these electrodes can be estimated from the GCD profiles according to Equation 5.5 [173].

$$C_{sp} = \int_{t_1}^{t_2} \frac{i}{(dV).m_{GF}} \cdot (dt) \quad \text{Equation 5-5}$$

Where, ' C_{sp} ' is the specific capacitance (F g⁻¹), ' dV/dt ' (V s⁻¹) is the shift in potential within initial ' t_1 ' and maximum time ' t_2 ' during charge or discharge under the applied potential range, whereas, ' i ' is the constant specific current (A g⁻¹) and ' m_{GF} ' has its usual meanings. The potential limits of $-0.6 \text{ V} \leq E_{OCP} \leq 0.4 \text{ V}$ were selected for both electrodes during charging and

discharging at various constant current densities (ranging from 0.01 – 0.10 A g⁻¹). The reason for selecting this potential range was to avoid the occurrence of any side reactions, i.e. H₂ evolution and/or water decomposition at the electrode surface. Since the charging was started from the OCP of the respective electrodes, we neglected the first cycle in the analysis. The discrete GCD cycles are shown in Figure 5-5a and b for both CF and composite electrodes, respectively. The CF electrode showed nearly symmetrical charging and discharging profiles corresponding to reversible behavior mostly arising from double layer capacitance and from the pseudocapacitive response of the surface functional groups. The reason for the sharp increase in potential after each charging step depicted the interfacial resistance possibly arising due to the mass transfer-controlled processes down the porous structure. During charging, the depletion of H⁺ species within the porous structure of the GF could also contribute to the overall potential drop across the electrode/electrolyte interface. This behavior is mostly due to the porous structure and has been well explained and in detail by Pell et al. [201].

The composite electrode showed asymmetrical but reversible charging/discharging behavior. During charging, the steep potential decay (plateau at about -0.365 ± 0.015 V vs. OCP (or $+0.105$ V_{SHE}) above E°(H⁺/H₂) was observed, which could be related with the quasi-reversible reaction of S₂²⁻/S²⁻ and/or to the adsorption (reaction 5.3 and 5.4) of H⁺ ions at the surface of the CuFeS₂ crystallites. The existence of irreversible faradaic reactions at the surface of CuFeS₂ cannot be neglected during cycling at low current densities (0.01 and 0.02 A g⁻¹). The limited reactions based on ion transport are always sluggish and at low current densities, the ions have sufficient time to diffuse within the porous structure and to interact with the thin polysulfide film that covers the CuFeS₂ crystallites. This behavior was prominent in Figure 5-5c in which we can see wide variation in C_{sp} at low current densities. This monotonic

variation in C_{sp} was apparent and attributed to partial oxidation of sulfide-rich species to elemental sulfur (S°) and Cu^+ to Cu^{2+} at the $CuFeS_2$ surface during discharge (pseudocapacitive faradaic reactions) process of the composite electrode. This fact was also apparent in Figure 5-5d, where coulombic efficiency at low current (0.01 A g^{-1}) was much greater than 100 % [214, 215]. The polarization effects beyond thermodynamic stability, $E^\circ (H^+/H_2)$ also indicated the depletion of ionic species within the porous structure, possibly because of surface limited faradaic reactions i.e. H_2 evolution and the formation of a conversion layer over the surface of $CuFeS_2$ particulates [203]. At relatively higher current densities (above 0.04 A g^{-1}), the variation in ' C_{sp} ' was much lower and both electrodes provided reversible behavior. However, the overall coulombic efficiency of the composite electrode ($\sim 95 \pm 1.5 \%$) was lower than the CF electrode ($98 \pm 1.4 \%$). It is interesting to note that the low conductivity of the surface film on $CuFeS_2$ (due to oxidation of sulfide species to elemental sulfur) could limit the reversible adsorption/desorption of H^+ during charge/discharge [38]. The ' C_{sp} ' of the composite electrode (1.265 F g^{-1}) at a high current density (0.1 A g^{-1}) was almost double than the value obtained for the CF electrode (0.588 F g^{-1}). Here we considered that the relatively large reversible C_{sp} manifested by the composite electrode at all current densities was caused by the reversible faradaic reactions (pseudocapacitive behavior) of the sulfide-rich passive film, which covers the $CuFeS_2$ crystallites.

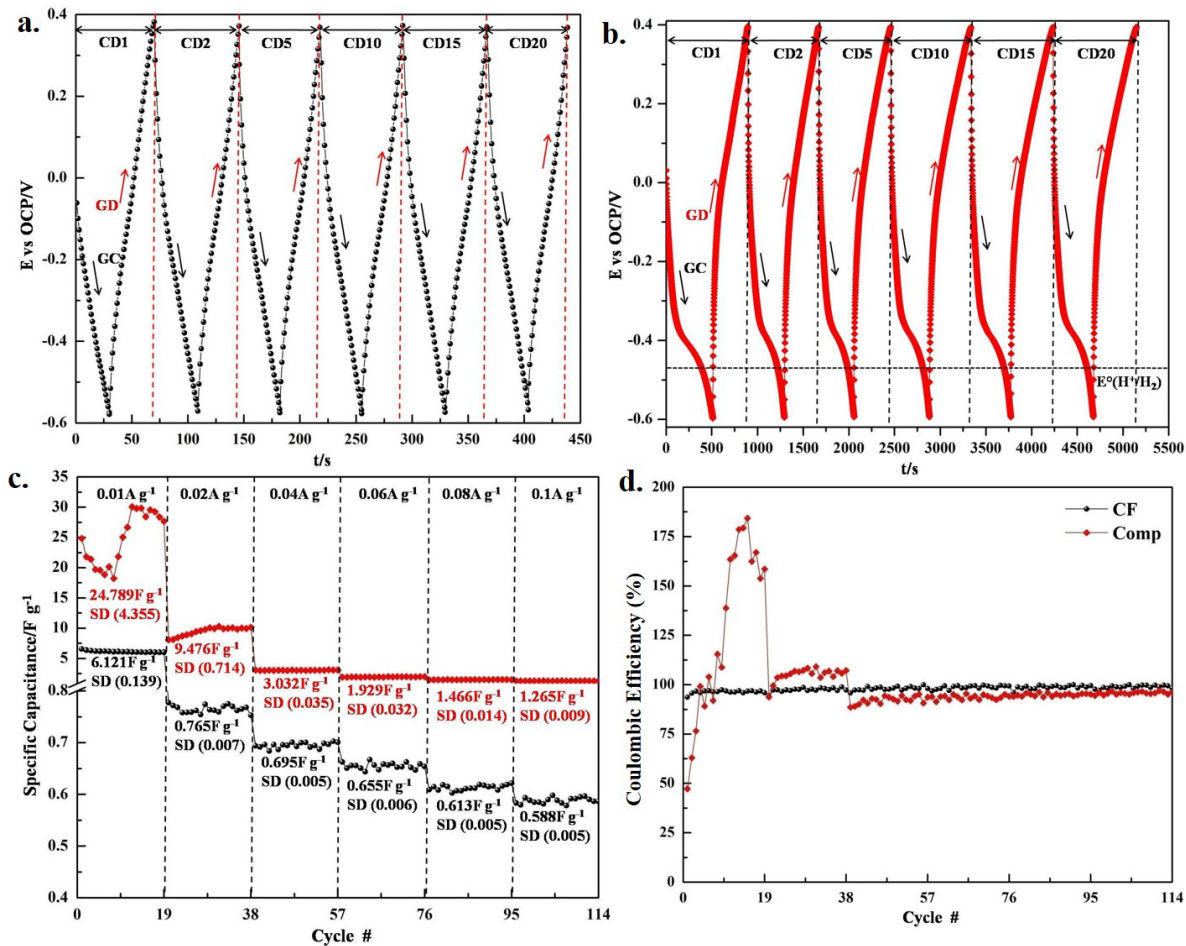


Figure 5-5 GCD cycling at 0.02 A g⁻¹ (a) of the CF and (b) the composite electrodes. (Note: arrows down and up represent the charging and discharging, respectively, the E_{oc} of composite electrode = 0.470 ± 0.005 V_{SHE} at pH = 0.702 ± 0.005). (c) The discharge-specific capacitance at various currents. (d)

Coulombic efficiency of the CF and composite electrodes

5.4 Mechanistic study of charge distribution on CF and Composite electrode

The potential-dependent current response in the CV and origin of potential plateau in the GCD of the composite electrode is believed to be due to pseudocapacitive effects controlled by the surface limited faradaic and non-faradaic reactions. The porous structure (large surface area) and the presence of sulfide species over the surface of CuFeS₂ crystallites are possible causes for the observed higher charge storage capability of the composite electrode. The porous

GF network and open structure of the CuFeS₂ microspheres would definitely induce polarization effects and the faradaic reactions would depend on the availability of H⁺ ions during charging of the composite electrode.

In order to understand the reaction mechanism, and for quantitative estimation of the charge distribution within the composite electrode, impedance spectra (Nyquist plots) were obtained at constant bias potentials. The character of GF in the composite electrode was estimated separately through EIS analysis. To evaluate the pseudocapacitive effects arising due to current leakage through adsorption and other possible redox reactions, the impedance spectra at very negative bias potential were obtained as shown in Figure 5-6. In this figure, the impedance behavior (Nyquist plots) can be split into two frequency regimes. At high frequency ($\omega \rightarrow \infty$) the impedance spectra represent coupled charge transport and polarization effects, as shown in Figure 5-6b and d. On the other hand, the impedance behavior at low frequency ($\omega \rightarrow 0$) is associated with interfacial charge transfer due to the occurrence of electrochemical faradaic reactions (Figure 5-6a and c). At high frequency, the low applied potential (av) signals (5 mV) were restricted to the surface of the electrode and resulted in the impedance response of a depressed semicircle. These signals can penetrate well into the porous structure of GF and CuFeS₂ at low frequency. This behavior is reflected as steep curves (large $-Z_{img}$ component) in the impedance plots. The impedance response in this regime corresponds to the pseudocapacitive behavior of the electrode materials [216]. It is interesting to note that with an increase in reduction potential ($< E_{OCP}$) of the GF and composite electrodes, the $-Z_{img}$ component became smaller, which indicates an increase in current leakage due to the occurrence of non-capacitive irreversible (conversion reactions) faradaic reactions. The

frequency response behavior was analyzed and simulated by using an EEC, as shown in Figure 5-7.

The overall ohmic drop across the electronic and ionic transport channels also contributes to the overall impedance and is designated as ' R_s '. The high frequency semicircles (Figure 5-6b and d) are represented as constant phase elements Φ_{dl} . The faradaic resistance is represented as R_F in the EEC. The under potential H^+ adsorption ($E_{OCP} > E > E^{\circ}_{H^+/H_2}$) at the electrode surface is helped by a small (R_F) and would permit the charge to either adsorb at the surface (presented as interfacial pseudocapacitive element (Φ_p)) or may lead to current leakage due to the progress of faradaic reactions at the electrode surface. These charge transfer processes are inversely related to the parallel resistive element ' R_p ' as shown in Figure 5-7. The n_1 and n_2 are the charge relaxation coefficients for the Φ_{dl} and Φ_p , respectively.

Physically, after the formation of the double layer at the electrode/electrolyte interface (presented as Φ_{dl} in the EEC), the current leakage through R_F could be related to the faradaic reactions such as hydrogen evolution and/or reduction reactions at the $CuFeS_2$ crystallites during charging at very low (negative) bias potentials [217]. The progress of reversible faradaic processes (pseudocapacitive response) result in high values of Φ_p . However, thermodynamically (at pH 0.702) under the applied conditions, potentials below -0.0415 V ($E < E^{\circ}_{H^+/H_2}$) may possibly increase the current leakage through R_p due to progress of irreversible faradaic reactions such as H_2 evolution (via either reaction 5.6 or reaction 5.7) on the surface of the electrode materials [218, 219]. In other words, the charge storage (pseudocapacitive behavior) capacity of an electrode material would decrease with decrease in R_p at more negative potentials due to the progress of irreversible reactions.

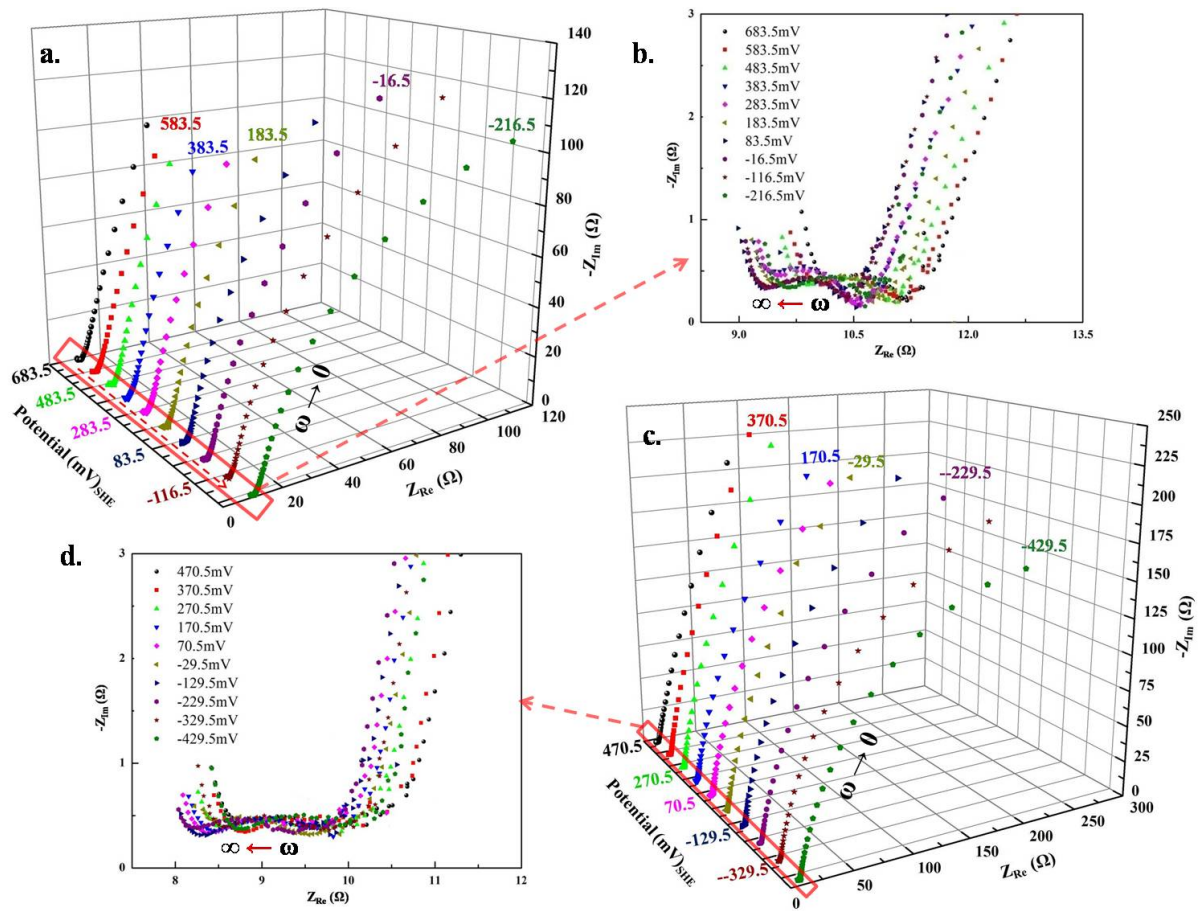


Figure 5-6 The Nyquist plots of (a) CF electrode (from $E_{OC} = 0.683 \text{ V}_{SHE}$ to $E_{max} -0.216 \text{ V}_{SHE}$ ($\eta = -0.9 \text{ V}$) in the cathodic (charge) direction). (b) The impedance behavior at $\omega \rightarrow \infty$ for CF electrode. (c) The Nyquist plots of the composite electrode at various potentials starting from 0.470 to -0.429 V_{SHE} ($\eta = -0.9 \text{ V}$) (d) high-frequency impedance behavior of composite electrode

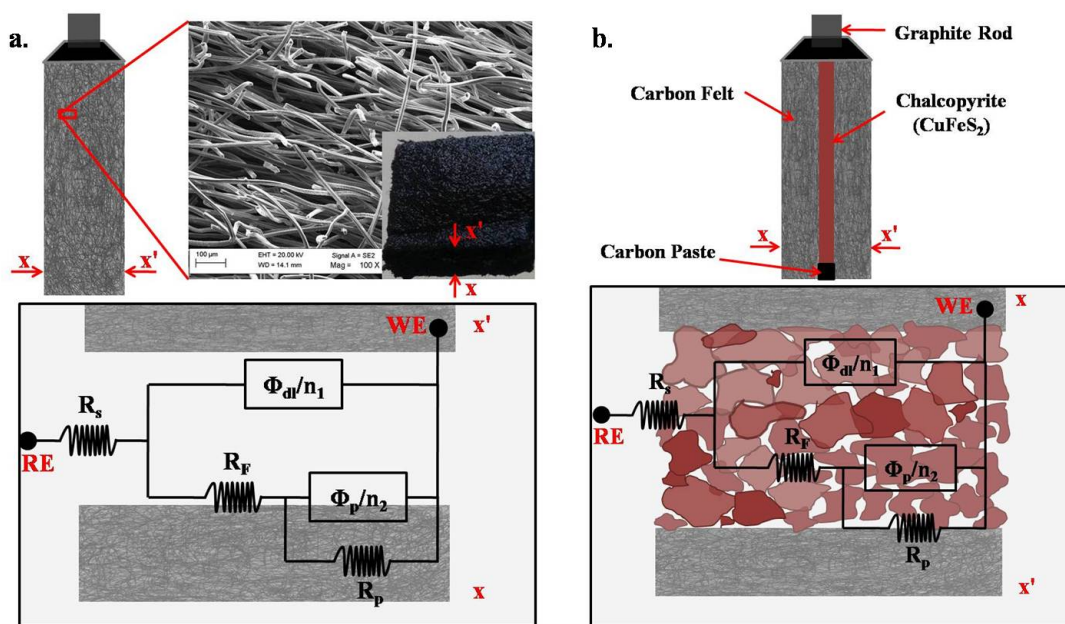
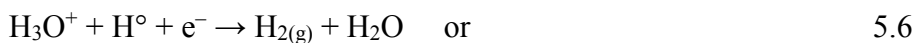


Figure 5-7 Schematic of (a) CF electrode and morphology of graphite fibers in the GF. The inset shows the EEC. (b) Composite electrode and EEC used to simulate impedance spectra for analysis



Quantitative information of the calculated parameters of both CF and composite electrodes are tabulated in Table A-1 (Appendix A). Figure 5-8a shows the relatively high Φ_{dl} value of the composite electrode vs. the CF electrode (above $\eta > -0.5$ V), which suggests a large amount of charge stored within the electrical double layer. On the other hand, the larger R_p and large Φ_p within the same potential regime for the CF electrode is attributed to the high adsorption capacity for H^+ (or H_3O^+) (reaction 5.2) and reversible redox reaction (reaction 5.3) at its surface (pseudocapacitive behavior).

For the composite electrode, the relatively small value of R_p (from $\square 3000$ to 1.23 k Ω) compared to the CF electrode (from 22770 to 2.3 k Ω), from $0 \geq \eta \geq -0.5$ V, is related to the reversible faradaic redox reactions at the surface of CuFeS_2 (i.e. reaction 5.4). The appreciable

hindrance provided by GF for recombination reactions (reactions 5.6 and 5.7) (large R_p and Φ_p) indicates its character as an '*internal charge mediator*' that promotes the adsorption of H^+ as an intermediate (H°) species. The appreciable decrease in R_p of the composite electrode (Figure 5-8b) (from 3000 to 1.23 k Ω) within the same cathodic overpotential regime ($0 \geq \eta \geq -0.5$ V) is due to the reaction of $CuFeS_2$ with this adsorbed intermediate species (conversion reaction; reaction 5.8) and has been discussed in detail by other researchers [91, 215, 220]. In simple words, the carbon fiber network behaves as a catalyst in the composite electrode to preferentially adsorb H^+ ions and supply the formed intermediate (H°) species to the coupled electroactive $CuFeS_2$ crystallites.



The GF provides almost two times higher R_p (2.13 k Ω) than that (1.231 k Ω) measured for the composite electrode at low potential ($\eta = -0.5$ V), which indicates the occurrence of conversion reactions on the composite electrode. $\eta = -0.5$ V was well within the thermodynamic stability of the electrolyte at the surface of GF ($E_{OCP} = 0.683$ V_{SHE}). However, at this large overpotential applied to the composite electrode ($E_{OCP} = 0.470$ V_{SHE}), there are fair chances of current leakage due to H_2 evolution and/or due to the progress of conversion reactions at the surface of $CuFeS_2$. But the high R_p value for the composite electrode at $\eta > -0.6$ (Figure 5-8b) highlights the delay in the H_2 evolution reaction.

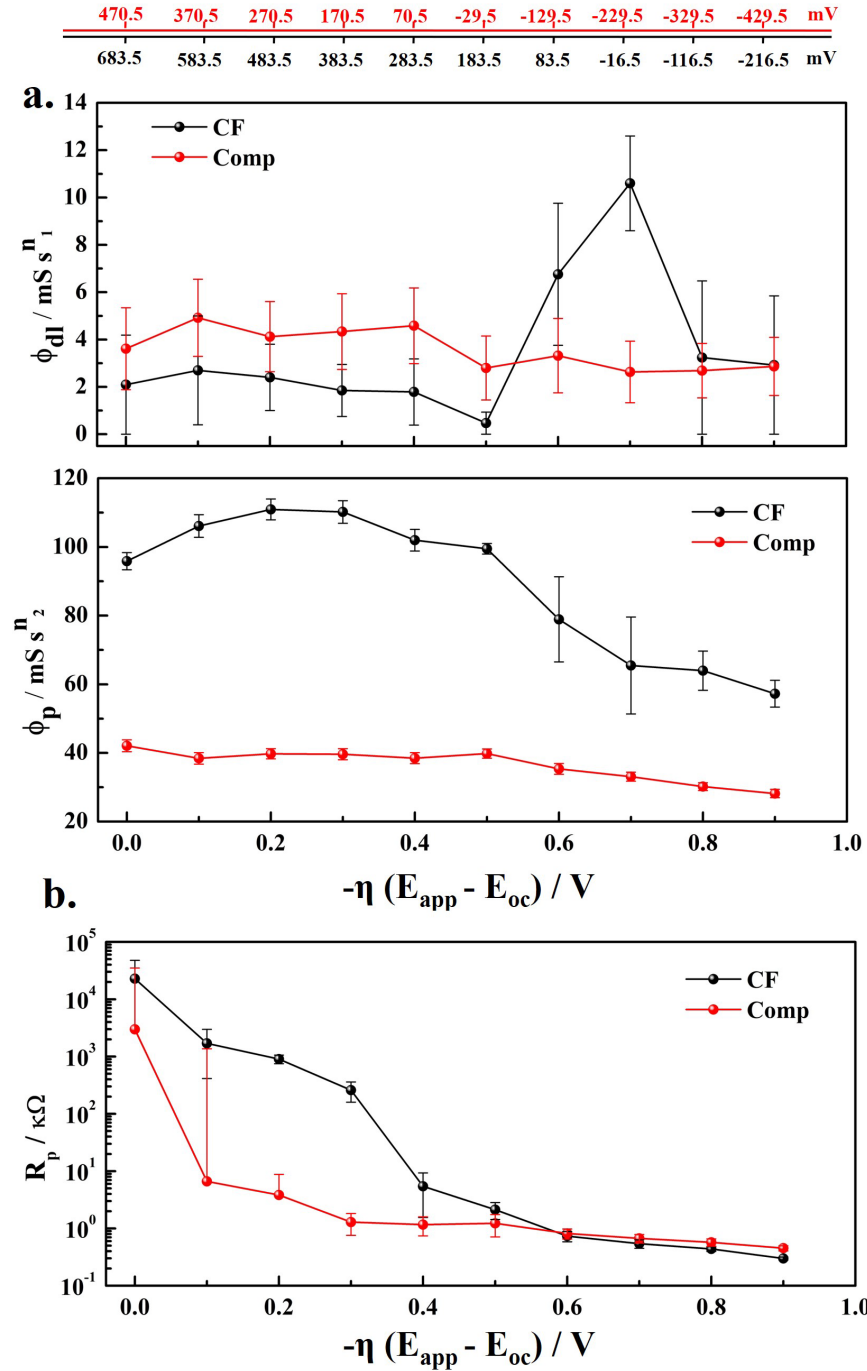


Figure 5-8 Variation in Φ_{dl} and Φ_p of CF and composite electrode. (b) The extent of current leakage through faradaic processes ($\eta = 0$ corresponds to the E_{OCP} (0.683 V_{SHE}) and mixed potential (0.470 V_{SHE}) for the CF and composite electrodes, respectively)

The increase in Φ_{dl} of the CF electrode at $\eta < -0.5$ V is due to surface charge balancing by H^+ (or H_3O^+) ions. At large negative potentials, the ingress of a large amount of H^+ ions toward the electrode surface would decrease once the maximum adsorption capacity (surface coverage) is achieved. This can be seen by the decrease in Φ_p . At overpotential below $\eta < -0.5$ V, the Φ_p of the composite electrode is significantly decreased due to parallel current leakage through R_p and is comparable to the value of the CF electrode as shown in Figure 5-8b. This behavior corresponds to the progress of faradaic (irreversible) reactions on these electrodes at such negative potentials.

During charging, the mechanism of charge distribution and character of GF as an internal *charge mediator* (which may supply charge and intermediate (H^0) species to the $CuFeS_2$ internally in a composite electrode) was also estimated from cathodic polarization scans as shown in Figure 5-9a. The polarization trends of the CF and composite electrodes are divided into three regions. The polarization trends for both the CF and composite electrodes at their respective ' E_{OCP} ' values in 'region 1' were similar. The ' E_{OCP} ' of GF was ~ 0.213 V more positive than the mixed potential of the composite electrode in 0.2 M H_2SO_4 . It was seen that at small-applied potentials, the composite electrode had larger (0.0995 V decade $^{-1}$) slopes than the CF electrode (0.0584 V decade $^{-1}$) as shown in the inset of Figure 5-9a. Almost half the value of the slope for the CF electrode at low applied potential suggested its quick electrochemical response (as indicated by its high $i_{o, CF} = 30.55$ mA cm $^{-2}$ compared to $i_{o, comp} = 17.93$ mA cm $^{-2}$) for the progress of reversible charge transfer processes [221, 222]. It is, therefore, considered that the kinetics of hydrogen adsorption at low field prior to the potential 0.457 V $_{SHE}$ (where the two plots intersect) was 1.7 times faster on GF than on $CuFeS_2$ on the

composite electrode based on the apparent exchange current density ($i_{o, CF}$) values (based on the geometrical surface area of the CF electrode) [223].

Below this potential, in 'region 2', the higher current provided by the composite electrode was therefore associated with faradaic reactions i.e. adsorption of H^+ preferentially on GF and pseudocapacitive processes (reaction 5.4) over the $CuFeS_2$ crystallites. Individually, in this region, the relatively small current response (slope = $0.981 \text{ V decade}^{-1}$) by the CF electrode compared to the composite electrode ($0.284 \text{ V decade}^{-1}$) indicated the large polarization of the GF possibly due to preferential adsorption of H^+ ions. In other words, it was evaluated that in composite electrode the rapid ingress of H^+ ions towards the porous GF at such negative potentials (as in region 2) could produce the transient intermediate species (H°) (reaction 5.2) and supply to the $CuFeS_2$ crystallites [89, 91].

To verify the *internal charge mediator* character of GF in the composite electrode, electrochemical behavior of a $CuFeS_2$ -carbon paste electrode (CPE) ($CuFeS_2$ 85 wt% +10 wt % CB and 5 wt% PVDF deposited on a platinum foil) was also determined and compared with the composite electrode under the same experimental conditions, as shown in Figure A- 1 (Appendix A). The ' E_{OCP} ' and low potential electrochemical behavior of the CPE was comparable to the composite electrode. At relatively large overpotential the limited current density (2.2 mA g^{-1}) followed by a gradual increase in the current density within the UPD region (before H_2 evolution) was observed below 0.420 V_{SHE} . The overall cathodic current density of the composite electrode was approximately 3 times higher than the CPE at $E \geq 0 \text{ V}_{SHE}$, which also indicated the preferential hydrogen adsorption on GF and effective transportation of intermediate species to the $CuFeS_2$.

The impedance behavior of the composite electrode in the same potential range ($E > E^{\circ}_{H^+/H_2}$) (region 2 in Figure 5-9) also provided higher Φ_{dl} and large R_p (Figure 5-8), which justified the internal transportation of H° from the GF fibers to the $CuFeS_2$ crystallites. The maximum Φ_P of the CF electrode (at $-\eta = \sim 0.2$ V), would be related to the adsorption of H^+ at the graphite fibers and the shuttling of the H° to the $CuFeS_2$ crystallites within the composite electrode [224]. The composite electrode also presented relatively lower polarization such that the shift in potential towards more negative values was delayed in comparison to the CF electrode (shaded area in Figure 5-9a). The faradaic response of the composite electrode was enhanced by approximately a factor of 5 within the region-2 as supported by the higher current in the polarization scans (Figure 5-9a). The impedance behavior of the composite electrode at ($-\eta=0.5$ V) also showed low R_p (1.23 k Ω) compared to CF electrode which further reinforces this argument. The very low R_p provided by CF and composite electrode at much more negative potentials represented the internal current leakage due to H_2 evolution and faradaic conversion reactions on the $CuFeS_2$ as evident from the current response in the polarization curve in region 3. The conversion of $CuFeS_2$ into the intermediate reduction products i.e. talnakhite ($Cu_9Fe_8S_{16}$), bornite (Cu_5FeS_4) and chalcocite (Cu_2S) is possible as proposed by Nava *et al.* [32].

Schematically, the electrochemical mechanism (Figure 5-9b) involved in the overall charge distribution within the composite electrode was proposed based on the experimental results as shown in Figure 5-9a. At very low overpotential ($\eta \rightarrow 0$), the internal charge distribution within the composite electrode was a function of intrinsic surface potential and charge storage capacity of both the GF and the CuFeS_2 . The difference in the electronic energy density of each component in the composite electrode i.e. GF and CuFeS_2 will ultimately establish a compromise potential in the electrolyte referred to as 'mixed potential'. In 'region 1' when a small potential perturbation ($\eta > -0.1$ V) is applied, the H^+ ions tend to ingress preferably towards the highly conductive GF, which also contains quinone/pyrone type functional groups. A further decrease in potential ($\eta < -0.1$ V) in 'region 2' results in the H^+ ions being adsorbed preferentially (UPD) according to reaction 5.2 and the intermediate transient species (H°) is transported to CuFeS_2 . These species (H^+ and H°) have the ability to react with the sulfide species in a reversible manner at the surface of CuFeS_2 according to reactions 5.3 and 5.4. The H_2 evolution (reaction 5.6 and 5.7) and conversion reactions may also occur when the potential applied is very negative ($\eta < -0.5$) in 'region 3'.

5.5 Summary

The main intension of this Chapter was to investigate the electrochemical behavior of the composite (GF+ CuFeS_2) electrode in 0.2 M H_2SO_4 for its prospective use as negative electrode in the battery setup (as discussed in subsequent Chapters 6 and 7). Based on the impedance analysis and potentiodynamic polarization results, the mechanism of charge distribution within this composite electrode was proposed. Under similar conditions, detailed CV analyses suggest that the large current response by the composite electrode was mostly due to the progress of reversible faradaic processes on its surface. However, the CF electrode had

a relatively large non-faradaic current response compared to the composite electrode, as determined quantitatively from the current partitioning analysis. The large specific capacitance of the composite electrode (1.265 F g^{-1} at 0.1 A g^{-1}) was also found to be almost double that of the GF alone. The reversible charging/discharging character of the composite electrode, and the appearance of an additional potential plateau at about $-0.365 \text{ V}_{\text{OCP}}$ (well within water stability), revealed its higher specific capacitance in comparison to GF. The interfacial charge distribution and transfer processes within the composite electrode were also explored through potentiostatic impedance spectroscopy and potentiodynamic polarization curves. The reversible behavior of the composite electrode is attributed to the preferential adsorption/desorption of H^+ (H° species) on the GF which may transport to the surface of CuFeS_2 internally within the composite electrode. This '*internal charge mediator*' character of the GF in the composite electrode was predicted from the impedance analysis, which demonstrated very high leakage resistance (R_p) and relatively large pseudocapacitance (Φ_p) at $\eta > -0.5 \text{ V}$ conditions that simulate charging in a battery setup. The decrease in R_p and large current response of the negative composite electrode at very negative applied potentials ($\eta < -0.5 \text{ V}$) indicated the possibility of irreversible faradaic reactions on the CuFeS_2 crystallites possibly due to the internal transport of intermediate (H°) species from the GF.

Chapter 6: The hybrid mineral battery: energy storage and dissolution

behavior of CuFeS₂ in an FBFC⁹

In this chapter, the first steps toward the development of a hybrid mineral battery-like setup are presented. This setup can be used simultaneously as an energy storage device and as a unit for metal extraction. Initially, the synthetic CuFeS₂ is used as an active anode material due to its unique ability to reduce or oxidize under different conditions, a characteristic that motivated this work. This hybrid setup consists of two electrodes in a fixed bed flow cell (FBFC) configuration. The composite electrode (synthetic CuFeS₂ mixed with carbon black and sandwiched in GF) was used as the negative electrode in which acidic solution (0.2 M H₂SO₄) was pumped from an external circuit. In the positive half of the cell, the acidic ferrous sulfate solution (anolyte) was circulated through the GF and separated by a PEM from the negative compartment. During charging, the oxidation of Fe^{II} is expected to reduce CuFeS₂ into Cu₂S. In the subsequent discharge cycle, the reduction of Fe^{III} to Fe^{II} is anticipated, which facilitates the oxidation of Cu₂S to CuS/Cu²⁺. Both electrodes were also characterized individually, in their respective electrolytes, to elucidate their respective electrochemical performances in the final FBFC. Based on the ex-situ characterization of the retrieved CuFeS₂ product from the FBFC after GCD cycling, a possible reaction mechanism is also proposed.

6.1 Physical characterization of as-synthesized CuFeS₂

The as-synthesized CuFeS₂ powder particles were examined in SEM and the formation of pure CuFeS₂ was confirmed by X-ray diffraction. Variable size open-pored and platelet-like spherical particles were formed during the hydrothermal synthesis process as shown in Figure

⁹ From the published work, K.M. Deen, E. Asselin, *ChemSusChem*, 11 (2018), 1533–1548.

5-1a. The open pores and thin platelet-like morphology could form during the synthesis process by the thermal decomposition of the reagents under high temperature and pressure conditions. Figure 5-1d shows the diffraction pattern of as synthesized CuFeS₂ particles, which matches well with the PDF 37–0471 reference pattern peaks and without presenting any impurity signatures. Laser particle diffraction of the as-synthesized CuFeS₂ showed a wide particle size distribution in the range of ~3 – 45 μm. However, from the cumulative distribution curve, it was determined that 80 vol. % of the particles (D80) were below ~23.5 ± 2.0 μm as reported in the previous Chapter (Figure 5-1b) [225].

The BET surface area, pore size distribution and pore volume of as-synthesized CuFeS₂ was evaluated from the N₂ adsorption/desorption isotherms as shown in Figure 6-1. The magnified region of the isotherm hysteresis (inset) observed at large relative pressure ($0.8 < P/P_0 < 0.97$) is associated with the mesoporous and macroporous platelet-like structure of spherical CuFeS₂ particles. The BET surface area of the CuFeS₂ particles ($3.5 \text{ m}^2 \text{ g}^{-1}$) was calculated from the linear portion of the isotherm as shown in Figure 5-1c. The surface area is related to the particle size, morphology, pore size, and distribution. The DFT method was employed to evaluate the pore size distribution in the as-synthesized CuFeS₂ particles. This assumes that the pore-filling takes place by either micro-pore filling or through capillary condensation. The pores of different sizes are considered to be of a regular shape (cylindrical or slit) and the adsorbent surface is assumed to be homogeneous as reported elsewhere [226]. It was found that the variable sized-pores (5 – 25 nm) were distributed within the CuFeS₂ particles and the total pore volume was calculated to be $0.011 \text{ cm}^3 \text{ g}^{-1}$.

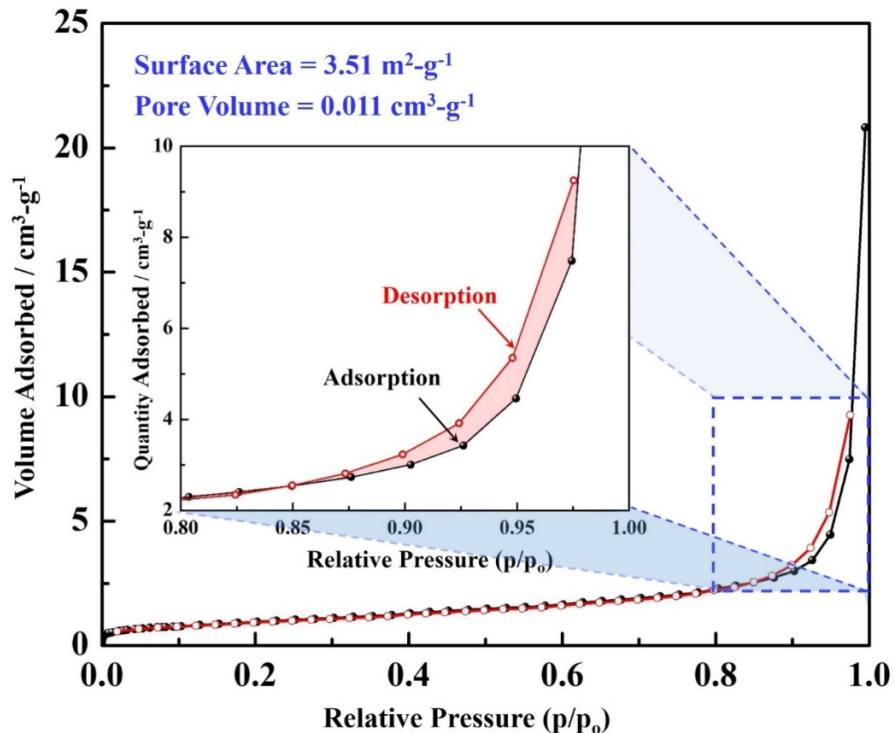


Figure 6-1 N₂ adsorption/desorption isotherm of as-synthesized CuFeS₂ particles (77 K).

To analyze the surface chemistry of as synthesized CuFeS₂, the positive (Figure 6-2a and b) and negative (Figure 6-2c and d) ToF-SIMS mass (m/z) spectra were obtained. The positive ion mapping showed Cu enrichment at the surface with relatively small Fe (blue area) concentrations. The mass spectra also provided a Cu/Fe ratio of 1.88, calculated from the corresponding normalized peak intensity. The characteristic peaks for Cu and Fe are shown in Figure 6-2b with some signals related to the hydrocarbon (HC) impurities [227].

The presence of HCs in the positive spectrum may be due to airborne moieties in the ambient environment during sampling and/or, most likely, the products formed because of decomposition of the mineral oil used in the vacuum system. These contaminants could adhere to the surface and may reflect in the spectrum.

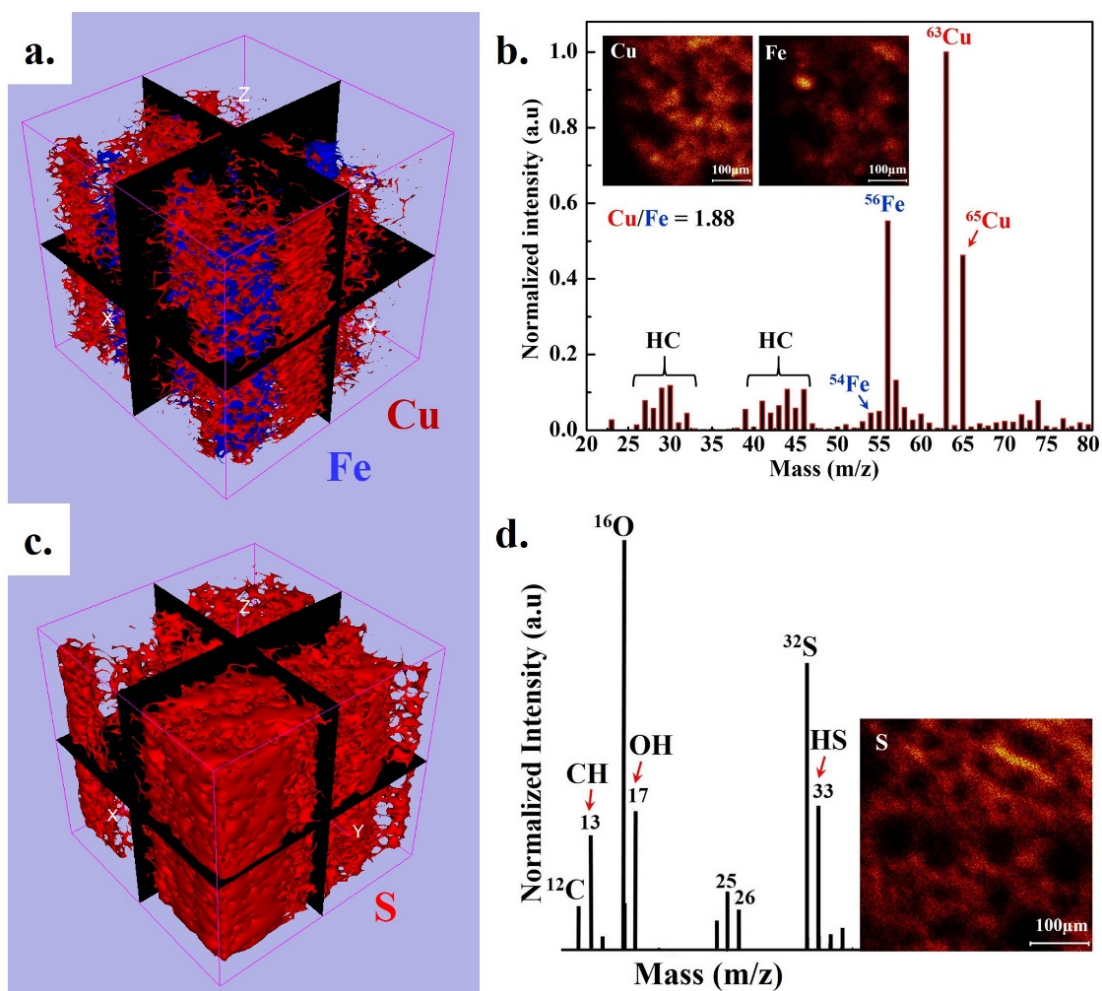


Figure 6-2 ToF-SIMS analysis of as-synthesized CuFeS₂ (a) 3D surface distribution of Fe and Cu (b) positive ion spectrum (c) 3D mapping for sulfur (S) (d) negative ion spectrum

The negative ion mapping (Figure 6-2c) clearly identified the presence of sulfur species at the surface. The mass spectrum of CuFeS₂ particles also provided prominent signals for O⁻, S⁻ and HS⁻ species, as shown in Figure 6-2d. The significantly higher intensity of O⁻ in the spectrum could be associated with the oxidation of the surface during exposure to air. However, the larger signals associated with the Cu and S (mostly ionic in nature as elemental sulfur is volatile under ultrahigh vacuum conditions) species at the surface were evident in both positive and negative ion mapping, respectively, which suggest the presence of Cu_x-S_z enriched species

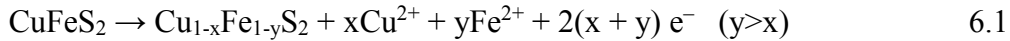
at the surface of the CuFeS₂ particles. These species may form during synthesis, washing, drying and/or the handling process. Buckley *et al.* [41] also explained the possibility for the formation of iron deficient CuS₂ and Cu_{0.8}S₂ species on the surface of CuFeS₂ upon exposure to air and during conditioning in acidic solutions, respectively. During exposure to air, a reconstruction process could occur on the fresh surface of CuFeS₂ implying that migration of Fe to the surface and reduction of Fe³⁺ would lead to the formation of thin layer enriched with oxide and Cu_{1-x}S_{2-x} (0 < x ≤ 1) species as discussed by Li *et al.* [24]. This proposed mechanism agrees with the ToF-SIMS and XPS results presented in this study, which also revealed the formation of an Fe deficient, CuS₂ layer on the as-synthesized CuFeS₂ particles.

6.2 Electrochemical behavior of individual electrode systems

Both the cathodic and anodic potentiodynamic polarization curves for the composite electrode were obtained at 1 mV s⁻¹ scan rate after achieving stability of the OCP (0.01 mV s⁻¹) at 25 °C, as shown in Figure 6-3. The composite electrode was prepared by mixing 10 wt. % CB in CuFeS₂ and by sandwiching in the GF. The cathodic and anodic polarization responses were measured separately on freshly prepared composite electrodes to avoid any effect the conversion products may have had on the polarization scan. The OCP of the composite electrode in 0.2M H₂SO₄ solution was measured to be 0.485 ± 0.01 V, which stabilized after three hours of immersion. The anodic and cathodic Tafel slopes (β_a and β_c) (measured within linear Tafel region but beyond OCP > 50 mV) were 0.202 and 0.303 V/decade corresponding to the charge transfer coefficients 0.29 and 0.19, respectively. Olvera *et al.* [228] also reported similar charge transfer values (α_a = 0.28 and α_c = 0.17 – 0.22) for CuFeS₂ in 0.5M H₂SO₄ solution containing ferric and ferrous at 25 °C. A possible reason for the larger β_a and β_c (low charge transfer coefficients < 0.5) could be the formation of intermediate species at the surface

of CuFeS₂ and preferential adsorption of H^o at GF, respectively. However, the open porous structure of GF and the microporosity of CuFeS₂ may also distort the polarization curves, which may result in larger Tafel slopes and lower transfer coefficients, as discussed in the literature [229]. Also at large overpotentials ($> \pm 0.2$ V), the effect of an increase in solution resistance within the porous structure of the composite electrode cannot be neglected.

Three polarization regimes can be observed for the anodic scan in Figure 6-3. In the low potential range (OCP \leq E < 0.65 V) (1a), the relatively rapid increase in current is associated with the formation of non-stoichiometric metal deficient polysulfide (Cu_{1-x}Fe_{1-y}S₂) at the surface of CuFeS₂ via reaction 6.1 as proposed by other researchers [47, 48]. This polysulfide film may restrict further dissolution of CuFeS₂ as indicated by the very small increase in anodic current within the (0.65 < E < 1.05 V) potential region (2a).



A further increase in potential leads to the transformation of this polysulfide film into CuS_x due to the preferred dissolution of iron over copper and with the enrichment of sulfide sulfur at the surface of CuFeS₂ [48, 230]. The stability of this polysulfide passive film is reduced at potentials above 1.05 V as indicated by the large increase in the current density (in region 3a). Ghahremaninezhad *et al.* [47] proposed that beyond this potential, the Fe is preferentially released and the dissolution rate of CuFeS₂ is further controlled by the copper enriched polysulfide film.

Cathodic polarization of a separate electrode also resulted in three potential regions. The relatively linear increase in current with shift in potential (OCP > E > 0.18 V) was followed by relatively large polarization effects within (0.2 > E > -0.5 V). This behavior is possibly related to the preferential underpotential deposition of H⁺ ions at the GF surface, followed by

transport to the CuFeS₂ within the composite electrode at more negative potentials (designated as region 1c in Figure 6-3). The electro-assisted reductive conversion of CuFeS₂ into less refractory Cu₂S by monoatomic hydrogen species has also been studied in an undivided cell by Fuentes-Aceituno *et al.* [91]. In the composite electrode, the internal mediator character of GF to generate H^o species and possible reduction of CuFeS₂ has been experimentally evaluated in our previous work (Chapter 5) [225]. Also, it has been discussed in the literature that atomic hydrogen was mobile in graphite and can diffuse along graphene planes at room temperature [231]. Details on the electrochemical reduction of CuFeS₂ and formation of intermediate species i.e. talnakhite (Cu₉Fe₈S₁₆) and bornite (Cu₅FeS₄) before conversion into chalcocite (Cu₂S) have been given by Nava *et al.* [32].

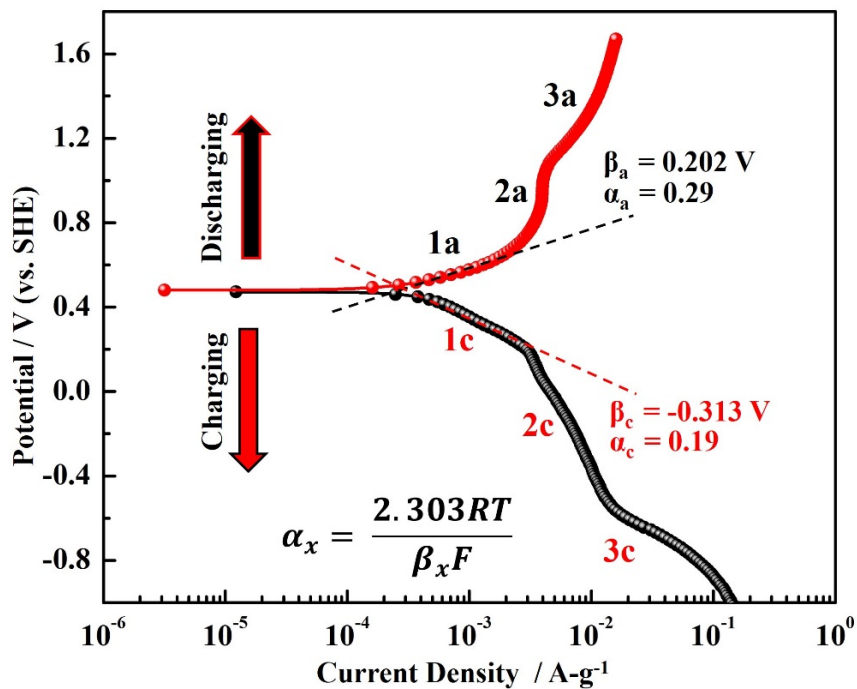


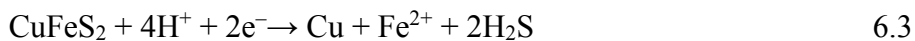
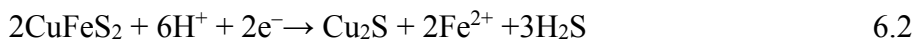
Figure 6-3 Potentiodynamic polarization scans of composite electrode (GF–CuFeS₂+CB) in 0.2 M H₂SO₄ solution; the current is normalized by the mass of CuFeS₂

As exhibited in Figure 6-3, it is expected that in region 2c, the increase in current below 0.18 V is associated with the formation of these Fe deficient reduced intermediate species on the surface of CuFeS₂. Further increase in current below -0.4 V (region 3c) may also indicate the reduction of CuFeS₂ directly into metallic Cu along with H₂ evolution.

In the two-electrode cell setup, during charging, the reduction of CuFeS₂ (at the negative electrode; GF – CuFeS₂) is facilitated by the oxidation of Fe^{II} into Fe^{III} on the positive electrode (GF – Fe). It is therefore important to study the electrochemical behavior of the individual electrode system and to explore the kinetic behavior of any possible faradaic redox reactions that may increase the charge storage capacity in the proposed FBFC system. The influence of 0.1 M Cu²⁺ in 0.5 M Fe²⁺ solution (catholyte) has also been investigated and this referred to as the GF – Fe/Cu electrode system. The CV curves of these electrodes were obtained at various sweep rates and are superimposed to verify the kinetic response as shown in Figure 6-4. In order to simulate the actual conditions in the final setup, the CV scan for the GF – CuFeS₂ (negative electrode) was initiated in the reverse direction before scanning in the positive (forward) direction. It can be seen that the rapid increase in the current density beyond -0.4 V and 1 V both in the reverse and forward directions, respectively, is associated with the dissociation of the electrolyte.

Independent of the sweep rate, the most dominant cathodic and anodic peaks were centered at ~0.50 V vs SHE for the GF–CuFeS₂ composite electrode system. Both cathodic and anodic peaks were composed of two separate peaks indicating the faradaic response of the surface functional groups present on the GF (indicated as Pc1 and Pa1) and possibly to the reversible character of the sulfide surface species (i.e. polysulfide) present on the CuFeS₂ (Pc2 and Pa2) as shown in Figure 6-4a. With the increase in sweep rate, a shift in cathodic peak

potentials (Epc1 and Epc2) and anodic peak potentials (Epa1 and Epa2) in both negative and positive directions, respectively, was observed. This is most likely associated with the quasi-reversible nature of the redox reactions. However, the solution resistance may also increase within the porous structure during repetitive cathodic and anodic scans due to the development of a depletion region that could influence the peak separation. Due to the overlapping current response (broad peaks) by the faradaic reactions affiliated with the surface functional groups and sulfide species (i.e. S_2^{2-} , S^{2-}) at similar potentials (from -0.2 V to 0.7 V vs. SHE), it is difficult to distinguish the individual contributions from the GF and $CuFeS_2$ [32, 211, 232-234]. But it is shown in Figure 6-4d that peak currents (Pa1 and Pc1) vary directly with $v^{1/2}$, corroborating the occurrence of facile reversible electron transfer (pseudocapacitive; faradaic) reactions at the electrode leading to a diffusion-controlled process. During the cathodic scan, the reduction of $CuFeS_2$ into talnakhite ($Cu_9Fe_8S_{16}$), bornite (Cu_5FeS_4) and chalcocite (Cu_2S) are also possible. At more negative potentials (< -0.1 V), iron is completely removed and the formation of Cu_2S occurs with H_2S generation according to reaction 6.2 as evident from region 2c in Figure 6-3 and discussed by Nava et al. [32].



For a further decrease in potential beyond -0.4 V the formation of metallic copper (reaction 6.3) in addition to H_2 evolution is also expected. This behavior is evident from region 3c in Figure 6-3 as discussed above. The small but relatively sharp peak at -0.15 V observed during the forward scan could either be associated with the oxidation of metallic copper into Cu^{2+} ions or to the formation of chalcocite as given in reaction 6.4. The relatively minor peaks observed (from -0.2 V to $+0.6$ V) during the anodic potential sweep were related to the

oxidation of the intermediate species (reaction 6.5, 6.6) formed during the reduction reactions [92, 234]. These results corroborate the potentiodynamic polarization behavior as discussed in the previous section.



The anodic and cathodic peaks in Figure 6-4b and c correspond to pseudocapacitive $\text{Fe}^{\text{II}}/\text{Fe}^{\text{III}}$ and $\text{Cu}^{2+}/\text{Cu}^+_{\text{ads, GF}}$ redox reactions taking place on the GF electrode surface. Thermodynamically, in sulfate media, Cu^+ in the bulk solution is not stable but it is thought that this intermediate species can form at the surface of GF during reduction of Cu^{2+} . This species may form complexes with the surface functional groups i.e. carbonyl, carboxylic, quinone, hydroquinone etc. present on the GF as evaluated from the IR spectra and reported in section 5.2, Figure 5-4 [225].

These redox reactions were further studied from the anodic and cathodic current peak dependency on the sweep rate in the voltammograms. However, the significant distortion in the voltammograms at higher sweep rates, i.e. the shift in both anodic and cathodic peak potentials toward more positive and negative potential values, respectively, was related to the hindered electron transfer processes at the electrode. This behavior could be associated with an increase in solution resistance within the porous structure of GF during forward and reverse scanning. The additional peak in Figure 6-4c, seen at relatively lower sweep rates ($<10 \text{ mV s}^{-1}$), corresponds to the $\text{Cu}^{2+}/\text{Cu}^+_{\text{ads, CF}}$ couple. The typical behavior of increase in peak current density with the square root of sweep rate (Figure 6-4d) corresponds to the faradaic but diffusion controlled electrochemical processes at the GF surface. The peak current for the

reverse scan was calculated by subtracting the background current [235] from the baseline produced by Echem® Analyst software 6.3 (Gamry Instruments).

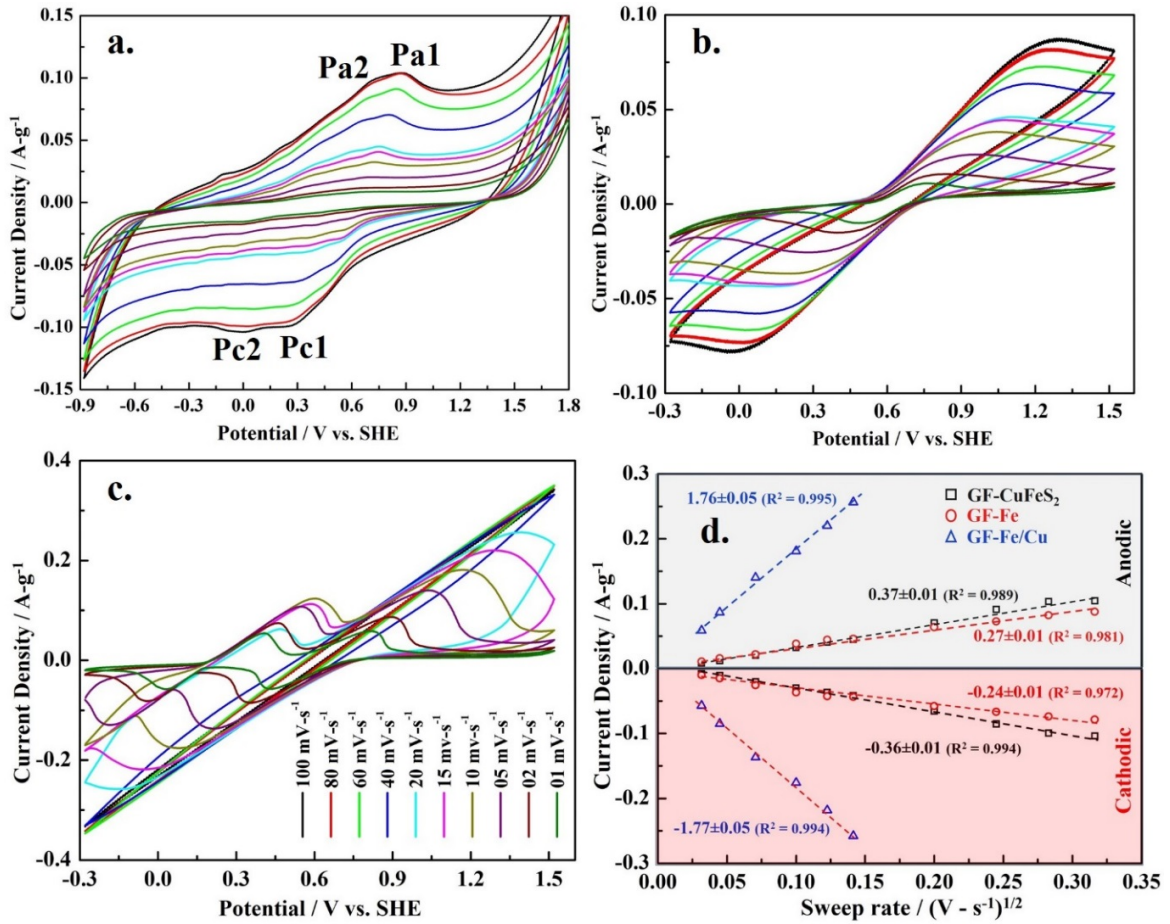


Figure 6-4 CV scans of (a) the composite electrode in 0.2 M H₂SO₄ (the current is normalized by the mass of composite electrode) and (b) GF electrode in 0.5 M Fe²⁺ + 0.2 M H₂SO₄ solution. (c) GF in solution as in (b) with 0.1 M Cu²⁺ (the current is normalized by the wt. of GF) (d) peak current vs. (sweep rate)^{1/2}.

The pseudocapacitive redox reactions for the Fe^{II}/Fe^{III} couple with and without the presence of Cu²⁺ may occur both at the surface and within the porous structure of the GF. This may lead to diffusion controlled kinetic reactions due to the depletion of ionic species within the porous structure of GF and may be validated from the linear dependency of both the anodic and cathodic peak currents on $v^{1/2}$ as shown in Figure 6-4d.

The GF–Fe/Cu electrode exhibited relatively larger slopes (peak current vs. $v^{1/2}$) (1.76 ± 0.05) (similar for both anodic and cathodic processes) compared to the GF–Fe electrode. This is attributed to the rapid kinetics of the Fe^{II}/Fe^{III} redox reaction at the GF electrode in the presence of Cu²⁺. The redox potential for the Fe^{II}/Fe^{III} couple was calculated to be 0.63 ± 0.03 V and the addition of 0.1 M Cu²⁺ did not influence this potential significantly. However, the addition of Cu²⁺ to the electrolyte resulted in an additional peak in the CV scans (Figure 6-4c), associated with the Cu²⁺/Cu⁺_{ads, GF} redox reaction. This species also increased the anodic and cathodic peak current density for the Fe^{II}/Fe^{III} couple (at slow sweep rates) compared to the GF–Fe electrode. This behavior indicates an increase in the stability of Fe^{III} obtained through the addition of Cu²⁺ in the solution according to reaction 6.7. However, the effect of increased ionic strength with the addition of Cu²⁺ to the electrolyte cannot be neglected either and further experiments are discussed below to rule this out. The Cu⁺_{ads, GF} species would form as an intermediate species before reduction to metallic ‘Cu’ and may adsorb by interacting with the surface functional groups present at the surface of GF. This explains the higher discharge current (reduction of Fe^{III}) for this electrode system.



To validate the catalytic effect of Cu²⁺ on Fe^{II} oxidation, step-wise linear sweep voltammetry (LSV) was applied on the GF electrode at 5 mV s⁻¹ to first simulate the charge cycle (oxidation of Fe^{II} into Fe^{III}) the electrolyte on the surface of a GF electrode (positive electrode), as shown in Figure 6-5. N₂ was sparged for 30 min prior to each experiment and the temperature was kept constant at 25 °C. After charging, and before each discharge (reduction of Fe^{III} into Fe^{II}) cycle, the potential of the GF electrode was relaxed at 0 V vs. OCP for 0, 1, 2, 4, 10, 20, 40 and 60 min, respectively in a sequential manner as presented in the

Figure 6-5a. The electrolytes were freshly prepared before each experiment by mixing $\text{FeSO}_4 \cdot 7\text{H}_2\text{O}$ (0.5 M) into 0.2 M H_2SO_4 . The LSV discharge curves for the GF electrode in both the electrolytes (without and with the addition of Cu^{2+} species) are shown in Figure 6-5b and c, respectively.

It is evident in Figure 6-5d that the discharge current was high in Cu^{2+} containing solution even after a prolonged delay at OCP. This increase in current even after an extended delay during the discharging (negative scan) was directly related with the concentration of Fe^{3+} ions in the solution which was produced during the charging (positive scan) step and catalyzed by Cu^{2+} ions. This behavior also predicts the increased stability of Fe^{III} ions in the electrolyte with the addition of Cu^{2+} species under applied conditions through reaction 6.7. The reduction of Cu^{2+} during discharge/negative scan would produce intermediate ' $\text{Cu}^+_{\text{ads, GF}}$ ' species at the surface of GF. This species would adsorb at the surface of GF by interacting with the surface functional groups and may increase the discharge current (reduction of Fe^{III}) as confirmed from the experimental sequence. Zhang *et al.* [236] reported the effect of Cu addition on the oxidation of Fe^{II} ions and proposed that Cu^{2+} could catalyze its oxidation in the presence of oxygen. In another study, Biniak *et al.* [237] described the mechanism of copper adsorption on activated carbon and the change in its oxidation state after interacting with the acid-base surface functionalities. Many other reports also described the cupric catalyzed oxidation of Fe^{II} at high temperature and pressure in sulfate media [238, 239]. Based on the experimental evidence, and with the support of available literature, we have demonstrated the effect of cupric on the catalytic oxidation of ferrous on GF electrodes, which may be beneficial for increasing the discharge current density, hence the specific energy of the final FBFC device.

It was also inferred (Figure 6-5d) that the addition of Cu^{2+} ions increased the cathodic current for Fe^{III} reduction, which is directly related to its high concentration and availability at the surface of GF even after a 60 min delay (between charging and discharging). In comparison, the GF-Fe system registered low peak current and validated the beneficial effect of Cu^{2+} addition in the electrolyte. As noted above, this was considered to occur due to the extended stability of Fe^{III} ions in the solution and catalytic oxidation of Fe^{II} in the presence of Cu^{2+} ions. However, the addition of 0.5 M Fe^{2+} in both electrolytes demonstrated that the increase in current for the Fe^{III} reduction peaks cannot be related to the increased ionic strength of the solution.

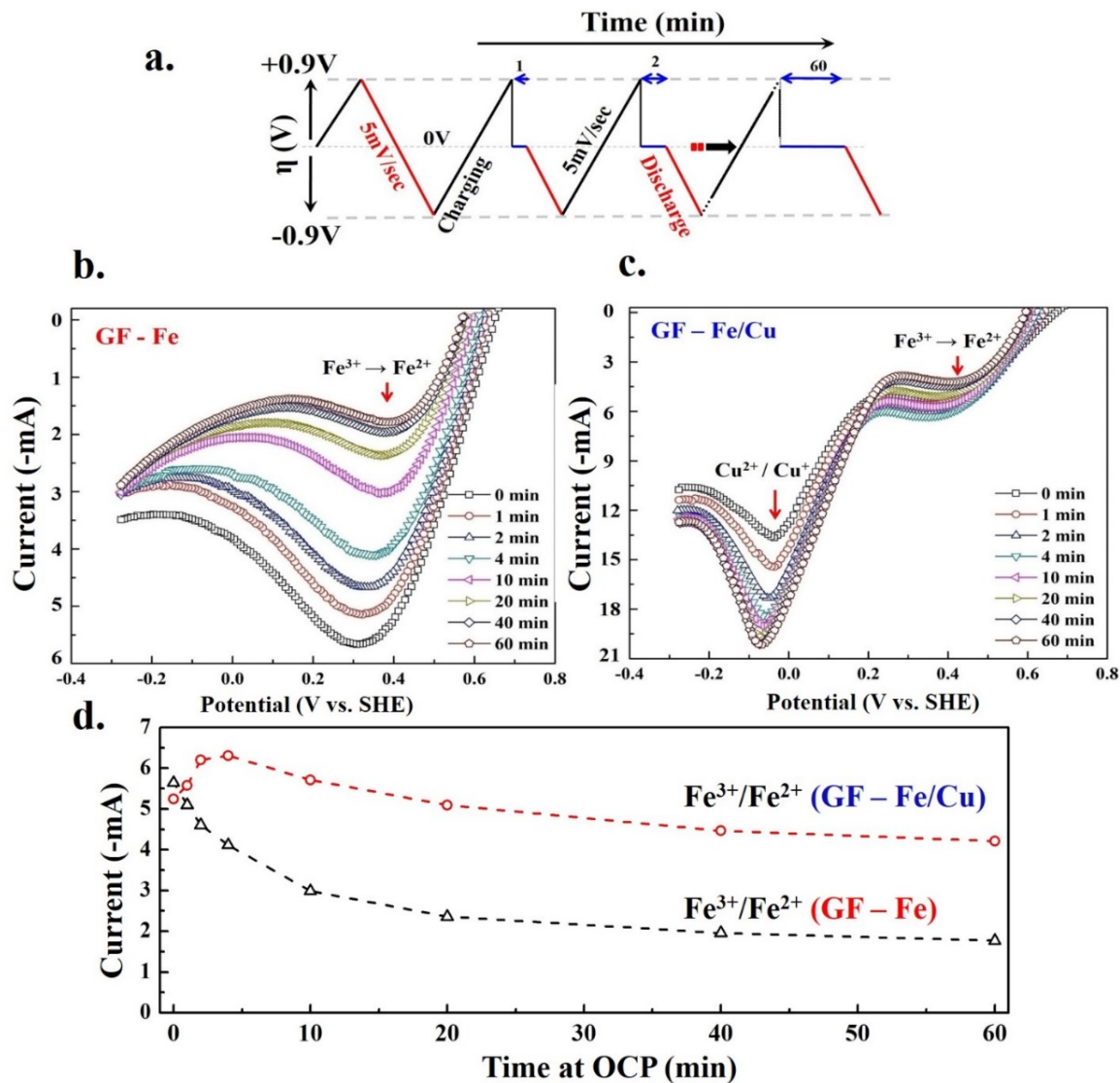


Figure 6-5 Stability analyses of Fe^{III} species in Cu²⁺ containing solution at a GF electrode. (a) Schematic of sequential protocol applied for the charging (Fe^{II} → Fe^{III}) and discharging (Fe^{III} → Fe^{II}). (b) The discharge current profiles of GF after sequential delay (0 to 60 min) in 0.5 M Fe²⁺ solution and in (c) 0.1 M Cu²⁺ ions containing electrolyte. (d) Discharge peak current profiles as a function of delay time (Note: mass (187 mg) and geometrical surface area (14.4 cm²) of GF electrode were same for each test).

The impedance spectra for the GF-CuFeS₂, GF-Fe and GF-Fe/Cu electrode systems were obtained by applying a 5 mV AC potential amplitude over OCP within the frequency range of 10 mHz – 100 kHz, as shown in Figure 6-6 (Nyquist plots) and Figure 6-7 (Bode plots).

The impedance at high frequency is associated with the solution resistance (R_s) and with the charge accumulated in the double layer, which is represented by the constant phase element (Q_{dl}). A constant phase element is used to account for the non-uniform charge distribution within the porous structure of the electrodes. The intermediate and low-frequency regimes correspond to the reversible faradaic response of the electrodes, which is inversely related to the charge transfer resistance (R_{ct}). These faradaic reactions (pseudocapacitive behavior) incorporate specific adsorption of ionic species at the electrode surface (Q_{ad}). In a physical system, the ionic species in the electrolyte (H^+ , HSO_4^- , Fe^{2+} etc.) may interact with the $CuFeS_2$ (in the composite electrode) and/or with the surface functional groups present on the GF [92, 225]. In the EEC model, the parallel resistor (R_{ad}) is used to model the barrier to charge transfer for the adsorption/desorption process.

The significant difference in the impedance behavior of the composite and GF electrodes at low frequency can be clearly seen in Figure 6-7a and b. For the composite electrode, the continuous increase in $-Z_{im}$ (at low frequency) is associated with the concentration gradient within the porous structure and to the pre-existing sulfide sulfur enriched species present on the $CuFeS_2$ particles (as confirmed from the ToF-SIMS and XPS analyses, Figure 6-2 and Figure 6-14a). This behavior is attributed to the limited mass transport across this film (finite length diffusion) and is modeled by a Warburg coefficient (σ_B) and a time constant (B) in the EEC. However, both GF-Fe and GF-Fe/Cu electrodes had similar trends in the low-frequency regime with a slight variation in the phase angle (Figure 6-7b). This behavior is most likely associated with the semi-infinite diffusion characteristics (σ_w) of the open porous structure of GF.

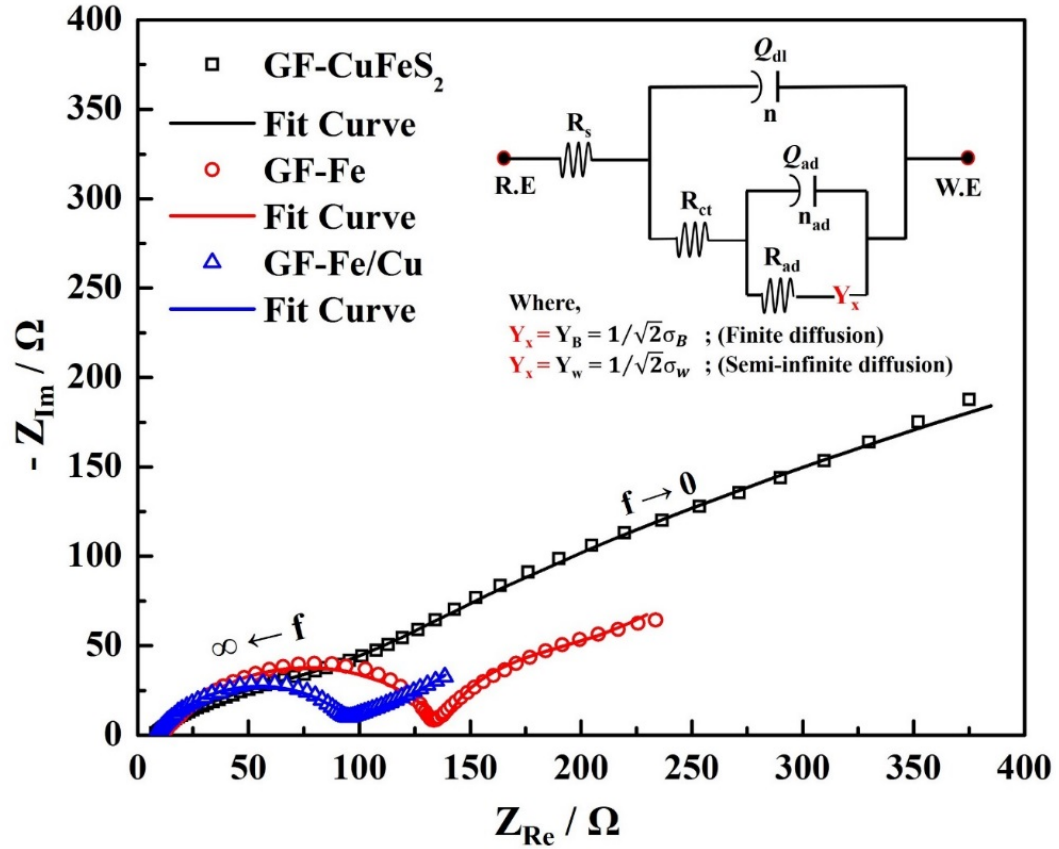


Figure 6-6 Impedance spectra of composite (GF – CuFeS₂ + CB), GF-Fe and GF-Fe/Cu electrodes (at 0 V vs. OCP). The EEC is shown in the inset in which Y_x is the admittance for the diffusion parameter and x=B, (for finite diffusion) and x=w (for semi-infinite diffusion), similarly σ_B = Warburg constant for GF-CuFeS₂, and σ_w = Warburg constant for GF-Fe and GF-Fe/Cu electrodes. In addition, the geometrical area of the GF in all electrodes was the same (14.4 cm²).

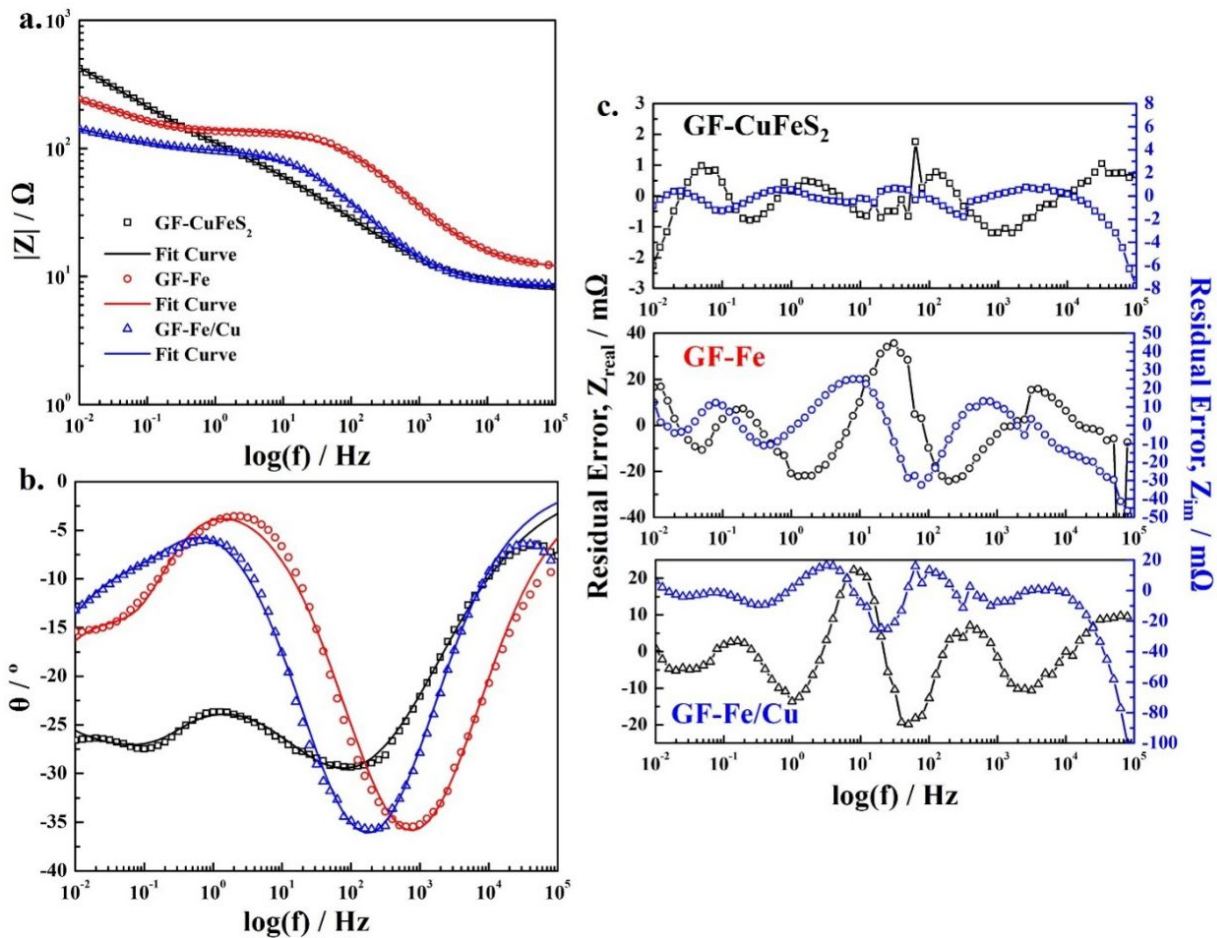


Figure 6-7 (a) Bode plots (b) Phase angle (c) Residual error plots obtained after fitting of impedance spectra with EEC. (Echem® Analyst 6.25 software; Gamry Instruments Inc.).

The data obtained after fitting the EEC model to the impedance spectra is provided in Table 6-1. The fitting was carried out through an iterative process and by adjusting the parameters of elements in the model editor (Echem Analyst 6.25 software; Gamry Instruments Inc.). There were small fitting errors for the EEC, as shown in Figure 6-7c. Compared to GF electrodes, the large ' Q_{dl} ' (1.12 mS sⁿ¹) registered by the composite electrode is most likely associated with the presence of CuFeS₂ in the composite electrode. The sulfide sulfur species (see Figure 6-14a) on the surface of CuFeS₂ and surface functional groups on GF can reversibly interact with ionic species resulting in an increase in ' Q_{dl} '. The kinetic activity (faradaic

response) of the composite electrode can be estimated from ' R_{ct} ' (84.74 Ω) and is comparable to the GF-Fe/Cu (93.11 Ω) electrode. The higher ' R_{ct} ' of GF-Fe (130.2 Ω) compared to GF-Fe/Cu further validated the catalytic behavior of Cu^{2+} in the catholyte as indicated by the improved current response by this electrode (Figure 6-4c, d and Figure 6-5). The reversible faradaic response of the surface sulfide sulfur species and surface functional groups in the composite electrode is reflected by the low ' R_{ad} ' (22.34 Ω) value. The small values of ' Q_{ad} ' and power index ($n_2 = 0.39$) are due to a highly distributed faradaic response of the composite electrode in which CuFeS_2 particles make a fix bed with additional inter-particulate porosity [32]. However, limited mass transport across the pre-existing surface film could restrict the non-capacitive faradaic (irreversible) reactions under applied conditions (5 mV AC perturbation at OCP). This behavior can be estimated from the ' σ_B ' (606.4 $\Omega \text{ s}^{-1/2}$) and ' B ' (1.99 $\text{s}^{1/2}$). The relatively large capacitive response ' Q_{dl} ' by the GF-Fe/Cu (330.5 $\mu\text{S s}^{n_1}$) compared to GF-Fe (93.9 $\mu\text{S s}^{n_1}$) clearly demonstrated the influence of Cu^{2+} ions in the electrolyte. Due to the porous structure of GF, the non-uniform charge distribution in both electrodes was predicted from $n_1 < 1$ and is evident in the phase shift at high frequency (Figure 6-7b). The almost double ' Q_{ad} ' value (54.9 mS s^{n_2}) and very small ' R_{ad} ' (16.92 Ω) for the GF-Fe/Cu compared to the GF-Fe electrode further validated the improved kinetic response of the GF in the presence of Cu^{2+} in the electrolyte. The n_2 value equal to 1 indicates the pure capacitor-like behavior in which charge is homogeneously distributed within the porous GF electrode as discussed by Cuenca *et al.* [240].

From these results, it can be evaluated that the reduction of Cu^{2+} at the GF/electrolyte interface (reaction 6.7) could significantly improve the charge transport characteristics of the GF [241]. On the other hand, the significantly reduced ' σ_w ' (7.6 $\Omega \text{ s}^{-1/2}$) for the GF-Fe/Cu

electrode compared to GF–Fe electrode is also due to the facile charge transfer process (reaction 6.7) leading to mass transfer control (semi-infinite diffusion characteristics).

Table 6-1 Impedance parameters evaluated after fitting the spectra by using the EEC model

Parameters	GF – CuFeS ₂ (Anode)	GF – Fe (Cathode)	GF – Fe/Cu (Cathode)
R _s (Ω)	7.77	11.13	8.31
Q _{dl} (μS s ⁿ¹)	1119	93.9	330.5
n ₁	0.54	0.67	0.68
R _{ct} (Ω)	84.74	130.2	93.11
Q _{ad} (mS s ⁿ²)	6.05	30.2	54.93
n ₂	0.39	0.99	1.00
R _{ad} (Ω)	22.34	57.64	16.92
σ _B (Ω s ^{-1/2})	606.4	–	–
σ _w (Ω s ^{-1/2})	–	13.8	7.6
B (s ^{1/2})	1.99	–	–
Chi-square	2.0x10 ⁻⁴	4.5x10 ⁻⁴	4.9x10 ⁻⁴

To verify this behavior, we immersed the as-received GF samples in each electrolyte for 48 h at 25 °C. The samples washed with DI–water several times were left in the air to dry. The SEM images and EDX analyses of these soaked GF samples showed clear morphological and compositional differences as shown in Figure 6-8. Compared to the as-received GF and GF–Fe, the GF–Fe/Cu contained higher Fe concentrations. Similarly, the signals for O and S species on the GF–Fe/Cu electrode were dominant, which we believe is due to the presence of surface functional groups and/or to the specifically adsorbed ionic species i.e. HSO₄⁻, SO₄²⁻, Fe²⁺, Fe³⁺, and Cu²⁺ etc.

Pakula *et al.* [241] also demonstrated the electro-adsorption of Fe³⁺ ions on activated carbon. They concluded that with an increase in the density of oxygen-containing acidic functional groups on carbon, they could significantly improve the adsorption capacity for water molecules and Fe³⁺ ions. The addition of Cu²⁺ to the electrolyte appears to catalyze the oxidation of Fe²⁺, as proposed in the preceding discussion, which is thought to be the reason

for the improved stability of the Fe^{3+} species according to reaction 6.7 and its adsorption on GF.

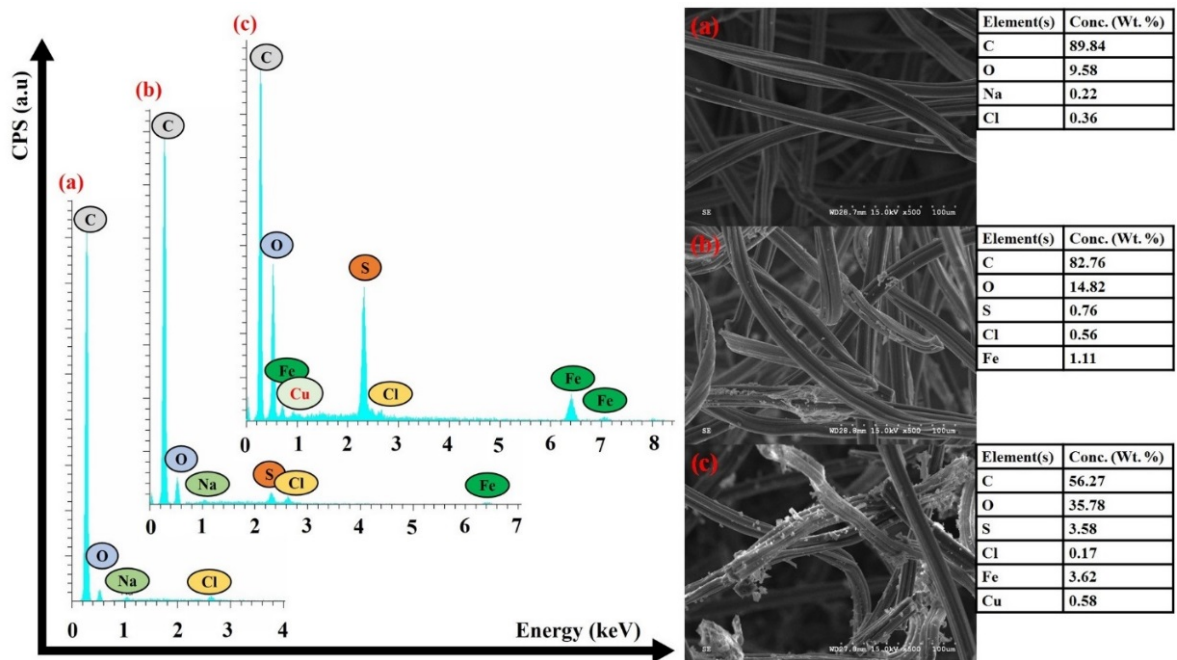


Figure 6-8 SEM images and EDX analyses of the (a) as received and (b) treated GF (in $0.5\text{M Fe}^{2+}/0.2\text{M H}_2\text{SO}_4$) (c) GF treated in $0.5\text{M Fe}^{2+}/0.1\text{M Cu}^{2+}/0.2\text{M H}_2\text{SO}_4$

6.3 Estimating the charge storage capability by the FBFC system

The charge storage capability of the composite electrode containing CuFeS_2 in the negative compartment of the FBFC system (as shown in Figure 4-3) was estimated using the $\text{Fe}^{2+}/\text{Fe}^{3+}$ couple with and without the addition of Cu^{2+} ions as positive electroactive species. Figure 6-9a and b show the CV for the $\text{CuFeS}_2|\text{Fe}^{2+}$ (CFe) and $\text{CuFeS}_2|\text{Fe}^{2+}-\text{Cu}^{2+}$ (CFeCu) FBFC systems, respectively, at different sweep rates ($0.1 - 0.001 \text{ V s}^{-1}$). A higher specific current density was achieved for the CFeCu system vs. the CFe system during charging (forward) and discharging (reverse scan) cycles. The decrease in specific current density at slow sweep rate is typical behavior in the CV analysis and depends on the kinetics of the charge transfer reactions and mass transport of the electroactive species at the electrode surface. The

charge transfer reactions at the high surface area GF electrode could also induce polarization effects due to the development of a concentration gradient within the porous structure of the electrode compared to the bulk electrolyte. The continuous flow of electrolyte (7.5 ml/min) within both compartments of the FBFC ensured the continuous supply of ionic species within the porous electrode to avoid diffusion control processes by the depletion of ionic species at the surface of each electrode. Also, the conversion reactions (reduction of CuFeS_2 and formation of intermediate species) that occur within the negative (composite) electrode during the charging cycle affect the charging and discharging behavior of the FBFC in successive cycles. For instance, the large potential drop with increase in sweep rate (Figure 6-9a and b) for both the CFe and CFeCu systems during forward (charging) and reverse cycles (discharging) is possibly due to the slow kinetics of the electroactive materials.

In CV scans at a high sweep rate, the relationship between current and cell potential indicates the limited kinetic response of the electrode materials, particularly associated with the charge transfer characteristics of the CuFeS_2 in the composite (negative) electrode. The mixing of CB (20 wt %) with the CuFeS_2 likely minimized the inter-particulate contact resistance but the formation of a sulfide sulfur enriched film on the surface of CuFeS_2 during the charge/discharge process likely restricts the electron transfer to or from the CuFeS_2 . The sweep rate dependency of the $\text{Fe}^{2+}/\text{Fe}^{3+}$ redox reaction on the GF electrode has already been discussed in the preceding section. Figure 6-9c shows a decrease in differential specific capacitance with an increase in sweep rate. This indicates a drop in the charge storage capability of the proposed system possibly either due to the formation of intermediate species on the surface of CuFeS_2 particles or by the quasi-reversible nature of the redox reactions in the catholyte ($\text{Fe}^{2+}/\text{Fe}^{3+}$ and or $\text{Cu}^{2+}/\text{Cu}^+$) as explained in section 7.2 (Chapter 7).

The rapid fall in the specific capacitance at high sweep rate (Figure 6-9c) also confirmed the slow kinetic response of the electrode materials [242]. This behavior suggests that the current density for charging and discharging of the proposed setup should always be lower than the maximum current density obtained in the CV scan at slow sweep rate (0.001 V s⁻¹). In this way, the maximum faradaic response of the electrode materials can be ensured in the FBFC setup. The average specific capacitance (C_{sp}) at slow sweep rate (0.001 V s⁻¹) during charging/discharging (at 1.0V cell potential) of the CFe and CFeCu systems was calculated from Equation 6.1. For this system, the specific capacitance was found to be 99.1 and 149.3 F g⁻¹, respectively, which decreased monotonically with increasing sweep rate as shown in Figure 6-9c.

$$C_{sp} = \frac{1}{msv} \int_{V_1}^{V_2} i(V) \cdot dV$$

Equation 6-1

Where, ‘ m ’ is the mass (gm) of CuFeS₂ used in the negative electrode, ‘ s ’ corresponds to the sweep rate (V s⁻¹), ‘ V ’ is the potential window (V), ‘ $i(V)dV$ ’ is the potential dependent current response (A) , V_1 and V_2 correspond to initial and final potential, respectively. The asymmetrical cyclic current response of both systems obtained at 0.001 V s⁻¹ is shown in Figure 6-9d. This behavior was associated with the slow kinetic response of the electrode materials. The well-known refractory nature of CuFeS₂, its low electrical conductivity and tendency to form a passive film under acidic conditions could be the possible reasons for very low specific capacitance with an increase in sweep rate.

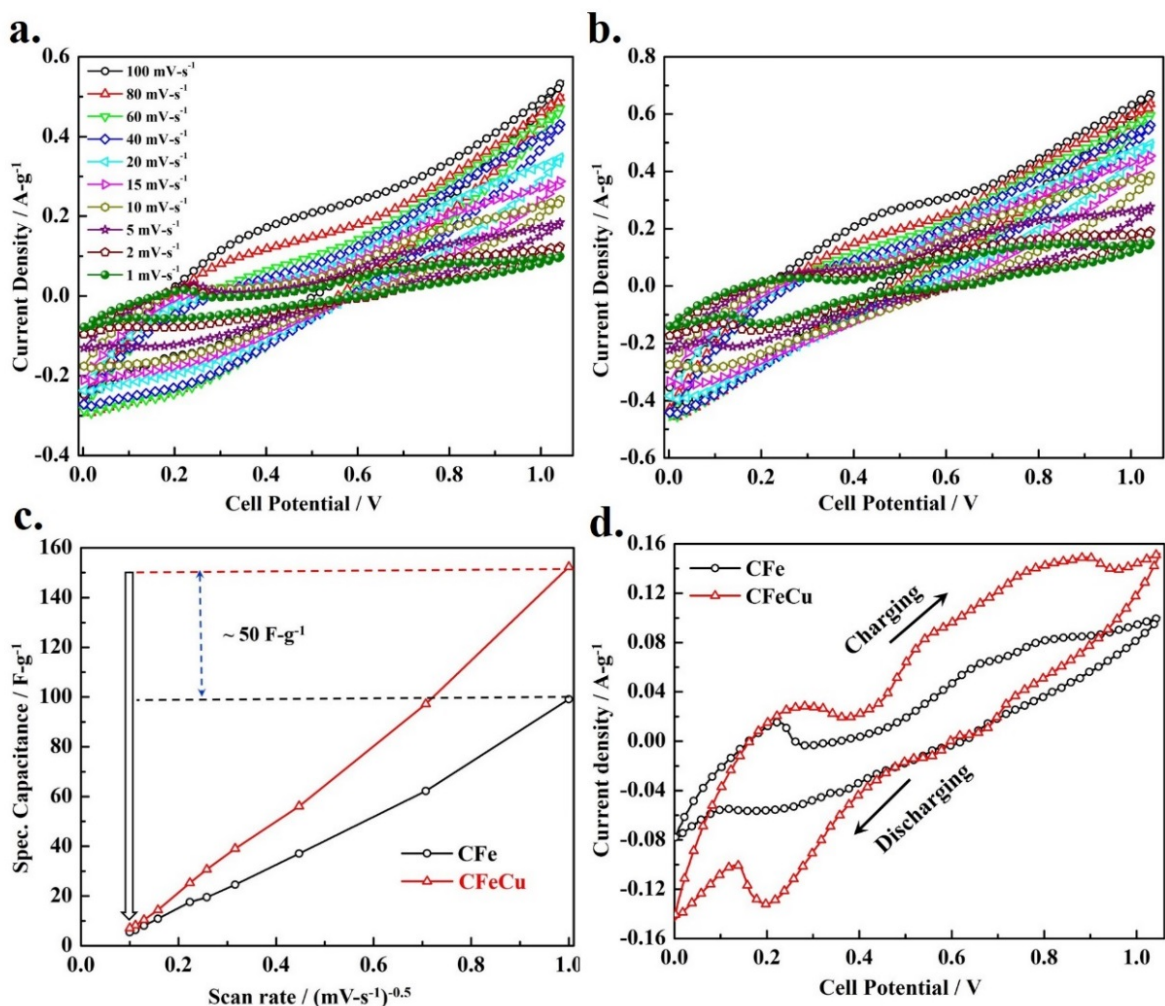


Figure 6-9 CV scans of (a) CFe and (b) CFeCu systems. (c) Trends showing the variation in the specific capacitance as a function of (sweep rate)^{-0.5} (at 1 V cell potential), (d) comparison of CFe and CFeCu system (voltammograms at 1 mV s⁻¹)

In the CFe system, during the charging cycle, the oxidation reactions taking place on the positive electrodes are supported by the reduction reactions at the negative composite electrode. Similarly, the oxidation reactions on the negative electrode would occur in the following discharge cycle facilitated by the reduction of Fe³⁺ and/or Cu²⁺ on the positive electrode. It can be estimated that for effective charge storage and retrieval, one would require high stability of Fe³⁺ ions in the catholyte. This could be achieved with the addition of Cu²⁺ in

the solution as proposed in the stability analysis (Figure 6-5). In a typical CV scan of the CFeCu system, higher anodic and cathodic current densities were observed, which were attributed to the increased stability of Fe^{3+} ions. However, based on the literature, the quasi-reversible minor redox peaks centered at about 0.55V in both the CFe and CFeCu systems represented the pseudocapacitive behavior of the GF due to the presence of surface functional groups [211].

To verify the charge storage behavior of the proposed systems and to estimate the coulombic (η_C) and energy (η_E) efficiencies of the process, GCD cyclic tests were performed from 0 to 1.05 V. The charging and discharging was carried out at 200 mA g^{-1} and 150 mA g^{-1} , respectively, and potential profiles for 500 cycles are provided for comparison in Figure 6-10. Analogous to the CV scans, the asymmetrical GCD plots reconfirmed the pseudocapacitive behavior of the proposed FBFC systems. A sudden potential drop of $\sim 0.2 \text{ V}$ at the onset of each discharge cycle was observed and may arise from the ionic resistance of the PEM, the electrolyte and/or due to the contact resistance between electrical connections. However, as noted above, the inter-particulate contact resistance in the negative composite electrode is expected to be small due to the mixing of 20 wt. % conductive CB with the CuFeS_2 . Compared to CFe, larger potential plateaus at approximately 0.2 and 0.6 V were observed in the CFeCu system during the 5th GCD cycle (Figure 6-10a and b), which indicated an improvement in the electrochemical response of the FBFC due to Cu^{2+} addition in the catholyte.

In the CFe system, during GCD cycling, the repetitive potential plateaus verify the occurrence of reversible redox reactions on the surface of both electrodes. In addition, the relatively lower current response of the $\text{Fe}^{\text{II}}/\text{Fe}^{\text{III}}$ redox reaction (in the absence of Cu^{2+} as discussed above) resulted in short potential plateaus in the GCD curves as evident in Figure 6-10a. This behavior also validates the beneficial effect of Cu^{2+} addition in the catholyte

enhances the Fe^{III} stability (as discussed in section 6.2) and the results are in agreement with the higher current density given by the CFeCu system as shown in Figure 6-9d and Figure 6-5. The formation of intermediate species at the GF–CuFeS₂ negative electrode is also possible. The enrichment of the CuFeS₂ surface with copper and sulfide sulfur species by the release of iron in the electrolyte under repetitive charging/discharging cycles changed the electrochemical response of the composite electrode. Sulfide species i.e. S₂²⁻ and S²⁻ formed on the surface of CuFeS₂ during cyclic charging/discharging and this is seen by the potential plateau at 0.2 V. Conway *et al.*[212], also explained the reversible pseudocapacitive character of these species over the surface of FeS₂ (pyrite) (reaction 6.8).



During the charging process, reduction of CuFeS₂ to talnakhite (Cu₉Fe₈S₁₆), bornite (Cu₅FeS₄) and/or chalcocite (Cu₂S) occurs at the negative electrode (CuFeS₂) [32]. These reactions are supported by the oxidation of Fe²⁺ to Fe³⁺ in the other half of the FBFC, at the positive electrode. It is also noted that during charging the potential plateaus were higher than the discharge potential for all cycles, which results from the irreversible faradaic reactions taking place on the surface of CuFeS₂. This behavior limits the reversible charge transfer processes during repetitive charge/discharge cycles and hence deteriorates the charge storage capability of the system, as observed in the following 300 cycles.

For the CFeCu system, due to improvement in the kinetic response of the Fe²⁺/Fe³⁺ redox reaction on the GF electrode (in the positive compartment of the FBFC) in the presence of Cu²⁺, the span of the plateau at ~ 0.25 V was increased during continuous GCD cycling as seen in Figure 6-10b.

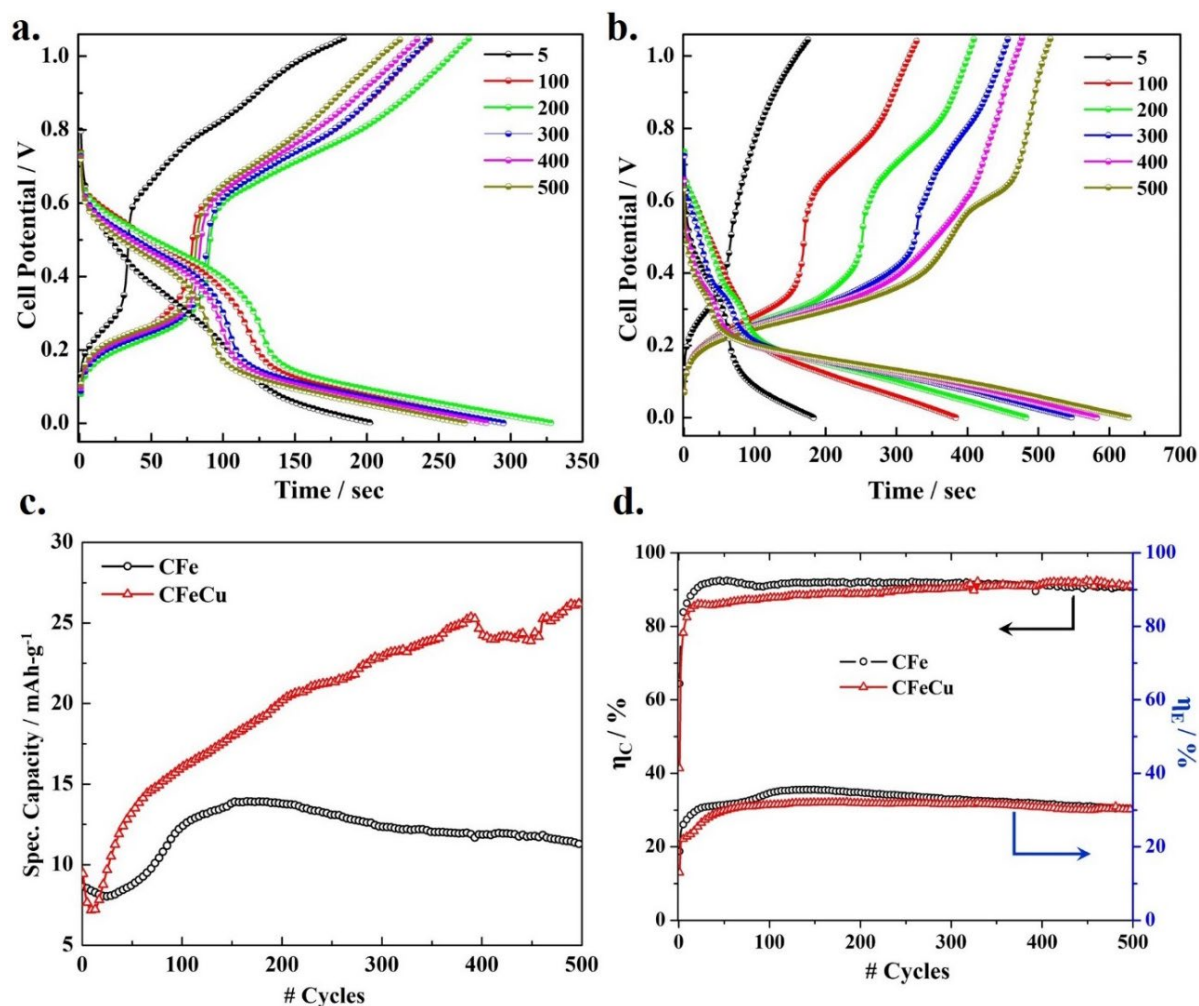


Figure 6-10 GCD cyclic trends of (a) CFe and (b) CFeCu systems (c) the specific capacity behavior of both systems (d) Trends of coulombic (η_c) and energy (η_E) efficiencies for both systems

These plateaus represent the concurrence of reversible redox reactions on both the electrodes and the increase in span indicates the improvement in the discharge capacity as calculated from Equation 6.2. The second plateau in the GCD plots also shifted to a lower cell potential, which is likely due to specific adsorption of copper species on the GF at the positive electrode. This is also corroborated by the low R_{ct} value obtained for the GF-Fe/Cu compared to GF-Fe electrode in the impedance analyses. A steep discharging profile for the CFeCu cell system is observed at higher cell potential (> 0.3 V) with a small potential plateau at

approximately 0.40 V. This shorter sloping plateau could be related with the oxidation of product formed in the negative electrode during the charging process. The appearance of this plateau in the repetitive discharge cycles also indicates the reversible pseudocapacitive character of some of the intermediate species. With the increase in GDC cycles, the gradual decrease in the potential below 0.25 V corresponds to an increase in charge storage capacity.

The similarity in the CV and GCD profile of the CFeCu system and relatively extended discharge cycles were linked with the increased stability of Fe³⁺ ions when Cu²⁺ was present. In simple words, the Fe³⁺ ions formed in the presence of Cu²⁺ ions during charging, would be readily available during discharge and hence could increase the overall specific capacity of the system. Mai *et al.* [243] also reported an increase in specific capacitance of functionalized porous carbon with the addition of Cu²⁺ in the electrolyte. They also proposed that the reversible adsorption/desorption of Cu⁺ species with the carbonyl functional group over porous carbon could be the reason for their observed ultrahigh pseudocapacitance (4700 F g⁻¹).

The anomalous increase of the discharge specific capacity in the CFeCu system beyond 10 GCD cycles was calculated from Equation 6.2 and can be seen in Figure 6-10c. The specific capacity gradually increased to 25.4 mAh g⁻¹ in 390 GCD cycles, which dropped approximately ~5% before reaching a maximum of 26.2 mAh g⁻¹ in the following (up to 500 DCD) cycles. This behavior is thought to be due to the reversible character of the sulfide sulfur species present on CuFeS₂ (reaction 5.8).

$$\text{Specific Capacity (mAh g}^{-1}\text{)} = \frac{i_d}{3.6m(V-i_dR)} \int_{t_1}^{t_2} V(t) \cdot dt \quad \text{Equation 6-2}$$

Where ‘*i_d*’ corresponds to discharge current (A), ‘*V*’ and ‘*R*’ are the overall cell potential and total cell resistance (Ω), respectively.

The function ' $\int_{t_1}^{t_2} V(t). dt$ ' is the area under galvanostatic discharge profile from the start (t_1) to the end of discharge (t_2) (s), respectively.

The faradaic contribution of the $\text{Cu}^{2+}/\text{Cu}^+$ redox couple in the catholyte could also facilitate the reversible pseudocapacitive response of the CFeCu system. Compared to CFeCu, the CFe system had a lower discharge capacity (13.9 mAh g^{-1}) in the initial 200 GCD cycles with a similar increasing trend. In the following 300 cycles, $\sim 18\%$ gradual decrease in capacity was seen with this system. This fade in capacity was related to the relatively lower stability of Fe^{III} species (within the positive electrode compartment) and its limited support for the $\text{S}_2^{2-}/\text{S}^{2-}$ (on the negative CuFeS_2 electrode surface) reversible redox reaction in the cell. The existence of large polarization (relatively steep profile) and contraction in the discharging curves confirmed this behavior. In addition, the refractory nature of CuFeS_2 , its passivation, and low electrical conductivity could effectively hinder the pseudocapacitive response that may ultimately deteriorate the performance of the designed cell systems.

Figure 6-11 represents the variation in specific discharge energy during 500 GCD cycles. The specific energy of both systems was calculated from Equation 6.3 in which each parameter has its usual meanings. The monotonic increase in the specific energy (3.29 Wh kg^{-1}) of the CFe for the initial 150 cycles was followed by a $\sim 30\%$ gradual decrease over 500 cycles. The CFeCu system had a continuous increase in specific energy over 200 cycles and plateaued ($3.60 \pm 0.05 \text{ Wh kg}^{-1}$) for the successive 390 cycles. However, the atypical behavior of a sudden decrease ($\sim 10\%$) and then increase of specific energy in the last 100 cycles could be related to the surface limited irreversible faradaic reactions (reactions 6.1–6.4 and 6.9–6.10 in the following discussion) at the CuFeS_2 particles in the negative composite electrode.

$$\text{Specific Energy (Wh kg}^{-1}\text{)} = \frac{1}{3.6m} \int_{t_1}^{t_2} \Delta V(t) \cdot i_d \cdot dt \quad \text{Equation 6-3}$$

The high η_C (~90%) obtained for both systems indicated the maximum utilization of charge in the pseudocapacitive faradaic reactions during charging and discharging of the system. Whereas, the low η_E (~30%) as presented in Figure 6-10d, suggested a large loss in specific energy during the discharge process. This loss in supplied energy was related with the cell internal resistance, IR drop and more importantly to the significant polarization effects seen in Figure 6-10a and b. In other words, the energy supplied to the systems during the charging process was utilized in the irreversible reactions specifically associated with CuFeS_2 reduction into talnakhite, bornite and/or chalcocite, which might not be available during the discharge process (for the oxidation of the CuFeS_2 and any reaction products). To understand this behavior, the CuFeS_2 retrieved from the negative electrode of the CFeCu cell (after 500 GCD cycles) was compared with the as-synthesized CuFeS_2 .

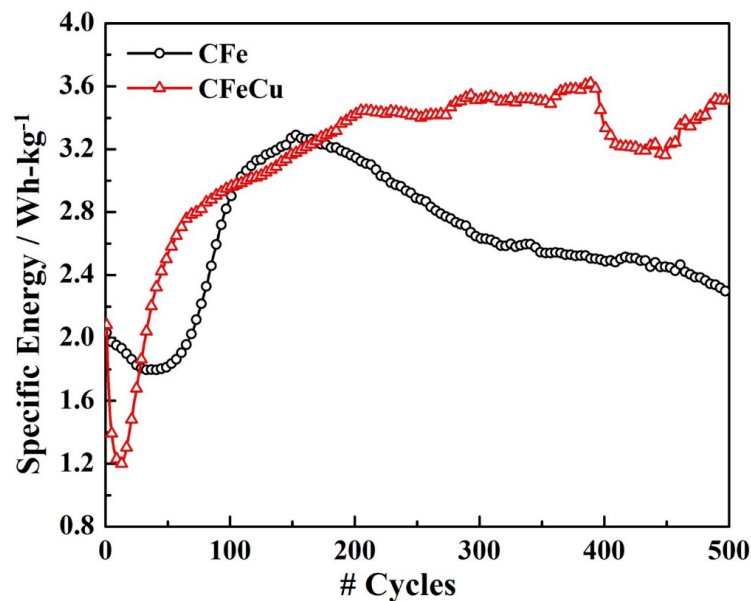


Figure 6-11 Specific energy trends of CFe and CFeCu system (Note: Charging and discharging was carried out at 200 mA g^{-1} and 150 mA g^{-1} , respectively)

6.4 Ex-Situ characterization of CuFeS₂

SEM, EDX, XRD, and XPS analyzed the surface morphology, composition, phase transformation and surface chemistry of the CuFeS₂ samples. The surface morphology of the retrieved CuFeS₂ samples was changed after 500 GCD cycles. The formation of a reaction product at the surface of the retrieved CuFeS₂ microspherical particles was evident as shown in Figure 6-12a and b. The EDX analysis confirmed the enrichment of copper and sulfur species in the final product after GCD cycling due to the dissolution of Fe from the surface of CuFeS₂ particles. The formation of copper and sulfur enriched species and depletion of iron during reduction (herein charging) and oxidation (discharging) of CuFeS₂ in the acidic solution has been widely discussed in the literature [87, 91, 244].

An increase in the copper content of the retrieved sample (47.8 vs. 26.3 at. %) was also detected. To probe the cause, ICP-OES was used (Varian 725-ES) to analyze both the anolyte and catholyte after cycling. A comparison of these results with the as-prepared electrolytes is shown in Figure 6-13. It was found that during the initial 200 cycles, the concentration of Fe and Cu in the anolyte was low (0.61 and 0.03 g l⁻¹, respectively), but that it gradually increased in the remaining 300 cycles. Approximately 2.23 and 0.45 g l⁻¹ of Fe and Cu, respectively, were found in the anolyte (0.2 M H₂SO₄) after 500 GCD cycles. These values include the Fe and Cu that migrated through the PEM from the catholyte and leached from the CuFeS₂. In order to quantify the Cu dissolution from CuFeS₂, the loss in mass of CuFeS₂ was determined after 500 cycles. It was determined that ~10.75 % Cu extraction was achieved as shown in the inset of Figure 6-13. The dual functionality of energy storage with an additional benefit of Cu extraction by this system makes it a hybrid for both purposes. The Fe and Cu species in the anolyte could also adsorb or deposit on the composite electrode. It is for this reason that the

retrieved $\text{CuFeS}_2 + \text{CB}$ mixture was thoroughly washed with DI water, filtered and dried in air prior to EDX and XRD analyses. Still, the presence of these species on the CuFeS_2 particles cannot be neglected and this may have increased the Cu contents in the retrieved product as determined by the EDX analysis (Figure 6-12b).

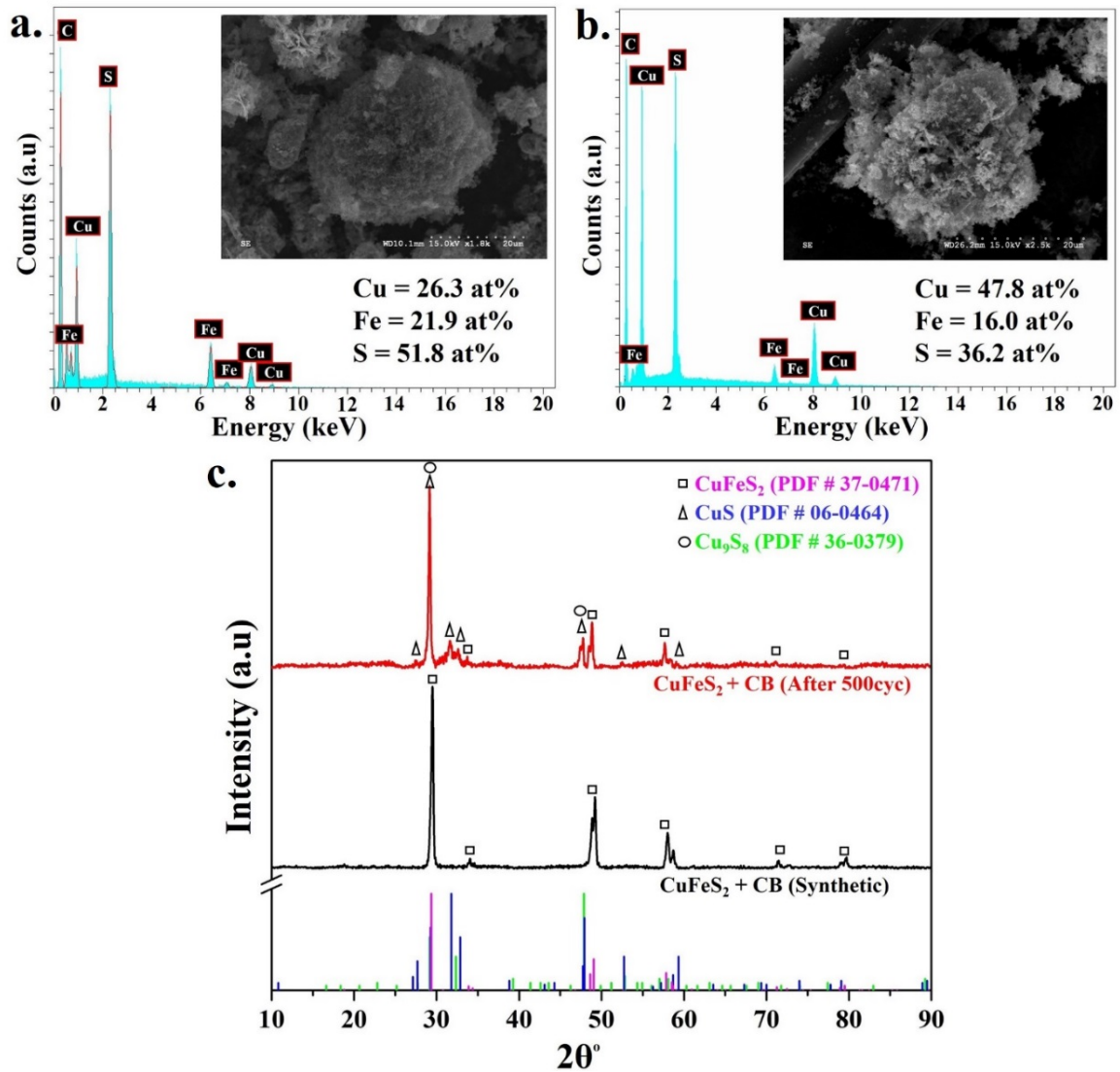


Figure 6-12 Morphological, compositional and structural changes in the CuFeS_2 before and after 500 GCD cycles in CFeCu system, SEM and EDX spectra of (a) as-synthesized, (b) and retrieved CuFeS_2 (c) XRD patterns comparison

The formation of copper and sulfur enriched species were also confirmed from the XRD patterns as shown in Figure 6-12c. The diffraction peaks originating at 2θ values 21.2° , 31.6° , 32.5° , 33.5° , 47.8° , and 52.7° correspond to the formation of CuS and Cu_9S_8 phases in the retrieved CuFeS_2 samples according to the 06–0464 and 36–0379 reference patterns, respectively. However, the diffraction pattern of the as synthesized sample demonstrated the characteristic peaks of pure CuFeS_2 that are indexed in Figure 5-1d, in accordance with the standard reference pattern (37–0471).

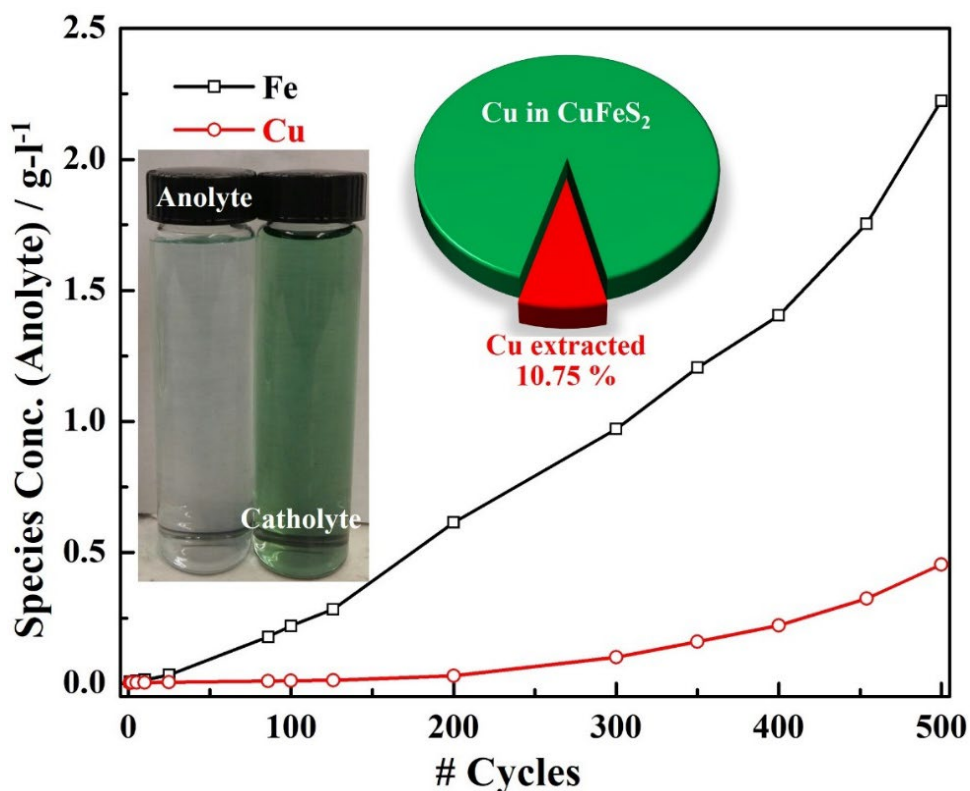


Figure 6-13 Fe and Cu species concentration in the anolyte after 500 GCD cycles (ICP-OES analysis), the % Cu extraction and retrieved anolyte and catholyte from CFeCu cell system after 500 cycles are shown as an inset.

The survey spectra of the as synthesized and retrieved CuFeS_2 were obtained on the binding energy scale. The characteristics peaks for sulfur (S) and copper (Cu) are shown in

Figure 6-14a, b, and c, respectively. The nature of the ‘S’ species present on the surface of CuFeS₂ was evaluated from the high-resolution spectra of the S 2p core peak. The deconvolution of the spectra was carried out by applying Shirley integration for background subtraction and the Gaussian-Lorentzian (80 %:20 %) function was used to split the spin-orbital core S 2p_{3/2} peak by using Peak 4.1 software. The deconvolution of the core S 2p peak provided the doublet S 2p_{3/2} peak at 161.41 and 162.44 eV, as shown in Figure 5.15a.

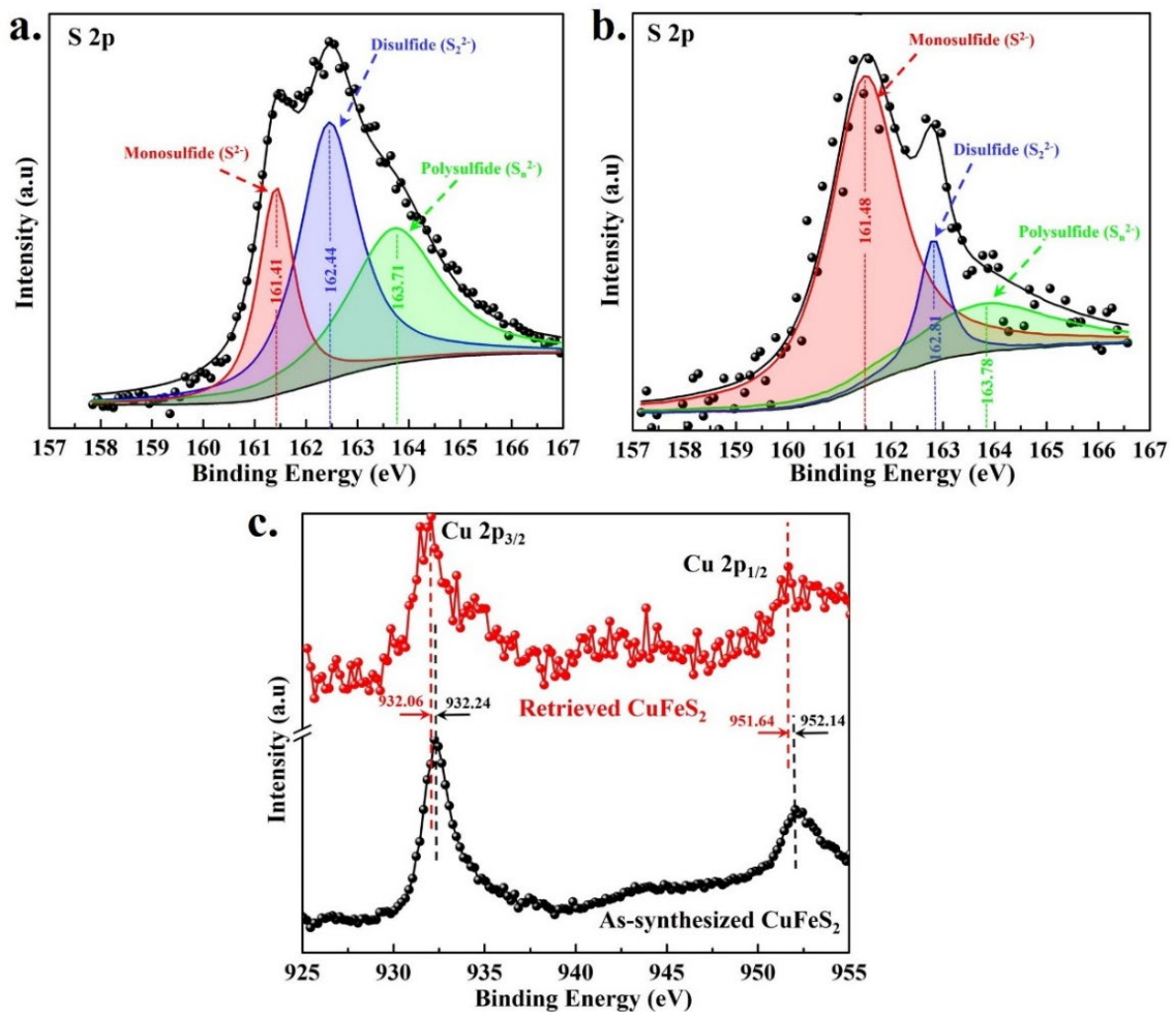


Figure 6-14 Deconvoluted X-ray photoelectron spectra of S 2p depicting the split of peaks associated with mono, di, and polysulfide species on the surface of (a) as-synthesized (b) retrieved CuFeS₂ samples (CFeCu cell system) (c) doublet peaks of Cu associated with Cu 2p_{3/2} and Cu 2p_{1/2} orbital

The peak at the lowest binding energy (161.41 eV) validated the existence of monosulfide (S^{2-}) species at the surface of as-synthesized $CuFeS_2$ particles according to the value (161.4 eV) provided in the literature [47]. The second doublet peak at 162.44 eV was assigned to S_2^{2-} species. The 1.03 eV difference between the doublet peaks was slightly lower than the 1.1 eV reported elsewhere and corresponds to partially coordinated sulfur species at the surface [45, 225]. It is well known that the S_2^{2-} can form by the dimerization of S^{2-} species via physical relocation of sulfur atoms at the surface of $CuFeS_2$ bonded directly with the copper and/or iron atoms [245]. The relatively broad satellite peak (FWHM 1.53 eV) observed at high binding energy (163.71 eV) corresponds to polysulfide species (S_n^{2-}) that most likely originate from the S 3p – Fe 3d inter-band excitation [47].

Figure 6-14b shows the S 2p core peak for the retrieved $CuFeS_2$ sample. A clear difference in the peak distribution and change in intensity was observed after 500 GCD cycles. In the retrieved $CuFeS_2$ sample, the binding energy for the S $2p_{3/2}$ doublet peaks also shifted to higher energy values compared to the as-synthesized $CuFeS_2$. It would be reasonable to speculate from this behavior that the metal-sulfur bonding energies may change due to the formation of iron deficient species at the surface of $CuFeS_2$ during repetitive charge/discharge cycles as confirmed from the EDX and XRD analyses. Although the peak binding energy 161.48 eV (FWHM=1.63) was lower than the energy of the sulfide (S^{2-}) species in CuS (161.6 \pm 0.1 eV), it was dominant having 1.57 times higher peak area than shown in Figure 6-14a. However, the peak for the S_2^{2-} disulfide species at 162.8 eV was consistent with the literature and may be associated with covellite (CuS) [246, 247]. In addition, the broad tail peak at high binding energy 163.78 eV (FWHM=3.27) is also consistent with the existence of polysulfide species (S_n^{2-}). The relatively small peak intensity of this polysulfide species was evident, and

it may decrease due to the formation of an iron-deficient surface layer [47]. The presence of elemental sulfur (S^0) cannot be confirmed through XPS analysis due to its volatile nature in ultra-high vacuum. Compared to as-synthesized $CuFeS_2$, the relatively higher binding energies and larger difference (1.33 eV) within the S $2p_{3/2}$ doublet peaks also suggest the formation of a metal-deficient structure surface film after GCD cycling at the surface of the $CuFeS_2$ samples [41].

The XPS analysis of as-synthesized $CuFeS_2$ had core peaks at 932.24 eV and 952.14 eV, which are associated with the Cu $2p_{3/2}$ and Cu $2p_{1/2}$, respectively. However, the small variation in the binding energy after GCD cycling (retrieved sample) and the presence of a small satellite band at around 942.5 eV, is likely due to the presence of divalent copper (Cu^{2+}) species within the surface layer [48] as shown in Figure 6-14c. However, the decrease in binding (0.21 eV) energy of Cu $2p_{3/2}$ validated the formation of a CuS phase within the surface layer according to the binding energies (932.0 eV and 951.8) recorded by Nakai *et al.* [247]. In agreement with the EDX and XRD results, and based on the binding energy shift for both S $2p$ and Cu $2p$ species, these data are consistent with the formation of iron deficient CuS and/or Cu_9S_8 phases at the surface of $CuFeS_2$. This information is used to predict a reaction sequence that is proposed in the next section.

6.5 Proposed reaction sequence during GCD process

The reactions that may proceed during charging and discharge cycles are graphically shown in Figure 6-15. Non-capacitive irreversible faradaic reactions over the $CuFeS_2$ particles in the negative electrode during repetitive cycling significantly decrease the extractable energy and hence adversely affect the energy storage efficiency. One of the possible reasons for the low energy efficiency is that approximately 11 % of the Cu in the $CuFeS_2$ was dissolved.

However, this is also a significant benefit to the proposed system as this Cu can be recovered hydrometallurgically for profit. The continuous increase in the specific capacity during repetitive charging and discharging cycles with high coulombic efficiency (~90%) is associated with surface limited pseudocapacitive reversible reactions (reactions 6.7 and 6.8). During initial charging cycles, the CuFeS₂ is expected to transform into intermediate species i.e. talnakhite (Cu₉Fe₈S₁₆) and bornite (Cu₅FeS₄) before converting into chalcocite Cu₂S (reaction 6.2) with the generation of Fe²⁺ and H₂S_(aq) species according to reactions 9 and 10, respectively, as pointed out by Biegler *et al.* [93] and Sauber *et al.* [248], and as shown schematically in Figure 6-15a.

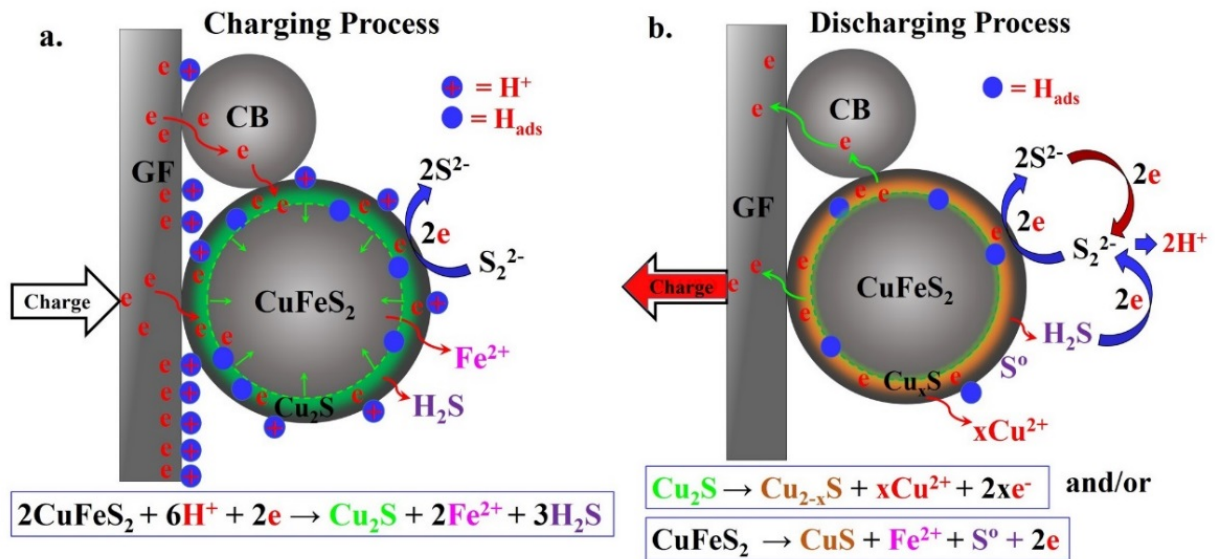
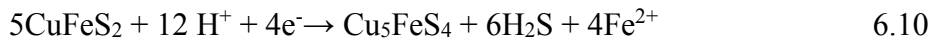
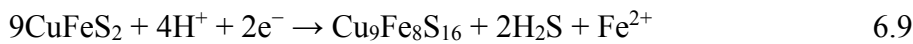


Figure 6-15 Schematic diagram showing the proposed reactions sequence on the negative electrode in the FBFC system during (a) charging and (b) discharging process

These non-capacitive irreversible conversion reactions likely consume a large amount of supplied energy during the initial charging cycles, which is consistent with the low η_E . It is

proposed that during discharging, any unreacted CuFeS₂ is oxidized into metal depleted sulfide Cu_{1-x}Fe_{1-y}S_{2-z} (reaction 1) or can convert into CuS. In the repetitive charging and discharging cycles the reduction of CuFeS₂ and oxidation of Cu₂S into a series of products i.e. djurleite (Cu_{1.92}S), digenite (Cu_{1.60}S) and CuS, is also possible (reaction 5) [232, 246] (Figure 6-15b).

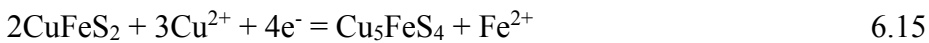
The possible H₂S_(aq) generation during the charging process can oxidize into either elemental sulfur (S⁰) or to the S₂²⁻ species by a non-oxidative dissolution mechanism (reaction 6.6 and 6.11, respectively) [24, 246]. These reactions were found to be reversible and enhanced the pseudocapacitive faradaic response as evident from the increased specific capacity and energy of the CFeCu system. Furthermore, the reversible transformation of S₂²⁻ into S²⁻ (reaction 6.8) during cyclic GCD is also possible as discussed above.

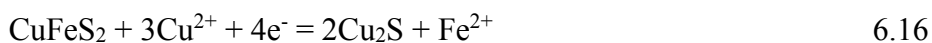


During continuous GCD cycling of the CFeCu cell setup, the generation of Fe^{II} and Cu^{II} species by the dissolution of CuFeS₂ in the negative electrode (or that diffused from the positive half of the cell) have been verified through ICP analysis. These species are beneficial to enhance the overall specific capacity and energy of the system. These species may react reversibly with the surface products formed at the CuFeS₂/electrolyte interface, e.g. CuS, S⁰ and/or H₂S_(aq) according to reactions 6.6, 6.12, 6.13 and 6.14, respectively [249, 250].



The literature also indicates that the addition of Cu²⁺ ions to the acidic solution could facilitate the reduction of CuFeS₂ into Cu₅FeS₄ and/or Cu₂S (reactions 6.15 and 6.16) [92].





The formation of iron deficient species at the surface of CuFeS_2 , and their reversible character (reactions 6.8, 6.12–6.14) has augmented the cyclic performance of the proposed system as evident from the continuous increase in specific capacity and energy during repetitive GCD cycling. However, the large amount of energy supplied during charging was utilized in the conversion reactions e.g. Cu extraction, which adversely affected the energy storage capacity and efficiency of the proposed systems. In other words, the non-capacitive irreversible faradaic reactions e.g. 10.75 % dissolution of Cu^{2+} from CuFeS_2 would consume energy during charge/discharge cycles. Although, the maximum specific energy provided by this system is low compared to the commercially available energy storage systems, the Cu^{2+} recovery from CuFeS_2 provides an additional benefit that may be monetized.

A very low pH is required for reduction reactions (reactions 6.9 and 6.10) to move in the forward direction during the charging process. In order to estimate the in-situ pH change in the CuFeS_2 slurry and to support the proposed mechanism, we also performed a few experiments in the two-electrode setup as shown in the inset of Figure 6-16a. The CuFeS_2 (80 wt. %) + CB (20 wt. %) slurry was thoroughly mixed and a 0.2 M H_2SO_4 solution was added to make a homogeneous slurry containing 20 wt. % solids. The measurements were made without stirring and the pH probe and counter electrodes were submerged in the semi-solid bed. The pH probe and the counter electrode were manually adjusted to an approximate 3 mm distance from the working electrode surface. The in-situ pH of the slurry at constant potentials (–1.0 V and +1.0 V) and the transient current were measured at different intervals as shown in Figure 6-16a and b, respectively.

The initial pH of the slurry was measured to be 0.72 at OCP. The OCP was 0 V in this case since both the counter and working electrode was graphite. During the change in cell potential (to -1.0 V), the pH of the slurry suddenly dropped to almost 0 indicating the abrupt migration of H^+ toward the negatively charged slurry particles. Under these conditions, it is possible that H^+ could reduce the $CuFeS_2$ into intermediate species i.e. talnakhite ($Cu_9Fe_8S_{16}$) and bornite (Cu_5FeS_4) before converting these into chalcocite Cu_2S as indicated in reactions 6.2, 6.9 and 6.10. The current was also found to increase (became less negative) due to the growth of a diffusion layer within the slurry, which approached a limiting current (Figure 6-16b). Under these transient conditions (charging process), the pH of the slurry increased to ~ 0.55 in 900 seconds.

It was interesting to see that the pH of the slurry shifted back toward the initial pH (~ 0.72) when the cell potential was reset to OCP. Following the charging process, the potential was shifted to $+1.0$ V (discharge) to evaluate the change in pH in this case. The current increased rapidly to a maximum of 35 mA and exponentially decayed before reaching a constant value (3.1 mA). This behavior corresponds to the oxidation of the $CuFeS_2$ and any intermediate species formed during the preceding charging process. The decrease in current and relatively low constant current also suggest that the decrease in dissolution rate is due to the formation of an Fe deficient and sulfide enriched surface film. The pH variation followed a similar trend to the current, and pH approached 1.96 upon sudden discharge attributed to the migration effect of cationic species in the opposite direction. The pH decayed to 0.94 during the initial 300 seconds and approached an almost constant value (0.89) in the next 600 seconds, which is most likely associated with the generation of oxidized species (Fe^{II} and Cu^{2+} etc.) by the partial dissolution of $CuFeS_2$.

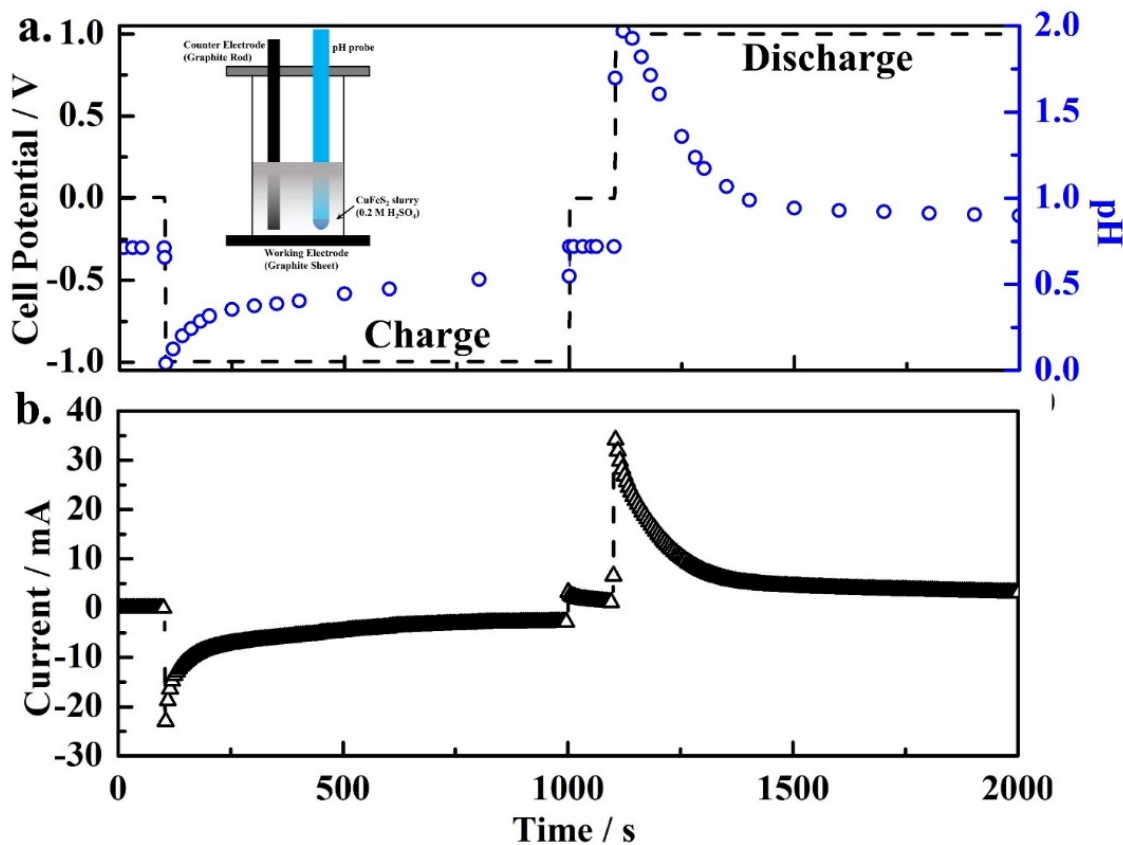


Figure 6-16 Potentiostatic polarization of CuFeS₂+ CB slurry (a) Variation in pH during charge (cell potential = -1.0 V) and discharge cycles (cell potential = 1.0), (b) Change in current profile (Note: only CuFeS₂ slurry in 0.2 M H₂SO₄ was used for pH measurements)

6.6 Summary

The use of synthetic CuFeS₂ as the negative composite electrode material in a laboratory designed FBFC system was presented in this chapter. This hybrid system has the dual capability of storing energy and extracting Cu from the CuFeS₂. The reduction of CuFeS₂ to Cu₂S (charge cycle) and oxidation of the reduced species i.e. Cu₂S, or any unreacted CuFeS₂, to CuS/Cu²⁺ (during discharge), was supported by the Fe^{II}/Fe^{III} redox reaction in this hybrid system. The main conclusions of this study were:

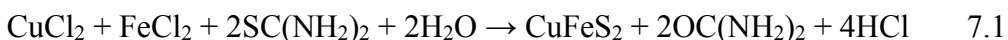
- The addition of 0.1 M Cu^{2+} in the catholyte increased the current response of the $\text{Fe}^{\text{II}}/\text{Fe}^{\text{III}}$ redox reaction, which was shown to be due to the increased stability of the Fe^{III} ionic species and catalytic behavior of Cu^{2+} towards Fe^{II} oxidation over the GF electrode. This increased the specific current density of the CFeCu system during charging and discharging processes as predicted from the CV scans at 0.001 V s^{-1} .
- The specific capacity of the CFeCu systems increased continuously to 26.2 mAh g^{-1} during 500 GCD cycles having a η_{C} over $\sim 90\%$. The CFe system, on the other hand, provided a relatively low capacity of 13.9 mAh g^{-1} in the initial 150 cycles followed by an 18% gradual decrease in the next 350 cycles.
- The energy storage capability of the CFeCu increased gradually to 3.60 ± 0.05 from 1.2 Wh kg^{-1} in 500 GCD cycles but the energy efficiency remained low at 30%. However, in the CFe system, the specific energy reached a maximum of 3.29 Wh kg^{-1} in the initial 150 cycles and decreased 30% in the successive 350 cycles.
- The cause of limited energy storage and low energy efficiency in this system (CFeCu) was also identified from the ex-situ analysis of the retrieved product. The energy consumed during charging of the CFeCu system was due to the progress of irreversible conversion reactions on the CuFeS_2 surface such as the dissolution of Cu from CuFeS_2 . While these reactions limit the energy storage of this system, they provide a source of copper that could be readily recovered.

Chapter 7: Use of a CuFeS₂ mineral concentrate in the FBFC¹⁰

In this chapter, we are reporting the use of a naturally sourced CuFeS₂ mineral concentrate as a negative electrode material in a hybrid setup, which is capable of storing energy. The additional benefit of this setup is the Cu extraction from CuFeS₂ that occurs during repetitive charging/discharging cycles. Thus, electrode degradation, which is normally undesirable in batteries, is an important and desirable feature in the present case. Indeed, the extraction of Cu in such a battery would result in its beneficial recovery. The Fe^{II}/Fe^{III} couple is used as the supporting reaction at the positive electrode. In addition, the kinetic behavior of the electrochemical reactions taking place on each electrode is also investigated. In this chapter, the energy storage and Cu extraction capabilities of both synthetic CuFeS₂ and the mineral concentrate in the FBFC setups are measured and compared. The analysis of the retrieved CuFeS₂ (post-testing) is carried out to further understand the reason for the observed increase in specific capacity during repetitive charging/discharging processes.

7.1 Characterization of synthetic and CuFeS₂ mineral concentrate

The spherically shaped CuFeS₂ particles produced in the laboratory via hydrothermal process consisted of platelets, which seemed to be connected at the core of sphere, similar to a pom-pom morphology. These particles have open pores at the surface which may develop during synthesis (similar to what is shown in Figure 5-1a) when it is believed that thiourea (SC(NH₂)₂) reduces Cu(II) and the following reaction (reaction 7.1) at high temperature and pressure occurs [251].



¹⁰ From published work, K.M. Deen, E. Asselin, *Electrochimica Acta* 297 (2019) 1079–1093.

Cu, Fe and S were detected by EDX and their molar ratio ($\text{Cu}_{1.08}\text{FeS}_{1.83}$) was close to the stoichiometric composition of chalcopyrite (Figure 7-1). The signals for C and O in the EDX spectrum during analysis possibly arise from the sputtered carbon and from the air oxidation of synthetic CuFeS_2 , respectively, and can be neglected.

The XRD pattern of the synthetic CuFeS_2 powder sample is shown in Figure 5-1d. The pattern confirmed the formation of CuFeS_2 that perfectly matched with the PDF # 37-0471 reference pattern. No impurity phases were detected. The diffraction peaks observed at 29.36° , 34.01° , 48.71° , 49.27° , 58.11° , 58.75° and 79.66° are from the (112), (200), (220), (204), (312), (116) and (316) planes, respectively. This is consistent with the typical tetragonal crystal structure of CuFeS_2 belonging to the (I – 42d (122)) space group.

The particle size distribution curves of both synthetic CuFeS_2 and MC samples were also obtained by the laser diffraction method (Malvern Mastersizer 2000) as shown in Figure 7-2. The D80 particle size ($34.9 \pm 3.0 \mu\text{m}$) was determined from the cumulative particle distribution curve. This signifies that 80 vol. % of the particles have a size less than the $34.9 \mu\text{m}$. However, the distribution curve also indicates a wide range of particle sizes (from 5 to $60 \mu\text{m}$) in the synthetic product. It was also observed that approximately 5 vol. % of the particles were less than $7 \mu\text{m}$. Similarly, the particle size distribution histogram of MC (Figure 7-2b) indicates the presence of particles ranging from $< 1 \mu\text{m}$ to $\sim 100 \mu\text{m}$. From the cumulative volume % distribution curve, the D50 and D80 were determined to be 19.5 ± 2.0 and $48.4 \pm 3.0 \mu\text{m}$, respectively.

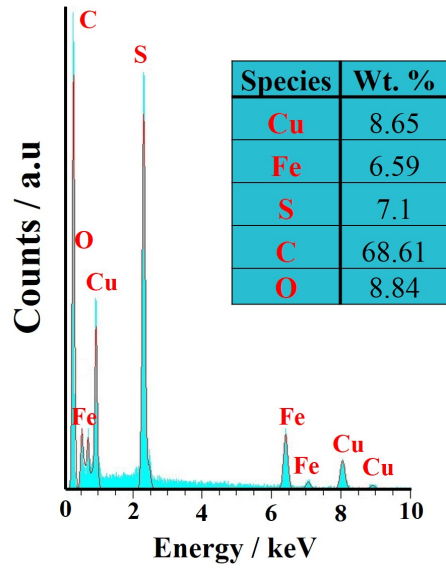


Figure 7-1 The EDX spectrum of the synthetic CuFeS_2

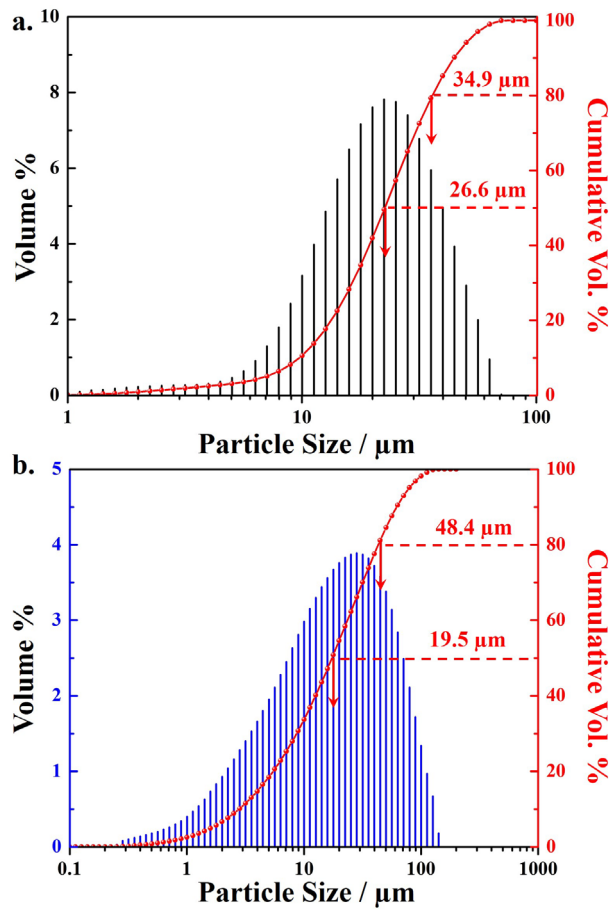


Figure 7-2 Particle size distribution histograms of (a) synthetic CuFeS_2 and (b) MC

The morphology and XRD pattern of the MC is shown in Figure 7-3. The irregularly shaped particles of the MC can be seen in the SEM image. The variable size and shape particles were generated from the mineral processing operations i.e. crushing, grinding and separation procedures (froth flotation), which were carried out at the mine site to enrich the CuFeS_2 mineral content in the ore extracted from mine. Analysis of the XRD pattern indicates the presence of several other phases in the MC. The diffraction peaks at 2θ : 29.3° , 49.3° , and 58.1° are associated with CuFeS_2 as confirmed from the standard reference pattern (PDF # 96-901-5235). However, additional peaks indicate the existence of other phases i.e. pyrite (96-901-5843), covellite (96-900-8371) and quartz (96-901-0145) as evident in Figure 7-3. Peaks at $2\theta < 20^\circ$ are also present and they are possibly related to silicate compounds. To further verify the composition of MC, quantitative X-Ray Powder Diffraction (QXRPD) analysis was also carried out. The quantity of all the crystalline phases present in the MC was obtained via Rietveld refinement of the XRD data using Topas 4.2 (Bruker AXS). The MC consists of pyrite (43.3 wt %), covellite (16.6 wt %) and chalcopyrite (26.6 wt %). Other minor impurity phases were quartz (4.0 wt %), illite-muscovite 2M1 (3.3 wt %), brochantite (2.2 wt %), enargite (1.6 wt %), pyrophyllite (1.2 wt %), kaolinite (0.9 wt %) and molybdenite (0.3 wt %). QXRPD, as practiced here, has a standard error of approximately 2 wt % in phase analysis, meaning that the identification of low concentration impurity phases is subject to significant error and should be considered indicative at best.

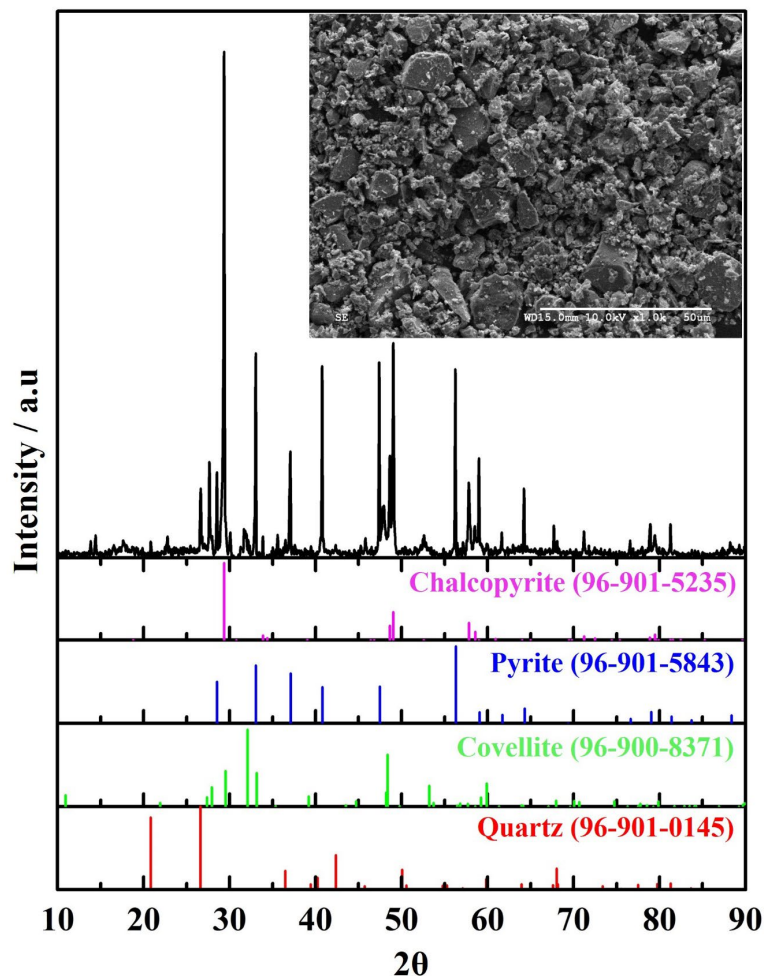


Figure 7-3 XRD pattern of the mineral concentrate (MC), the inset shows an SEM image of the MC particles

7.2 Electrode Kinetics

To simulate the electrochemical behavior of each composite (GF–CuFeS₂, GF–MC) and GF–Fe/Cu electrode in the FBFC setup, the kinetic response of each electrode was analyzed through CV scans. In the case of the composite (negative) electrodes, the CV scans were initiated in the cathodic direction from their open circuit potentials (OCP) to –1.5 V (vs. SHE) and reversed to 1.8 V (vs. SHE). In both GF–CuFeS₂ and GF–MC electrodes, reproducible cathodic and anodic peaks were observed, indicating the occurrence of redox

reactions (pseudocapacitive responses) at the electrode surface. The rapid increase in the current with an increase in potential beyond (< -0.5 V and > 1.2 V (vs. SHE)) is due to the dissociation of the electrolyte. Binary peaks, designated as $P1c$, $P2c$, (cathodic) and $P1a$, $P2a$, (anodic) are shown in Figure 7-4a and b. The redox potential ($E_{p1} = \frac{E_{P1a} + E_{P1c}}{2}$) of the first anodic and cathodic peaks (designated as $P1a$ and $P1c$) of both composite electrodes was calculated to be 0.64 ± 0.01 V (vs. SHE). These peaks are associated with the interaction of H^+ and HSO_4^- species with surface functional groups present on the GF electrode. Andreas et. al. [211] also reported that in acidic solutions, the redox peaks (centered at ~ 0.55 V) in CV scans were associated with the adsorption/desorption of H^+ species on the surface functional groups i.e. the Quinone functionalities (Q): $Q + 2H^+ + 2e^- \leftrightarrow QH_2$ of the C cloth. At high sweep rates, the current response is only related to surface reactions, whereas the potential dependent current (heterogeneous current response) associated with the redox and conversion reactions is observed at low sweep rates. At high sweep rates ($\nu \geq 0.04$ V s^{-1}), the surface limited adsorption/desorption processes should obey the Langmuir or Henry isotherms. In this case, the peak current varies linearly with ν according to Equation 7.1 as evaluated by Laviron [252].

$$I_{p1} = 0.25 A (nF)^2 (RT)^{-1} \Gamma_T \nu \quad \text{Equation 7-1}$$

Where, I_{p1} is the peak current for either $Pa1$ or $Pc1$, A is the surface area of the electrodes, n is the number of electrons involved during the adsorption/desorption process, F is Faraday's constant, R is the universal gas constant and T is the temperature (298 K). The Γ_T in the above relation is the total surface concentration of the electroactive adsorbed species.

At 0.1 V $s^{-1} > \nu \geq 0.04$ V s^{-1} , the large peak current associated with the $P1a$ and $P1c$ for both GF–CuFeS₂ and GF–MC electrodes varied linearly with ν , as shown in Figure 7-5. This behavior confirms the occurrence of surface limited reversible adsorption/desorption

processes particularly occurring on the GF electrode. It can be seen that the peak potentials were sweep rate dependent and with an increase in sweep rate, the potentials of both cathodic and anodic peaks were shifted to more negative and positive values, respectively. The shift in potential could originate either from quasi-reversible or electrochemically irreversible electrochemical processes on the electrode surface [253, 254]. Also, the potential drop (due to the increase in solution resistance within the porous structure by the development of a concentration gradient across the electrode/electrolyte interface) may influence the peak separation (ΔE_p). To circumvent this issue, the electrolyte was continuously stirred and the positive feedback IR compensation mode was applied in the potentiostat during testing. In this case, the ΔE_p ($\Delta E_1 = E_{p1a} - E_{p1c}$ or $\Delta E_2 = E_{p2a} - E_{p2c}$) as a function of ν can be used to predict the kinetics of electrochemical reactions according to the Laviron method described elsewhere [252, 255].

At the lowest sweep rate of 0.001 V s^{-1} , the peak separation ΔE_1 and ΔE_2 for the GF–CuFeS₂ electrode was negligible: 0.038 V and 0.044 V, as shown in Figure 7-4c. This is possibly related to the reversibility of H⁺ adsorption/desorption on the surface of GF and CuFeS₂ particles [211]. Similarly, in the case of the GF–MC electrode, ΔE_1 and ΔE_2 were significantly lower (0.053 and 0.046 V, respectively) than the ΔE_p at high ν , as shown in Figure 7-4c. Electrochemical reactions that are kinetically facile (Nernstian), as compared to mass transport (dimensionless rate constant (Λ) > 15), are designated as fully reversible. However, based on electron and mass transport characteristics, moderate ($15 > \Lambda > 10^{-3}$) and very slow reactions ($\Lambda \leq 10^{-3}$) are considered quasi-reversible and electrochemically irreversible reactions, respectively [256]. Furthermore, from the CV analysis for a Nernstian reaction (completely reversible), the ΔE_p should be $2.18(RT/nF) = \sim 57 \text{ mV}$ at low sweep rate for a

one electron transfer process [257]. These comparable values of peak potential shifts indicate the reversibility of the electrochemical processes (at 0.001 V s⁻¹) progressing on the surface of the composite electrodes. However, the significant increase in the peak separation at higher sweep rates (0.001 < ν ≤ 0.02 V s⁻¹) indicates the heterogeneous quasi-reversible and/or irreversible nature of the electrochemical reactions on the electrodes.

To diagnose the nature of the electrochemical processes, further analysis of the peak current (I_p) vs. $\nu^{1/2}$ was carried out. This relationship is linear for the GF-CuFeS₂ and GF-MC electrodes, as shown in Figure 7-6a and c, respectively. The porous electrodes have an accelerated kinetic response leading to diffusion-controlled processes at (ν ≤ 0.02 V s⁻¹). In this particular case, the heterogeneous current response is expressed by the Randle-Sevcik relation (Equation 7.2) [258].

$$i = \pm nFAC_o^* \left(\sqrt{\frac{D\nu\pi\alpha nF}{RT}} \right) \cdot x(bt) \quad \text{Equation 7-2}$$

Where $\pi^{1/2}x(bt)$ is the current function and it approaches 0.496 at the current peak ($i = i_p$), C_o^* is the concentration of ionic species in the bulk solution, D and α are the diffusion and charge transfer coefficients, respectively. The other parameters in Equation 7.2 have the usual meaning as mentioned above [258].

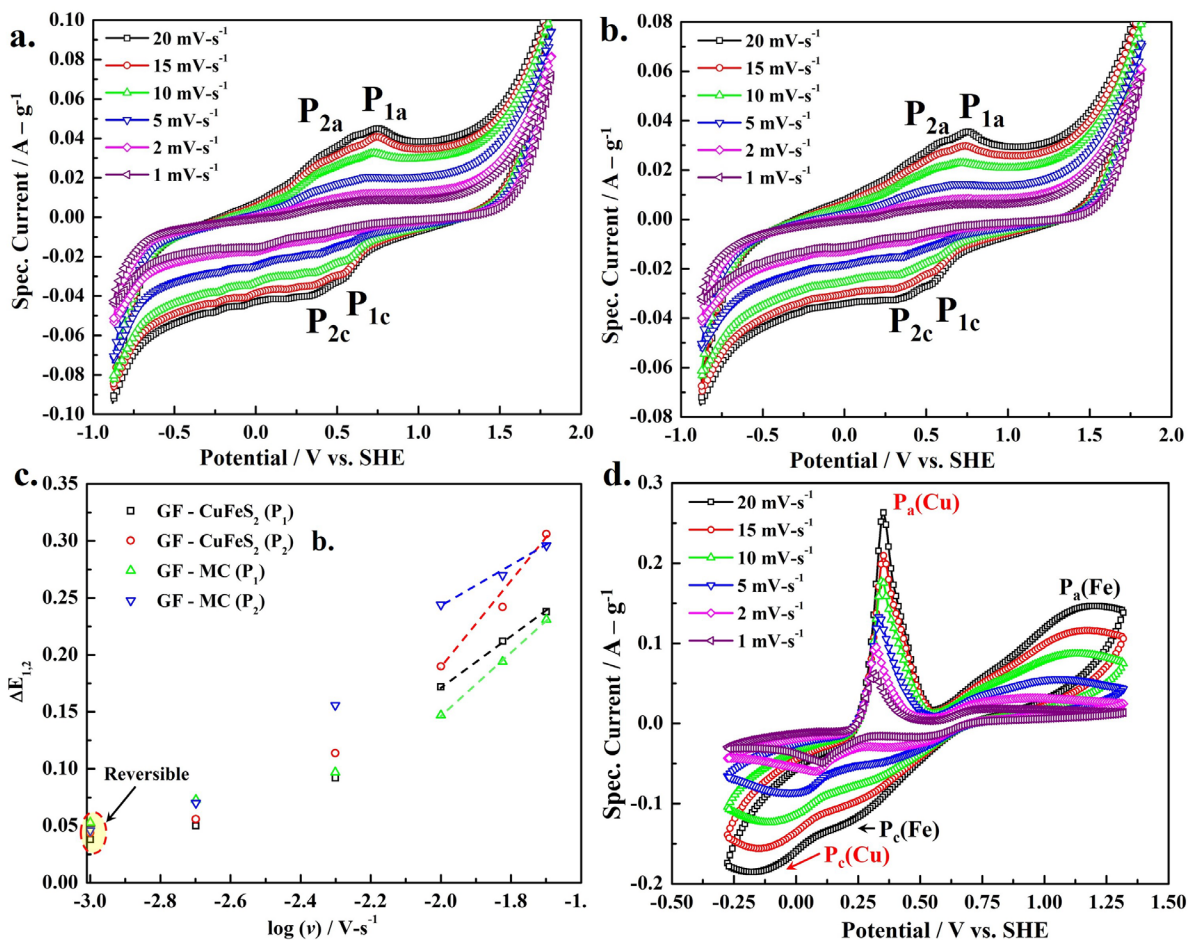


Figure 7-4 Cyclic voltammograms of composite (a) GF-CuFeS₂, (b) GF-MC electrodes obtained at various sweep rates. (c) $\log(v)$ vs. $\Delta E_{1,2}$ (peak separation) trends for the composite electrodes. (d) CV of GF-Fe/Cu electrode at different sweep rates (For composite electrodes, the current is normalized by the weight of GF + CuFeS₂ / MC, whereas for the GF-Fe/Cu electrode, the weight of GF was used to calculate the specific current).

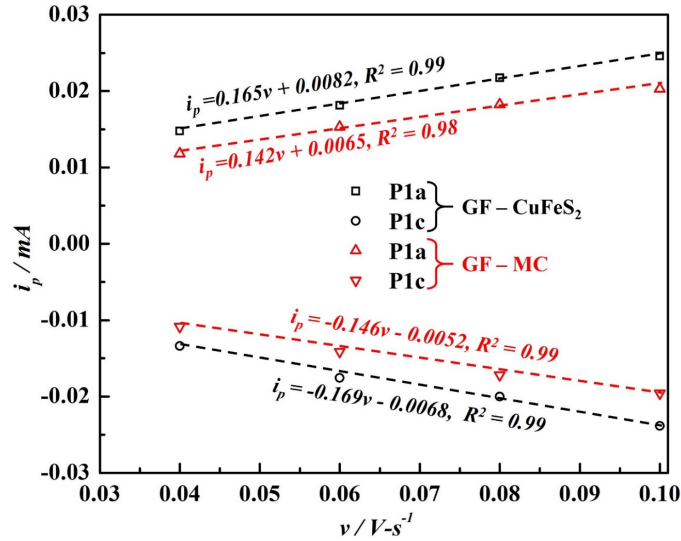


Figure 7-5 Peak current (for P_{a1} and P_{c1} only) variation vs. sweep rate (v) ($0.04 \geq v < 0.1 V s^{-1}$)

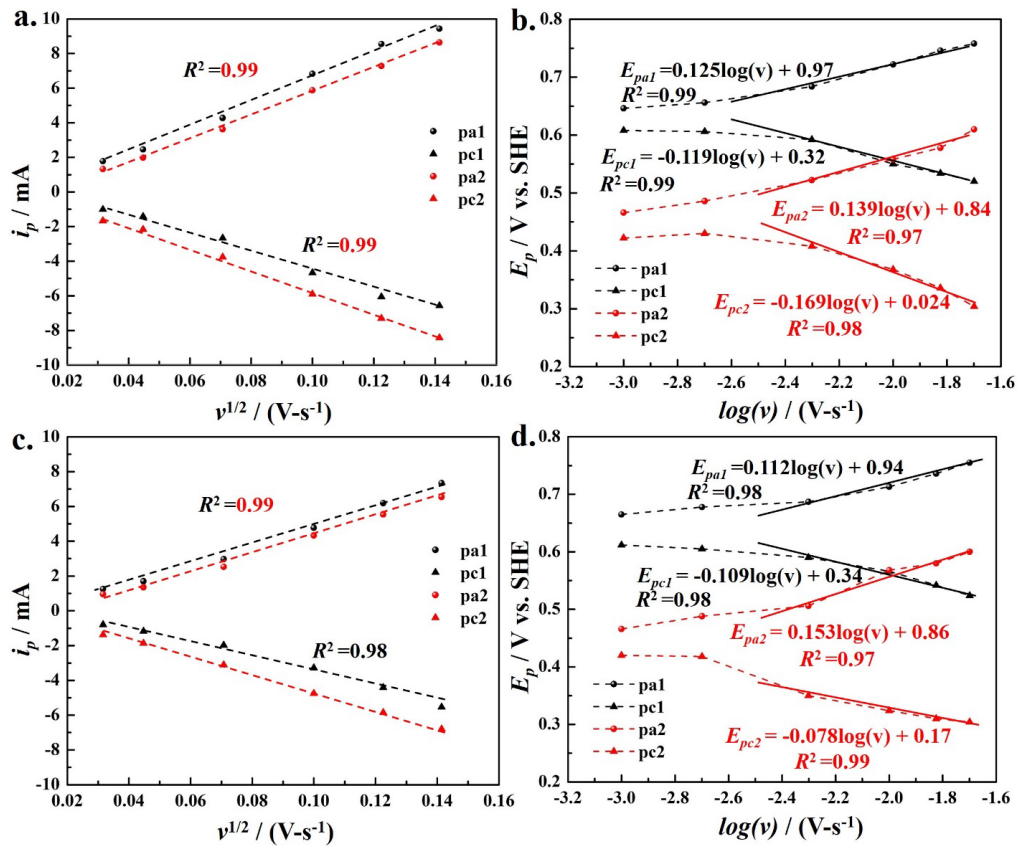


Figure 7-6 From the CV scans ($0.001 \leq v \leq 0.02 V s^{-1}$) and Equation 6.2, i_p vs. $v^{1/2}$ of (a) GF-CuFeS₂ (b) E_p vs. $\log(v)$ of GF-CuFeS₂ electrode (c) i_p vs. $v^{1/2}$ and (d) E_p vs. $\log(v)$ trends for the GF-MC electrode used to calculate charge transfer coefficient, α , values

The heterogeneous rate constant (k_h) of the redox reactions strongly depends on the D of the ionic species and the symmetry of the energy barrier, which is represented as α . Therefore, to determine D from Equation 7.2, it is important to first calculate the value of α . The Laviron method was used and the trends between $\log(v)$ vs. peak potentials are shown in Figure 7-6b and d. The slopes indicated on the asymptotes were used to calculate the α values according to Equation 7.3 [255, 256, 258, 259].

$$\text{Slope} = -\frac{2.303RT}{\alpha nF} \text{ (Cathodic)} = \frac{2.303RT}{(1-\alpha)nF} \text{ (Anodic)} \quad \text{Equation 7-3}$$

It is calculated that for both peaks ($P1a$, $P1c$, and $P2a$, $P2c$), the α values are comparable for both GF–CuFeS₂ and GF–MC electrodes, as given in Table 7-1. Furthermore, α associated with the $P1$ of both the electrodes is approximately 0.5, which validates the one-electron transfer process. From the slope (i_p vs. $v^{-1/2}$) for peak 1 ($P1$) as shown in Figure 7-6a and c (Equation 7.2), the D of H⁺ species within the GF–CuFeS₂ and GF–MC electrodes was 1.53×10^{-6} and $1.37 \times 10^{-6} \text{ cm}^2 \text{ s}^{-1}$, respectively. These results also support that $P1$ is associated with the GF according to reaction 7.2. From the analysis of $P2$, $\alpha = 0.65$ and 0.24 , for the GF–CuFeS₂ and GF–MC, respectively. These charge transfer coefficient values are believed to be due to the complex two electron transfer process occurring within these composite electrodes [258]. The redox potential (E_{p2}) of the peaks $P2a$ and $P2c$ in both GF–CuFeS₂ and GF–MC was $0.45 \pm 0.02 \text{ V}$ (vs. SHE) (Figure 7-4a and b) and these peaks are due to the pseudocapacitive response of the sulfide sulfur species present on the surface of CuFeS₂ or other sulfide minerals in MC (for example FeS₂) [212, 260]. In other words, the reproducible $P2a$ and $P2c$ peaks in the CV scan correspond to the redox reaction between S₂²⁻ and S²⁻ (reaction 7.3) species. Both are expected to be present on the surface of CuFeS₂ particles and/or on the surface of other sulfide minerals in the MC.

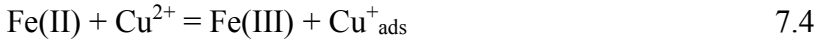
On the surface of GF (P1)



On the surface of CuFeS₂ or other sulfide minerals in the MC (P2)



Similarly, for the positive electrode (GF–Fe/Cu), the redox potentials E_{pFe} (Fe^{II}/Fe^{III}) and E_{pCu} (Cu^{II}/Cu^I) were 0.7±0.05 V and 0.15±0.05 V (vs. SHE), respectively, as evident in Figure 7-4d. By using Equation 7.2 and Equation 7.3 for the peaks associated with Fe^{II} and Cu^{II}, the kinetic parameters of the GF–Fe/Cu electrode calculated are given in Table 7-1. A one order of magnitude higher D (9.45 x 10⁻⁵ cm² s⁻¹) for Cu²⁺ compared to Fe²⁺ (3.07 x 10⁻⁶ cm² s⁻¹) was determined, which may effectively improve the kinetic response of the GF–Fe/Cu electrode according to reaction 7.4 as mentioned elsewhere [196]. Comparable values for the Fe^{II}/Fe^{III} redox potential (0.68 V (vs. SHE)) and D for Fe^{II} (5.6 x 10⁻⁶ cm² s⁻¹) on porous carbon nanotube electrode systems have also been reported by Friedl et al. [261].



The heterogeneous rate constant (k_h) at 25 °C was also calculated from the intercept of the linear trends (log i_p vs. ($E_p - E_{px}$)) as shown in Figure 7-7 according to Equation 7.4 [258].

$$i_p = 0.227 FAC_0^* k_h e^{-\frac{\alpha n F (E_p - E_{px})}{RT}} \quad \text{Equation 7-4}$$

Where E_p is the peak potential and E_{px} is the redox potential of the peaks (obtained from the average of the anodic and cathodic peak potentials). The corresponding values of α for each electrode (given in Table 7-1) are calculated from Equation 7.3 (discussed above). k_h for reaction 7.2 was sensitive to the composition of the electrode. For instance, for the GF–CuFeS₂ electrode, k_h (4.1 x 10⁻⁴ cm s⁻¹) was almost 1.5 times higher than on GF–MC. This behavior

reflects the combined effect of GF, CuFeS₂ and/or MC on the kinetics of the H⁺ adsorption/desorption process.

The relatively larger faradaic response of the composite electrode than that of the GF-only electrode has previously been discussed in detail [225]. It is proposed that the preferential adsorption of H⁺ on GF and its transport to CuFeS₂ in the composite electrode could significantly improve its pseudocapacitive response. For the GF–MC electrode, the large number of impurity phases may influence this process as seen from the relatively small value of k_h . On the other hand, the k_h of the S₂²⁻/S²⁻ reaction (Peak P2) on GF–CuFeS₂ ($3.6 \times 10^{-4} \text{ cm s}^{-1}$) was almost double the k_h value calculated for the GF–MC ($1.4 \times 10^{-4} \text{ cm s}^{-1}$) electrode. Thus, other impurity phases in the MC may restrict the electrochemical reversibility of this reaction in the GF–MC electrode.

The kinetics of the Fe^{II}/Fe^{III} redox reaction ($k_h = 4.1 \times 10^{-5} \text{ cm s}^{-1}$) on the GF electrode was two orders of magnitude lower than for the Cu^{II}/Cu^I redox reaction ($k_h = 1.1 \times 10^{-3} \text{ cm s}^{-1}$), which further validates the well-known catalytic behavior of Cu^{II} species in this catholyte [196, 238, 262]. Furthermore, the calculated k_h values ($> 2 \times 10^{-5} \text{ cm s}^{-1}$) for each reaction were consistent with quasi-reversible reactions [258].

Another criterion proposed by Matsuda et. al. [263] was used to differentiate the nature of the electrochemical reaction according to the following relation (Equation 7.5).

$$A = \frac{k_h}{\sqrt{\frac{FDv}{RT}}}$$

Equation 7-5

Where, A is a dimensionless rate constant parameter, and $A \geq 15$, $15 > A > 10^{-3}$, and $A \leq 10^{-3}$ correspond to reversible, quasi-reversible and irreversible electrochemical reactions, respectively. Based on the experimental results and kinetic parameters, the ‘ A ’ values at 0.001

$V s^{-1}$ sweep rate are given in Table 7-1. According to this criterion, the corresponding A values of each reaction further confirm the quasi-reversible nature of the electrochemical processes on GF–CuFeS₂, GF–MC and GF–Fe/Cu electrodes.

Table 7-1 Parameters calculated from the CV scans obtained at various sweep rates at 25 °C (Note: Geometrical surface area of the GF (14.4 cm²) was used in the calculation)

Electrode (s)		Species	α	D (cm ² s ⁻¹)	k_h (cm s ⁻¹)	A^*
GF – CuFeS ₂	<i>P1</i>	H ⁺	0.47	1.53 x 10 ⁻⁶	4.1 x 10 ⁻⁴	1.68
	<i>P2</i>	–	0.65	–	3.6 x 10 ⁻⁴	–
GF – MC	<i>P1</i>	H ⁺	0.52	1.37 x 10 ⁻⁶	2.6 x 10 ⁻⁴	1.13
	<i>P2</i>	–	0.24	–	1.4 x 10 ⁻⁴	–
GF – Fe/Cu	–	Fe ²⁺	0.24	3.07 x 10 ⁻⁶	4.1 x 10 ⁻⁵	0.12
	–	Cu ²⁺	0.24	9.45 x 10 ⁻⁵	1.1 x 10 ⁻³	0.57

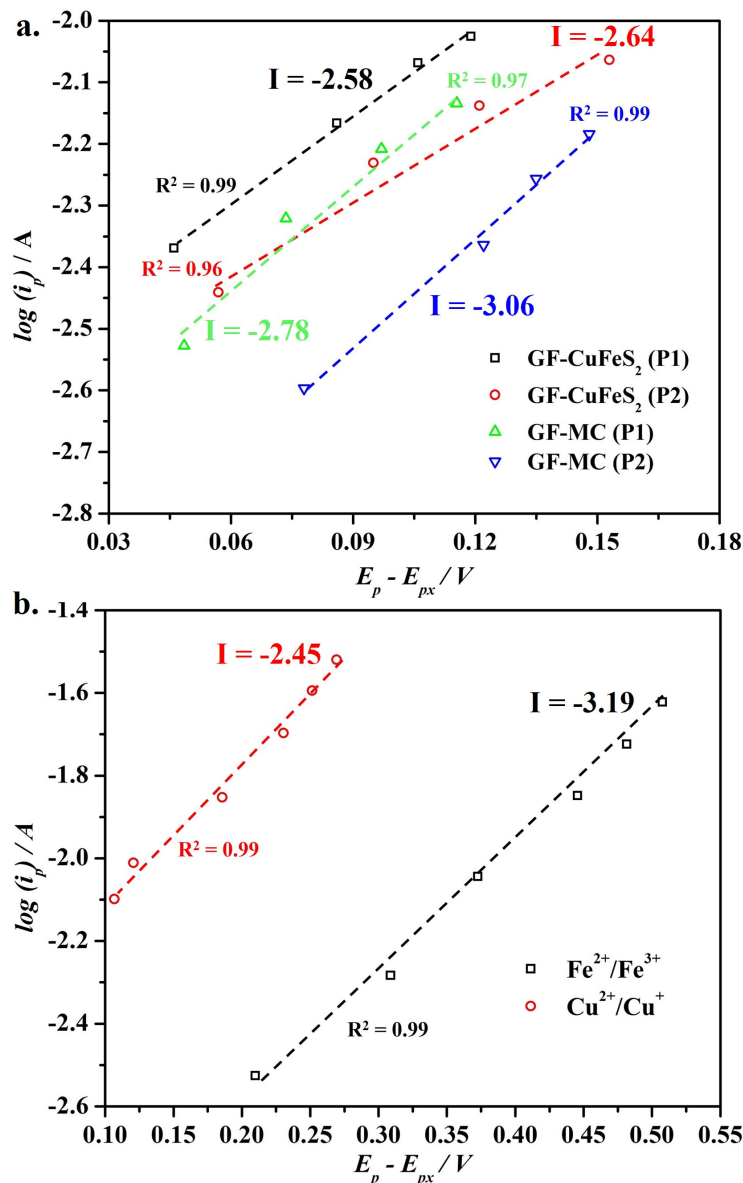


Figure 7-7 The $E_p - E_{px}$ vs. $\log(i_p)$ trends for the calculation of k_h (Equation 7.4) from the peak shift and peak current variation in the CV scans of (a) GF-CuFeS₂ and GF-MC (b) GF-Fe/Cu electrodes, where I represents the intercept on the y-axis after linear fitting of data

7.3 Estimating the energy storage capability of CuFeS₂ and MS in the FBFC

Figure 7-8 represents the cyclic voltammetry (CV) trends of the GF - CuFeS₂/GF and GF - MC/GF FBFC setups, designated as C-1 and C-2, respectively. The CV scans were obtained at various v (from 0.001 to 0.02 V s⁻¹). An increase in the peak current with an

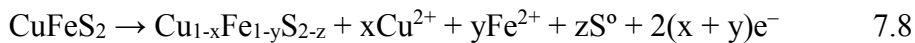
increase in ν was typically observed, which is normally associated with the rapid migration of electroactive ionic species towards the electrode surface. The anodic peak (pa) during charging indicates the oxidation of Fe^{II} in the positive half, which is driven by the reduction reactions (reactions 7.2 and 7.3) in the negative compartment of the FBFC. The reverse of these reactions during the discharge process is also reflected by the peak (pc) in the CV scans, as shown in Figure 7-8a and b. The relatively small anodic and cathodic peaks designated as a and c , respectively, are due to the oxidation of adsorbed Cu^+_{ads} species on the positive (GF) electrode (reaction 7.4).

On the negative (composite) electrode, the reduction of surface functional groups on the GF and/or sulfide sulfur species existing on the surface of CuFeS_2 and MC particles is also possible. It has been shown (section 7.2) that the peak potentials are ν -dependent and a large separation between pa and pc potentials with an increase in ν suggests the occurrence of quasi-reversible reactions on both electrodes in the FBFC. The slight decrease in anodic current density beyond pa is either related to scarcity of the electroactive species (i.e. Fe^{II} in the electrolyte and/or $\text{Cu}^{\text{I}}_{\text{ads}}$) on the GF surface (positive electrode) or to the quasi-reversible reactions on the composite (negative) electrode. This behavior can also be anticipated from the direct relation of both anodic (i_{pa}) and cathodic currents (i_{pc}) with ($\nu^{1/2}$), as shown in Figure 7-8c. The linear trends suggest the progress of diffusion-controlled processes within the porous structure of both C-1 and C-2. Since electrolytes were circulated separately at a fixed flow rate (7.5 ml/min) in both compartments in a closed-loop, and since ionic species were readily available on the surface of both electrodes, it is likely that the delay in current response is related to the kinetics of the electrochemical reactions in these cell systems. The larger anodic ($50.3 \text{ mA V}^{-1/2} \text{ s}^{1/2}$) and cathodic ($-35.7 \text{ mA V}^{-1/2} \text{ s}^{1/2}$) slopes (Figure 5c) for C-2 suggest that

kinetics of the electrochemical processes on the MC are faster than on synthetic CuFeS₂. The presence of a large amount of FeS₂ (approx. 43 %) in the MC could effectively improve the overall current response of C-1 due to the progress of reversible reactions on its surface (reaction 7.3, 7.5 and 7.6) as discussed in the literature [212, 264].



Figure 7-8d shows the variation in the peak current ratio (i_{pa}/i_{pc}) and peak separation, ΔE_p , as a function of ν . At high ν ($> 0.005 \text{ V s}^{-1}$), the $i_{pa}/i_{pc} > 1$ of the C – 1 setup is attributed to the charge consumed in the partial conversion of CuFeS₂ into Cu₂S (non-capacitive irreversible faradaic reaction) during the charging process (reaction 7.7). On the other hand, the $i_{pa}/i_{pc} < 1$ at low ν indicates the oxidation of CuFeS₂ and/or products formed during the preceding charging step (i.e. the formation of a metal-deficient sulfide film at the surface of CuFeS₂ and/or conversion of Cu₂S into CuS (reactions 7.8 and 7.9), respectively, with the possible dissolution of Cu^{II}). The large ΔE_p at high sweep rates demonstrates the quasi-reversible kinetics of the electrochemical processes in these cells. In simple words, the electrochemical response of the electrodes is delayed during repetitive charge/discharge cycles at higher sweep rates. From this behavior, it is clear that to increase the charge storage capacity and to achieve maximum Cu²⁺ dissolution, these systems should be charged and discharged at low rates i.e. 200 mA g⁻¹ and 150 mA g⁻¹ (as discussed in section 6.3).



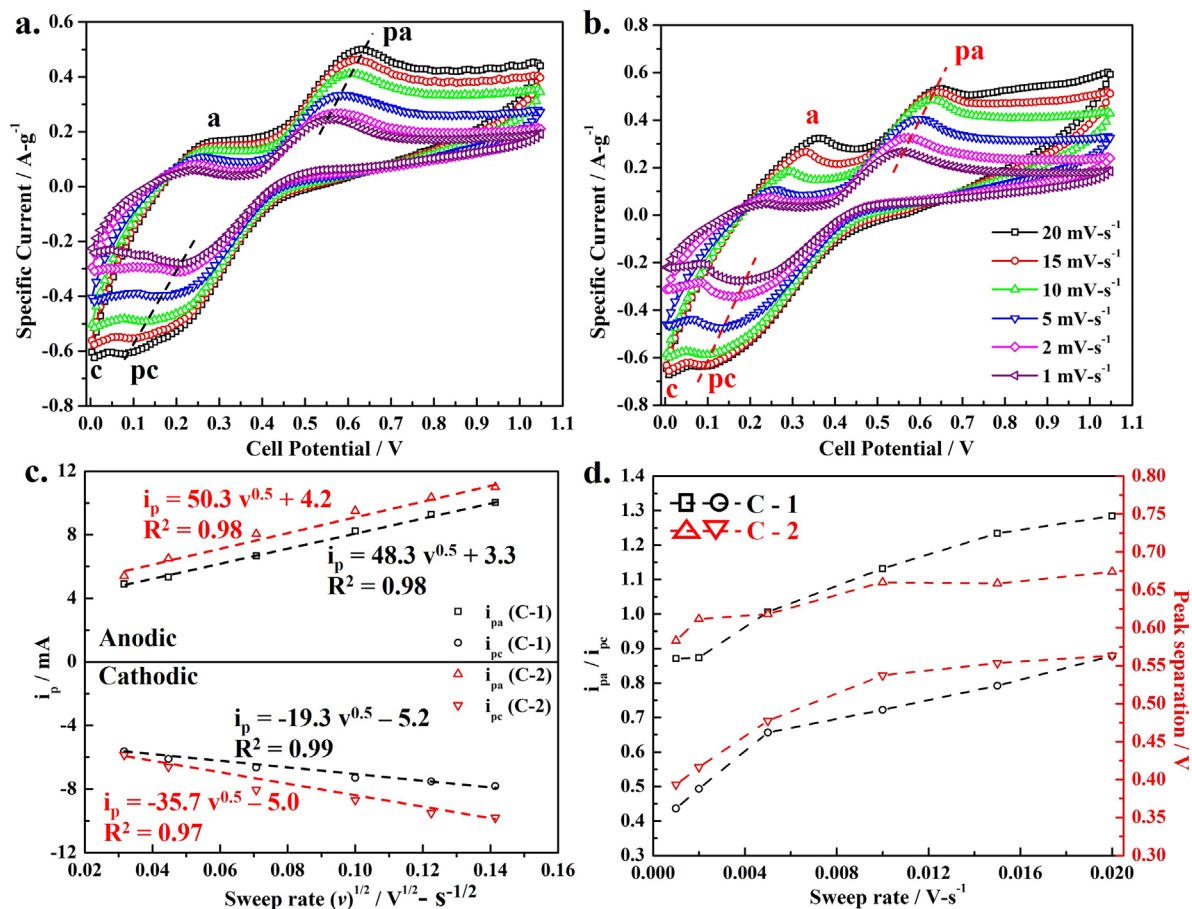


Figure 7-8 CV scans obtained for FBFC at various sweep rates when the negative electrode is (a) GF-CuFeS₂ (C-1) and (b) GF-MC (C-2), whereas the positive electrode used was GF. 0.5 M Fe²⁺ + 0.1 M Cu²⁺ in 0.2 M H₂SO₄ was circulated from the external thermostatic reservoirs. (Note: The current is normalized by the weight of either synthetic CuFeS₂ or MC) (c) The i_p vs. $v^{1/2}$ trends of the C-1 and C-2 cells (d) variation of i_{pa}/i_{pc} and peak separation due to change in sweep rate

During the discharge cycle, the availability of Fe^{III} at the surface of GF and its reductions to Fe^{II} is facilitated by the Cu^{II} species in the catholyte (reaction 7.4). The catalytic behavior of Cu^{II} in the oxidation of Fe^{II} and the concomitant improvement in the stability of Fe^{III} species have previously been discussed in Chapter 6 (Figure 6-5) [196]. By comparing the current response of the GF electrode in 0.5 M Fe²⁺ and in 0.5 M Fe²⁺ + 0.1 M Cu²⁺ solution, it is concluded that Cu^{II} and Cu^I_{ads} species, formed on the surface of GF during reversible cycling,

can enhance the current response of the Fe^{II}/Fe^{III} redox reaction (reaction 7.4) by approximately 25 %.

These reactions on the positive electrode reversibly supported by the S₂²⁻/S²⁻ redox reaction at the negative electrode of C-1 are discussed above (reaction 7.3). These are called pseudocapacitive faradaic reactions due to their reversible charge transport character. The existence of these species on the surface of as-synthesized CuFeS₂ particles has been confirmed with XPS analysis, as discussed in the next section of this Chapter.

It has also been reported that H₂S_(aq) (which may form during the charge cycle on the negative electrode via reaction 7.7) may either oxidize to elemental sulfur (S⁰) or may be reversibly transformed into S₂²⁻ species at the surface of CuFeS₂ according to reactions 7.10 and 7.11, respectively [85, 212, 225, 264]. The electrochemical response of the C-2 setup will depend on the composition of MC and presence of other sulfide minerals besides CuFeS₂, such as FeS₂. In this case, it was predicted that FeS₂ in the MC could also contribute to the charge storage capacity by promoting the occurrence of additional reversible adsorption/desorption reactions (reaction 7.5 and 7.6) on the surface.



However, the partial conversion reactions (faradaic but irreversible) in the negative electrode could definitely decrease the discharge capacity and coulombic efficiency. In simple words, the partial amount of charge consumed (during the charging step) in the conversion reactions would not be available during the discharge process. Based on the CV analyses, the decrease in ΔE_p and $i_{pa}/i_{pc} < 1$ at low sweep rates can also be used to estimate these effects in the C-1 and C-2 FBFC cells during GCD cycling.

Figure 7-9 presents the GCD plots for C-1 and C-2 obtained within a 1 V cell potential. During charging/discharging, the potential profiles reflected similar trends to those seen in the CV scans. The CuFeS_2 in the negative composite electrodes, either synthetic or in the MC, are reduced to Cu_2S (reaction 7.7) during charge cycles. The partial oxidation of the Cu_2S or unreacted CuFeS_2 in the discharge cycles dissolves Cu^{II} in the anolyte (via reaction 7.8 and 7.9) in addition with the release of stored charge/energy.

At the start of each discharge curve, the rapid fall in the potential can be quantified as $i_d R$, which includes the total potential drop across the electrode/electrolyte interface, membrane, and electrical contacts. The potential drop within the porous structure of the fixed bed electrode and quasi-reversible nature of the electrode materials may also account for the large polarization effects during initial GCD cycles. This behavior is seen by the steep discharge profiles and potential plateau at approximately 0.38 V and 0.2 V cell potential in the discharge curves, designated as x and y (Figure 7-9b and d). Due to the surface activation (discussed below) and/or formation of the sulfide sulfur species, the discharge period of both setups was also extended, which indicates the improvement in the kinetic response of the electrode materials upon repetitive GCD cycling. In C-1, the steep GCD profiles indicate activation polarization of the electrode materials as shown in Figure 7-9a and b. The sloping potential plateau at 0.5 V and 0.38 V in the charge and discharge curves, respectively, can be observed at the 250th and 500th GCD cycles. These plateaux represent the occurrence of quasi-reversible charge transfer processes on the electrode materials as confirmed from the CV results discussed above (section 7.2). The quasi-reversible nature of the electrochemical processes associated with these potential plateaux (designated as x and y) also replicate the peaks in the CV scans (Figure 7-8).

During continuous GCD cycling, the adsorption/desorption of Cu^+_{ads} species would enhance the current response of the $\text{Fe}^{\text{II}}/\text{Fe}^{\text{III}}$ redox reaction (reaction 7.4) on the positive GF electrode. This may also increase the stability of Fe^{III} ions in the catholyte [196]. This faradaic process in the positive compartment is facilitated by the redox reactions (reactions 7.2, 7.3, 7.5, 7.6, 7.10, 7.11) in the negative compartment of C-1 and C-2. However, besides these quasi-reversible reactions (pseudocapacitive, faradaic reactions), the occurrence of conversion reactions (reactions 7.7 – 7.9) cannot be neglected. These reactions are non-capacitive irreversible faradaic reactions. Below ~ 0.2 V cell potential, the descending potential plateau (y) in the discharge curves corresponds to the reversible character of the sulfide sulfur species (reaction 7.3). The reversible faradaic response of the surface species (S^{2-} , S_2^{2-} , S_n^{2-} etc.) formed on CuFeS_2 (in C-1) and/or other sulfide minerals (in the MC, C-2) during GCD cycling is reflected by the potential plateau (y). I

It was observed that in C – 1, this potential plateau in the 500th discharge curve was almost 7 times larger than the plateau in the 1st cycle (Figure 7-9b). On the other hand, the ‘y’ potential plateau was also extended (~ 3 times) after 400 GCD cycles in case of C-2, which is evident in Figure 7-9c. In contrast to C – 1, the sharp potential plateaux at 0.48 V and 0.38 V in the charge and discharge curves, respectively, were only observed in the 1st GCD cycle of C-2 (Figure 7-9c). Also, the potential plateaux below 0.2 V were also seen in the GCD plots that represent the overall faradaic (pseudocapacitive) response by the CuFeS_2 and/or FeS_2 in the MC. Interestingly, after 250 GCD cycles of the C-2 setup, an additional potential plateau at ~ 0.3 V also emerged in the discharge curves as shown in Figure 7-9d. This was most likely associated with the kinetic response of the other sulfide phases in the MC, particularly with the FeS_2 phase due to reactions 7.5 and 7.6. In both cells (C-1 and C-2), the continuous expansion

in the discharge time was directly related with the increase in specific capacity as calculated from Equation 7.6 [196].

$$\text{Specific Capacity (mAh-g}^{-1}\text{)} = \frac{i_d}{3.6m(V-i_dR)} \int_{t_1}^{t_2} V(t) \cdot dt \quad \text{Equation 7-6}$$

Where, i_d is the discharge current, m is the mass of CuFeS_2 (in the C-1 cell setup) or mass of the MC (in the C-2 cell), V is the applied cell potential and i_dR represents the potential drop at the start of each discharging cycle. The operating variable $V(t)$ corresponds to the decay in the cell potential as a function of time during the discharge cycle. The times t_1 and t_2 represent the start and end of the discharge cycle, respectively.

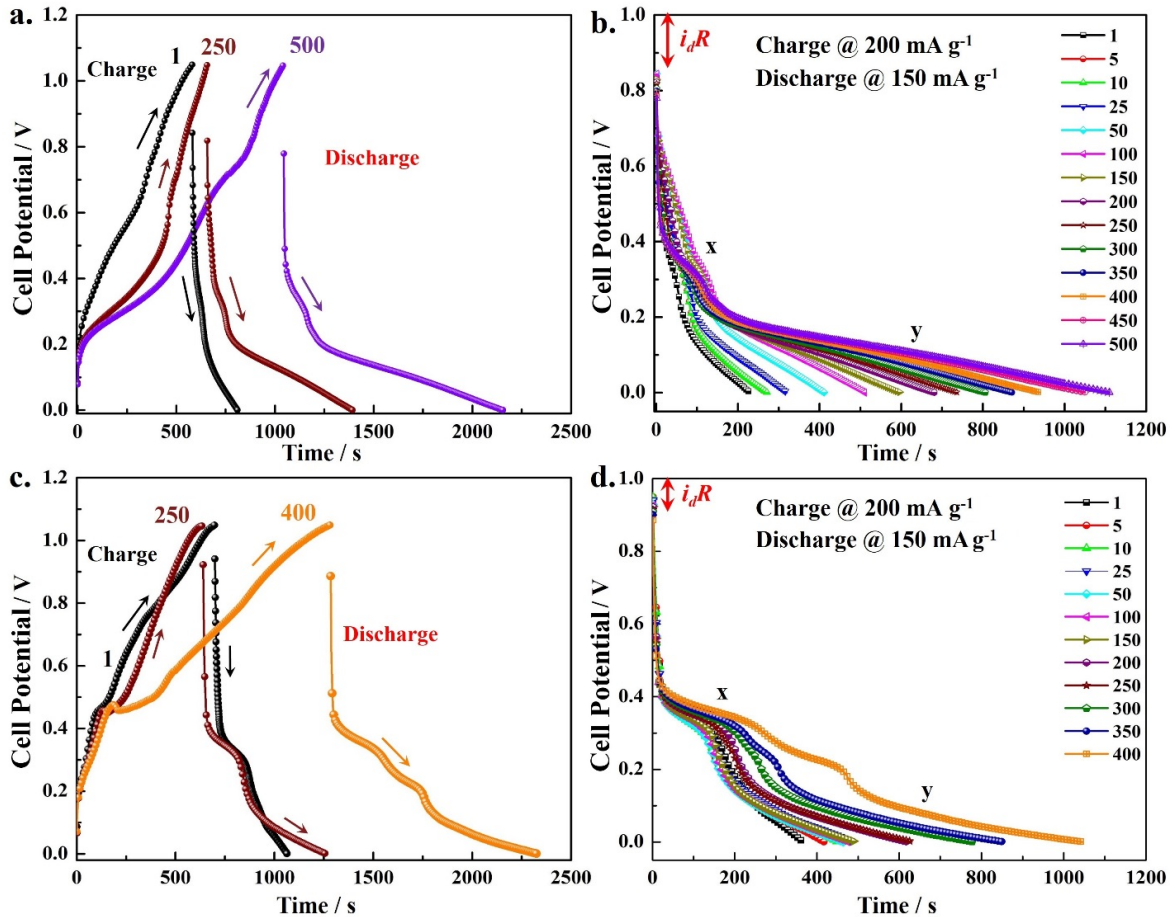


Figure 7-9 GCD tests showing the (a) 1st, 250th and 500th charge / discharge cycles and (b) discharge curves of C-1 (c) 1st, 250th and 400th charge/discharge cycles of C-2 (d) discharge profiles of C-2.

Each potential plateau attributed to the pseudocapacitive behavior of the electrode materials corresponds to the occurrence of faradaic reactions in the FBFC cells. The almost linear increase in the specific capacity of the C-1 cell over 500 GCD cycles (from 9 to 48 mAh g⁻¹) is shown in Figure 7-10a. This behavior confirms the results reported in our previous work (Chapter 6) [196]. Initially (during the first 80 GCD cycles), the discharge specific capacity for C-2 (approx. 20 mAh g⁻¹) was higher than C-1. This relatively high specific capacity for the C-2 setup was likely due to the combined effect of CuFeS₂ and FeS₂ in the MC. The specific capacity registered by the C-2 cell also remained relatively constant during the first 150 GCD cycles in contrast to the ever-increasing specific capacity of C-1 over 500 GCD cycles. In the following 150 cycles (up to 300 cycles), the specific capacity of C-2 gradually increased to ~ 30 mAh g⁻¹. The additional potential plateau (at 0.3 V) in the GCD plots for C-2 (Figure 7-9d) resulted in the monotonic increase in specific capacity as shown in Figure 7-10a.

From this behavior, it was deduced that the significant faradaic contribution of FeS₂ (reaction 7.5, 7.6) and formation of sulfide species (S²⁻, S₂²⁻, S_n²⁻ etc.) on its surface (via reaction 7.3) could enhance the reversible faradaic response of the GF-MC electrode in the C-2 cell setup. The coulombic efficiency of the C-1 setup remained constant (~80 %) over 500 GCD cycles. However, for C-2, the coulombic efficiency reached a maximum (~ 78 %) during the initial 100 cycles and it then decayed gradually to approx. 60 % in the following 300 cycles. The relatively low efficiency of C-2 compared to C-1 corresponds to the significant consumption of supplied charge via non-capacitive irreversible faradaic reactions (reaction 7.7 – 7.9). These faradaic reactions involve Cu dissolution from the MC in addition to energy storage during continuous GCD cycling.

The literature generally cites the use of FeS₂ in Li-ion batteries, which use aprotic electrolytes [265, 266]. Despite the commercialization of Li/FeS₂ batteries, the cyclic performance of this system is limited due to the progress of conversion (irreversible) reactions of Li with S in organic electrolytes [267, 268]. For instance, Choi et al. [269] reported the use of naturally sourced pyrite in Li-ions batteries and identified a decrease in specific capacity from 772 to 313 mAh g⁻¹ in 25 cycles. On the other hand, Wu et al. [162] studied the use of nanorod-shaped synthetic CuFeS₂ as an anode material in Li-ion batteries, which exhibited a maximum 865.5 mAh g⁻¹ specific capacity in the first discharge cycle and decreased ~ 60 % in the following 50 cycles.

Figure 7-10b shows the trends for specific energy, which can be stored and retrieved during charge and discharge cycles. Equation 7.7 was used to calculate the specific energy from the discharge curves [196].

$$\text{Specific Energy (Wh kg}^{-1}\text{)} = \frac{1}{3.6m} \int_{t_1}^{t_2} \Delta V(t) \cdot i_d \cdot dt \quad \text{Equation 7-7}$$

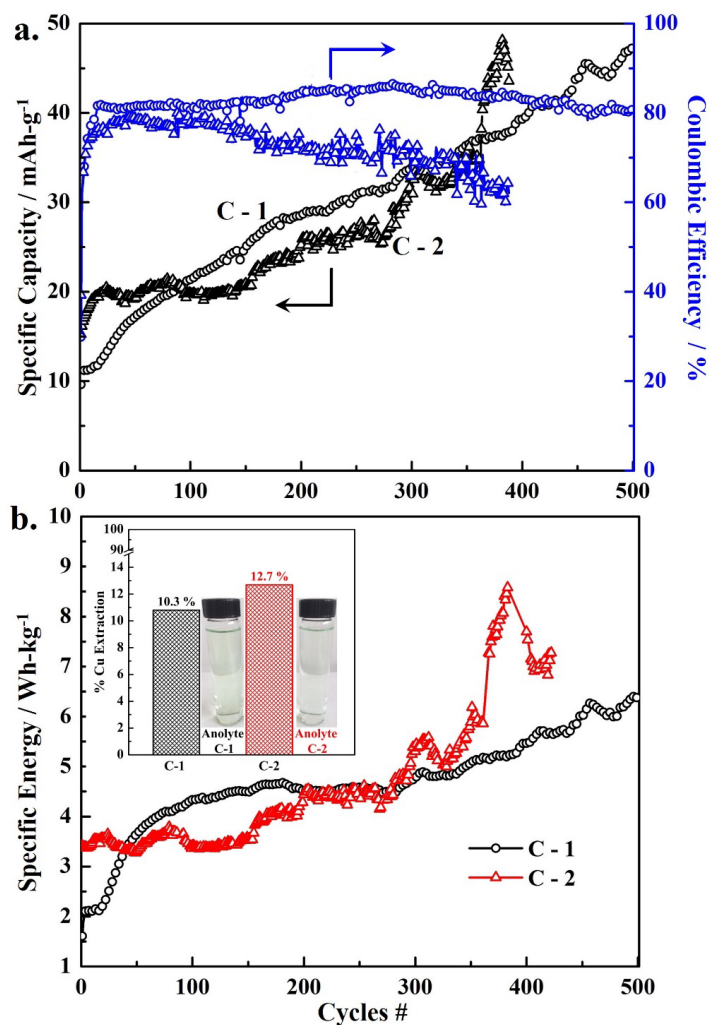


Figure 7-10 (a) Variation in discharge specific capacity and coulombic efficiency of C – 1 and C – 2 cells (b) the maximum specific energy that can be stored by C–1 and C–2 FBFC setups. The inset shows the % Cu extraction calculated based on the weight of CuFeS₂ in the C–1 and C–2 cells

The energy storage capability of C–1 rapidly increased from 2 to 4.5 Wh kg⁻¹ during the initial 100 GCD cycles followed by a gradual rise to 6.3 Wh kg⁻¹ in the succeeding 400 cycles. On the other hand, the specific energy supplied by C–2 remained relatively constant (3.5 ± 0.3 Wh kg⁻¹) during the initial 150 GCD cycles. A monotonic increase in specific energy (up to 8.5 Wh kg⁻¹) was then observed in the following GCD cycles, which corroborates the presence of the additional potential plateau in the discharge curves of C–2, as discussed above.

As evident from these results, the formation of sulfide sulfur species during repetitive GCD cycles could significantly enhance the non-capacitive response (faradaic) of the overall cell setup.

The 80 % coulombic efficiency of C-1 and appreciable decrease (~ 20 %) in the coulombic efficiency of C-2 after 400 GCD cycles is due to irreversible faradaic (conversion) reactions. To verify the dissolution of Cu via these conversions (from either the synthetic CuFeS₂ or the MC), the anolyte and catholyte concentrations were measured by ICP – OES (Varian 725–ES). The higher copper (~ 300 ppm) and iron (~ 1900 ppm) concentration in the anolyte beyond the theoretical concentration of copper that could originate from CuFeS₂ (92 ppm) or from the MC (56 ppm) (used in the negative electrode) confirmed the migration of these ionic species from the catholyte through the PEM during GCD cycling. Based on the original weight of the CuFeS₂, the percentage Cu extraction from C-1 and C-2 after GCD cycling was found to be 10.3 and 12.7 %, respectively. Copper (either because of migration from the catholyte and/or via extraction from either CuFeS₂ or MC) in the anolyte can interact with the CuFeS₂ and may specifically adsorb on its surface. It has been reported in the literature that this adsorbed Cu could also chemically activate the surface of CuFeS₂ via metathesis (reaction 7.12), which forms a covellite-type surface layer [85, 270].



Such a surface activation could significantly improve the kinetic response of the synthetic CuFeS₂, leading to an increase in the specific capacity as shown in Figure 7-10a. To verify this effect, ex-situ characterization of the CuFeS₂ retrieved from C-1, after 500 GCD cycles was also carried out as discussed below.

7.4 Ex-situ characterizations of the retrieved CuFeS₂ from the C-1 system

Figure 7-11 shows the morphology and elemental composition of the retrieved synthetic CuFeS₂. The difference in the morphology of as-synthesized (Figure 7-1a) and retrieved particles can be clearly seen. The spherical shape of the CuFeS₂ was severely damaged during GCD cycling and the clustered platelet structure disintegrated as shown in Figure 8a. EDX analysis (Figure 7-11b) also revealed a difference in the chemical composition of the retrieved and as-synthesized CuFeS₂. The depletion of Fe in the former suggests the formation of S and Cu enriched phases in the final product after cycling, which is consistent with the chemical activation of CuFeS₂ (reaction 7.12). In comparison with the as-synthesized CuFeS₂ (Figure 7-3c), the diffraction pattern revealed the formation of covellite (CuS) in the retrieved CuFeS₂. The diffraction at $2\theta = 10.8^\circ, 27.6^\circ, 29.2^\circ, 31.7^\circ, 32.8^\circ, 47.9^\circ, \text{ and } 59.3^\circ$ correspond to the (002), (101), (012), (013), (006), (110) and (116) planes, respectively, of CuS according to PDF # 96-900-0063 as shown in Figure 8c. However, the existence of CuFeS₂ (PDF # 96-901-5637) cannot be neglected due to strong diffraction signals from the (112), (220), (312) and (316) planes. The depletion of 'Fe' from CuFeS₂ as seen by the EDX analysis and the presence of the covellite phase in the XRD pattern verified the partial conversion of chalcopyrite to CuS during GCD cycling (via reactions 7.7 – 7.9).

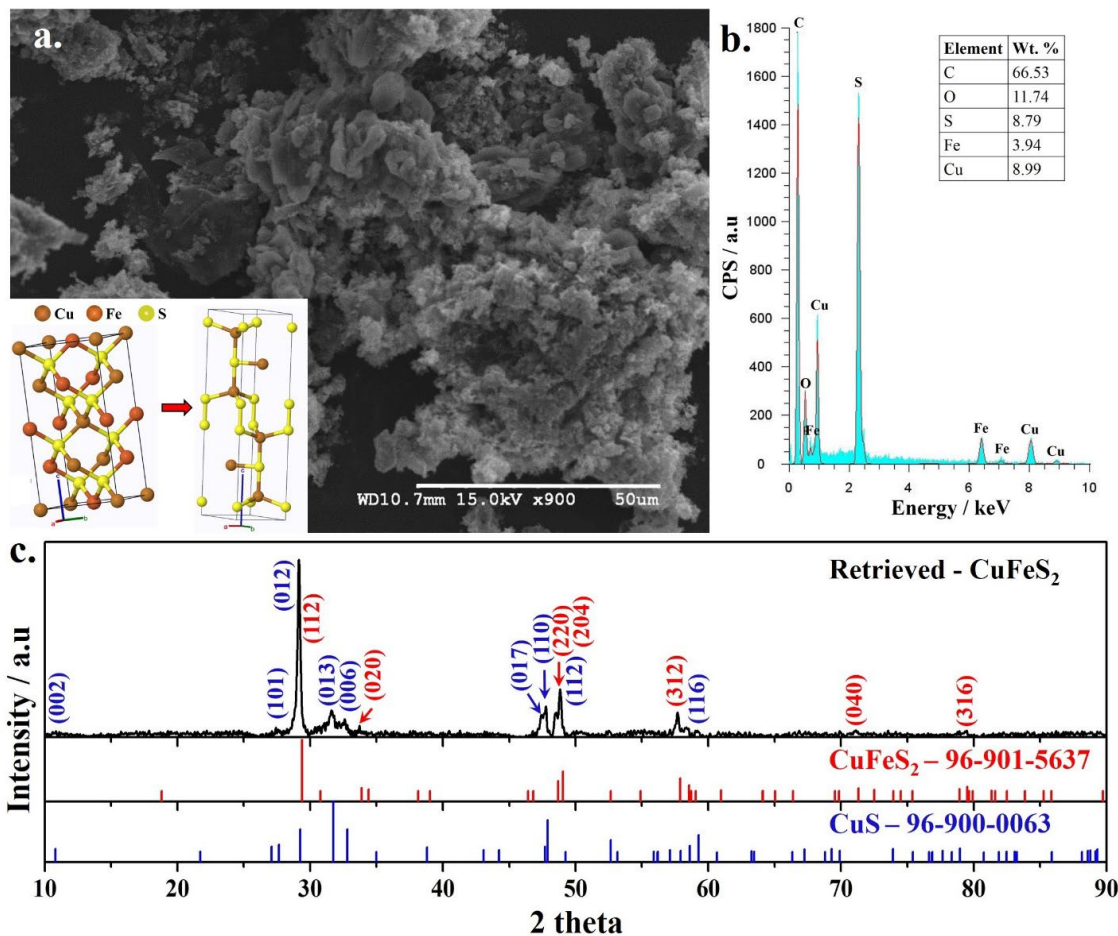


Figure 7-11 (a) SEM image of retrieved CuFeS_2 from C-1 after GCD cycling, the inset shows the lattice structure of CuFeS_2 and CuS (b) EDX spectrum shows the elemental composition (c) XRD pattern of CuFeS_2 after 500 GCD cycles

To detect the nature of the surface species formed on the surface of the CuFeS_2 particles after GCD cycling, XPS analysis was carried out and the spectra were with those obtained from the as-synthesized CuFeS_2 . The background of the spectra was subtracted via Shirley integration and the ionization states of Cu and S species was determined through deconvolution of the Cu 2p core peaks (Cu $2p_{3/2}$ and Cu $2p_{1/2}$) and S $2p_{3/2}$ peak. An 80 % Gaussian – 20 % Lorentzian function was applied to identify the degenerated sub-orbital states within these core peaks using the Peak 4.1 software package. To avoid misinterpretation of the peak position,

the experimental spectra were calibrated with the C 1s adventitious peak position (284.8 eV). The variation in the Cu 2p core peaks (compared to Cu 2p peaks of as-synthesized CuFeS₂) elucidate the effect of GCD cycling on the surface chemistry of CuFeS₂. Figure 7-12 shows the high-resolution spectra of Cu 2p and S 2p_{3/2} on the binding energy scale. The core level Cu spectra of the as-synthesized CuFeS₂ (Figure 7-12a) represents the doublet peaks at 931.85 eV and 951.65 eV which correspond to Cu 2p_{3/2} (*FWHM* = 1.61 eV) and Cu 2p_{1/2} (*FWHM* = 2.25 eV), respectively for Cu⁺ species. The shake-up satellite peak associated with the Cu²⁺ species was not observed in the high-resolution spectra of as-synthesized CuFeS₂. The peak area ratio (Cu 2p_{1/2} : Cu 2p_{3/2}) of 1.8 and the 19.8 eV difference in the binding energy of these peaks further confirms the dominant presence of monovalent Cu species in the as-synthesized CuFeS₂ [27, 247].

In the case of the retrieved CuFeS₂, after deconvolution and background fitting of the Cu 2p core peaks, an additional doublet peak (*FWHM* = 2.24) at higher binding energy (934.47 eV) was seen in Figure 7-12b. However, no change in the Cu 2p_{3/2} peak position (931.87 eV) was observed except for a slight broadening (*FWHM* = 2.00) in the peak compared to as-synthesized CuFeS₂. On the other hand, the Cu 2p_{1/2} peak shifted (~1.2 eV) to a higher binding energy for the retrieved CuFeS₂ samples. A very strong and broad (*FWHM* = 3.73) satellite peak appeared at 942.27 eV, which corresponds to divalent Cu species. The broadening of the core peaks and shift of the Cu 2p_{1/2} peak to a larger binding energy further supports the formation of Cu²⁺ species on the surface of CuFeS₂ after 500 GCD cycles. The evidence of both Cu⁺ and Cu²⁺ species on the surface of the retrieved CuFeS₂ confirms the formation of a covellite-type (CuS) phase. However, the existence of other species i.e. CuO, Cu(OH)₂ and

CuSO₄ cannot be ruled out due to the splitting of the Cu 2p_{3/2} peak and the origin of the peak affiliated with Cu²⁺ species at 934.47 eV [40, 271-273].

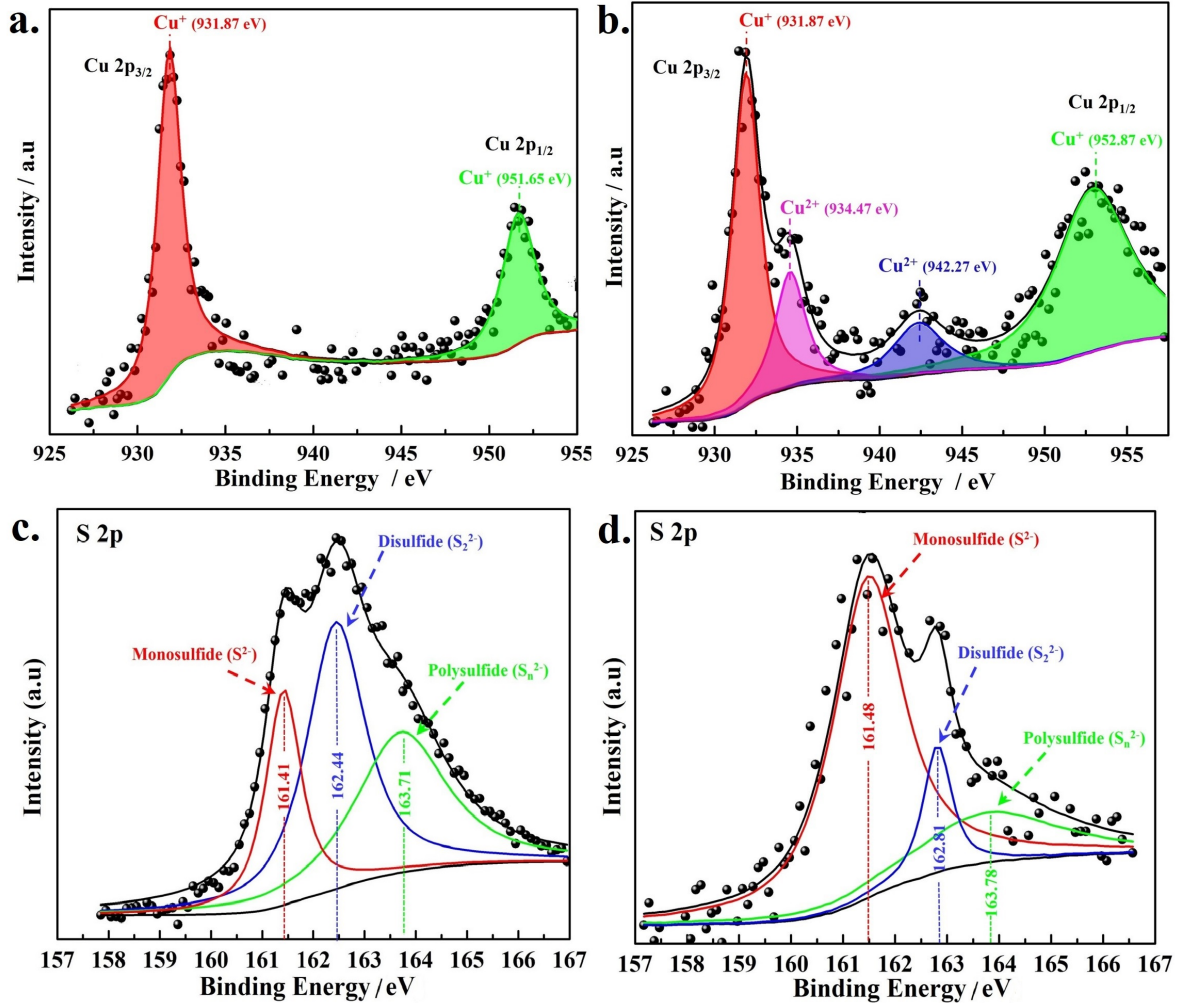


Figure 7-12 XPS core Cu 2p peaks of (a) as-synthesized and (b) retrieved CuFeS₂ particles (from the C-1 cell) show the presence of 2p_{3/2} and 2p_{1/2} spin orbitals (c) high-resolution S 2p_{3/2} peak of the as-synthesized and (d) retrieved CuFeS₂

Figure 7-12c and d show high-resolution S 2p_{3/2} spectra of the as-synthesized and retrieved CuFeS₂ sample, respectively. The S²⁻, S₂²⁻ and S_n²⁻ species were evident on the surface of as-synthesized CuFeS₂ from the splitting of S 2p_{3/2} into triplet peaks at 161.4 eV, 162.4 eV, and 163.7 eV. The S bonded with Cu and Fe atoms on the surface of CuFeS₂ may

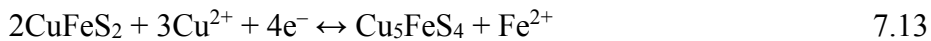
relocate and transform from S^{2-} to S_2^{2-} species through dimerization; whereas due to interband excitation of S 3p and Fe 3d sub-orbitals, the S_n^{2-} species may also form as reported in the literature [47, 245].

For the retrieved $CuFeS_2$ sample (Figure 7-12d), the variation in the peak distribution was clear and the peaks associated with the S^{2-} , S_2^{2-} and S_n^{2-} species are slightly shifted to higher binding energies compared to the as-synthesized $CuFeS_2$. From this behavior, it can be assessed that depletion of Fe from the surface of $CuFeS_2$ after 500 GCD cycles may change the binding energy of these species. Also, the peak affiliated with the S^{2-} species became more dominant, however, its binding energy (161.5 eV) was lower than the same species on CuS (161.6 eV). On the other hand, the binding energy of S_2^{2-} (162.8 eV) species and low intensity of the S_n^{2-} broadened peak at 163.8 eV are consistent with the development of a metal-deficient covellite type phase (via reaction 7.9 and/or via reaction 7.12) on the surface of $CuFeS_2$ during GCD cycling [246, 247].

It was shown that a significant amount of Cu^{II} can diffuse/migrate from the catholyte to the anolyte during GCD cycling (in addition to the Cu^{II} produced from the partial dissolution of $CuFeS_2$). Furthermore, analysis of the retrieved $CuFeS_2$ suggested the formation of an Fe deficient surface film. Therefore, it is important to elucidate the influence of Cu^{II} ions on the electrochemical behavior of the negative composite electrode (GF- $CuFeS_2$). Figure 7-13 shows potentiodynamic cathodic polarization data for the composite electrode in 0.2 M H_2SO_4 with and without Cu^{II} in solution. The cathodic polarization was used to simulate the charging cycle in the FBFC. The composite electrode was polarized from its OCP to -1.5 V (vs. OCP) at a scan rate of 1 mV s^{-1} . The OCP of the GF- $CuFeS_2$ shifted gradually from +0.47 V (in the absence of Cu^{II}) to +0.55 V (vs. SHE) with 0.07 M Cu^{2+} in 0.2 M H_2SO_4 solution.

The cathodic Tafel slope (β_c) of the composite electrode also decreased rapidly from -0.313 to -0.25 V decade $^{-1}$ with the addition of 0.02 M Cu^{2+} . At 0.07 M Cu^{2+} , the β_c decreased to -0.236 V decade $^{-1}$, as shown in the inset of Figure 7-13. This trend suggests an improvement in the faradaic response of the composite electrode with the addition of Cu^{II} . The increase in cathodic current density beyond the Tafel region and appearance of a current peak in the polarization curves is directly related to the Cu^{II} concentration. This increase in current density is consistent with results reported elsewhere [85, 92, 270] and suggests the transformation of CuFeS_2 into copper enriched phases which are more electrochemically active. This behavior also corroborates the results obtained from EDX and XPS (Figure 7-11 and Figure 7-12, respectively), which confirmed the formation of CuS in the retrieved CuFeS_2 after 500 GCD cycles.

From these results, it can also be concluded that the presence of Cu^{II} in the anolyte (either via migration from the catholyte or leached from the CuFeS_2) can improve the kinetic response of the GF- CuFeS_2 electrode and hence the overall charge storage capacity of the FBFC increases, as discussed above. Warren et al. [87] described the reduction of CuFeS_2 to bornite and chalcocite, respectively in the presence of Cu^{II} (reactions 7.13 and 7.14). In addition, the reduction of Cu^{II} to metallic Cu on CuFeS_2 can result in the formation of Cu_2S through galvanic coupling (reaction 7.15). This behavior is consistent with the improvement in the reversible faradaic response of the electrode materials in the FBFC due to the formation of Cu enriched phases.



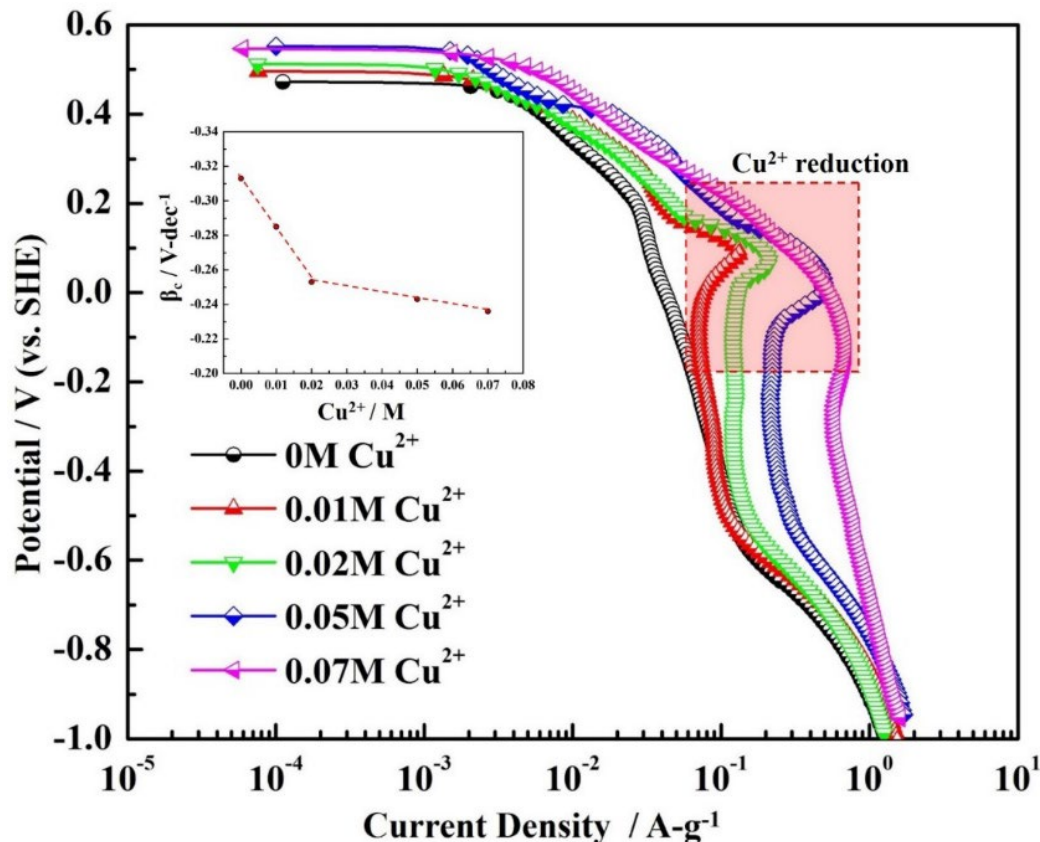


Figure 7-13 Potentiodynamic cathodic polarization of the GF-CuFeS₂ electrode in 0.2 M H₂SO₄ (anolyte) containing various amounts of Cu²⁺. The inset shows the cathodic Tafel slope (β_c) as a function of Cu²⁺ concentration.

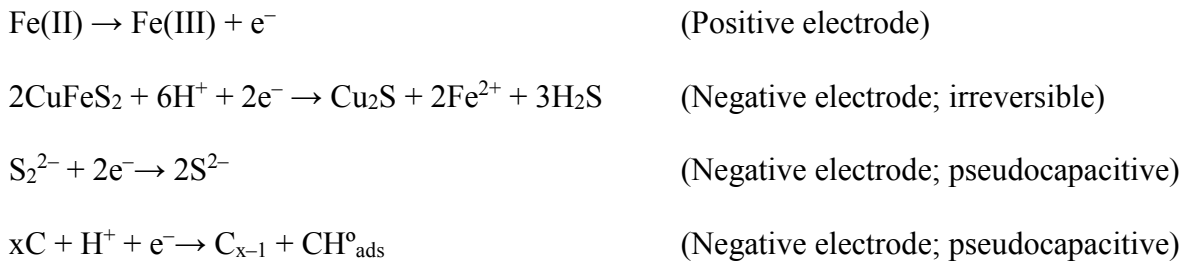
7.5 Summary

As-synthesized CuFeS₂ and MC were sandwiched in GF and used as a negative composite electrode in an FBFC. The Fe^{II}/Fe^{III} redox reaction (in the presence of Cu^{II}) in the positive compartment was used to support the charge and discharge process in this battery-like setup. The electrochemical kinetic parameters (i.e. α , D and k_h) of the GF-CuFeS₂, GF-MC and GF-Fe/Cu were also calculated from the CV scans obtained at various sweep rates. This data proved that the redox reactions in the FBFC were quasi-reversible. This was further confirmed from the quantitative values of the dimensionless heterogeneous rate constant (A)

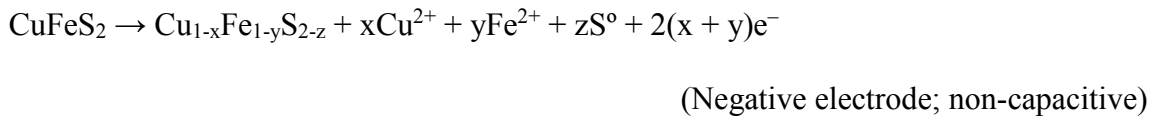
calculated experimentally from the CV data. The continuous increase in the specific capacity (~ 9 to 48 mAh g^{-1}) and energy (2 to 6.3 Wh kg^{-1}) of the C-1 setup is associated with the reversible faradaic response of the sulfide surface species (most likely $\text{S}_2^{2-}/\text{S}^{2-}$), which were formed over 500 GCD cycles. The coulombic efficiency in this setup was ($\sim 80 \%$). However, in 400 GCD cycles, the monotonic increase in specific capacity (up to 49 mAh g^{-1}) and energy (up to 8.5 Wh kg^{-1}) of the C-2 setup after 300 GCD cycles is attributed to the additional pseudocapacitive faradaic contribution of the FeS_2 in the MC. The decrease ($\sim 20 \%$) in the coulombic efficiency over 400 GCD cycles also suggested the occurrence of non-capacitive (irreversible) conversion reactions. Concurrent to the low coulombic efficiency, 10.3 and 12.7 % Cu was also extracted from C-1 and C-2, respectively, which makes these cells attractive units for combined energy storage and Cu extraction. The presence of Cu in the anolyte and ex-situ analyses of the retrieved synthetic CuFeS_2 through EDX, XRD and XPS confirmed the formation of an Fe deficient covellite phase on the surface of retrieved CuFeS_2 particles.

Also, the presence of Cu^{II} species in the anolyte significantly enhanced the current response of the composite electrode, as exhibited by the potentiodynamic cathodic polarization data. For the MC, due to the presence of other impurity phases, the exact sequence of the electrochemical reactions is difficult to deduce. However, based on the experimental observations, the following general reaction sequence in the FBFC is proposed.

Charging step:



Discharging Step:



Chapter 8: Integrating the Cu extraction and Zn electrowinning processes for energy storage¹¹

Considering that the oxidative leaching of CuFeS₂ and electrodeposition of Zn are energy intensive, the radically novel concept of coupling these two processes in one setup is described in this chapter. A TFB is introduced which is capable of electrodepositing Zn on the negative electrode and dissolving Cu from CuFeS₂ at the positive electrode. In addition, this energy storage unit can release energy during the discharge cycle, but at the expense of deposited Zn. A TFB coupled with renewable energy generating facilities, i.e. wind turbines and/or solar cells, could be an attractive technology for remote mining locations in Canada's far North or elsewhere.

The aqueous-based chemistry in this setup innately suppresses the fire hazards and other safety concerns that are specifically associated with the scale-up of Li-ions batteries for stationary applications. The cyclic charge/discharge performance with sufficient amount of Cu extraction is another compelling feature of this setup in contrast to the existing Ag-Zn and Zn-air primary batteries [19-21].

8.1 Physical characterization of the electrode materials

The morphology of the as-synthesized CuFeS₂ was of spherical-shaped particles having an open porous structure, as shown in Figure 8-1a. Under applied conditions, the reduction of Cu^{II} to Cu^I and oxidation of thiourea into carbamide and Fe^{II} into Fe^{III} species would promote the formation of Cu^I+Fe³⁺S₂²⁻ according to reaction 8.1, as reported in

¹¹ The results in this Chapter are submitted for publication

Chapter 7. It is well recognized that Cu and Fe in CuFeS_2 retain +1 and +3 oxidation states, respectively [274, 275].

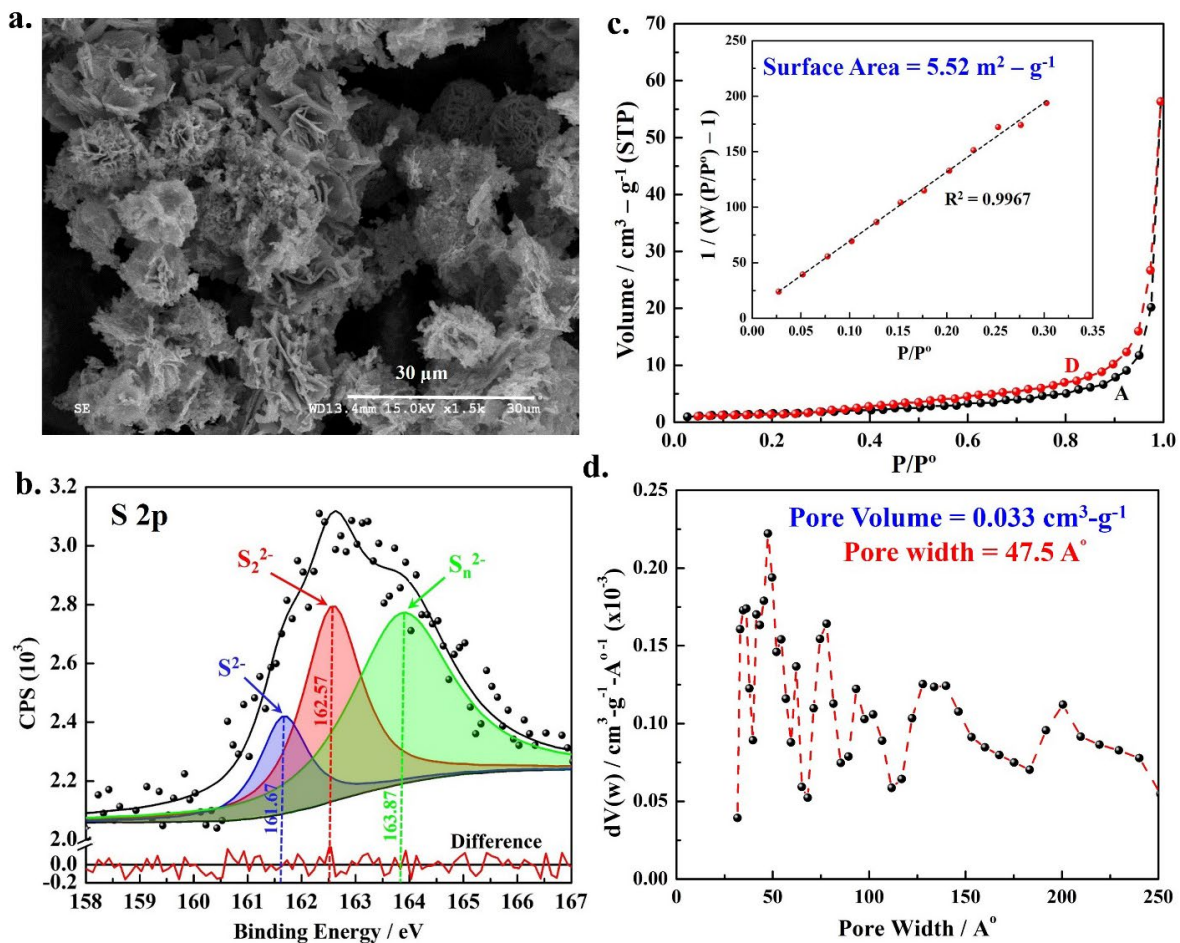
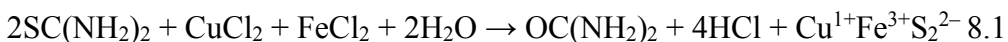


Figure 8-1 (a) SEM image showing the morphology and (b) Deconvoluted S 2p_{3/2} high-resolution spectra of synthetic CuFeS_2 . (c) N_2 adsorption/desorption isotherm for surface analysis and (d) multi-pore size/volume analysis curve of CuFeS_2 particles

The XRD pattern of the synthetic product confirms the formation of pure CuFeS_2 according to the reference pattern (*PDF # 37 – 0471*) (Figure 8-2a) as discussed in section 5.1 and reported elsewhere [276]. No peak associated with any impurity phases was detected in the diffraction pattern.

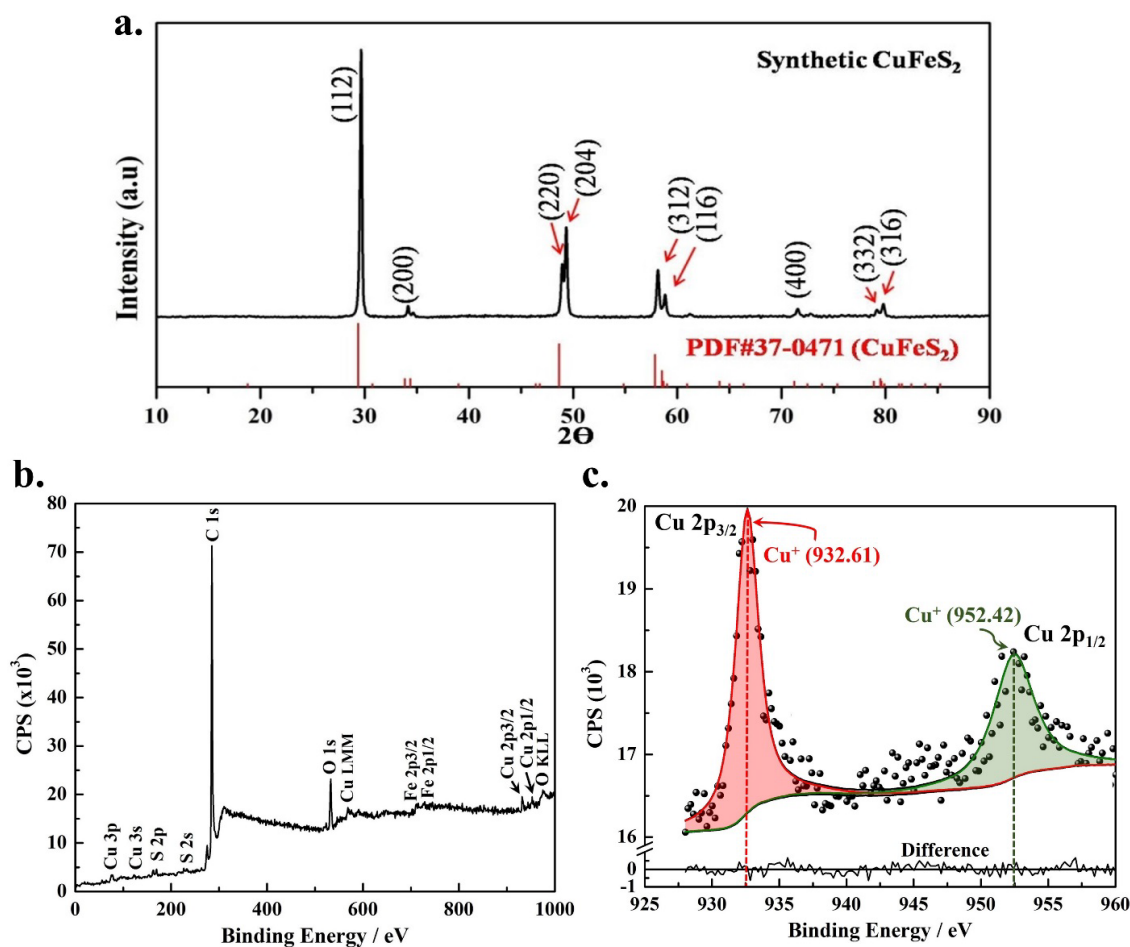


Figure 8-2 (a) XRD pattern (b) XPS survey scan and (c) the deconvoluted high-resolution spectra of Cu 2p_{1/2} and Cu 2p_{3/2} bands of as-synthesized CuFeS₂

Figure 8-2b presents the XPS survey spectrum of synthetic CuFeS₂ on the binding energy scale. Conforming to the XRD pattern, the only characteristics peaks associated with the Cu, Fe, and S were evident in the survey spectrum. The origin of C 1s (284.94 eV) and O 1s (531.75 eV) peaks was associated with the surface contaminants and to the airborne surface oxidation of CuFeS₂. The C 1s adventitious peak typically at 284.8 eV is used as a reference for peak positioning and to evaluate any surface charging effects during XPS measurement. The small deviation of C 1s peak at higher binding energy (0.14 eV) may also be related to the satellite signals arising from the delocalized electrons associated with the surface functional

groups, particularly aromatics species [277]. The S $2p_{3/2}$ core peak after background subtraction and deconvolution splits into three peaks representing the nature of the sulfide sulfur species present on the surface of CuFeS_2 as shown in Figure 8-1b. The doublet peaks at 161.67 eV and 162.57 eV are associated with the monosulfide (S^{2-}) and disulfide (S_2^{2-}) species. The 1.1 eV difference in the binding energy of these doublet peaks is related to the partially coordinated sulfur species [278]. The relatively larger full width at half maximum ($FWHM = 1.293$ eV) and intensity of the S_2^{2-} peak, as compared to S^{2-} ($FWHM = 1.072$ eV) peak also indicates the dimerization of the later species through physical relocation of S bonded directly with the Cu and Fe atoms in the crystal lattice of CuFeS_2 [196, 225, 278]. The excitations of photoelectrons from S $3p - \text{Fe } 3d$ inter-bands may occur as a broad satellite peak observed at 163.87 eV ($FWHM = 2.207$ eV) and correspond to the existence of polysulfide (S_n^{2-}) species at the surface [45, 278]. The high-resolution core Cu $2p_{3/2}$ and Cu $2p_{1/2}$ peaks at 932.61 eV ($FWHM = 2.043$ eV) and 952.42 eV ($FWHM = 3.626$ eV) is due to Cu^+ species (Figure 8-2c). The binding energy of these peaks is slightly higher than the reported values in the literature (932.4 and 952.1 eV) [247, 278]. However, no satellite peak associated with divalent Cu^{2+} was observed (this usually appear at 942 eV). These results are in agreement with the literature and they confirm the monovalent state of Cu atoms in the CuFeS_2 lattice structure [45, 196, 247, 274, 279].

Surface morphology can significantly affect the electrochemical response of synthetic CuFeS_2 . Therefore, the specific surface area, pore size and distribution were measured from the N_2 adsorption/desorption isotherms as shown in Figure 8-1c. For the specific surface area, the physisorption isotherms were transformed into the BET plot shown in the inset of Figure 8-1c. The multipoint BET method was used within the relative pressure (P/P^0) range of 0.025

– 0.30 to calculate the sorbed N₂ monolayer capacity, (W_m) according to Equation 8.1 [275, 280]. A linear trend between P/P^o and $1/(W(P/P^o) - 1)$ was found within this P/P^o range. The positive slope ($s = 623.3$) and intercept ($i = 7.21$) were calculated by linear regression with an acceptable correlation factor of 0.997.

$$\frac{1}{W[P/P^o - 1]} = \frac{C-1}{W_m} \left(\frac{P}{P^o} \right) + \frac{1}{CW_m} \quad \text{Equation 8-1}$$

In this equation, C is the BET constant which exponentially depends on the monolayer adsorption energy, W is the experimentally measured weight of the adsorbed N₂, P and P^o are the equilibrium and saturation pressures, respectively. The corresponding values of C, W_m and specific surface area (S) were calculated from Equation 8.2, Equation 8.3, and Equation 8.4.

$$C = 1 + \frac{s}{i} \quad \text{Equation 8-2}$$

$$W_m = \frac{1}{s+i} \quad \text{Equation 8-3}$$

$$S = \frac{N_A \cdot s \cdot W_m}{V \cdot W_{CuFeS_2}} \quad \text{Equation 8-4}$$

Where N_A is the Avogadro's number, V is the volume of gas adsorbed and W_{CuFeS₂} is the initial mass of CuFeS₂ sample after degassing. From these calculations, the specific surface area of the as-synthesized CuFeS₂ was found to be 5.52 m² g⁻¹. It is important to note that the synthetic CuFeS₂ used in this study has a relatively larger surface area than the synthetic CuFeS₂ used in Chapters 5 and 6.

As shown in Figure 8-1c, the hysteresis loop formed at low relative pressure ($0.4 < P/P^o < 0.8$) confirms the presence of fine size pores on the surface of CuFeS₂. However, at large relative pressure ($0.8 < P/P^o < 1$), the hysteresis loop indicates porosity in the inter-aggregated particles. This behavior is also evident in the pores distribution curve as shown in Figure 8-1d. The pore size/volume was calculated from the adsorption/desorption isotherms

using DFT which is a reliable method for pore size analysis at the nanoscale [280]. The adsorption/desorption curve was used to calculate an average pore size of $\sim 47.5 \text{ \AA}$, which is consistent with the mesoporous surface structure of as-synthesized CuFeS_2 particles. As evident in the SEM image (Figure 8-1a), the hysteresis loop observed at $P/P^o < 0.8$ (Figure 8-1c), and multimodal distribution of pore sizes in Figure 8-1d confirm the formation of variable dimension pores on the surface of spherical CuFeS_2 particles. The specific pore volume is $0.033 \text{ cm}^3 \text{ g}^{-1}$, and this value represents the total specific pore volume that may include the volume of variable size surface and inter-particulate porous network developed during synthesis and/or by the agglomeration of the fine particles after drying.

8.2 Reaction sequence and optimization of the process conditions

Initially, the electrochemical behavior of both positive and negative electrodes was evaluated from CV scans obtained separately in a three-electrode cell setup. To simulate the actual charging/discharging scenario in the TFB, the CV curves of GP and other slurry constituents were acquired by sweeping the potential in the positive direction to facilitate oxidation reactions before reversing the scan in the negative direction. The three-electrode cell setup used to study the electrochemical performance of a positive slurry electrode is schematically shown in Figure 8-3a. The minimal current response by GP in $0.2 \text{ M H}_2\text{SO}_4$, as shown in Figure 8-4a, confirms its negligible contribution in the overall charge/discharge process. However, with the addition of AC in $0.2 \text{ M H}_2\text{SO}_4$, large anodic and cathodic specific currents were observed. For instance, at 0.4 V (vs. SHE) , the specific current of $\sim 20 \text{ mA-g}^{-1}$ registered by the GP-AC electrode was approximately 10 times higher than for the GP electrode. This overall current response was attributed to the sum of the current contributions by the non-faradaic (double layer charging/discharging), and faradaic (charge transfer)

processes occurring on the surface of AC. The large specific current response of AC is related to its high surface area ($2545 \text{ m}^2 \text{ g}^{-1}$) and fine platelets-like morphology as shown in Figure 8-3b.

Multipoint BET surface area and pore size distribution were also determined from the N_2 adsorption/desorption isotherm of the AC sample. The pore size distribution curve (Figure 8-3c) shows the mesoporous structure of AC (pore width $< 2.5 \text{ nm}$). The large specific surface area and pore volume ($1.24 \text{ cm}^3 \text{ g}^{-1}$) could enhance the charge storage capacity of the positive electrode as manifested by the large anodic and cathodic current response in the CV scan (Figure 8-4a). The broad peaks observed at 0.71 and -0.24 V (vs. SHE) validate the occurrence of faradaic processes (pseudocapacitive behavior) at the surface of AC in sulfuric acid solution. These peaks are most likely affiliated with surface functional groups which may oxidize and reduce in the presence of H^+ and/or HSO_4^- in a reversible manner (pseudocapacitive behavior) as reported in the literature [202, 281, 282].

With the addition of synthetic CuFeS_2 , the current response of the positive slurry electrode (PSE) composed of GP-AC- CuFeS_2 was significantly affected (Figure 8-4a). The cyclic behavior of GP-AC- CuFeS_2 was measured from the CV scans obtained at 5 mV s^{-1} . Multiple anodic and cathodic peaks were evident in the forward and reverse scans, respectively, corresponding to the oxidation and reduction reaction on CuFeS_2 in synergism with the pseudocapacitive response of AC. During the 1st cycle, the anodic and cathodic currents were found to be slightly higher than observed in the rest 4 cycles, as shown in Figure 8-5a and b. The current peaks originated during forward and reverse CV scans are also labeled. The rapid initial increase in current and origin of peak A at $0.53 \text{ V}_{\text{SHE}}$ corresponds to the partial oxidation of CuFeS_2 into sulfide enriched surface species via reaction 8.2.

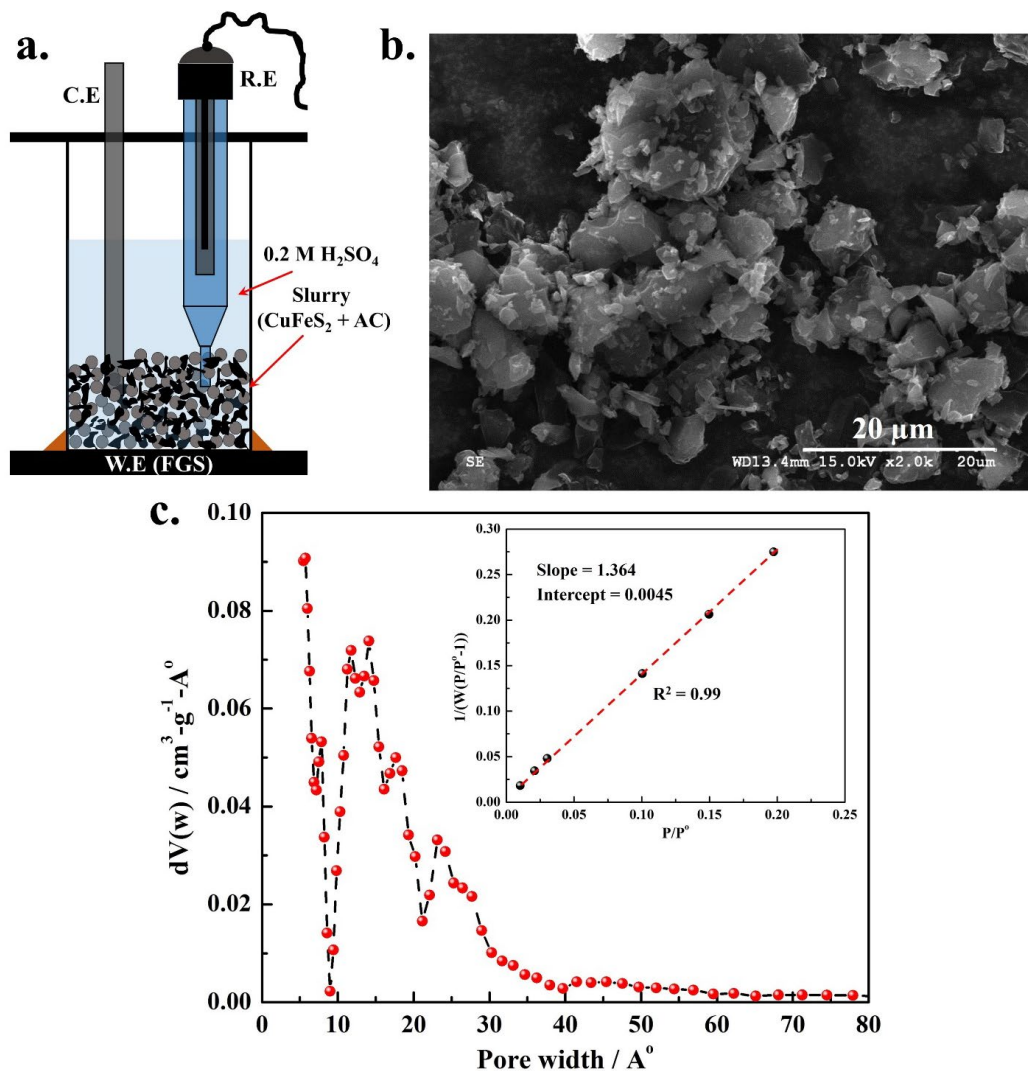
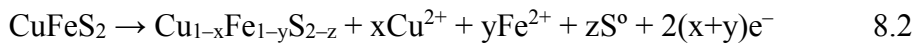


Figure 8-3 (a) A three-electrode setup for measurement of electrochemical behavior of the PSE containing (80 wt. % CuFeS_2 + 20 wt. % AC) in 0.2 M H_2SO_4 . (b) SEM image of AC (c) Multipoint BET surface area and pore size distribution curve for AC

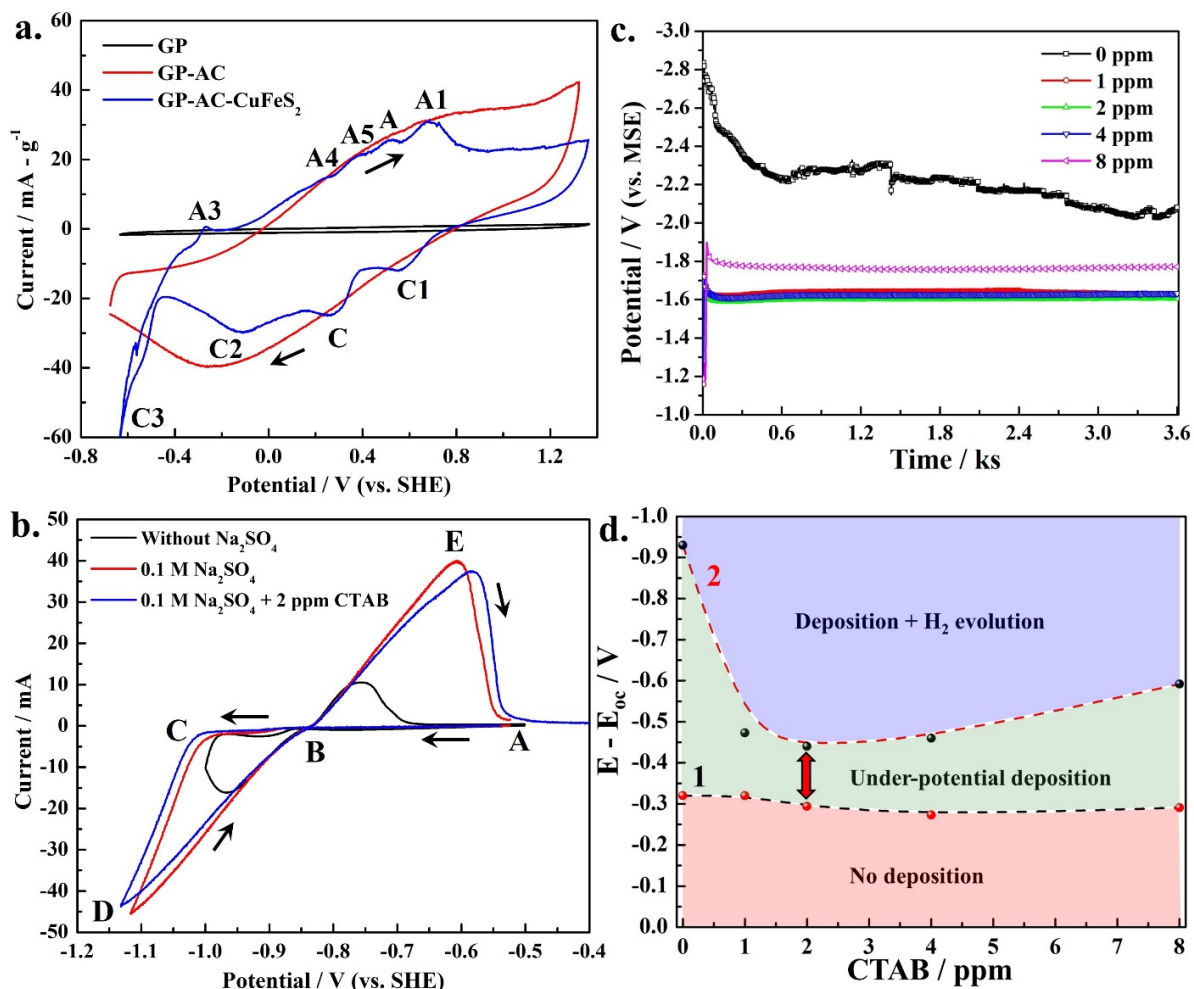
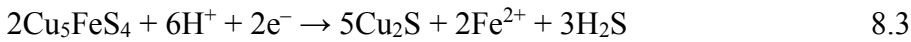


Figure 8-4 (a) CV (4th cycle) of positive electrode components; GP, GP-AC and GP-AC-CuFeS₂. (Note: exposed area of GP = 6.28 cm², 20 wt. % total solids in the slurry) (b) CV curves of negative electrode (Al strip ≈ 2 cm²). (c) Chronopotentiometry scans (30 mA cm⁻²) depicting the effect of CTAB concentration in the anolyte (vs. MSE = 0.62 V_{SHE}) (d) a potential/concentration (PC) diagram developed from the CV and chronopotentiometry results.

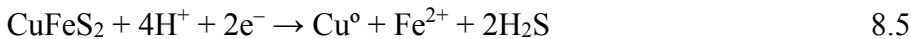
With an increase in potential, peak A1 is observed at 0.69 V_{SHE} and is related to the oxidation of surface functional groups present on AC [211]. Following this peak, a limiting current response up to 0.9 V_{SHE} is obtained and it corresponds to the formation of a passive film on the surface of CuFeS₂, which is composed of Cu_{1-x}Fe_{1-y}S_{2-z} and S⁰ species [196, 278]. These

species can form as a thin layer on CuFeS₂, and a limiting current below 0.9 V_{SHE} corresponds to its barrier characteristics. During the reverse scan, the current increased in the cathodic direction and the appearance of current peak C1 (at 0.56 V_{SHE}) corresponds to the reduction of surface functional groups on AC.

As discussed in the literature on the behavior of carbon-based materials in acids, the set of anodic and cathodic peaks centered at ~0.6 V_{SHE} are normally associated with the oxidation-reduction of surface functional groups [211, 283]. The reduction of reaction products formed at peak (A) results in the detection of the current peak (C) at 0.31 V_{SHE} during the reverse scan. The large decrease in reduction current at peak C and a current plateau observed within 0.37 – 0.1 V SHE indicates the partial conversion of CuFeS₂ into other intermediate species i.e. talnakhite (Cu₉Fe₈S₁₆) and bornite (Cu₅FeS₄) [87]. However, further decrease in cathodic potential resulted in the broad peak (C2) at –0.12 V_{SHE}, which corresponds to the removal of Fe from the lattice and bornite and/or CuFeS₂ is converted into chalcocite (Cu₂S) (reaction 8.3 and 8.4) [32].



At negative potential, below –0.43 V_{SHE}, the rapid increase in current can be attributed to the simultaneous reduction of CuFeS₂ into metallic copper Cu⁰ (reaction 8.5) and H₂S evolution.



Upon positive return of the scan from –0.65 V_{SHE}, a sharp anodic peak A3 observed at –0.27 V_{SHE} is consistent with the oxidation of previously-formed Cu⁰ (at peak C3) by reaction with dissolved H₂S and conversion into Cu₂S via reaction 8.6. During the forward scan beyond peak A3, the current increases almost linearly with potential shift with the development of multiple

peaks (A4 and A5) at 0.23 and 0.37 V_{SHE} which are consistent with the oxidation of H₂S and Cu₂S into S⁰ and Cu_{2-x}S species, respectively according to reaction 8.7 and 8.8 [32, 87, 92, 284].



The high current response of GP-AC-CuFeS₂ was supported by the pseudocapacitive behavior of AC in the slurry, which may possibly enhance the kinetics of redox reactions during cyclic charge/discharge. However, the occurrence of non-capacitive faradaic reactions on the surface of CuFeS₂ could decrease the overall current response during repetitive oxidation/reduction processes, as revealed by the variation in the current response of five repetitive CV cycles (Figure 8-5a). It is reported that Cu₂S formed during the cathodic scan (a simulation of discharge cycle in a TFB) could transform to various non-stoichiometric intermediate products i.e. Cu_{2-x}S with the generation of Cu²⁺ in the following forward scan (the charge cycle in a TFB). This repetitive charge/discharge process would thus facilitate Cu extraction from the refractory CuFeS₂ aside with energy storage. Mixing CuFeS₂ with AC, in the form of a slurry, significantly enhances its charge storage capacity and Cu extraction during cyclic charge/discharge processing. This behavior was predicted from the large anodic and cathodic current response (large loop) and current peaks in the CV scans.

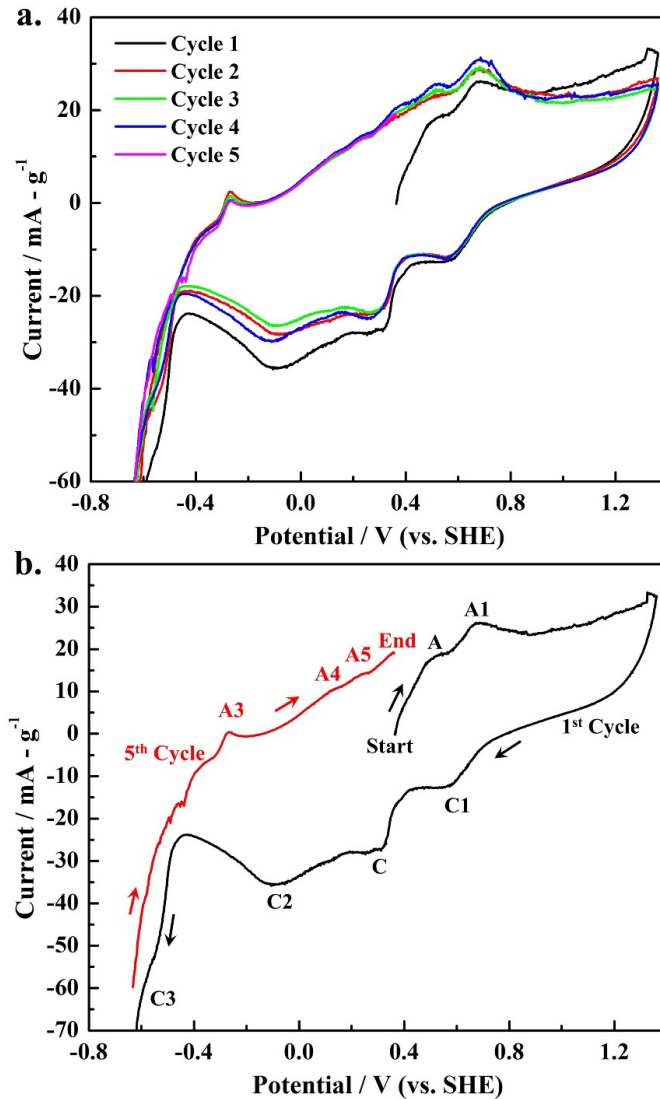


Figure 8-5 The CV of the PSE (5mV s^{-1} sweep rate). (a) The cyclic performance of the positive electrode (5 cycles). (b) The 1st and 5th cycles show the current peaks (as labeled) used to predict the reactions sequence during actual charge/discharge process in the TFB.

Industrially, Zn electrowinning is carried out by depositing Zn on Al from pure acidic zinc sulfate leach solution. Most cationic impurities are removed via purification processes before the electrowinning step to improve the process current efficiency and morphology of the Zn deposit. To increase the ionic conductivity and to avoid an excessive potential drop, Na_2SO_4 was added here as a supporting electrolyte. To evaluate the influence of the supporting

electrolyte (0.1 M Na₂SO₄) and addition of cationic surfactant (CTAB) in 100 g⁻¹ Zn²⁺ + 0.2 M H₂SO₄, CV and GS scans were obtained, and they are shown in Figure 8-4b and c, respectively. An apparent increase in the charge (Zn deposition) and discharge current (stripping) was observed with the addition of 0.1 M Na₂SO₄ in 100 g⁻¹ Zn²⁺ + 0.2 M H₂SO₄ as pictured in Figure 8-4b. These results show the effectiveness of Na₂SO₄ addition on the Zn deposition and stripping process. Moreover, the addition of Na₂SO₄ in the electrolyte also decreases the IR drop in the electrolyte and improves the kinetics of the Zn/Zn²⁺ couple [285].

CV scans were initiated from point A (Figure 8-4b), which arbitrarily corresponds to the OCP of Al in each electrolyte. Sweeping the potential in the negative current direction, toward point C, resulted in a negligible increase in reduction current. The abrupt increase in current to point D with a slight increase in potential from point C (plating overpotential) indicates the commencement of Zn deposition. Upon reversal, the current approached a maximum (point E), preceded by zero current at point B (crossover potential). The origin of the anodic peak at point E and the following decay in current is attributed to the complete re-dissolution of Zn. At the same potential, the higher current during the positive scan (from D to B) compared to the negative scan (point C to D) also highlights the availability of a large number of dissolving nuclei on the Al substrate during the stripping process. In these scans, the nucleation hysteresis (BCD) and stripping hysteresis (BEA) were greatly affected by the added Na₂SO₄ and CTAB. For example, the addition of 2 ppm CTAB shifted the nucleation potential (point C) to more negative potential. Similarly, the anodic peak (point E) also moved toward more positive potential in the presence of CTAB which indicates a slight increase in the hindrance of Zn re-dissolution. In the absence of CTAB, the relatively small stripping hysteresis in Na₂SO₄ is related to the charge consumed by the parasitic H₂ evolution reaction

during Zn deposition. Also, no shoulder cathodic peak between point B and C was observed in the presence of CTAB, which is consistent with minimal H₂ evolution on the electrode surface [286]. Uniform growth of the Zn deposit happened in the diffusion-controlled regime of the CV curve at potential that is more negative than point C.

The effect of CTAB in 0.1 M Na₂SO₄ was investigated by GS tests as shown in Figure 8-4c. It was evident that in the absence of CATB, the deposition proceeded at a very negative potential (−1.38 V_{SHE}). However, with the addition of CTAB, Zn deposition took place at less negative potential. The least negative deposition potential (−0.98 V_{SHE}) occurred at 2 ppm CTAB. The importance of CTAB can be seen in the potential/concentration (PC) diagram in Figure 8-4d. In this diagram, line–1 represents the nucleation overpotential and line–2 represents the deposition potential. These were obtained separately from the CV and GS test, respectively. Point A is the OCP of the Al substrate in each solution. Zn nucleation begins beyond the crossover potential (point B); and uniform growth, along with H₂ evolution, occurs once the potential becomes more negative than point C, as depicted in Figure 8-4b. In the region below line–1, which is the potential difference between point A and B in the CV scans, there are very minimal chances for Zn nucleation and this is thus designated as the ‘*no deposition*’ region. Above this line (beyond crossover), there are a fair chance of Zn nuclei formation and this region is referred to as ‘*under-potential deposition*’.

From the GS tests conducted at 30 mA cm^{−2} (Figure 8-4c), steady-state potential values were measured after 1 h of polarization in the presence of various CTAB concentrations, and these are shown as a line–2 in Figure 8-4d. At potentials more negative than line–2, one can expect uniform Zn deposition with possible H₂ evolution. The relatively large nucleation and deposition overpotentials (> −0.5 V) (relative to *E*_{OCP}) below 2 ppm CTAB concentration are

directly related to the cell potential and therefore suggested the requirement for a large energy input for Zn deposition. The lowest deposition overpotential (-0.44 V) at 2 ppm CTAB indicated that nucleation and growth of Zn crystallites on the Al substrate would be most favorable, with less energy consumption, which is always desirable for an efficient energy storage system. An additional increase in CTAB concentration > 2 ppm, the minor effect on the nucleation overpotential was observed (line-1 in Figure 8-4d). However, the deposition overpotential values increased further with the addition of 4 and 8 ppm CTAB (line-2). It is well known that with an increase in CTAB concentration, which is above the critical micelle concentration (CMC) > 1 mM (in water at 25 °C), micelles may form multilayers on the cathode surface and may increase the overpotential for Zn deposition [287, 288]. Moreover, at low concentration, it is expected that CTAB may dissociate into cetrimonium cations, which may adsorb specifically on the active sites during Zn deposition and effectively suppress dendrite formation and H_2 evolution. With the increase in CTAB concentration > 2 ppm, the surface coverage by cetrimonium cations restricted the Zn^{2+} deposition on the cathode surface as exhibited by < 90 % current efficiency.

Figure 8-6a–e presents the morphology of the Zn deposits formed without and in the presence of CTAB. The localized growth of Zn in the form of flake-type crystal clustered in pyramidal-shape morphology shows the development of dendritic structure in the deposit without CTAB addition (Figure 8-6a). These crystals were branched in multi-directions, indicating the non-uniform current distribution at the surface during electrodeposition. However, in the presence of CTAB, the cetrimonium cation species are expected to adsorb on the active sites and may hinder localized dendritic crystal growth. In this way, the cationic micelles may also tailor the orientation of growing crystals in the Zn deposit and restrict

undesirable dendritic growth [114, 289, 290]. At low (1 ppm) CTAB concentration, coarse multi-faceted crystals containing small pores were deposited on the Al substrate. These pores may form due to the generation of H₂ bubbles at the local active sites which may disrupt the continuity of the deposit.

The current efficiency of Zn deposition during GS tests was increased to 90.83 % from 83.7 % with the addition of 1 ppm CTAB and 0.1 M Na₂SO₄. Further increase in the CTAB concentration from 1 to 2 ppm improved the current efficiency to 92.3 %. A smooth and refined polycrystalline structure was developed in the presence of 2 ppm compared to 1 ppm CTAB. The fine platelet-like crystals were formed and oriented in various crystallographic directions as shown in Figure 8-6c. However, at the high CTAB concentration (4 and 8 ppm), a coarse-grained structure and porosity in the deposit were visible (Figure 8-6d and e). The current efficiency at these CTAB concentrations also decreased to 89.1 and 88.8 %, respectively. This behavior is due to parasitic H₂ evolution or possibly due to the preferential adsorption of cetrimonium species at the active sites that may restrict Zn deposition if present in large amounts.

The influence of CTAB concentration on the orientation of crystal growth was further evaluated through XRD patterns as shown in Figure 8-6f. In the presence of CTAB, the major diffraction peaks were observed at 36.3°, 39.0°, 43.2°, 54.3°, 70.0°, 70.7°, 82.1° and at 86.6° corresponds to the (002), (100), (101), (102), (103), (110), (112) and (201) planes, according to standard pattern (JCPDS card no. 00-004-0831) and these are in agreement with the literature [286, 291, 292]. However, variations in the peak intensities represent preferential orientation of the crystals.

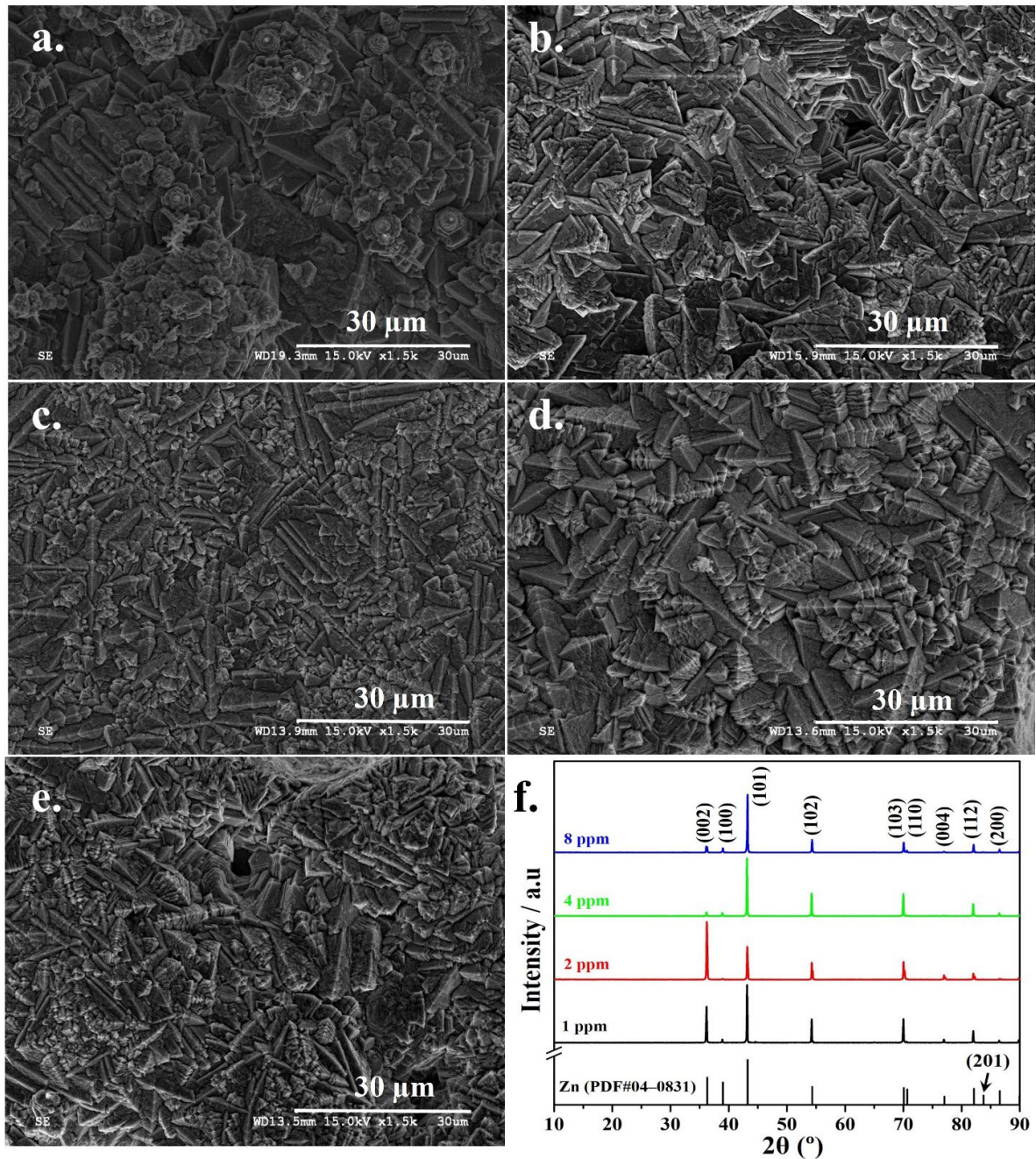


Figure 8-6 SEM images of Zn deposit on Al substrate obtained in the base solution containing, (a) 0.1 M Na_2SO_4 , (b) a + 1 ppm CTAB, (c) a + 2 ppm CTAB, (d) a + 4 ppm CTAB (e) a + 8 ppm CTAB (f) XRD patterns of Zn deposits formed in a – e

The XRD patterns of Zn deposits produced in the presence of 1, 4 and 8 ppm CTAB, registered the major diffraction peak at 43.2° indicating the preferential Zn growth in the (101)

planar orientation. In contrast, the 2 ppm CTAB condition results in a dominant peak at 36.3° (the (002) basal plane). The change in growth orientation from the (101) to the (002) crystallographic plane in the presence of optimum (2 ppm) CTAB concentration significantly refined the grain structure (Figure 8-6c) and inhibited the H_2 evolution, as predicted from the highest current efficiency achieved (92.3 %).

8.3 Estimation of energy and Cu extraction capabilities of the TFB

The original experimental setup used to estimate the energy storage and Cu extraction capability is shown in Figure 8-7. In this setup, the PSE is injected in the positive compartment of TFB and Zn^{2+} solution (anolyte) is circulated from the water jacketed external reservoir by using peristaltic pump. Figure 8-8a can be used to predict the possible reactions during the charging and discharging process. Initially, during the charge cycle, the partial oxidation of $CuFeS_2$ in the positive electrode compartment is supported by the reduction of Zn^{2+} and its deposition on the Al surface. In the discharge cycle, the deposited Zn redissolves from the negative electrode and this encourages the reduction of oxidized species formed on the surface of $CuFeS_2$ (charge cycle) in the positive compartment as observed from the cathodic peaks during discharge (Figure 8-8a). From these results, it is also anticipated that intermediate species will form on the surface of $CuFeS_2$ (reaction 8.2) i.e. $Cu_{1-x}Fe_{1-y}S_{2-z}$ and S^0 , in the positive electrode. Parasitic H_2 evolution also occurs on the negative electrode during charge cycles, which may significantly decrease the coulombic and energy efficiencies in the TFB. However, also with the reversible transformation of sulfide sulfur species (S_2^{2-}/S^{2-}) on the surface of $CuFeS_2$, AC in the positive slurry electrode enhances its pseudocapacitive response. The reversible faradaic reactions on AC are adsorption/desorption of ionic species and their interaction with surface functional groups [209, 211]. The AC also increases the overvoltage

for oxygen evolution on the positive electrode because no sharp increase in current during forward scans was observed beyond the water stability region (-0.06 to 1.18 V_{SHE} at $\text{pH } 0.9 \pm 0.06$) (Figure 8-8a).

During the reverse scan, the potential for H_2 evolution also took place at relatively more negative (-0.43 V_{SHE}) potentials than the thermodynamic value (-0.05 V_{SHE} at $\text{pH } 0.9$). This may correspond to the adsorption of H^+ ($\text{C} + \text{H}^+ + \text{e}^- \leftrightarrow \text{C-H}_{\text{ads}}$) within the mesoporous structure of the high surface area AC in the positive slurry electrode [281, 293, 294]. Similarly, during Zn deposition in the charging process, the slow kinetics of H_2 evolution over Zn is seen by the large overpotential (point B–C in Figure 8-4b). The OCP of each positive slurry ($E_{\text{OCP}}^{\text{P}}$) and negative Al current collector ($E_{\text{OCP}}^{\text{N}}$) in the anolyte measured separately in three electrodes cell were found to be 0.46 ± 0.02 V and -0.55 ± 0.03 V, respectively. The variation in the potential difference E_{D} ($E_{\text{OCP}}^{\text{P}} - E_{\text{OCP}}^{\text{N}}$) is shown in Figure 8-8b. The experimentally measured cell voltage (E_{C}) of the TFB was 0.95 ± 0.03 V which was ≈ 60 mV lower than E_{D} . This decrease in the E_{C} is due to the IR drop in the positive and negative compartments, as well as across the AEM, as presented schematically in Figure 8-8b.

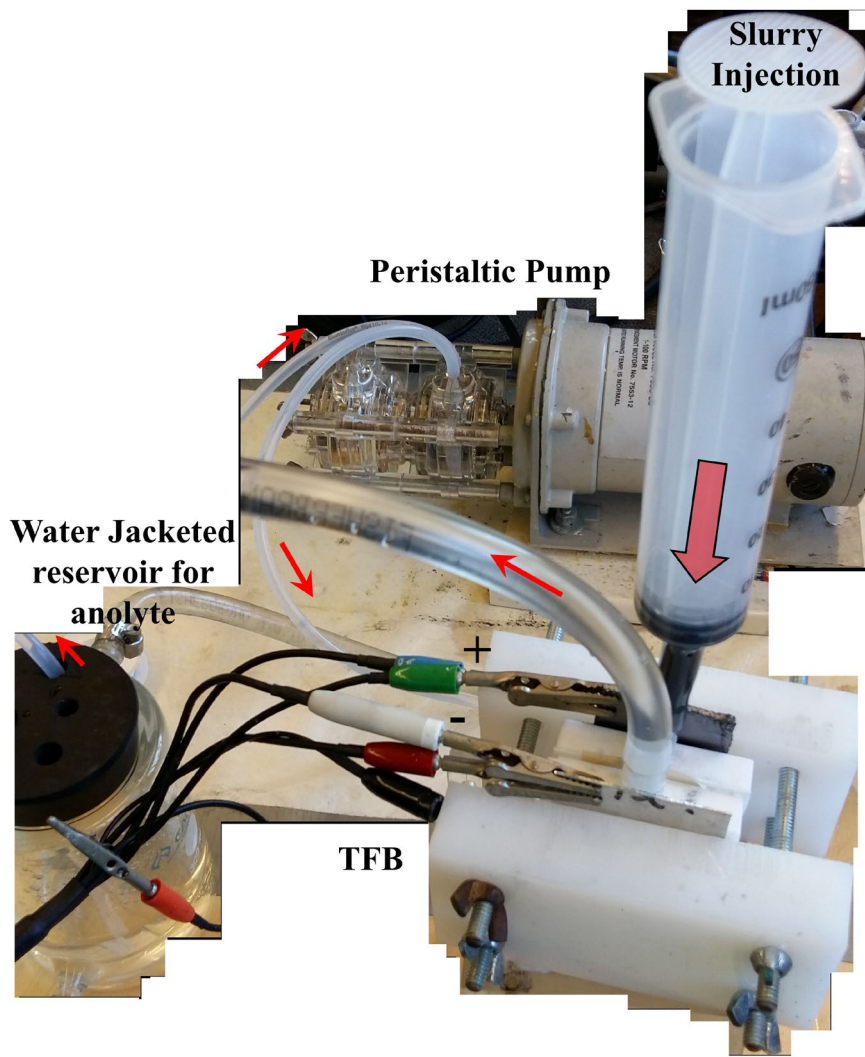


Figure 8-7 TFB showing the assembly of a cell connected to a potentiostat

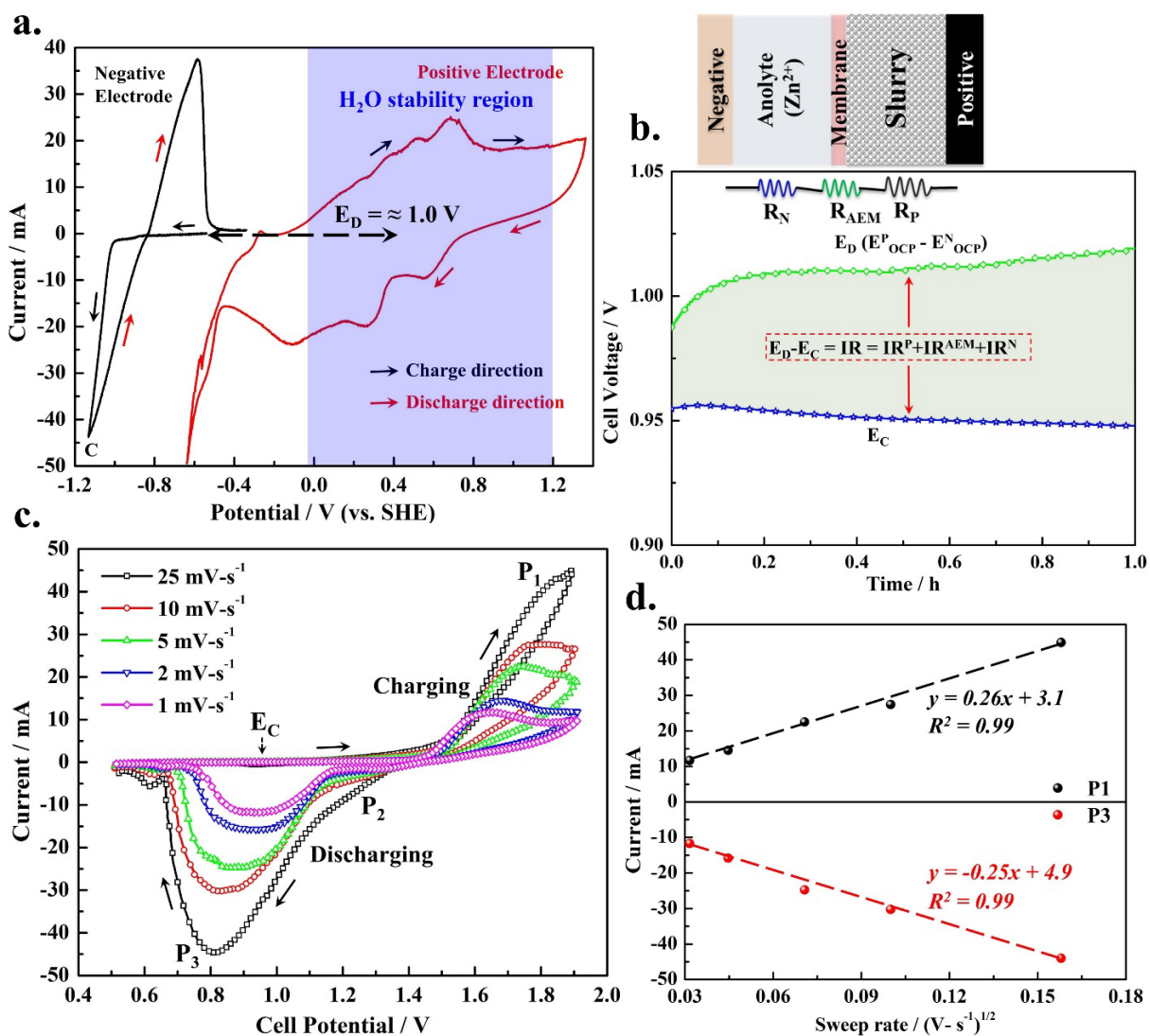


Figure 8-8 Performance evaluation of TFB (a) CV curves of negative and positive electrode, (5 mV s⁻¹). (b) Equilibrium cell potential (EC) and schematic of potential drop within the TFB. (c) CV scans of TFB at various sweep rates and (d) the trends of peak current vs. (sweep rate)^{0.5}

To evaluate the reversibility of the electrochemical reactions in the TFB, the CV scans were obtained at various sweep rates from 1 – 25 mV s⁻¹ as presented in Figure 8-8c. The continuous increase in current from ≈ 1.1 V and the origin of peak P₁ at highly positive cell potential (> 1.55 V) during charging process corresponds to the oxidation of CuFeS₂ and Zn deposition in the positive and negative electrode compartments, respectively. However, this

rapid increase in current includes the electrochemical response of both AC and CuFeS₂ in the PSE. In other words, no separate current peak associated with the AC was apparent, owing to the preferential oxidation of CuFeS₂ in the positive compartment of the TFB [295]. In the discharge cycle, the peak P2 (Figure 8-9a) was observed at ≈ 1.32 V, which is related to surface adsorption of cationic species within the mesoporous structure of AC (pseudocapacitive behavior) or due to the reduction of species (i.e. Fe^{III} and Cu^{II}) formed in the preceding charge cycle. Furthermore, the prominent broad current peak (P3) demonstrates the re-dissolution of Zn in the anolyte. This re-dissolution supports the electro-reduction of unreacted CuFeS₂ or the underpotential deposition of various ionic species (i.e. dissolved Cu^{II}, Fe^{II}, H⁺ species etc.) in the PSE these species having formed in the preceding charge cycle (forward scan). The overall current associated with the charge (P1) and discharge (P3) peaks could also include the reversible faradaic response of sulfide sulfur species present on CuFeS₂ via reaction 8.9 [196].



The separation between peaks P1 and P3 tended to increase with the rise in sweep rate. In other words, P1 and P3 shifted away from E_C in both directions with increasing sweep rate, as shown in Figure 8-9b. This behavior was linked to the sluggish kinetics of reversible electrochemical reactions at the surface of both electrodes in the TFB. On the negative electrode, this may be connected to the presence of CTAB in the anolyte, which has a slightly increased the Zn deposition overvoltage during the charging step as revealed by the extension in the B–C region (Figure 8-4b). From the analysis of P1 and P3, peak currents (i_{peak}) varied linearly with the square root of the sweep rate ($v^{1/2}$) as presented in Figure 8-8d. The highest charge and discharge current at a sweep rate of 25 mV s^{-1} is due to a thin diffusion layer across the electrodes/electrolyte interface in the TFB. With decreasing v , the progress of

electrochemical reactions on the electrode surface lead to an increase in the thickness of the diffusion layer and an apparent decrease in the current response follows the Randles–Sevcik relation (Equation 8.5) [296].

$$i_{peak} = 0.446nFAC\left(\frac{nFvD_0}{RT}\right)^{0.5} \quad \text{Equation 8-5}$$

In this equation, n , F , A , C and D_0 represented the number of electrons involved in the redox reaction, Faraday’s constant (96484 C eq. mol⁻¹), electrode surface area, the concentration of active species in the bulk electrolyte and their diffusion coefficient, respectively.

The continuous flow of anolyte in the TFB restricts the growth of the diffusion layer on the surface of the negative electrode. However, it is expected that during the charging process, at low cell potential (< 1.55 V), charge transport processes are limited by the formation of reaction products on the surface of the CuFeS₂ particles (reaction 8.2) [278, 297]. During charging at high cell potential, the stability of the passive film (Cu_{1-x}Fe_{1-y}S_{2-z} and S⁰ species) is decreased and CuFeS₂ is forced to directly oxidize into Cu^{II} and Fe^{II} species which can be justified from the large peak current (P1) in Figure 8-8c.

Due to the significant potential difference (positive cell potential) between positive and negative electrodes, the reduction of oxidized products (i.e. Fe³⁺, Cu²⁺ extracted from CuFeS₂) and/or reduction of CuFeS₂ itself into other species i.e. Cu₉Fe₈S₁₆, Cu₅FeS₄ and/or Cu₂S (reactions 8.3, 8.4) is possible in the following discharge cycle, if the TFB is discharged to very low cell potentials. But due to the selection of a large cut-off cell potential (0.8 V), the tendency of these species to form was expected to be low. However, the reversible (S₂²⁻/S²⁻) behavior of surface species (via reaction 8.9) and the pseudocapacitive behavior of AC in the PSE are matched by the re-dissolution of highly electro-active Zn at the negative electrode during discharge cycles. These reversible processes promote charge storage in this device.

Peak P2 in the CV scans (Figure 8-9a) and the linear dependency of its current vs. ν (Figure 8-9c), is consistent with adsorption of ionic species in its porous structure. Also, the peak potential (P2) was remained almost independent of ν , which is consistent with the adsorption and/or reduction of leached ionic species (from CuFeS_2 i.e. Cu(II) and Fe(III)) in the preceding charge cycle [237, 298]. These species may interact with the surface functionalities of AC and may augment the overall charge storage capability (pseudo-capacitance) of the TFB.

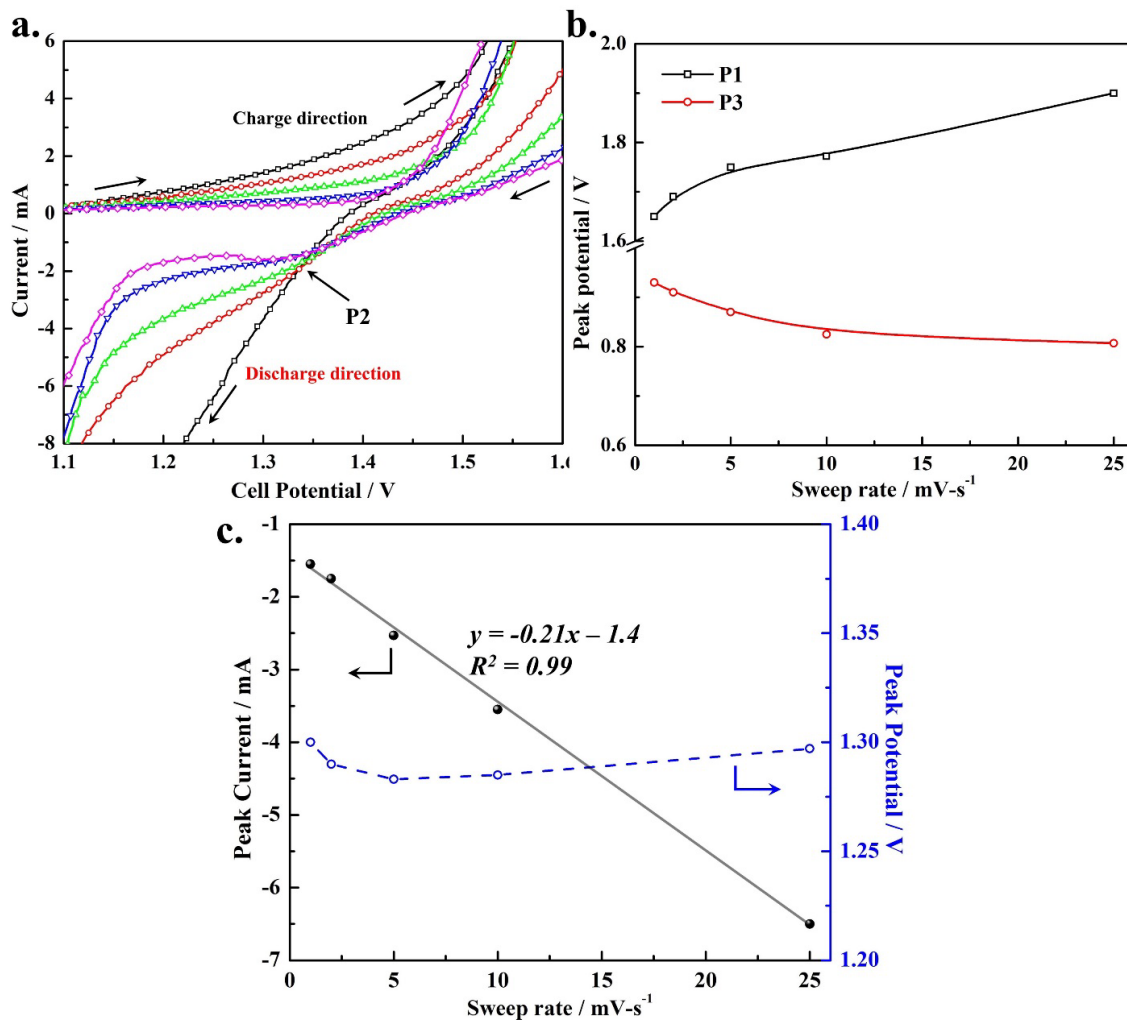


Figure 8-9 (a) CV curves of TFB as shown in Figure 8-8c indicating peak P2 (b) shift in peak potentials (P1 and P3) vs. sweep rate (c) variation in peak current and potential vs. sweep rate for peak P2

GCD cyclic tests were performed to measure the specific capacity, energy storage capability and % Cu extraction with the TFB. The charging and discharging were carried out at 1C and 0.5C rates, respectively and the polarization trends are shown in Figure 8-10a and b. It is apparent that the plateaus in the GCD cycles (Figure 8-10a) replicate the current peaks in the CV scans (Figure 8-8c). However, as seen in the charging trends, compared to first charge cycle, the polarization effect in the subsequent cycles is dominant, which is attributed to the hindrance in the progress of pseudocapacitive (reversible) faradaic reactions within the TFB. This may be related to the passivation of CuFeS₂ in the PSE during the first charge cycle, or to the parasitic reactions occurring on the negative electrode that affect the reversibility of the Zn/Zn²⁺ reaction.

The significant decrease in the discharge-specific capacity during 10 repetitive GCD cycles is related to the area under each discharge curve and it was calculated from Equation 8.6.

$$Q_c (\text{mAh} - \text{g}^{-1}) = \frac{i_d}{3.6m_{\text{Zn}}(V - i_d R)} \int_{t_1}^{t_2} V(t) \cdot dt \quad \text{Equation 8-6}$$

In this equation, i_d , m_{Zn} , V and $i_d R$ represent the discharge current, the mass of Zn deposit, cell potential and potential drop at the start of each discharge cycle, respectively. The general function $\int_{t_1}^{t_2} V(t) \cdot dt$ presents the area under the discharge potential profile on a time scale.

Upon repetitive GCD cycling, particularly in the subsequent discharge cycles, the plateaus (P3) at 1.2 V are becoming shorter as shown in Figure 8-10b (similar to current peak P3 observed in CV scan, Figure 8-8c). It is also noteworthy that upon repetitive cycling in the following GCD cycles, the plateau (P3) (at ≈ 1.2 V) disappears. The pseudocapacitive response is most likely controlled by either the sulfide sulfur species formed on the surface of CuFeS₂ (reaction,

reaction 8.9) or by the reversible adsorption/desorption processes on AC (in PSE) as represented by the steep plateaus (P2) in Figure 8-10b and c. It is also interesting that during repetitive CV scans of the TFB, the current response (both charge and discharge) in each successive cycle decrease continuously, as shown in Figure 8-10d. Akin to the GCD plots, this behavior confirms the limited pseudocapacitive response of the TFB, due to the occurrence of irreversible reactions in the PSE (reactions 8.2 and 8.4). Upon repetitive cycling, the shift in peak potentials to higher cell potentials in the CV scan also indicate the commencement of electrochemically irreversible reactions in the TFB, i.e. Cu and Fe dissolution (non-capacitive, irreversible faradaic reactions) from CuFeS_2 [53, 296]. At such high cell potential, the pseudocapacitive response of the TFB is fully managed by the reversible (adsorption desorption and $\text{S}_2^{2-}/\text{S}^{2-}$) reactions on the surface of CuFeS_2 and AC in the positive electrode.

The specific capacity (Equation 8.6), η_C , η_E and η_V efficiencies of the TFB were determined from the repetitive GCD plots as shown in Figure 8-11a. A large specific capacity ($343.2 \text{ mAh g}^{-1}_{\text{Zn}}$) is measured during the 1st discharge cycle. Based on total volume of slurry (V_S) in the PSE compartment, this discharge capacity in the 1st cycle was equivalent to $\sim 1.0 \text{ Ah l}^{-1}$. Over the initial 10 GCD cycles, the specific capacity of the TFB decreases abruptly to $69.6 \text{ mAh g}^{-1}_{\text{Zn}}$ (equivalent to 0.235 Ah l^{-1}). The supplied charge (during charging) is consumed by irreversible conversion reactions in the TFB as verified from the low η_C ($44 \pm 2 \%$) and η_E ($32 \pm 3 \%$) over the initial 15 GCD cycles.

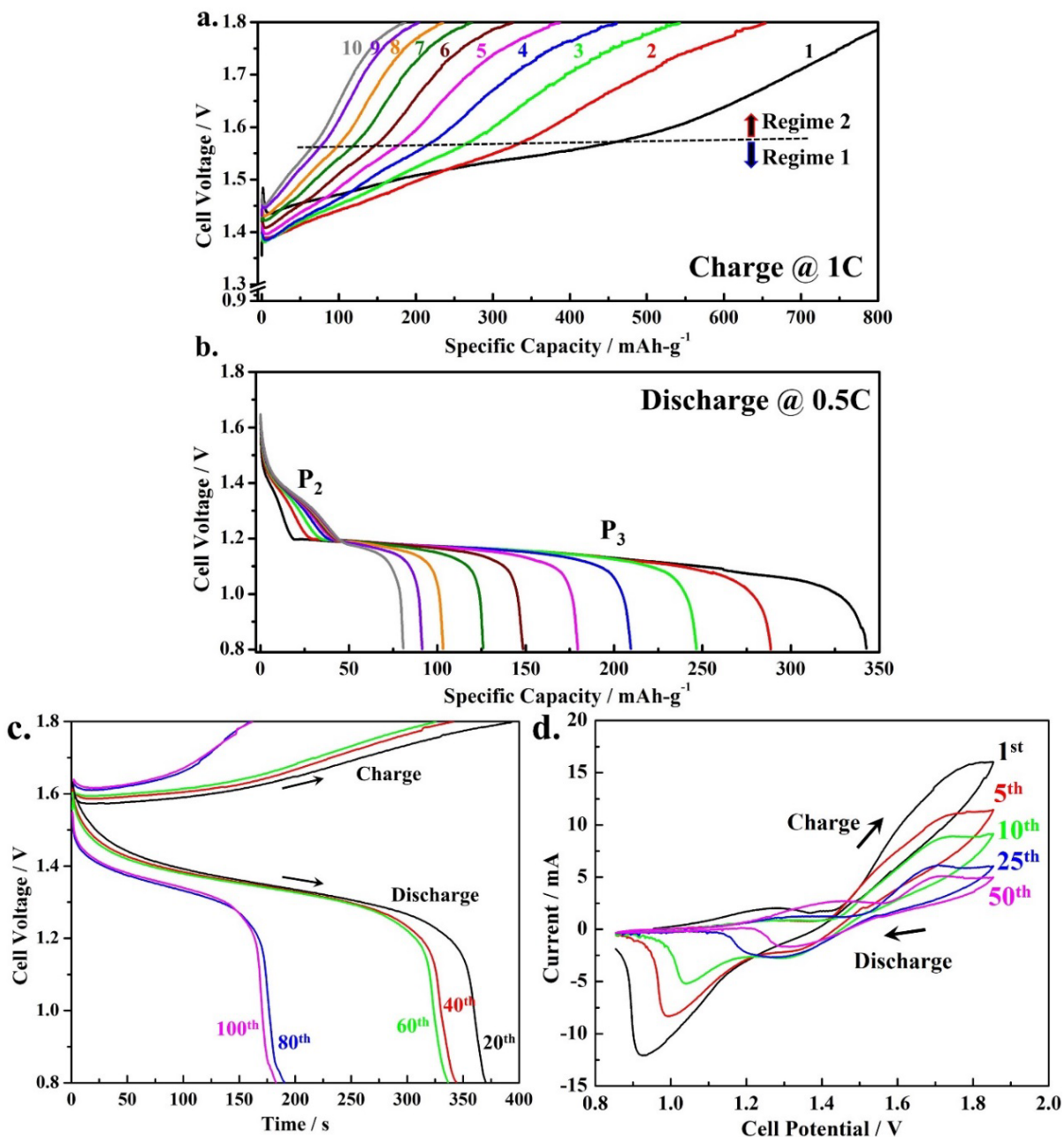


Figure 8-10 The 10 GCD cycles (a) charge and (b) discharge cycles. (c) 20 to 100 GCD cycles; the specific capacity is calculated based on the mass of Zn deposit during the first charge cycle. (d) Repetitive CV scans of TFB obtained at 0.002 V s^{-1}

From these values, it is clear that a large amount of energy is lost in the successive cycles, mostly due to the formation of a polysulfide surface layer ($\text{Cu}_{(1-x)}\text{Fe}_{(1-y)}\text{S}_{(2-z)} + \text{S}^0$). This

is also caused by the Cu and Fe dissolution from CuFeS₂ in the PSE in parallel with H₂ evolution on the negative electrode. After 20 GCD cycles, the TFBS provides almost constant discharge specific capacity ($\sim 32 \text{ mAh g}^{-1}_{\text{Zn}}$ or $\sim 0.1 \text{ Ah l}^{-1}$) with little improvement in the η_C , η_E , and η_V , which all remain constant at approximately 52 %, 41 % and 80 %, respectively. During the discharge cycles, the occurrence of faradaic processes at large cell potentials (corresponding to P2 and P3) results in high η_V (80 %), which is considered an encouraging feature for any energy storage device.

The energy storage capability of the TFB was calculated from the discharge profiles using Equation 8.7 (Figure 8-11b).

$$\text{Specific Energy (Wh kg}^{-1}\text{)} = \frac{1}{3.6mZn} \int_{t_1}^{t_2} \Delta V(t) \cdot i_d \cdot dt \quad \text{Equation 8-7}$$

The maximum specific energy of 388.6 Wh kg⁻¹ (energy density = $\sim 1.1 \text{ Wh l}^{-1}$) during the 1st GCD cycle corresponds to the portion of the supplied energy that can be retrieved upon discharge by the re-dissolution of Zn in the anolyte. The specific energy then decreases rapidly to $\sim 50 \text{ Wh kg}^{-1}$ ($\sim 0.17 \text{ Wh l}^{-1}$) in the subsequent 15 cycles. This behavior is due to the non-capacitive irreversible faradaic reactions (Cu and Fe extraction from the CuFeS₂), which consume a large amount of input energy within the TFB during each charging cycle, as evident from the 6.7 % Cu dissolution after 20 cycles determined separately from solution concentrations. It is important to note that the % Cu extracted in the 20th, 40th, 60th, 80th and 100th cycles was determined in separate GCD experiments.

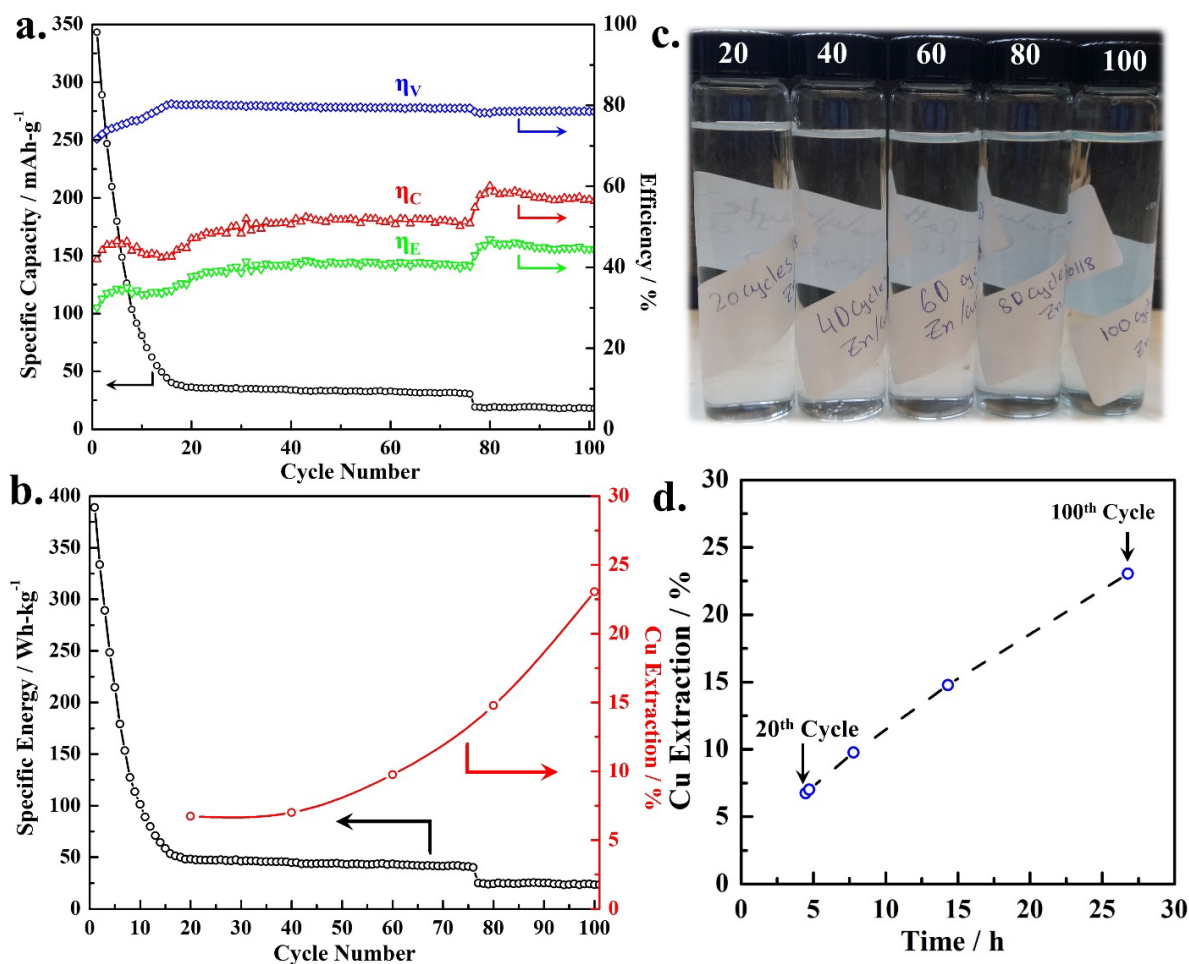


Figure 8-11 Quantitative assessment of (a) Specific capacity (discharge), coulombic, energy and Voltage efficiencies of the TFB. (b) Energy storage capability and % Cu extraction as a function of GCD cycles (Note: The % Cu extraction was calculated from the ICP-OES analysis). (c) The filtrate retrieved from the PSE. (d) Instantaneous % Cu extraction from CuFeS_2 in the TFB during 100 GCD cycles

A maximum 23.4 % Cu extraction was achieved after 100 GCD cycles. Visually, the presence of dissolved Cu was evident from the filtrate color, as shown in Figure 8-11c. The total time accumulated during GCD cycling and the instantaneous % Cu extraction was plotted as shown in Figure 8-11d. The rapid decrease in specific capacity (Figure 8-11a) from 344 $\text{mAh}\cdot\text{g}^{-1}$ to $\approx 32\text{ mAh}\cdot\text{g}^{-1}$ during the initial 20 cycles indicates the progress of irreversible reactions (via reaction 8.2 and 8.10) within the PSE which was reflected from the 6.3 % Cu

extraction from CuFeS₂. Therefore, the limited charge storage capability of the TFB is related to the continuous increase in Cu dissolution.



In 100 GCD cycles which were completed in approximately 26 h, a maximum of 23.4 % Cu was extracted. The oxidation of CuFeS₂ (irreversible reactions) in the PSE also markedly decrease the η_C (50 %) and η_E (40 %). However, these poor energetic performance numbers are offset by the simultaneous and valuable Cu extraction from an otherwise refractory mineral. Based on these results, it is speculated that this battery-like setup could be utilized as a unit for both energy storage and as a source of Cu production from mineral concentrate on a large scale. In the 100th GCD cycle the specific energy was found to be 23.5 Wh kg⁻¹ (or 0.07 Wh l⁻¹).

In addition to dissolved Cu, the filtrate also contains dissolved Fe species, which must be removed prior to recovery of valuable Cu metal through an SX/EW (or other appropriate) process. The pH of the PSE filtrate should also be increased to ~2.0 from 0.9 by the addition of lime and to precipitate soluble Fe as oxides or hydroxides. After solid/liquid separation, the catholyte can be further enriched with dissolved Cu through the well-established SX process before circulating it through the electrowinning cell for the recovery of Cu metal.

It is evident in Figure 8-10b that the potential plateau (P3) tends to shrink and the discharge capacity is controlled by the AC and possibly by sulfide sulfur species in the PSE (as demonstrated by the P2 plateau). Also, the reversible transformation of the dissolved species (i. e. Fe^{II} and Fe^{III}) from CuFeS₂ could also contribute to the formation of this potential plateau. The plateau (P2) at high cell potential, (Figure 8-10c) therefore indicates the transformation of the TFB from battery to capacitor like behavior after repetitive GCD cycles. With this hybrid feature in mind, Figure 8-12a shows the rated capacity by discharging the

TFB at various C-rates. The specific capacity decreases significantly from 344 to 92.8 mAh g⁻¹ when the discharge rate is increased from 0.5C to 1C. Furthermore, upon discharging at 1.5, 2.0 and 2.5C, the specific capacity gradually decreases to 44.3, 31.1 and 30.0 mAh g⁻¹, respectively. This behavior is dominated by the reversible reactions occurring on the surface of AC and CuFeS₂. As discussed above, the presence of sulfide sulfur species on the surface of CuFeS₂ (i.e. S²⁻, S₂²⁻ etc.) and adsorption/desorption of cationic species i.e. H⁺, Cu^{II}, Fe^{II}, Fe^{III}, on the surface of AC and CuFeS₂ likely facilitate this pseudocapacitive response [243, 299]. In other words, the high specific power and low specific energy at large C-rate correspond to surface or near surface reactions for which the charge transfer is limited at the electrode/electrolyte interface. The Ragone plot of the TFB (Figure 8-12b) shows the highest specific power (2.05 kW kg⁻¹) and the lowest specific energy of 34.8 Wh kg⁻¹ when discharged at 2.5C. This typical behavior of high specific power and low specific energy at high C-rates and vice versa is attributed to the kinetic limitation of reversible (pseudocapacitive) faradaic reactions in the TFB as reported in the literature [132, 300, 301].

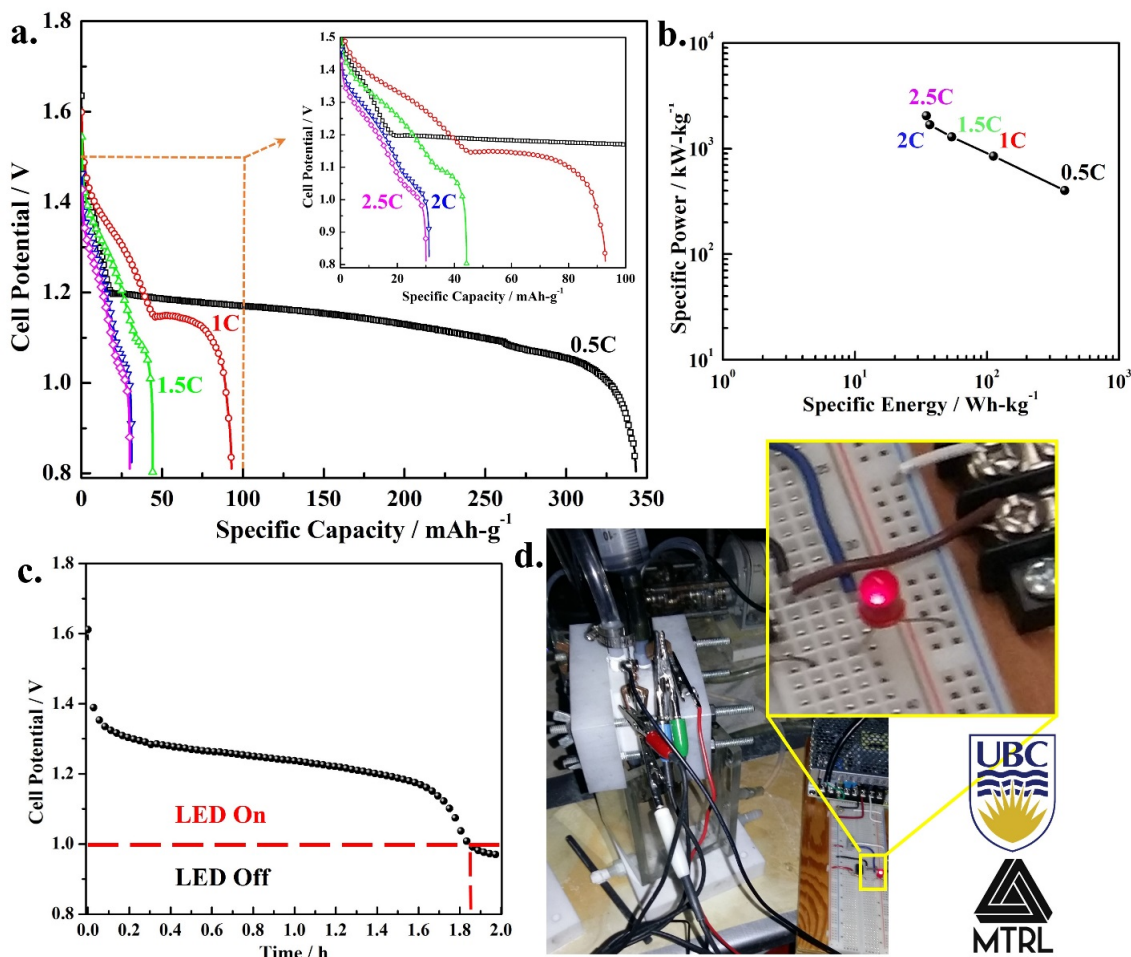


Figure 8-12 (a) Discharge profiles of the TFB obtained at various C-rates, (charged at the 1C rate) (b) Ragone plots developed based on the first GCD cycle (c) Cell potential variation of fully charged TFB under an applied load of single LED (d) Illuminated LED when connected to fully charged TFB

To further demonstrate the practical use of the TFB, the cell was initially charged to 1.8 V at a rate of 1C and connected to a light emitting diode (LED), mounted on a single board microcontroller (Arduino). This Arduino was designed to keep the LED illuminated until the cell potential fell to <1.0 V by applying the LED load (discharge). The cell potential of the TFB setup under an applied load of ~ 0.5 mA (single LED) was measured with the external potentiostat as shown in Figure 8-12c. Under applied load, the high initial cell potential (≈ 1.5 V) decreased rapidly to ≈ 1.3 V in 400 s, followed by a gradual potential decay to 1.2 V in 1.4

h. The TFB was able to keep the LED lit for ≈ 1.8 h until the 1.0 V cut-off potential was reached (Figure 8-12d), which is an impressive feature of this setup, thus demonstrating its practical applicability as energy storage device. Gradual decay of the cell potential from ≈ 1.3 V to the cut-off potential under the applied LED load also indicated a negligible corrosion of deposited Zn. However, there is a possibility of solution-level corrosion of deposited Zn once the TFB is fully charged and left at OCV. This process is called the self-discharge of the TFB. To use the TFB as a hydrometallurgical unit, the solution-level corrosion of the deposited Zn can be prevented by stopping the anolyte flow into the cell and by rapid replacement of the cathode after each charge cycle.

8.4 Cause of capacity fade and mass balance in TFB

8.4.1 Diagnosing possible reactions in TFB

During charging, it is expected that CuFeS_2 will passivate at low cell potential (< 1.50 V) and polysulfide passive film forms on the surface of CuFeS_2 in PSE (regime-1) as discussed above (reaction 8.2). Also, at large cell potentials (regime-2), the stability of this passive film is decreased and CuFeS_2 in the PSE can oxidize either via reactions 8.10 and/or 8.11 supported by Zn deposition and H_2 evolution on the negative electrode (these potential regimes are shown in Figure 8-10a) during the charge cycle.



It has been reported that at sufficiently large cell potentials, CuFeS_2 may oxidize directly to Cu^{2+} and Fe^{III} species via these reactions 8.10 and 8.11 [36, 53]. In addition, it is important to note that according to reactions 8.2 and 8.10, the oxidation of CuFeS_2 was pH independent. During charging at high cell potential (> 1.7 V), it is expected that H_2O may oxidize at the surface of CuFeS_2 and some of the sulfide sulfur may oxidized to sulfate. This

reaction (reaction 8.11) may decrease the pH of the catholyte due to the generation of a large amount of H^+ . To determine the extent of these reactions in the TFB, the total charge consumed during each charge/discharge cycle was estimated from the Equation 8.8.

$$Q_c = \frac{i_c}{(V - i_c R)} \sum_{i=1}^p \int_{t_1}^{t_2} V(t) \cdot dt \quad \text{Equation 8-8}$$

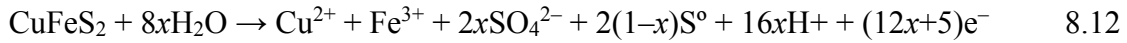
Where, i_c is the charging current and V is the maximum applied cell potential (1.8 V) subtracted by the $i_c R$ drop across the cell during the charge cycle. The number of cycles (p) is the area under each charge curve (i) and is presented as the operator $\int_{t_1}^{t_2} V(t) \cdot dt$. Similarly, the total charge during each discharge curve (Q_d) is estimated, and the charge consumed for the faradaic (non-capacitive) irreversible reactions (reactions 8.2, 8.10 and 8.11) (Q_{irr}) was calculated as $Q_c - Q_d$.

Under applied conditions, it was considered that the charge consumed during passive film formation and ionic release of Cu and Fe (reaction 8.2) was small at low cell potentials compared to the total current involved in reactions 8.10 and 8.11 at large cell potentials. It is, therefore, essential to calculate the extent of each reaction (8.10 and 8.11) based on the degree of sulfide sulfur oxidation to sulfate as proposed by Biegler et al [302]. It is assumed that if x is the fraction of $CuFeS_2$ oxidized according to reaction 8.11, then the overall reaction can be written as reaction 8.12.

In this regard, the *number moles of electrons per mole of Cu^{2+}* (n) were calculated from the total irreversible charge ($Q_{irr} = Q_c - Q_d$) from the GCD tests and from the concentration of Cu extracted from $CuFeS_2$ (as determined from ICP-OES analysis), as a function of GCD cycles according to Equation 8.9.

$$n = \frac{\sum_i Q_{irr}}{(m_{Cu/M}) \cdot F} \quad \text{Equation 8-9}$$

In this equation $\sum_i^p Q_{irr}$ is the total charge consumed in the non-capacitive faradaic reactions (reactions 8.10 and 8.11). Also, p is equal to 20, 40, 60, 80 and 100 cycles and the subscript i , m_{Cu} , M and F represent the cycle number, mass of Cu extracted as determined from the ICP-OES analysis, molecular mass of Cu and Faraday constant (96485 C-mole⁻¹), respectively. By assuming that x is the fraction of CuFeS₂, which was oxidized via reaction 8.11, then the cumulative reaction can be written as reaction 8.12.



Based on the procedure adopted in other studies [36, 53, 302], the extent of reaction (x) was calculated by equating the number of electrons per mole of Cu²⁺ produced with the number of electrons per mole of Cu²⁺ formed via reaction 8.12 that is $n = 12x + 5$, and the values are given in Table 8-1. It is also important to mention here that the decrease in n (number of electrons transfer per mole of Cu²⁺ dissolution) with increase in charge/discharge cycles was possibly attributed to the limited dissolution of Cu²⁺ due to possible thickening of sulfide sulfur layer on the surface of CuFeS₂ (via reaction 8.10) during GCD cycling. In other words, the dominant non-capacitive irreversible faradaic process in the PSE was identified as Cu²⁺ dissolution from CuFeS₂ preferably via reaction 8.10. This was validated from the negative x values (Table 8-1) which indicated the restricted oxidation of S⁰ into SO₄²⁻ according to reaction 8.11. In addition, these results have been reinforced by the large overpotential for H₂O oxidation in the positive slurry electrode as confirmed from the CV scan (Figure 8-8a).

Table 8-1 Quantitative determination of the extent of reaction from GCD and ICP-OES analysis

No. of Cycles (<i>p</i>)	* $\sum_i^p Q_{irr}$ (C)	\dot{m}_{Cu} (mg)	<i>n</i>	Extent of reaction (<i>x</i>)
20	58.64	37.28	1.03	-0.33
40	73.17	38.80	1.24	-0.31
60	85.76	54.07	1.04	-0.33
80	96.68	81.85	0.78	-0.35
100	102.6	127.7	0.53	-0.37

8.4.2 SO₄²⁻ transport and mass balance

Due to Zn deposition in the charge cycle, the excess of SO₄²⁻ species in the anolyte would transport through the membrane to catholyte and is balanced by Cu^{II} and Fe^{III} species generated from the oxidation of CuFeS₂ (reaction 8.10). It is therefore suggested that presence of high concentration of total sulfate $\{(SO_4^{2-})_T = SO_4^{2-} + HSO_4^- + NaSO_4^-\}$ in the anolyte not only increased its conductivity but also suppressed the acid generation in the catholyte during the charge cycle. It was obvious that anionic diffusion flux from catholyte {low (SO₄²⁻)_T} to anolyte {high (SO₄²⁻)_T} was negligibly small compared to migration component during the discharge cycle. Also, due to the high selectivity of AEM (95 %) used in this TFB, it is expected that cations cross over through the membrane would be very small. In support to this, the very low concentration of Fe (1.5 ppm) and Cu (1.7 ppm) in the anolyte after 100 GCD cycles were determined from ICP-OES analysis, which verified the negligible cross-contamination of electrolytes during TFB operation. In the discharge cycle, the cationic species (H⁺, Cu^{II}, Fe^{II} and Fe^{III} species etc.) can adsorb on the CuFeS₂ and AC surface, giving rise to the discharge capacity and by reverse transport of SO₄²⁻ from catholyte to anolyte to balance the redissolved Zn²⁺.

During charging/discharging, the anionic species in both anolyte and catholyte can transport through the membrane (AEM) via diffusion and/or migration due to the existence of both concentration and electric field gradients in the TFB. Consequently, the mass transport from anolyte to catholyte and vice versa is highly dependent on the membrane characteristics. During operation, as the cell potential is continuously varying during each charge and discharge cycle, the variable electric field ($\frac{d\psi}{x_m}$) (where, $d\psi$ and x_m are the cell voltage and membrane thickness, respectively) across the AEM significantly influence the migration of ionic species. To simulate the mass transport during the GCD process, it is therefore essential to consider the membrane characteristics. During charging the anionic species diffuse and migrate from the anolyte to catholyte. However, only migration of anionic species from the catholyte to anolyte was possible during the discharge process due to positive concentration gradient across the membrane. To incorporate the membrane characteristics, the extended Nernst–Planck Equation 8.10 and Equation 8.11 were used [303] in this work.

$$J = k_m \left[-\overline{D}_S \frac{[C_S^c - C_S^a]}{x_m} - \frac{zF}{RT} \overline{D}_S C_S^a \frac{d\psi}{x_m} \right] + C_S v \quad \text{Equation 8-10}$$

$$k_m = \frac{v_p \overline{D}_S}{\theta^2 D_S} \cdot \frac{1}{x_m} \quad \text{Equation 8-11}$$

In Equation 8.10, the k_m is the membrane constant and can be determined from Equation 8.11. D_S , C_S^c , C_S^a , v_p , \overline{D}_S , and θ^2 are the diffusion coefficient, bulk concentration of SO_4^{2-} ions at the membrane/catholyte and membrane/anolyte interface, pore volume fraction in the membrane, the diffusion coefficient of SO_4^{2-} in the membrane pore solution, and tortuosity of the membrane, respectively. In this case, a value of $k_m = 0.0074$ for the AEM was used, which has been reported by Koter et. al. [304].

It is assumed that the convective flux ($C_s v$) of ionic species within the membrane is negligible and by including both diffusion and migration effects on the mass transport of ionic species, the total flux of anionic species during the 1st charge and discharge was calculated. The values of other parameters used in the calculation are given Table 8-2. Due to high selectivity (0.95) of the AEM used in this study and pre-treatment in dilute saline solution, it was assumed that in sulfate based anolyte and catholyte, the transport of bisulfate (HSO_4^-) and $NaSO_4^-$ was limited as shown schematically in Figure 6-13c. It has also been reported in the literature that, depending on the water content of the AEM, and its weak base characteristics, only SO_4^{2-} ions would carry through the membrane as electric charge [305-307]. It is assumed that the diffusion coefficient of SO_4^{2-} in the pore solution of the membrane is $\overline{D}_s = D_s/10$ is 10 times lower than in the bulk solution [308, 309] as given in the Table 8-2.

Table 8-2 Parameters used to determine the mass transport across the AEM

Symbol (Abbreviation) (Units)	Value (Reference)
k_m (Membrane Constant)	0.0074 [304]
x_m (Membrane Thickness) (m)	1.3×10^{-4}
\overline{D}_s (SO_4^{2-} -Diffusion coefficient within membrane) (m^2/s)	1.06×10^{-10} [280, 310, 311]
A_m (Area of the membrane) (m^2)	3.0×10^{-4}
V_A & V_C (Volume of anolyte and catholyte) (m^3)	3.0×10^{-6}
z (Charge number of SO_4^{2-})	-2
R (Universal gas constant) (J/mole-K)	8.314
T (Absolute Temperature) (K)	298.15
F (Faraday's constant) (C/mole)	96485

Certainly, the ingress of anionic species towards and from the catholyte during charging and discharging steps, respectively, strongly depends on the AEM characteristics, it is, therefore, important to consider the membrane properties in the calculation. As shown in the

schematic diagram (Figure 8-13a), owing to the water content in the pore solution of the membrane, it was considered that SO_4^{2-} species can preferably transport through AEM which was due to its weakly basic nature and can reject cationic part of HSO_4^- , NaSO_4^- species at the electrolyte/membrane interface, as reported elsewhere [305-307]. The excess of SO_4^{2-} in the anolyte (due to Zn deposition) was partially compensated by these rejected cationic species. In this calculation, the $(\text{SO}_4^{2-})_T$ concentrations in the anolyte and catholyte were used to calculate the total mass transfer during each GCD cycles.

The concentrations of individual species in the anolyte under study were also determined thermodynamically from the equilibrium constant approach by using PHREEQC software package [312, 313]. It was evaluated that free Zn^{2+} represented approximately 27% of the total ionic concentration (equivalent to $\approx 50 \text{ g l}^{-1}$ free Zn^{2+} in the anolyte) at $\text{pH } 1.1 \pm 0.1$ and $25 \text{ }^\circ\text{C}$ (initial experimental conditions). The other dominant species i.e. HSO_4^- and SO_4^{2-} in the anolyte accounted approximately 20 % and 17 %, respectively of the total ionic concentration as shown in Figure 8-13b. In addition, a very small fraction of NaSO_4^- ($\approx 2 \%$) was available to carry the ionic current during the charge/discharge process. From these calculations, it was revealed that large concentration of undissociated $\text{ZnSO}_{4(\text{aq})}$ (almost equivalent to Zn^{2+} concentration) was present in the anolyte which may further increase to (approx. 40 %) if the pH becomes higher than 2. The small amount of H_2 evolution during Zn deposition could increase the pH at the surface of the negative electrode.

From anolyte speciation study, it can be predicted that due to a local change in pH change at the electrode surface could result in the decrease of Zn^{2+} concentration compared to $\text{ZnSO}_{4(\text{aq})}$ hence effective Zn deposition may be affected. This effect may also deteriorate the TFB cyclic performance. During charge cycle, in addition to migration, the diffusion of SO_4^{2-}

due to the relatively large concentration gradient of $(\text{SO}_4^{2-})_r$ at the anolyte (1.83 M) | membrane | catholyte (0.2 M) interfaces could promote the SO_4^{2-} transport towards positive slurry electrode compartment.

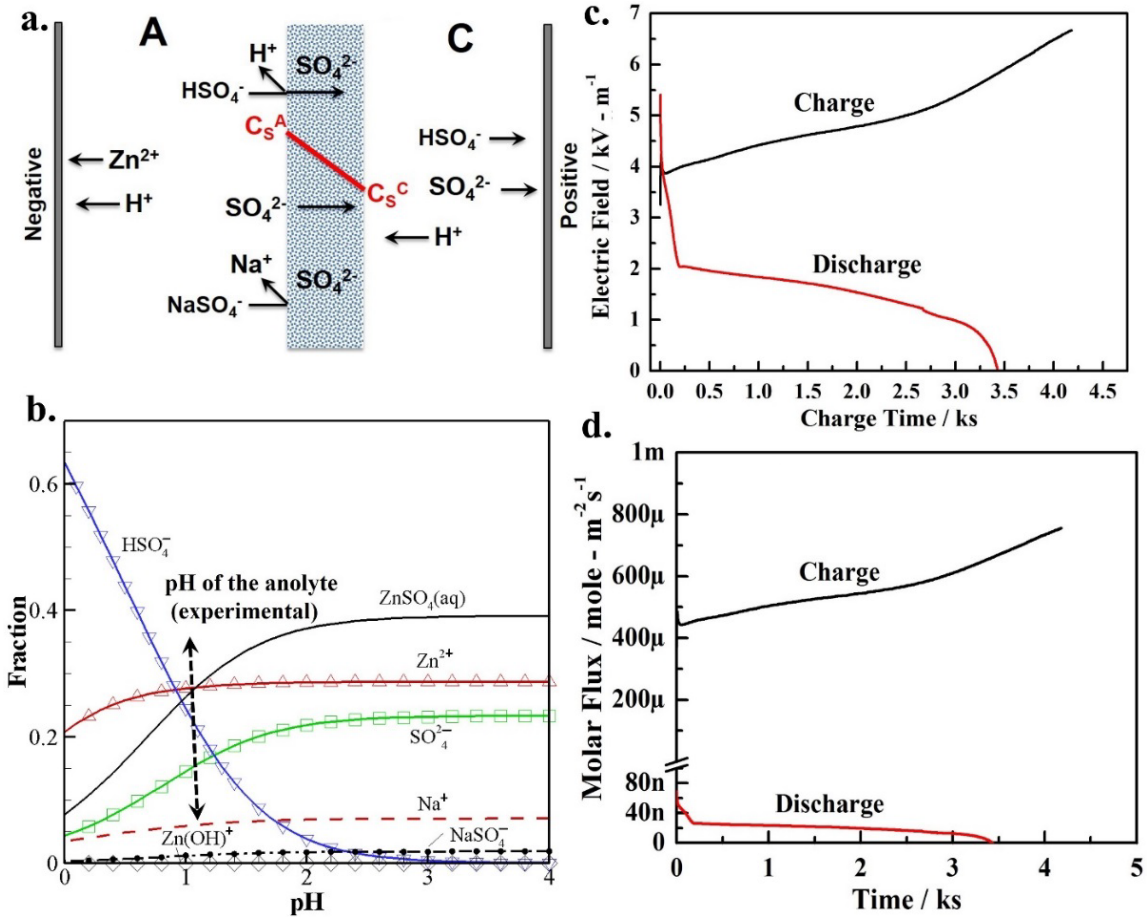


Figure 8-13 (a) Schematic diagram of ionic species transport across AEM. (b) The molar fraction of ionic species in the anolyte at 25° C (c) The transient electric field and (d) the molar flux of SO_4^{2-} across AEM

Based on the transient electric field across the AEM (Figure 8-13c), the instantaneous molar flux (J) of the SO_4^{2-} was determined from the first GCD cycle. It is important to note that only the second term (migration effects) in Equation 8.10 was used to calculate the flux during the discharge cycle. By integrating the instantaneous molar flux curves, shown in Figure 8-13d, the amount of SO_4^{2-} transferred per unit surface area of the membrane towards and from

the catholyte was determined and designated as m_{nc} and m_{nd} , where n is the number of GCD cycles and c and d in the subscripts represent the charge and discharge cycle, respectively.

During 100 GCD cycles, the concentration of overall SO_4^{2-} transferred to the catholyte (or depleted in the anolyte) was determined by considering the fractional capacity decay during each successive charge/discharge cycle by Equation 8.12.

$$m_{nc} = \prod_{nc=2}^{100} [m_{nc-1} (1 - \frac{C_{nc-1} - C_{nc}}{C_{nc-1}})] \quad \text{Equation 8-12}$$

Where, m_{nc} is the amount of SO_4^{2-} transferred to catholyte during n number of charge cycles and C_{nc} represents the charge capacity. Similarly, the amount of SO_4^{2-} transferred from the catholyte to anolyte during the discharge cycle (m_{nd}) was calculated. The $m_n = m_{nc} - m_{nd}$ was used to quantify the total SO_4^{2-} transported to the catholyte. The concentration of SO_4^{2-} species transported to the catholyte during the 100 GCD cycle was calculated to be 0.083 moles l^{-1} . It was considered that the most dominant HSO_4^- species in the anolyte (Figure 8-13b) and $NaSO_4^-$ may dissociate to produce H^+ and Na^+ cations, respectively at the interface of the highly selective AEM. These rejected cationic species may again complex with the SO_4^{2-} (formed during Zn deposition) to regenerate parent species (HSO_4^- , $NaSO_4^-$) in the anolyte. Under applied conditions, the cumulative SO_4^{2-} transferred to the catholyte during the 100th GCD cycles (calculated from the Nernst–Planck equation) was found to be approximately equal to the total concentration of Cu + Fe species (0.085 moles– l^{-1}) as measured from ICP–OES analysis after 100 GCD cycles. These results explain that the excess of SO_4^{2-} transporting from anolyte to catholyte was balanced by the total concentration of Cu and Fe species that were generated in the catholyte during the 100 GCD cycles. However, the local variation of pH on the surface of Al during Zn deposition, continuous anolyte flow, membrane selectivity

and generation of Cu and Fe species in the catholyte are considered dominant factors that could directly influence the SO_4^{2-} transport and overall performance of the battery.

8.5 Polarization behavior of TFB

The overall performance and polarization effects in the TFB were evaluated from the I–V curve as shown in Figure 8-14. The cell voltage is found to decrease linearly from 1.3 V to 1.13 V with an increase in discharge current up to 4.2 mA. This polarization trend at low currents is related to the kinetics of electrochemical processes within TFB corresponding to the electrochemical response of the CuFeS_2 in the PSE and Zn redissolution in the negative compartment. However, it is expected that kinetically, Zn re-dissolution in the acidic electrolyte is more favorable than CuFeS_2 reduction (and/or reduction of surface species formed during the preceding charge cycle) in the PSE during discharge. On the other hand, the reversible adsorption/desorption of ionic species on the AC surface could significantly improve the kinetic response of the slurry system. Maximum specific power delivered by the TFB at 4.2 mA was 0.84 kW kg^{-1} , which is comparable to the value registered by this setup at 1C discharge rate (Figure 8-12b). The narrow potential plateau at 1.1 V exhibited by the TFB could be related with the overall reversible (faradaic) response by sulfide sulfur species (reaction 8.9) and surface adsorption/desorption on AC. The appreciable decay in cell potential at a large discharge current ($> 6 \text{ mA}$) points to the dominance of ohmic drop and mass transport-controlled processes within the TFB, most likely associated with the membrane characteristics. Also, the low conductivity of CuFeS_2 and its slow kinetic response in addition to IR drop across the electrode/electrolyte/membrane interfaces could cause the steep potential decay at large applied currents. The significant decay in the cell potential at high currents (up to 0.9 V) could also be related to the slow ionic mobility of anionic species across the

membrane. The maximum specific power ($\approx 2.6 \text{ kW kg}^{-1}$) achieved at high discharge current (15 mA) confirmed the hybrid behavior of the TFB. This value is comparable to the existing asymmetrical supercapacitors (see Table 2-5 and references cited therein for further details). This behavior is thought to be explicitly controlled by the AC and sulfide sulfur species within the slurry electrode. During the GCD cycling (Figure 8-10b, c and Figure 8-12a), the highly pseudocapacitive response of the TFB was controlled by the potential plateau (P2), which corresponds to the surface limited reversible faradaic reactions on the AC and CuFeS_2 (reaction 8.9) as discussed above.

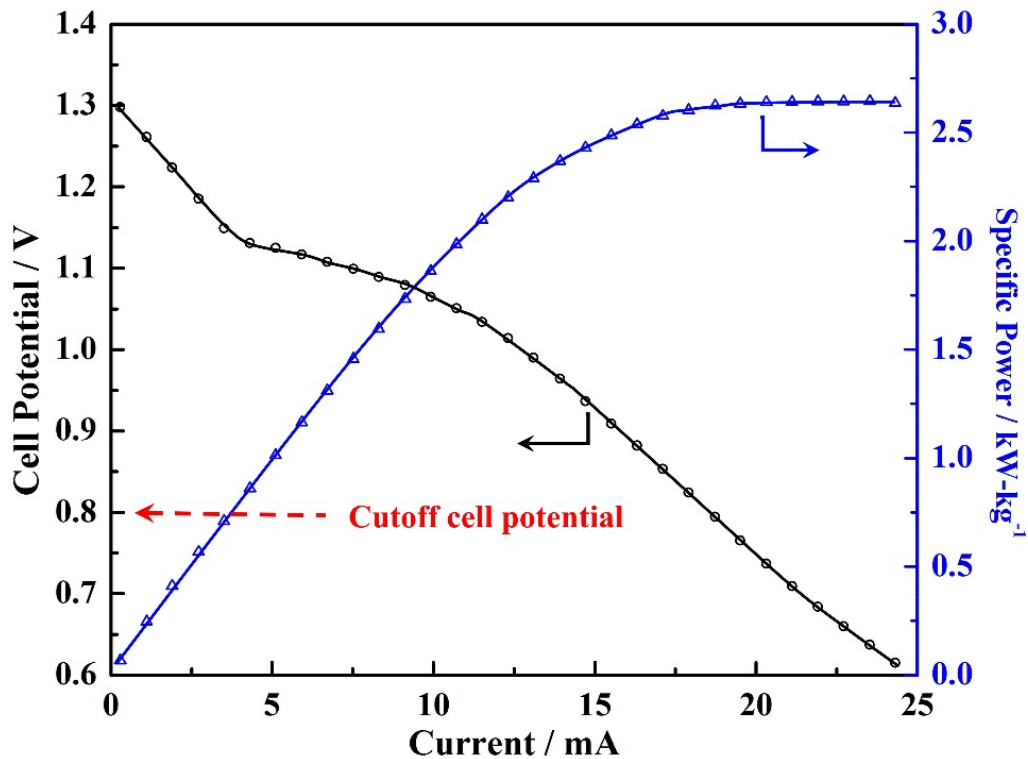


Figure 8-14 I-V curve of the fully charged TFB (at 1C) showing the polarization trend and variation in specific power at various discharge currents.

8.6 Energy storage by TFB equivalent to energy produced by a diesel generator

Based on the TFB performance, its energy storage capability was compared with the energy produced by a diesel generator. It was assumed that the TFB setup could accommodate one tonne of synthetic CuFeS_2 in the PSE. From the experimental results, this setup might store up to 8.83 kWh t^{-1} of CuFeS_2 at 40 % energy efficiency. The cyclic life of the TFB was 100 GCD cycles, which was completed in 26 h and this setup is capable of extracting 23.5 % Cu from the CuFeS_2 . According to these parameters, the TFB should be operated for 100 GCD cycles before refreshing the PSE in the positive compartment having capacity of 1.875 m^3 to accommodate slurry (20 wt. % solids containing CuFeS_2 to AC ratio of 4:1) containing 1 tonne of CuFeS_2 . Based on these assumptions, the total amount of energy required to operate the TFB for one year was calculated as tabulated in Table 8-3. From these calculations, it was estimated that this TFB setup can store and deliver $2975 \text{ kWh year}^{-1}$. Considering the calorific value of diesel and energy efficiency of the diesel generator (60 %), the same energy can be generated from 0.39 tonnes of diesel per year. Based on these calculations, it is estimated that to supply the energy produced by 1 tonne of diesel (7584 kWh t^{-1} of diesel) the TFB would require 860 tonnes of synthetic CuFeS_2 .

Table 8-3 Estimation of energy storage by a TFB, which has the capacity to accommodate 1 tonne of CuFeS₂ in PSE and comparison with the energy generated by a diesel generator

Design of a TFB, which can accommodate 1.0 t of CuFeS ₂ in PSE		
	Values	units
Assumptions		
Amount of energy stored in one cycle	0.0883	kWh/t of CuFeS ₂
Energy storage efficiency	40	%
Cyclic life of TFB	100	cycles
Time to complete 100 cycles	26	hours
Efficiency of Cu extraction in 100 cycles	23.4	%
Capacity of the TFB	336.92	t of CuFeS ₂ /year
Calculations based on the performance of TFB and by using synthetic CuFeS₂		
Volume of each compartment in a TFB	1.875	m ³ /t of CuFeS ₂
Amount of energy stored in 100 cycles	8.83	kWh/t of CuFeS ₂
Amount of energy supplied in 100 cycles	22.08	kWh/t of CuFeS ₂
Cu extraction capacity	27.30	t of Cu/year
Total amount of energy required to operate TFB	7446.00	kWh/year
Total amount of energy stored in TFB	2975.03	kWh/year
Total energy required for TFB including pre-processing	24820.00	kWh/year
Calculations of energy storage by TFB equivalent to diesel generator		
Calorific value of Diesel	12640	kWh/t of diesel
Energy efficiency of a diesel generator	60	%
Amount of energy available from diesel	7584	kWh/t of diesel
Total amount of diesel required to operate TFB	3.27	t of diesel/year
TFB energy storage equivalent to energy supplied by diesel generator	0.39	t of diesel/year
CuFeS ₂ to diesel ratio for energy supply	860 / 1	t/t

8.7 Summary

In this Chapter, we have presented the coupling of two energy-intensive hydrometallurgical processes in a battery-like setup capable of extracting Cu from CuFeS₂ and electrowinning Zn during a charge cycle. In the discharge cycle, part of the supplied energy is retrieved at the expense of deposited Zn. The occurrence of both pseudocapacitive (reversible)

and non-capacitive (irreversible) faradaic reactions in the positive slurry electrode containing synthetic $\text{CuFeS}_2 + \text{AC}$ in $0.2 \text{ M H}_2\text{SO}_4$ was identified from the CV scans. On the other hand, the conditions for efficient Zn deposition were optimized with the addition of $0.1 \text{ M Na}_2\text{SO}_4$ and different concentrations of CTAB in $100 \text{ g l}^{-1} \text{ Zn}^{2+}$ anolyte prepared in $0.2 \text{ M H}_2\text{SO}_4$.

A potential-concentration (PC) diagram was developed to estimate the overpotential required for efficient Zn deposition as a function of CTAB concentration. The lowest overpotential of -0.44 V and maximum 92.3% current efficiency for Zn deposition was achieved at 2 ppm CTAB concentration.

The high cell potential (0.96 V) and capability to leach Cu from CuFeS_2 during the charging cycle are promising features of this TFB. In this setup, the pseudocapacitive response of AC in synergism with the sulfide sulfur species ($\text{S}_2^{2-}/\text{S}^{2-}$) redox reaction in the positive slurry electrode facilitated the reversible deposition/re-dissolution of Zn in the negative compartment as predicted from the CV data.

Based on the results of GCD cyclic tests and Cu extraction from CuFeS_2 (from ICP-OES analysis), it is suggested that no acid is produced during charging up to 1.8 V . The transient molar flux of SO_4^{2-} from anolyte to catholyte and vice versa through the AEM was determined via mass balance. It was found that during charging, the total sulfate transported from anolyte was compensated by the Cu and Fe species generated in the catholyte.

In the 1st GCD cycle, the highest discharge specific energy of 388 Wh kg^{-1} was achieved (1.13 Wh l^{-1}), which rapidly decreased to 50 Wh kg^{-1} ($\sim 0.17 \text{ Wh l}^{-1}$) during the initial 15 repetitive GCD cycles followed by gradual fall to 23.5 Wh kg^{-1} ($\sim 0.07 \text{ Wh l}^{-1}$) in 85 cycles. The low specific energy at low coulombic ($\approx 50 \%$) and energy efficiency ($\approx 40 \%$) indicated the progression of irreversible reactions in the TFB. This was validated by ICP-OES analyses

of the catholyte and anolyte. The maximum $\approx 23\%$ Cu extracted from CuFeS_2 is an incentive from this setup in the form of valuable metal. The highest 2.05 kW kg^{-1} specific power and 34.8 Wh kg^{-1} specific energy (at 2.5C discharge rate) as well as the polarization response of the system, confirm the hybrid behavior of TFB as battery and supercapacitor.

Chapter 9: Using a CuFeS₂ mineral concentrate in the TFB-M

This chapter reports preliminary results on the use of an industrial MC of CuFeS₂ as a positive slurry electrode (PSE-M) in the TFB (designated as TFB-M) setup. Both energy storage and Cu extraction capabilities of the TFB-M setup were measured. In this setup, the electropositive PSE-M separated by a membrane was coupled with the circulating acidic Zn²⁺ containing anolyte. During charging of the TFB-M, the oxidation of the MC in the PSE-M would promote the deposition of Zn on the negative current collector (Al sheet). Part of the supplied energy could be stored in the form of deposited electroactive Zn metal. However, the large cell potential and re-dissolution of Zn from the negative electrode could release a portion of the stored energy during the discharge cycle. During the charge process, the progress of irreversible reactions in the PSE-M (i.e., Cu and Fe dissolution from CuFeS₂) and any H₂ evolution on the negative electrode would consume a large amount of energy. Consequently, the overall energy storage capability of the TFB depends on the reversible electrochemical reactions on the MC and on the Zn deposition side of the process.

9.1 Difference between TFB and TFB-M

The TFB-M uses the same experimental setup as shown in Figure 4-4 and Figure 8-7. The only difference is the addition of MC + AC mixture to form a positive slurry electrode (designated as PSE-M) in the TFB-M instead of the PSE (as used in the TFB). The same MC was injected (in the form of PSE-M) in this setup as used in the FBFC (C – 2) setup (see section 7.3 for details). Section 4.2.1 and section 7.1, respectively, describe the pre-washing procedure and mineralogy of the MC determined from QXRPD analysis and is reported in our previously published work [276]. The MC contains ~26.6 wt. % CuFeS₂ and FeS₂ (43.3 wt. %) as a major impurity as evident in the XRD pattern (Figure 7-3). The cumulative distribution curve (Figure

7-2b) of MC shows the D80 of 48.4 μm . This distribution curve also indicates the presence of variable size particles in the MC ranging from $< 1 \mu\text{m}$ to $\sim 100 \mu\text{m}$. The same anolyte (100 g Zn^{2+} + 0.1 M Na_2SO_4 + 2 ppm CTAB in 0.2 M H_2SO_4) was circulated in the negative compartment of the TFB-M.

9.2 Energetics of the TFB-M

The energetics of the battery setup depends on the electrochemical behavior of each electrode and on a sufficiently large potential difference between positive (cathode) and negative (anode) energy storage materials [314]. Similar to the TFB (Figure 8-8b), the approximate 1.0 V OCV of the TFB-M is an attractive feature of this setup, indicating the possible use of MC as an electrode material for energy storage (Figure 9-1a).

To confirm this, CV curves of the TFB-M were obtained at various sweep rates (from 100 to 1 mV s^{-1}). The positive current obtained by varying the potential from OCV to 1.9 V cell potential ($\sim 0.9 \text{ V}$ vs. OCV) in the forward scan exhibits the charging of the TFB-M. On the other hand, by reversing the scan from 1.8 V to low cell potential ($\sim 0.5 \text{ V}$) the discharge current profile is measured. During the discharge cycle, the current peaks demonstrated the reversal of electrochemical reactions, which occurred in the preceding charge step. As discussed in Chapter 8, the appreciable increase in the anodic current (during the charge step) as shown in Figure 9-1b, indicates the progress of Zn deposition on negative electrode and oxidation reactions in the PSE-M. The re-dissolution of Zn in the anolyte and occurrence of reversible reaction on the PSE-M during the discharge process were responsible for the current output in the reverse scan. The decrease in both positive and negative current with a decrease in sweep rate attributed to the growth of diffusion layer on the surface of electrodes materials. In other words, with the progress of kinetically controlled electrochemical reactions, the

diffusion layer at the electrode/electrolyte interface, which would grow. The decrease in current response at slow sweep rates confirms this behavior. For instance, at 100 mV s^{-1} , the large peak current during the charging/discharging process shows the oxidation/reduction reactions in the PSE-M.

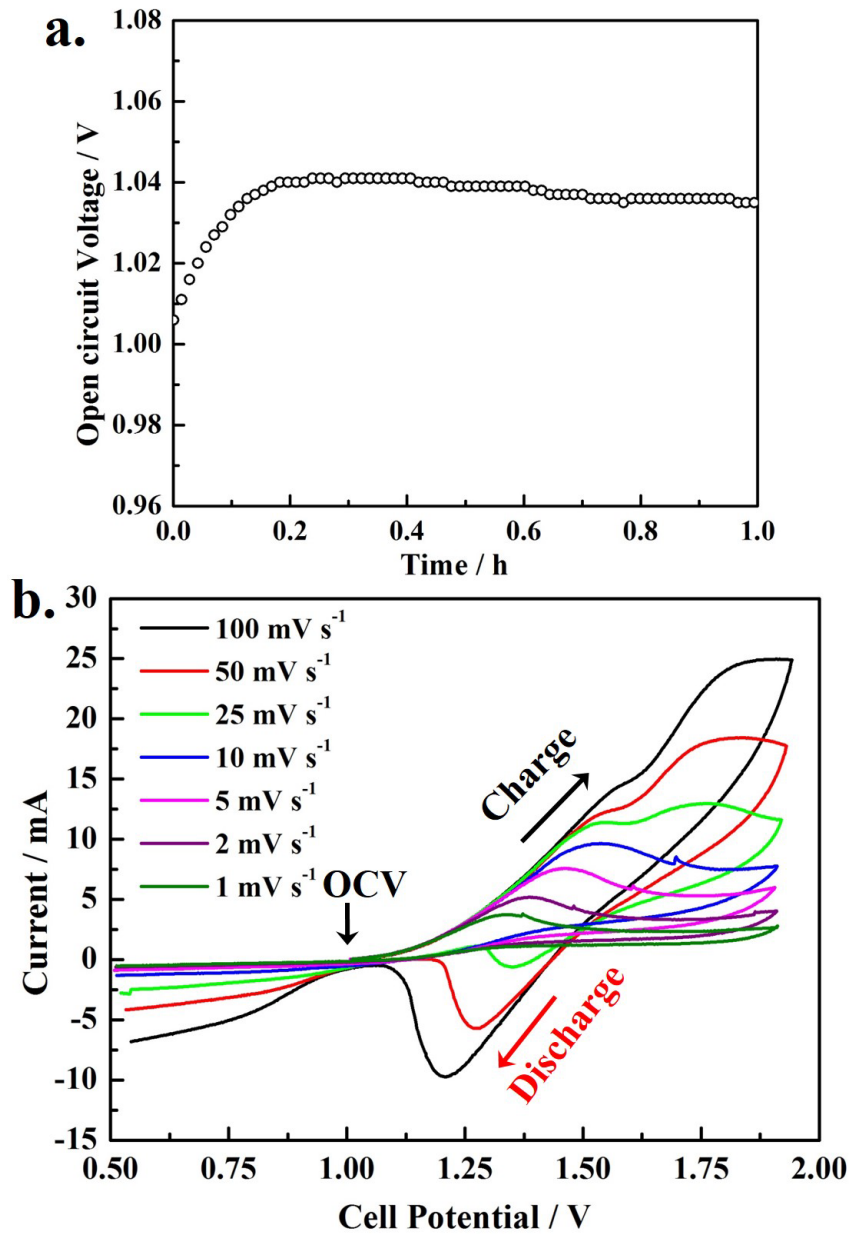


Figure 9-1 (a) OCV of the TFB-M and (b) CV scans of the TFB-M at various sweep rates.

In addition, at slow sweep rates, it was interesting to note the disappearance of a discharge current peak (between 1.25 – 1.50 V), which indicated the occurrence of irreversible reactions (non-capacitive faradaic response) in the TFB-M. This behavior corresponds to the oxidation reactions in the PSE-M that consumed a considerable amount of the supplied charge in the charge cycle, possibly due to the formation of reaction product (i.e. metal-deficient polysulfide film via reaction 6.1) on the surface of CuFeS_2 . Therefore, the relatively small discharge current at low potential (< 1 V) compared to charging current showed irreversibility in the TFB-M. This effect also indicates that impurity phases in the MC would consume a large amount of supplied energy and may induce polarization effects in the TFB-M.

During discharge, the small limiting current response represents diffusion-controlled processes, which are most likely associated with the conversion layer that may form on the surface of MC particles during the charge process and to the large impurity phases in the PSE-M. To further, explore this irreversibility in the TFB-M, CV cycles repeated at 25 mV s^{-1} sweep rate are shown in Figure 9-2. In cycle-1, the charge current was relatively larger than the charge current response in the second cycle (cycle-2). The increase in current during charge cycle corresponded to the dissolution of Cu and Fe from the PSE-M and Zn deposition in the negative electrode. However, decrease in charge current in the second cycle indicated the restricted oxidation reactions in the PSE-M possibly due to the passivation of CuFeS_2 in the PSE-M. During charging, the first peak (P1c) at ~ 1.5 V (cell potential) was related to the pseudocapacitive response of the AC and active dissolution of CuFeS_2 in the PSE-M supported by Zn deposition on the negative electrode. However, an increase in the current beyond 1.5 V and peak P2c at (~ 1.75 V) corresponds to the formation of a passive film on the surface of CuFeS_2 . In the reverse scan (discharge cycle), the large IR drop (~ 0.5 V) (see Figure 9-2) also

highlights the restricted kinetic response of the TFB-M, mainly associated with the irreversible charge transfer processes and impurity contents in the PSE-M. A current peak (Pd1) at ~1.35 V similar to the peak P2 observed in case of TFB (see Figure 8-8c) corresponds to the pseudocapacitive response of the AC in the PSE-M.

Further discharging to low cell potential resulted in a slight increase in the current (cycle 1). Owing to the concentration of CuFeS_2 in the MC, this limiting discharge current further validated the formation of the surface film and its non-capacitive (irreversible) character in the PSE-M. However, after the first discharge cycle, in the charging scan (cycle-2), a small peak P3c was observed at approximately 1.0 V, which was attributed to the oxidation of the products formed in the PSE-M during the preceding discharge cycle. The small charging current associated with this peak (P3c) compared to the discharge current in cycle-1 confirmed the occurrence of irreversible reactions in the TFB-M. Compare to the discharge current in cycle-1, the relatively small discharge current in cycle-2 indicated that this setup could be used as a primary battery. This is obtained by applying only one charge and discharge cycle on the TFB-M and then replacing the PSE-M with fresh MC feed prior to next GCD cycle.

From the hydrometallurgical perspective, the attractive feature of this TFB-M is its use as a unit for Zn electrowinning. Instead of using the water oxidation reaction in the conventional Zn electrowinning cell, one could use the PSE-M in the TFB-M. The additional benefit of this setup could be the Cu extraction from the MC during repetitive charge cycles and the depleted PSE-M (due to Cu dissolution) could be replaced with the fresh slurry after a certain number of charge cycles (for example after 10 –14 cycles as discussed in the following section).

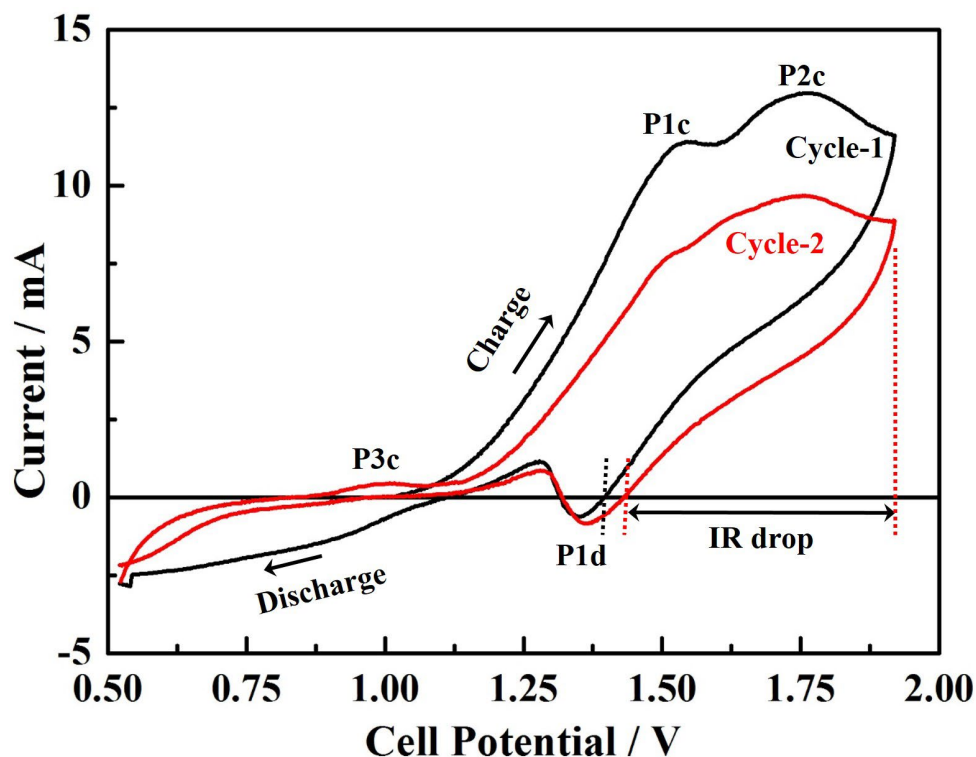


Figure 9-2 CV curves of TFB-M (at 25 mV s^{-1}) showing the variation in current response during repetitive cycling

9.3 Energy storage and Cu extraction capabilities

Based on the electrochemical behavior and small current response of the TFB-M during repetitive charge and discharge (CV scans), it was estimated that this setup should be charged and discharged at low currents. To evaluate the cyclic performance of the TFB-M, the charging and discharging was carried out at 2 mA and 0.5 mA, respectively. In addition, 1.6 and 0.6 V cut-off cell potentials during charge and discharge cycles respectively, were selected for the TFB-M. The mass of the Zn^{2+} deposited on the negative electrode during the charge cycle is equal to the amount of Zn^{2+} re-dissolved during the discharge cycle and can be estimated from the discharge capacity. Figure 9-3 shows the three repetitive charge and discharge cycles and the total charge (volumetric capacity) was determined by integrating the charge/discharge

profiles according to Equation 8.6. In this relation the charge was normalized by the volume of slurry in the positive electrode compartment of the TFB-M.

In the 1st charge cycle, akin to the current peak (P1c) in the CV scan, the extended potential plateau at ~1.53 V represents the effective Zn deposition on the negative electrode and oxidation of the MC in the PSE-M. It is important to note that the total charge consumed by the TFB-M in the 1st charge was approximately 5 times larger than the 1st discharge capacity. This behavior corroborates to the progress of non-capacitive faradaic (irreversible reactions) processes. In confirmation to the discharge peak Pd1 (Figure 9-2), the potential plateau at ~1.4 V during the 1st discharge represents the possible adsorption of Cu^{II} and Fe^{II} species on the AC in addition to its non-faradaic capacitive response (charge stored in the electrical double layer). During the discharge cycle, these processes in the PSE-M were supported by the Zn re-dissolution in the negative compartment of the TFB-M. Cu^{II} and Fe^{II} species were generated from the oxidation of CuFeS₂ in the PSE-M during the charging step. The appearance of the small potential plateau at ~1.44 V in the 2nd charge cycle is due to the pseudocapacitive response of the AC and oxidation of the reaction products formed in the PSE-M in the preceding discharge. The shift in the potential plateau to 1.57 V in the 2nd charge cycle reflects the hindrance in the charge transfer processes that was associated with the possible irreversible character of the impurity phases in the PSE-M. This was confirmed by the significant decrease in the capacity from 16.5 to 9.4 mAh l⁻¹ in the 2nd discharge cycle.

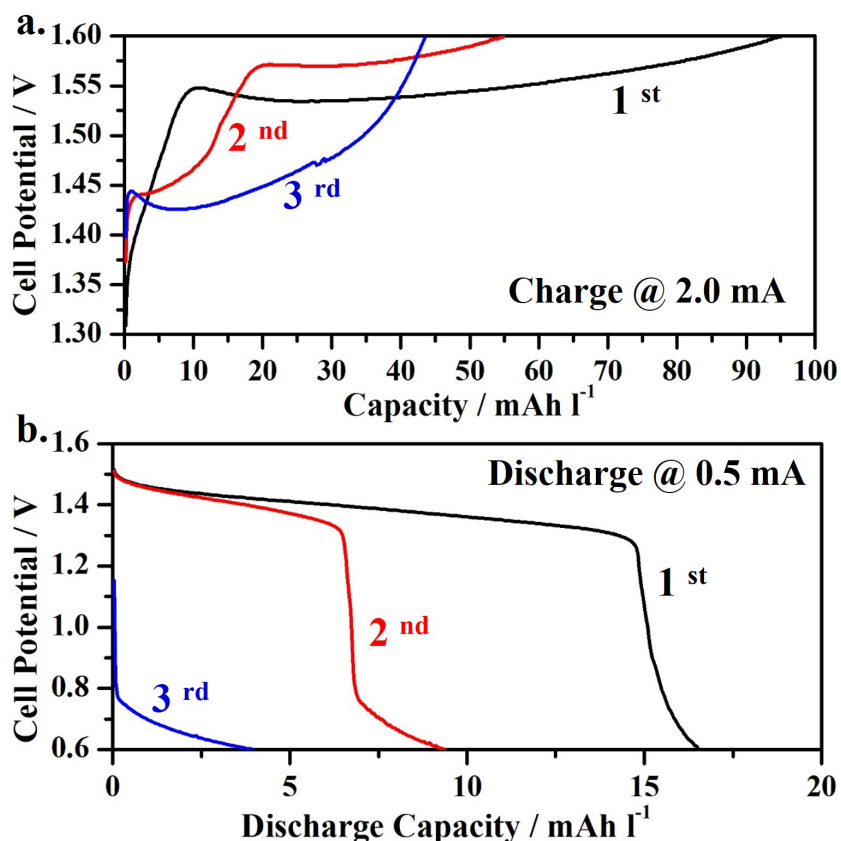


Figure 9-3 The galvanostatic (a) charge and (b) discharge profiles of TFB-M (initial 3 cycles).

Large polarization effects in the TFB-M are evident in the 3rd cycle, which has a decrease in the charging potential plateau followed by a limiting non-capacitive faradaic response (rapid increase in the cell potential). This trend indicated the diffusion-controlled processes in the TFB-M, mostly associated with the passivation of CuFeS₂ in the MC and possibly to the impurity phases in the PSE-M, which may not support reversible reactions during repetitive GCD cycling. Similarly, in the following discharge (3rd cycle), the rapid potential drops to ~0.8 V and slightly extended decaying potential profile up to 0.6 V (cutoff potential) highlighted the hindrance in the progress of pseudocapacitive faradaic reactions due to kinetic limitations in the PSE-M. In simple words, the discharge capacity of the TFB-M setup is related to the amount of Zn that will deposit during the charge cycle. The cyclic

charge/discharge performance of the TFB-M was dependent on both the reversible Zn^{2+} deposition/dissolution and pseudocapacitive behavior of PSE-M. The discharge capacity of $\sim 4 \text{ mAh l}^{-1}$ and low η_C ($\sim 9 \%$) was obtained by the TFB-M in the 3rd GCD cycle. This confirmed the progress of irreversible reactions (e.g. conversion reactions and dissolution of Fe and Cu from $CuFeS_2$) in the PSE-M during the initial 3 cycles. The very small η_C also reflects the significant amount of supplied charge that was consumed in the irreversible reaction (conversion reaction), and that was not available in the following discharge cycle.

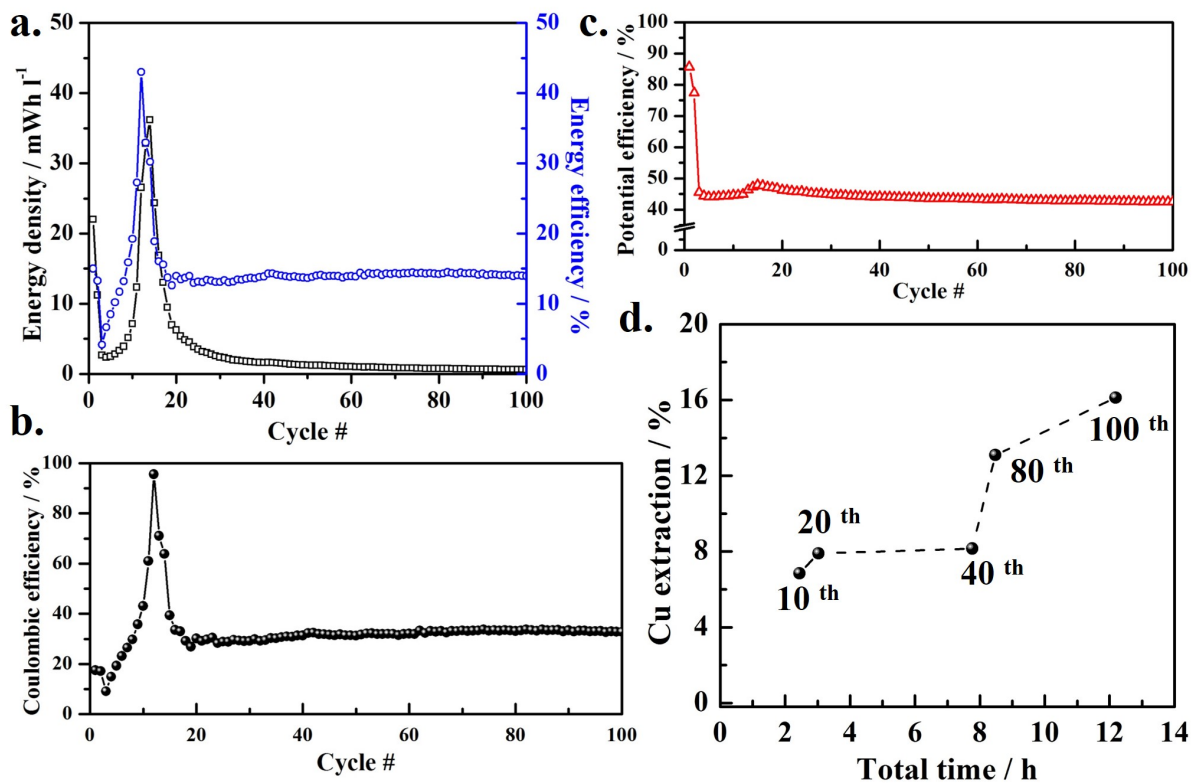


Figure 9-4 The performance of TFB-M setup (a) energy density vs. no. of cycles, (b) coulombic efficiency, (c) potential efficiency and (d) rate of Cu extraction measured from ICP–OES analysis of the PSE-M filtrate after various GCD cycles. (Note: the specific energy is calculated based on the volume of slurry in the PSE-M).

Repetitive GCD cyclic tests were also conducted to estimate the cyclic discharge energy density, η_E , η_C , and η_V of the TFB-M. As shown in Figure 9-4a, the discharge energy density was calculated from the GCD plots and by using Equation 9-1.

$$\text{Energy density (Wh l}^{-1}\text{)} = \frac{1}{3.6V_S} \int_{t_1}^{t_2} \Delta V(t) \cdot i_d \cdot dt \quad \text{Equation 9-1}$$

Where V_S is the volume of slurry in the PSE-M and other parameters have their usual meaning as discussed in Chapter 7. The rapid fall in the energy density from 22 to 2.6 mWh l⁻¹ with sharp decrease in η_E (from 15 to 4 %) in the first three cycles represents the enormous loss in the supplied energy mostly consumed by conversion and parasitic reactions in the TFB-M.

Interestingly, in the following 10 cycles, the monotonic increase in the energy density (max. ~36.2 mWh l⁻¹ at 14th cycle) and a considerable increase in energy efficiency to 43% reflects an improvement in the charge storage capability of the TFB-M. As discussed in section 8.3, the enhancement in the pseudocapacitive response is attributed to the reversibility of the S₂²⁻/S²⁻ redox reaction on the surface of sulfidic minerals i.e., CuFeS₂ and FeS₂ in the MC.

In previous chapters (see section 7.2, 8.3 and 8.4.1 and reference cited therein for further details), the formation of a polysulfide film and the existence of sulfide sulfur species on the surface of CuFeS₂ are examined and discussed. In addition, the presence of ~43 % FeS₂ in the MC and the reversible character of S₂²⁻/S²⁻ species on its surface could further augment the pseudocapacitive response of MC as found in the FBFC setup (C-2) (see section 7.3) [212, 264].

Similarly, as shown in Figure 9-4b, the considerable increase in the η_C (from ~17 to ~95 %) between the 4th and 12th GCD cycles further confirms this behavior. The reversible character of sulfide sulfur species formed on the surface of CuFeS₂ and FeS₂ in the PSE-M was responsible for this increase in the η_C . On the other hand, the η_V of the TFB-M setup

decreased rapidly from 85.7 to 45.5 % in the first three GCD cycles, which with slight variation, remained almost constant in the successive 97 cycles (Figure 9-4c). As depicted in Figure 9-3b, the disappearance of high potential plateau and origin of the relatively small decaying potential profile at low cell potential was evident and attributed to the reversible character of the sulfide sulfur species as discussed in Chapters 5, 6, and 7. The reason for the rapid decrease in the potential efficiency was associated with the decay in discharge potential and due to kinetic limitation of reversible faradaic processes. From these results, the rapid potential drop (IR drop) during discharge cycles may also be related with the high inter-particulate contact resistance in the PSE-M.

The ICP–OES analysis of the PSE-M filtrate after the 10th cycle (2.4 h) revealed 6.8 % Cu dissolution from the MC. From these results, it can be predicted that during the initial 3 charge/discharge cycles, a large amount of supplied charge is consumed in the formation of a passive film on the surface of CuFeS₂ with partial dissolution of Cu and Fe in the PSE-M (irreversible reactions). However, parasitic H₂ evolution reaction on the negative electrode during the charging step may also influence the cyclic performance of the TFB-M. Further increase in the η_C and η_E in the next 10 cycles were related to the growth of metal-deficient polysulfide surface film that could facilitate the reversible processes in the TFB-M. The Cu extraction increased to approximately 16.1 % in 100 GCD cycles, which completed in almost 12.2 h. Nevertheless, during this GCD cycling, ~ 86 % of the supplied energy was consumed in the progress of irreversible reactions (e.g., dissolution of Cu and Fe from CuFeS₂) in the TFB-M as shown in Figure 9-4a. The reversible charge storage capacity (< 1 mAh l⁻¹) of the TFB-M was low in the last 85 GCD cycles.

9.4 Energy storage equivalent to energy produced by a diesel generator

A design of the TFB-M that could process 1 tonne of MC (containing 26.6 % CuFeS_2) is proposed in this section. The PSE-M used in the TFB-M contains 20 wt. % total solids (MC to AC ratio of 4) in 0.2 M H_2SO_4 . The TFB-M can be operated in batches and each batch would consist of 100 GCD cycles, which completes in 12.2 hours. The average energy storage capability of this setup over 100 GCD cycles (each batch) is 1.5 mWh l^{-1} based on the volume of the PSE-M. This setup could process approximately 718 tonnes of MC per year and could produce 16.1 % of this mass in Cu, which is equivalent to 10.65 tonnes of Cu per year as given in Table 9-1. In addition, this single unit, which accommodates 1 tonne of MC in each batch, could store and supply approximately $673 \text{ kWh year}^{-1}$ of energy at 30 % efficiency. Based on the calorific value of diesel ($12.64 \text{ kWh kg}^{-1}$) and considering 60 % efficiency of a commercial diesel generator, 1 tonne of diesel would generate (7584 kWh) of energy. As a result, it is calculated that to store the same amount of energy as produced from 1 tonne of diesel, approximately 8089 tonnes of MC would have to be processed in the TFB-M. Thus to store the energy equivalent to 7584 kWh t^{-1} of diesel, approximately 11 TFB-M setups each having a capacity to process 718 tonnes of MC per year and energy storage capability of $673 \text{ kWh year}^{-1}$, would be required. Compared to the TFB that uses synthetic CuFeS_2 (as given in Table 8-3), the TFB-M would require approximately 9 times more MC over one year to store the same amount of energy (7584 kWh t^{-1} of diesel). However, this ratio strongly depends on the average amount of energy storage in each cycle during operation of the TFB-M. In addition, the grade of MC and the effect(s) of impurities could significantly influence the energy storage capability of this setup.

The requirement for ~8089 tonnes of MC to store the equivalent energy to 1 tonne of diesel at the mine site is not a significant issue in terms of the concentrate mass. Indeed, copper concentrators often produce approximately 35,000 tonnes of mineral concentrate *per day*.

Table 9-1 Energy storage capability of TFB-M, which can process 1 tonne of MC in one batch and estimation of MC to diesel ratio for the supply of same amount of energy

Design of a TFB-M, which can accommodate 1.0 t of MC in PSE-M		
	Values	units
Assumptions		
Amount of energy stored in one cycle	0.009	kWh/t of MC
Energy storage efficiency	30	%
Cyclic life of TFB-M	100	cycles
Time to complete 100 cycles	12.2	hours
Efficiency of Cu extraction in 100 cycles	16.1	%
Capacity of the TFB-M	718.03	t of MC/year
Calculations based on the performance of TFB-M and by using MC		
Volume of each compartment in a TFB-M	1.875	m ³ /t of MC
Amount of energy stored in 100 cycles	0.94	kWh/t of MC
Amount of energy supplied in 100 cycles	3.13	kWh/t of MC
Cu extraction capacity	10.65	t of Cu/year
Total energy required to operate TFB-M	2243.85	kWh/year
Total energy stored in TFB-M	673.16	kWh/year
Total energy required for TFB-M including pre-processing	7479.51	kWh/year
Calculations of energy storage by TFB-M equivalent to diesel generator		
Calorific value of Diesel	12640	kWh/t of diesel
Energy efficiency of a diesel generator	60	%
Amount of energy available from diesel	7584	kWh/t of diesel
Total amount of diesel required to operate TFB	0.99	t of diesel/year
TFB-M energy storage equivalent to energy supplied by diesel generator	0.09	t of diesel/year
MC to diesel ratio for energy supply	8089.6 / 1	t/t

9.5 Summary

This Chapter focused on the use of the TFB-M as a hybrid unit for both energy storage and Cu extraction. The discharge energy density of the TFB-M increased sharply to 36.2 mWh l^{-1} during the initial 14 GCD cycles. This is attributed to the formation of a polysulfide passive film and to the reversible character of $\text{S}_2^{2-}/\text{S}^{2-}$ species, which exist and may grow on the surface of CuFeS_2 and FeS_2 particles in acidic media during repetitive charge cycles. The η_C and η_E also increased monotonically to 95.6 % and 43 %, respectively, with approximately 6.8 % Cu extraction from the TFB-M during the initial 10 GCD cycles (about 2.4 hours). However, in the following 85 cycles, the low η_C (~33 %) and η_E (~14 %) suggested the progress of irreversible reactions in the TFB-M (i.e., the formation of the passive film, dissolution of Cu and Fe in the PSE-M and H_2 evolution on the negative electrode). In 100 GCD cycles, a maximum 16.1 % Cu extraction was achieved in 12.2 h.

Chapter 10: Conclusion

10.1 Remarks on the important findings

This thesis presents the first use of synthetic CuFeS_2 and MC in aqueous-based battery like setups that are capable of extracting Cu and storing energy. In the existing secondary battery setups, the non-capacitive faradaic (irreversible) reactions are always undesired because these reactions deteriorate their cyclic performance and charge storage capability. However, in this research work, irreversible faradaic reactions, i.e., Cu dissolution from CuFeS_2 is a desirable feature. Two-hybrid batteries, i.e. FBFC and TFB setups, were introduced. Using synthetic CuFeS_2 and MC as electrode materials in these setups, the energy storage and Cu extraction capabilities were determined. Following are the pointwise conclusions from the experimental results discussed in the preceding chapters.

Setup-1: (FBFC)

1. The detailed electrochemical analyses of the composite electrode (negative GF- CuFeS_2 electrode) and GF (positive) electrode in their respective electrolytes revealed the occurrence of quasi-reversible redox reactions (pseudocapacitive; faradaic reactions) in the FBFC that were responsible for energy storage.
2. The designed FBFC is capable of storing 2 to 6.3 Wh kg^{-1} energy over 500 GCD cycles. The coulombic and energy efficiencies of this setup were ~80 % and ~30 %, respectively. The cause of limited energy storage and low energy storage efficiency in the FBFC is related to the progress of irreversible conversion reactions on the CuFeS_2 surface such as the dissolution of Cu from CuFeS_2 , which consumed ~70 % of the supplied energy.

3. A maximum 10.3 % Cu was also extracted from CuFeS₂ during cycling, which is a unique feature of this setup suggesting the simultaneous use of FBFC for both energy storage and as a unit for Cu extraction.
4. The use of naturally sourced MC in this FBFC could supply up to 8.5 Wh kg⁻¹ specific energy in addition with 12.7 % Cu extraction in 400 GCD cycles.

Setup–2: (TFB)

5. We introduced the trifunctional battery setup for the very first time in which both Zn deposition and Cu extraction take place simultaneously during the charge cycle. The deposition of highly electroactive Zn metal on the negative Al electrode was facilitated by the oxidation of CuFeS₂ (dissolution of Cu and Fe) in this setup. Both of these processes are very important from a hydrometallurgical perspective. The re-dissolution of deposited Zn supported by the pseudocapacitive reactions in the PSE during the discharge cycle resulted in the release of stored energy which is an important feature of this setup.
6. In the first GCD cycle, the TFB setup provided the highest discharge specific energy of 388 Wh kg⁻¹ (1.13 Wh l⁻¹), which decreased to 50 Wh kg⁻¹ (0.17 Wh l⁻¹) during the initial 15 repetitive GCD cycles and to 23.5 Wh kg⁻¹ (~0.07 Wh l⁻¹) in the following 85 cycles. The low specific energy at low coulombic ($\approx 50\%$) and energy efficiency ($\approx 40\%$) indicated the progression of irreversible reactions in the TFB.
7. These irreversible reactions in the TFB resulted in approximately 23 % Cu extraction from the synthetic CuFeS₂ in 100 GCD cycles (~26 h).
8. The highest 2.05 kW kg⁻¹ specific power and 34.8 Wh kg⁻¹ specific energy (at 2.5C discharge rate) in the first GCD cycle also highlighted the hybrid character of the TFB.

This is another promising feature of this setup and may be used to overcome momentary power outages.

9. By using MC as PSE-M in the TFB-M setup, the energy density increased from 2.6 to $\sim 36.2 \text{ mWh l}^{-1}$ monotonically from 3 to 14 GCD cycles and approximately 16.1 % Cu was extracted from the MC in 100 GCD cycles, which were completed in 12.2 h.
10. Based on these results, it is suggested that the TFB-M can be used either as primary battery or as a unit for Cu extraction and Zn electrowinning, as required by the user. For instance, by restricting the process to the charge step, one could use TFB-M as a Zn electrowinning setup, which uses MC in the positive compartment. Also, after various charging steps, Cu extraction from MC is possible as evident from the GCD tests and ICP-OES analyses in Chapter 9.

10.2 The practical implications of the current research work

This research work used a widely available natural mineral as an electrode material in battery like setups. The relatively low energy efficiency by these systems compared to existing commercial batteries is offset by the valuable Cu extraction from the mineral and the relatively low cost and inexhaustible supply of the electrode material (MC). To recover Cu, existing hydrometallurgical practices, i.e., solid/liquid separation, solvent extraction, and electrowinning processes can be adopted without modification. These battery setups coupled with renewable energy generating units could be installed at remote mining sites to partially fulfill the energy demands for stationary applications with an additional advantage of Cu extraction. Certainly, to improve both energy efficiency and Cu extraction capabilities, the modification in the electrode(s) system, cell design and change in electrolyte composition is required. In this regard, some key points are highlighted in the following section, which may

be considered in the future research work to further enhance the performance of these batteries. By using MC in the TFB-M, the energy storage capacity increased monotonically in the initial 15 cycles. However, the low energy efficiency (14 %) of this setup corresponds to the occurrence of parasitic reactions in the cell, which limit the cyclic life of this setup. However, by injecting fresh PSE every 15 cycles this setup becomes more attractive for a continuous process.

10.3 Future perspectives and recommendations

To improve the performance of these setups there are many aspects that need further research. Mainly, testing of various MC concentrates (taken from different sources and of different compositions) in these systems is the key recommendation for future research. However, a few points are highlighted that may be considered in any future research.

Setup 1: FBFC

Depending on the requirement and use of the FBFC, either as a Cu extraction unit or as a device for energy storage, upscaling and modification in the existing design is proposed based on the following conditions.

- In the composite electrode, the surface modification of the GF, the addition of pseudocapacitive activated carbon in the CuFeS₂/MC could improve the coulombic and energy efficiencies of FBFC.
- Use of highly conductive and kinetically active materials (Pt-doped graphite felt) in the positive electrode may enhance the electrochemical kinetics of Fe^{II}/Fe^{III} redox reaction, which may ultimately improve the cyclic charge/discharge performance of the FBFC.

- The temperature, electrolyte flow rate and initial acid (in both anolyte and catholyte) concentration effects may be studied to further enhance the Cu extraction and energy storage capability.
- During continuous GCD cycling, the consumption of CuFeS_2 (due to Cu dissolution) would require the frequent replacement of the composite electrodes in FBFC. Modification of the existing FBFC design is therefore recommended. For this, the intermittent CuFeS_2/MC slurry (instead of fixed bed) flow cell design is suggested. In this setup, slurry could be injected in the negative compartment to make this setup more flexible for a continuous supply of energy and Cu from the mineral concentrate.
- The rigorous characterization of the slurry electrode, i.e., the effect of mineral particle size, acid concentration, temperature, impurities and solid contents in the slurry and its effect on the viscosity is recommended due to its direct impact on the pumping requirements and related cost for injection and circulation.
- To simulate the effect of impurities on the electrochemical performance of the mineral concentrates, a varying amount of impurities such as pyrite in the synthetic CuFeS_2 may be added to explore the optimum conditions for impurity level in the FBFC in order to achieve maximum Cu extraction and energy efficiency from MC.

Setup 2: TFB

In the TFB, for only hydrometallurgical interest, to achieve both Cu extraction and Zn-electrowinning, the operation of this setup must be stopped after the charge cycle. However, both Cu extraction and energy retrieval is possible upon sacrificing the deposited Zn during the discharge cycle.

- To enhance the Cu extraction and energy storage capability of the TFB, investigation of the optimum amount of solid contents in the PSE and adjustment of CuFeS₂/AC ratio is required. These factors could significantly influence the conductivity of the PSE, pumping requirements and may affect the particle-particle and particle to current collector contact during operation of the TFB.
- The amount of deposited Zn on the negative electrode is proportional to the oxidation reactions in the PSE compartment. Thus, the energy storage capability and Cu extraction rate in the TFB can be enhanced by increasing the surface area of the negative current collector. The use of porous metal (Al foam) electrodes could be used in the TFB to increase surface area.
- It is important to understand the local changes on the surface of the negative electrode during Zn deposition in the charge cycle. For instance, hydrogen evolution at the surface will change the local pH, which could affect the Zn deposition efficiency and may deteriorate the cyclic performance of the TFB. Therefore, in-situ pH monitoring at the electrode surface during charge and discharge cycle can provide useful information to adjust the anolyte composition in the external reservoir and to adjust its flow rate.
- To use the TFB as a high-energy storage device, the PSE can be replaced by injecting fresh slurry in the cell after a specific number of cycles depending on the GCD cyclic performance.
- To avoid the cross-contamination of the anolyte and catholyte, a novel design of TFB will be studied. In this setup, an ion-exchange resin and membranes will be used together to improve the efficiency for both Cu extraction and energy storage. Additionally, with slight

modification, the preferential loading of Cu on the resin could eliminate the extra purification step before Cu electrowinning.

References

- [1] G. Calvo, G. Mudd, A. Valero, A. Valero, Decreasing Ore Grades in Global Metallic Mining: A Theoretical Issue or a Global Reality?, *Resources* 5(4) (2016).
- [2] J. Kulczycka, Ł. Lelek, A. Lewandowska, H. Wirth, J.D. Bergesen, Environmental impacts of energy-efficient pyrometallurgical copper smelting technologies: The consequences of technological changes from 2010 to 2050, *Journal of Industrial Ecology* 20(2) (2016) 304-316.
- [3] R. Memary, D. Giurco, G. Mudd, L. Mason, Life cycle assessment: a time-series analysis of copper, *Journal of Cleaner Production* 33 (2012) 97-108.
- [4] G. Lagos, D. Peters, A. Videla, J.J. Jara, The effect of mine aging on the evolution of environmental footprint indicators in the Chilean copper mining industry 2001–2015, *Journal of Cleaner Production* 174 (2018) 389-400.
- [5] W. Kuckshinrichs, P. Zapp, W.-R. Poganietz, CO₂ emissions of global metal-industries: The case of copper, *Applied Energy* 84(7) (2007) 842-852.
- [6] S. Northey, S. Mohr, G. Mudd, Z. Weng, D. Giurco, Modelling future copper ore grade decline based on a detailed assessment of copper resources and mining, *Resources, Conservation and Recycling* 83 (2014) 190-201.
- [7] D. Dreisinger, Copper leaching from primary sulfides: Options for biological and chemical extraction of copper, *Hydrometallurgy* 83(1) (2006) 10-20.
- [8] G. Yue, E. Asselin, Kinetics of Ferric Ion Reduction on Chalcopyrite and its Influence on Leaching up to 150°C, *Electrochimica Acta* 146 (2014) 307-321.
- [9] R. Garrels, C. Christ, *Solutions, minerals, and equilibria*, Harper and ROW, New York, 1965.
- [10] E.M. Córdoba, J.A. Muñoz, M.L. Blázquez, F. González, A. Ballester, Leaching of chalcopyrite with ferric ion. Part I: General aspects, *Hydrometallurgy* 93(3) (2008) 81-87.
- [11] A. Ghahremaninezhad, D.G. Dixon, E. Asselin, Kinetics of the ferric–ferrous couple on anodically passivated chalcopyrite (CuFeS₂) electrodes, *Hydrometallurgy* 125-126 (2012) 42-49.
- [12] L. Mureşan, G. Maurin, L. Oniciu, D. Gaga, Influence of metallic impurities on zinc electrowinning from sulphate electrolyte, *Hydrometallurgy* 43(1) (1996) 345-354.
- [13] J.-M. Lu, H.-J. Guo, D. Dreisinger, B. Downing, Effects of Current Density and Nickel as an Impurity on Zinc Electrowinning, *Journal of Metallurgical Engineering* 2(3) (2013) 79-87.
- [14] D.J. Mackinnon, P.L. Fenn, The effect of germanium on zinc electrowinning from industrial acid sulphate electrolyte, *Journal of Applied Electrochemistry* 14(4) (1984) 467-474.
- [15] M.P. Hu, D.L. Piron, The effects of arsenic and lead impurities on the current efficiency and deposit composition in alkaline zinc electrowinning, *The Canadian Journal of Chemical Engineering* 70(3) (1992) 553-558.
- [16] A.M. Alfantazi, D.B. Dreisinger, The role of zinc and sulfuric acid concentrations on zinc electrowinning from industrial sulfate based electrolyte, *Journal of Applied Electrochemistry* 31(6) (2001) 641-646.
- [17] A.P. Brown, J.H. Meisenhelder, N.P. Yao, The alkaline electrolytic process for zinc production: a critical evaluation, *Industrial & Engineering Chemistry Product Research and Development* 22(2) (1983) 263-272.

- [18] F. Parada T, E. Asselin, Reducing power consumption in zinc electrowinning, *JOM* 61(10) (2009) 54.
- [19] E. Hu, X.-Q. Yang, Rejuvenating zinc batteries, *Nature Materials* 17(6) (2018) 480-481.
- [20] F. Wang, O. Borodin, T. Gao, X. Fan, W. Sun, F. Han, A. Faraone, J.A. Dura, K. Xu, C. Wang, Highly reversible zinc metal anode for aqueous batteries, *Nature Materials* 17(6) (2018) 543-549.
- [21] J.F. Parker, C.N. Chervin, E.S. Nelson, D.R. Rolison, J.W. Long, Wiring zinc in three dimensions re-writes battery performance—dendrite-free cycling, *Energy & Environmental Science* 7(3) (2014) 1117-1124.
- [22] S. Panda, A. Akcil, N. Pradhan, H. Deveci, Current scenario of chalcopyrite bioleaching: A review on the recent advances to its heap-leach technology, *Bioresource Technology* 196 (2015) 694-706.
- [23] F. Habashi, *Chalcopyrite: Its chemistry and metallurgy*, McGraw-Hill New York 1978.
- [24] Y. Li, N. Kawashima, J. Li, A.P. Chandra, A.R. Gerson, A review of the structure, and fundamental mechanisms and kinetics of the leaching of chalcopyrite, *Advances in Colloid and Interface Science* 197-198 (2013) 1-32.
- [25] J. Petiau, P. Saintavit, G. Calas, K X-ray absorption spectra and electronic structure of chalcopyrite CuFeS_2 , *Materials Science and Engineering: B* 1(3) (1988) 237-249.
- [26] R.T. Jones, *Electronic structures of the sulfide minerals sphalerite, wurtzite, pyrite, marcasite, and chalcopyrite*, University of South Australia, 2006, pp. 151-156.
- [27] S. Conejeros, P. Alemany, M. Llunell, I.d.P. Moreira, V.c. Sánchez, J. Llanos, Electronic structure and magnetic properties of CuFeS_2 , *Inorganic chemistry* 54(10) (2015) 4840-4849.
- [28] M. Fujisawa, S. Suga, T. Mizokawa, A. Fujimori, K. Sato, Electronic structures of CuFeS_2 and $\text{CuAl}_{0.9}\text{Fe}_{0.1}\text{S}_2$ studied by electron and optical spectroscopies, *Physical Review B* 49(11) (1994) 7155-7164.
- [29] T. Teranishi, K. Sato, K.i. Kondo, Optical Properties of a Magnetic Semiconductor: Chalcopyrite CuFeS_2 : I. Absorption Spectra of CuFeS_2 and Fe-Doped CuAlS_2 and CuGaS_2 , *Journal of the Physical Society of Japan* 36(6) (1974) 1618-1624.
- [30] E. Peters, Direct Leaching of sulfides: Chemistry and applications, *Metallurgical Transactions B* 7(4) (1976) 505-517.
- [31] D.L. Jones, *The leaching of chalcopyrite*, Department of Metals and Materials Engineering, University of British Columbia, Vancouver, Canada, 1974.
- [32] D. Nava, I. González, D. Leinen, J.R. Ramos-Barrado, Surface characterization by X-ray photoelectron spectroscopy and cyclic voltammetry of products formed during the potentiostatic reduction of chalcopyrite, *Electrochimica Acta* 53(14) (2008) 4889-4899.
- [33] E.C. Todd, D.M. Sherman, J.A. Purton, Surface oxidation of chalcopyrite (CuFeS_2) under ambient atmospheric and aqueous (pH 2-10) conditions: Cu, Fe L- and O K-edge X-ray spectroscopy, *Geochimica et Cosmochimica Acta* 67(12) (2003) 2137-2146.
- [34] Q. Yin, G. Kelsall, D. Vaughan, K. England, Atmospheric and electrochemical oxidation of the surface of chalcopyrite (CuFeS_2), *Geochimica et Cosmochimica Acta* 59(6) (1995) 1091-1100.
- [35] S.L. Harmer, J.E. Thomas, D. Fornasiero, A.R. Gerson, The evolution of surface layers formed during chalcopyrite leaching, *Geochimica et Cosmochimica Acta* 70(17) (2006) 4392-4402.

- [36] Q. Yin, G.H. Kelsall, D.J. Vaughan, K.E.R. England, Atmospheric and electrochemical oxidation of the surface of chalcopyrite (CuFeS_2), *Geochimica et Cosmochimica Acta* 59(6) (1995) 1091-1100.
- [37] P. Eadington, Study of oxidation layers on surfaces of chalcopyrite by use of Auger-electron spectroscopy Transactions of the institution of mining and metallurgy section C-Mineral processing and extractive metallurgy 86 (1977) C186-C189.
- [38] T. Biegler, M.D. Horne, The electrochemistry of surface oxidation of chalcopyrite, *Journal of The Electrochemical Society* 132(6) (1985) 1363-1369.
- [39] J.C.W. Folmer, F. Jellinek, G.H.M. Calis, The electronic structure of pyrites, particularly CuS_2 and $\text{Fe}_{1-x}\text{Cu}_x\text{Se}_2$: An XPS and Mössbauer study, *Journal of Solid State Chemistry* 72(1) (1988) 137-144.
- [40] J.C.W. Folmer, F. Jellinek, The valence of copper in sulphides and selenides: An X-ray photoelectron spectroscopy study, *Journal of the Less Common Metals* 76(1) (1980) 153-162.
- [41] A. Buckley, R. Woods, An X-ray photoelectron spectroscopic study of the oxidation of chalcopyrite, *Australian Journal of Chemistry* 37(12) (1984) 2403-2413.
- [42] Y.J. Xian, S.M. Wen, J.S. Deng, J. Liu, Q. Nie, Leaching chalcopyrite with sodium chlorate in hydrochloric acid solution, *Canadian Metallurgical Quarterly* 51(2) (2012) 133-140.
- [43] J. Dutrizac, The leaching of sulphide minerals in chloride media, *Hydrometallurgy* 29(1-3) (1992) 1-45.
- [44] H. Linge, Reactivity comparison of Australian chalcopyrite concentrates in acidified ferric solution, *Hydrometallurgy* 2(3) (1977) 219-233.
- [45] C. Klauber, A. Parker, W. van Bronswijk, H. Watling, Sulphur speciation of leached chalcopyrite surfaces as determined by X-ray photoelectron spectroscopy, *International Journal of Mineral Processing* 62(1-4) (2001) 65-94.
- [46] A. Parker, R. Paul, G. Power, Electrochemistry of the oxidative leaching of copper from chalcopyrite, *Journal of Electroanalytical Chemistry and Interfacial Electrochemistry* 118 (1981) 305-316.
- [47] A. Ghahremaninezhad, D.G. Dixon, E. Asselin, Electrochemical and XPS analysis of chalcopyrite (CuFeS_2) dissolution in sulfuric acid solution, *Electrochimica Acta* 87 (2013) 97-112.
- [48] R.P. Hackl, D.B. Dreisinger, E. Peters, J.A. King, Passivation of chalcopyrite during oxidative leaching in sulfate media, *Hydrometallurgy* 39(1) (1995) 25-48.
- [49] F.K. Crundwell, The semiconductor mechanism of dissolution and the pseudo-passivation of chalcopyrite, *Canadian Metallurgical Quarterly* 54(3) (2015) 279-288.
- [50] M.J. Nicol, Photocurrents at chalcopyrite and pyrite electrodes under leaching conditions, *Hydrometallurgy* 163 (2016) 104-107.
- [51] F.K. Crundwell, A. Van Aswegen, L.J. Bryson, C. Biley, D. Craig, V.D. Marsicano, J.M. Keartland, The effect of visible light on the dissolution of natural chalcopyrite (CuFeS_2) in sulphuric acid solutions, *Hydrometallurgy* 158 (2015) 119-131.
- [52] M.J. Nicol, The anodic behaviour of chalcopyrite in chloride solutions: Overall features and comparison with sulfate solutions, *Hydrometallurgy* 169 (2017) 321-329.
- [53] G.W. Warren, M.E. Wadsworth, S.M. El-Raghy, Passive and transpassive anodic behavior of chalcopyrite in acid solutions, *Metallurgical Transactions B* 13(4) (1982) 571-579.

- [54] J. Marsden, J. Wilmot, Medium-temperature pressure leaching of copper concentrates-Part 1: Chemistry and initial process development, *Minerals & Metallurgical Processing* 24(4) (2007) 193-204.
- [55] H. Kametani, A. Aoki, Effect of suspension potential on the oxidation rate of copper concentrate in a sulfuric acid solution, *Metallurgical Transactions B* 16(4) (1985) 695-705.
- [56] G. Viramontes-Gamboa, B.F. Rivera-Vasquez, D.G. Dixon, The Active-Passive Behavior of Chalcopyrite: Comparative Study Between Electrochemical and Leaching Responses, *Journal of The Electrochemical Society* 154(6) (2007) C299-C311.
- [57] M. Khoshkhoo, M. Dopson, F. Engström, Å. Sandström, New insights into the influence of redox potential on chalcopyrite leaching behaviour, *Minerals Engineering* 100 (2017) 9-16.
- [58] Å. Sandström, A. Shchukarev, J. Paul, XPS characterisation of chalcopyrite chemically and bio-leached at high and low redox potential, *Minerals Engineering* 18(5) (2005) 505-515.
- [59] S. Wang, Copper leaching from chalcopyrite concentrates, *JOM* 57(7) (2005) 48-51.
- [60] H.R. Watling, Chalcopyrite hydrometallurgy at atmospheric pressure: 1. Review of acidic sulfate, sulfate-chloride and sulfate-nitrate process options, *Hydrometallurgy* 140 (2013) 163-180.
- [61] A. Ahmadi, M. Schaffie, Z. Manafi, M. Ranjbar, Electrochemical bioleaching of high grade chalcopyrite flotation concentrates in a stirred bioreactor, *Hydrometallurgy* 104(1) (2010) 99-105.
- [62] A.E. Torma, P.R. Ashman, T.M. Olsen, K. Bosecker, Microbiological leaching of a chalcopyrite concentrate and recovery of copper by solvent extraction and electrowinning, *Metall* 33(5) (1979) 479-484.
- [63] A. Bruynesteyn, D.W. Duncan, Microbiological leaching of sulphide concentrates, *Canadian Metallurgical Quarterly* 10(1) (1971) 57-63.
- [64] A. Pinches, F.O. Al-Jaid, D.J.A. Williams, B. Atkinson, Leaching of chalcopyrite concentrates with thiobacillus ferrooxidans in batch culture, *Hydrometallurgy* 2(2) (1976) 87-103.
- [65] J.E. Dutrizac, Elemental Sulphur Formation During the Ferric Sulphate Leaching of Chalcopyrite, *Canadian Metallurgical Quarterly* 28(4) (1989) 337-344.
- [66] P.B. Munoz, J.D. Miller, M.E. Wadsworth, Reaction mechanism for the acid ferric sulfate leaching of chalcopyrite, *Metallurgical Transactions B* 10(2) (1979) 149-158.
- [67] A. Vizsolyi, H. Veltman, I.H. Warren, V.N. Mackiw, Copper and elemental sulphur from chalcopyrite by pressure leaching, *JOM* 19(11) (1967) 52-59.
- [68] J.D. Batty, G.V. Rorke, Development and commercial demonstration of the BioCOP™ thermophile process, *Hydrometallurgy* 83(1) (2006) 83-89.
- [69] J.O. Marsden, R.E. Brewer, N. Hazen, Copper concentrate leaching developments by Phelps Dodge Corporation, *Electrometallurgy and Environmental Hydrometallurgy* 2 (2003) 1429-1446.
- [70] G. Richmond, D. Dreisinger, Processing of copper sulfide ores by autoclave leaching followed by extraction and electrowinning, Australian patent 749257 (2002) 2002.
- [71] I.J. Corrans, J.E. Angove, Activation of a mineral species, in: U.S. Patent (Ed.) Dominion Mining Limited, Western Australia, Australia, 1993.
- [72] M.M. Hourn, D.W. Turner, I.R. Holzberger, Atmospheric mineral leaching process, in: U.S. Patent (Ed.) M.I.M. Holdings Limited, Queensland Australia, Highlands Frieda Pty. Limited Port Moresby, Papua New Guinea, 1999.

- [73] P. Dempsey, D.B. Dreisinger, Process for the extraction of copper, Google Patents, 2003.
- [74] D.G. Dixon, D.D. Mayne, K.G. Baxter, Galvanox™ – A novel galvanically-assisted atmospheric leaching technology for copper concentrates Canadian Metallurgical Quarterly 47(3) (2008) 327-336.
- [75] D. Dreisinger, N. Abed, A fundamental study of the reductive leaching of chalcopyrite using metallic iron part I: kinetic analysis, Hydrometallurgy 66(1) (2002) 37-57.
- [76] N. Hiroyoshi, H. Miki, T. Hirajima, M. Tsunekawa, A model for ferrous-promoted chalcopyrite leaching, Hydrometallurgy 57(1) (2000) 31-38.
- [77] A. Adebayo, K. Ipinmoroti, O. Ajayi, Dissolution kinetics of chalcopyrite with hydrogen peroxide in sulphuric acid medium, Chemical and biochemical engineering quarterly 17(3) (2003) 213-218.
- [78] P.A. Olubambi, J.H. Potgieter, Investigations on the mechanisms of sulfuric acid leaching of chalcopyrite in the presence of hydrogen peroxide, Mineral Processing and Extractive Metallurgy Review 30(4) (2009) 327-345.
- [79] V. Mahajan, M. Misra, K. Zhong, M.C. Fuerstenau, Enhanced leaching of copper from chalcopyrite in hydrogen peroxide–glycol system, Minerals Engineering 20(7) (2007) 670-674.
- [80] O.J. Solis-Marcial, G.T. Lapidus, Improvement of chalcopyrite dissolution in acid media using polar organic solvents, Hydrometallurgy 131-132 (2013) 120-126.
- [81] J.E. Dutrizac, The dissolution of chalcopyrite in ferric sulfate and ferric chloride media, Metallurgical Transactions B 12(2) (1981) 371-378.
- [82] S. Aydogan, G. Ucar, M. Canbazoglu, Dissolution kinetics of chalcopyrite in acidic potassium dichromate solution, Hydrometallurgy 81(1) (2006) 45-51.
- [83] M. Nicol, H. Miki, L. Velásquez-Yévenes, The dissolution of chalcopyrite in chloride solutions: Part 3. Mechanisms, Hydrometallurgy 103(1) (2010) 86-95.
- [84] M.D. Sokić, B. Marković, D. Živković, Kinetics of chalcopyrite leaching by sodium nitrate in sulphuric acid, Hydrometallurgy 95(3) (2009) 273-279.
- [85] A.P. Karcz, A.J. Damø, J.B. Illerup, S. Rocks, K. Dam-Johansen, D. Chaiko, Electron microscope investigations of activated chalcopyrite particles via the FLSmith® ROL process, Journal of Materials Science 52(20) (2017) 12044-12053.
- [86] Y. Li, B. Wang, Q. Xiao, C. Lartey, Q. Zhang, The mechanisms of improved chalcopyrite leaching due to mechanical activation, Hydrometallurgy 173 (2017) 149-155.
- [87] G.W. Warren, H.J. Sohn, M.E. Wadsworth, T.G. Wang, The effect of electrolyte composition on the cathodic reduction of CuFeS₂, Hydrometallurgy 14(2) (1985) 133-149.
- [88] J.B. Hiskey, M.E. Wadsworth, Galvanic conversion of chalcopyrite, Metallurgical and Materials Transactions B 6(1) (1975) 183-190.
- [89] F. Doyle, G. Lapidus, Reductive Leaching of Chalcopyrite by Aluminum, ECS Transactions 2(3) (2006) 189-196.
- [90] M. Nicol, Mechanism of aqueous reduction of the chalcopyrite by copper, iron and lead, Transactions of the Institution of Mining and Metallurgy-Section C: Mineral Processing and Extractive Metallurgy 84 (1975).
- [91] J.C. Fuentes-Aceituno, G.T. Lapidus, F.M. Doyle, A kinetic study of the electro-assisted reduction of chalcopyrite, Hydrometallurgy 92(1) (2008) 26-33.

- [92] A.E. Elsherief, The influence of cathodic reduction, Fe^{2+} and Cu^{2+} ions on the electrochemical dissolution of chalcopyrite in acidic solution, *Minerals Engineering* 15(4) (2002) 215-223.
- [93] T. Biegler, D.A. Swift, The electrolytic reduction of chalcopyrite in acid solution, *Journal of Applied Electrochemistry* 6(3) (1976) 229-235.
- [94] M.P. Hu, D.L. Piron, THE EFFECTS OF ARSENIC AND LEAD IMPURITIES ON THE CURRENT EFFICIENCY AND DEPOSIT COMPOSITION IN ALKALINE ZINC ELECTROWINNING, *CANADIAN JOURNAL OF CHEMICAL ENGINEERING* 70(3) (1992) 553-558.
- [95] M.J. Mahon, Dynamic process simulation of zinc electrowinning, University of British Columbia, 2016.
- [96] M.R.C. Ismael, J.M.R. Carvalho, Iron recovery from sulphate leach liquors in zinc hydrometallurgy, *Minerals Engineering* 16(1) (2003) 31-39.
- [97] D.J. Mackinnon, J.M. Brannen, P.L. Fenn, Characterization of impurity effects in zinc electrowinning from industrial acid sulphate electrolyte, *Journal of Applied Electrochemistry* 17(6) (1987) 1129-1143.
- [98] D.J. Mackinnon, The effect of copper on zinc electrowinning from industrial acid sulphate electrolyte, *Journal of Applied Electrochemistry* 15(6) (1985) 953-960.
- [99] D.J. Mackinnon, J.M. Brannen, R.C. Kerby, The effect of cadmium on zinc deposit structures obtained from high purity industrial acid sulphate electrolyte, *Journal of Applied Electrochemistry* 9(1) (1979) 71-79.
- [100] B.C. Tripathy, S.C. Das, G.T. Hefter, P. Singh, Zinc electrowinning from acidic sulphate solutions Part II: Effects of triethylbenzylammonium chloride, *Journal of Applied Electrochemistry* 28(9) (1998) 915-920.
- [101] B.C. Tripathy, S.C. Das, G.T. Hefter, P. Singh Zinc electrowinning from acidic sulfate solutions: Part I: Effects of sodium lauryl sulfate, *Journal of Applied Electrochemistry* 27(6) (1997) 673-678.
- [102] B.C. Tripathy, S.C. Das, P. Singh, G.T. Hefter, Zinc electrowinning from acidic sulphate solutions. Part III: Effects of quaternary ammonium bromides, *Journal of Applied Electrochemistry* 29(10) (1999) 1229-1235.
- [103] B.C. Tripathy, S.C. Das, P. Singh, G.T. Hefter, V.N. Misra, Zinc electrowinning from acidic sulphate solutions Part IV1Part I, Part II and Part III are published in *J. Appl. Electrochem*, 27 (1997) 673, 28 (1998) 915, 29 (1999) 1229, respectively.1: effects of perfluorocarboxylic acids, *Journal of Electroanalytical Chemistry* 565(1) (2004) 49-56.
- [104] D. Dhak, M. Mahon, E. Asselin, A. Alfantazi, The effects of mixtures of acid mist suppression reagents on zinc electrowinning from spent electrolyte solutions, *Hydrometallurgy* 108(1) (2011) 1-10.
- [105] D. Majuste, V.S.T. Ciminelli, P.R. Cetlin, E.L.C. Martins, A.D. Souza, An Approach to Evaluate the Effect of Organic Compounds (Impurities and Additives) on Metal Electrowinning, Springer International Publishing, Cham, 2018, pp. 1473-1483.
- [106] E.J. Frazer, T. Lwin, Identification of optimum conditions for zinc electrowinning in high-purity synthetic electrolytes, *Journal of Applied Electrochemistry* 17(3) (1987) 453-462.
- [107] A.E. Saba, A.E. Elsherief, Continuous electrowinning of zinc, *Hydrometallurgy* 54(2) (2000) 91-106.

- [108] D.J. MacKinnon, J.M. Brannen, Effect of manganese, magnesium, sodium and potassium sulphates on zinc electrowinning from synthetic acid sulphate electrolytes, *Hydrometallurgy* 27(1) (1991) 99-111.
- [109] P. Guillaume, N. Leclerc, C. Boulanger, J.M. Lecuire, F. Lapique, Investigation of optimal conditions for zinc electrowinning from aqueous sulfuric acid electrolytes, *Journal of Applied Electrochemistry* 37(11) (2007) 1237-1243.
- [110] H. Kim, G. Jeong, Y.-U. Kim, J.-H. Kim, C.-M. Park, H.-J. Sohn, Metallic anodes for next generation secondary batteries, *Chemical Society Reviews* 42(23) (2013) 9011-9034.
- [111] G.D. Wilcox, P.J. Mitchell, The electrodeposition of zinc from zincate solutions. A review, *Transactions of the IMF* 65(1) (1987) 76-79.
- [112] M.Z. Mayers, J.W. Kaminski, T.F. Miller, Suppression of Dendrite Formation via Pulse Charging in Rechargeable Lithium Metal Batteries, *The Journal of Physical Chemistry C* 116(50) (2012) 26214-26221.
- [113] J.-S. Lee, S. Tai Kim, R. Cao, N.-S. Choi, M. Liu, K.T. Lee, J. Cho, Metal–Air Batteries with High Energy Density: Li–Air versus Zn–Air, *Advanced Energy Materials* 1(1) (2011) 34-50.
- [114] S.J. Banik, R. Akolkar, Suppressing Dendrite Growth during Zinc Electrodeposition by PEG-200 Additive, *Journal of The Electrochemical Society* 160(11) (2013) D519-D523.
- [115] S.J. Banik, R. Akolkar, Suppressing Dendritic Growth during Alkaline Zinc Electrodeposition using Polyethylenimine Additive, *Electrochimica Acta* 179 (2015) 475-481.
- [116] K.E.K. Sun, T.K.A. Hoang, T.N.L. Doan, Y. Yu, X. Zhu, Y. Tian, P. Chen, Suppression of Dendrite Formation and Corrosion on Zinc Anode of Secondary Aqueous Batteries, *ACS Applied Materials & Interfaces* 9(11) (2017) 9681-9687.
- [117] C.W. Lee, K. Sathiyarayanan, S.W. Eom, M.S. Yun, Novel alloys to improve the electrochemical behavior of zinc anodes for zinc/air battery, *Journal of Power Sources* 160(2) (2006) 1436-1441.
- [118] C. Zhang, J.M. Wang, L. Zhang, J.Q. Zhang, C.N. Cao, Study of the performance of secondary alkaline pasted zinc electrodes, *Journal of Applied Electrochemistry* 31(9) (2001) 1049-1054.
- [119] Y.F. Yuan, J.P. Tu, H.M. Wu, B. Zhang, X.H. Huang, X.B. Zhao, Electrodeposited Growth Habit and Growth Mechanism of ZnO as Anode Material of Secondary Alkaline Zn Battery, *Journal of The Electrochemical Society* 153(9) (2006) A1719-A1723.
- [120] T. Kousksou, P. Bruel, A. Jamil, T. El Rhafiki, Y. Zeraoui, Energy storage: Applications and challenges, *Solar Energy Materials and Solar Cells* 120 (2014) 59-80.
- [121] Z. Yang, J. Zhang, M.C.W. Kintner-Meyer, X. Lu, D. Choi, J.P. Lemmon, J. Liu, Electrochemical Energy Storage for Green Grid, *Chemical Reviews* 111(5) (2011) 3577-3613.
- [122] A.S. Aricò, P. Bruce, B. Scrosati, J.-M. Tarascon, W. van Schalkwijk, Nanostructured materials for advanced energy conversion and storage devices, *Nature Materials* 4 (2005) 366.
- [123] P. Simon, Y. Gogotsi, Materials for electrochemical capacitors, *Nature Materials* 7 (2008) 845.
- [124] C. Liu, F. Li, L.-P. Ma, H.-M. Cheng, Advanced Materials for Energy Storage, *Advanced Materials* 22(8) (2010) E28-E62.
- [125] Z. Niu, L. Zhang, L. Liu, B. Zhu, H. Dong, X. Chen, All-Solid-State Flexible Ultrathin Micro-Supercapacitors Based on Graphene, *Advanced Materials* 25(29) (2013) 4035-4042.

- [126] Z. Niu, P. Luan, Q. Shao, H. Dong, J. Li, J. Chen, D. Zhao, L. Cai, W. Zhou, X. Chen, S. Xie, A “skeleton/skin” strategy for preparing ultrathin free-standing single-walled carbon nanotube/polyaniline films for high performance supercapacitor electrodes, *Energy & Environmental Science* 5(9) (2012) 8726-8733.
- [127] X. Dong, Y. Cao, J. Wang, M.B. Chan-Park, L. Wang, W. Huang, P. Chen, Hybrid structure of zinc oxide nanorods and three dimensional graphene foam for supercapacitor and electrochemical sensor applications, *RSC Advances* 2(10) (2012) 4364-4369.
- [128] B. Kang, G. Ceder, Battery materials for ultrafast charging and discharging, *Nature* 458(7235) (2009) 190.
- [129] V. Augustyn, J. Come, M.A. Lowe, J.W. Kim, P.-L. Taberna, S.H. Tolbert, H.D. Abruña, P. Simon, B. Dunn, High-rate electrochemical energy storage through Li⁺ intercalation pseudocapacitance, *Nature Materials* 12 (2013) 518.
- [130] P. Simon, Y. Gogotsi, B. Dunn, Where Do Batteries End and Supercapacitors Begin?, *Science* 343(6176) (2014) 1210-1211.
- [131] J. Wang, J. Polleux, J. Lim, B. Dunn, Pseudocapacitive contributions to electrochemical energy storage in TiO₂ (anatase) nanoparticles, *The Journal of Physical Chemistry C* 111(40) (2007) 14925-14931.
- [132] A. Vlad, N. Singh, J. Rolland, S. Melinte, P. Ajayan, J.-F. Gohy, Hybrid supercapacitor-battery materials for fast electrochemical charge storage, *Scientific reports* 4 (2014) 4315.
- [133] M. Armand, J.M. Tarascon, Building better batteries, *Nature* 451 (2008) 652.
- [134] D. Cericola, R. Kötz, Hybridization of rechargeable batteries and electrochemical capacitors: Principles and limits, *Electrochimica Acta* 72 (2012) 1-17.
- [135] N.-S. Choi, Z. Chen, S.A. Freunberger, X. Ji, Y.-K. Sun, K. Amine, G. Yushin, L.F. Nazar, J. Cho, P.G. Bruce, Challenges Facing Lithium Batteries and Electrical Double-Layer Capacitors, *Angewandte Chemie International Edition* 51(40) (2012) 9994-10024.
- [136] H. Zhang, X. Yu, P.V. Braun, Three-dimensional bicontinuous ultrafast-charge and-discharge bulk battery electrodes, *Nature nanotechnology* 6(5) (2011) 277.
- [137] Y. Wang, Y. Wang, E. Hosono, K. Wang, H. Zhou, The design of a LiFePO₄/carbon nanocomposite with a core-shell structure and its synthesis by an in situ polymerization restriction method, *Angewandte Chemie International Edition* 47(39) (2008) 7461-7465.
- [138] T. Brezesinski, J. Wang, S.H. Tolbert, B. Dunn, Ordered mesoporous α -MoO₃ with iso-oriented nanocrystalline walls for thin-film pseudocapacitors, *Nature Materials* 9 (2010) 146.
- [139] W. Wang, S. Guo, I. Lee, K. Ahmed, J. Zhong, Z. Favors, F. Zaera, M. Ozkan, C.S. Ozkan, Hydrous Ruthenium Oxide Nanoparticles Anchored to Graphene and Carbon Nanotube Hybrid Foam for Supercapacitors, *Scientific Reports* 4 (2014) 4452.
- [140] G.J. May, A. Davidson, B. Monahov, Lead batteries for utility energy storage: A review, *Journal of Energy Storage* 15 (2018) 145-157.
- [141] L. Zhou, K. Zhang, Z. Hu, Z. Tao, L. Mai, Y.-M. Kang, S.-L. Chou, J. Chen, Recent Developments on and Prospects for Electrode Materials with Hierarchical Structures for Lithium-Ion Batteries, *Advanced Energy Materials* 8(6) (2018) 1701415.
- [142] S.-H. Chung, C.-H. Chang, A. Manthiram, Progress on the Critical Parameters for Lithium-Sulfur Batteries to be Practically Viable, *Advanced Functional Materials* 28(28) (2018) 1801188.
- [143] Y. Wang, J. Yi, Y. Xia, Recent Progress in Aqueous Lithium-Ion Batteries, *Advanced Energy Materials* 2(7) (2012) 830-840.

- [144] Y. Fang, L. Xiao, Z. Chen, X. Ai, Y. Cao, H. Yang, Recent Advances in Sodium-Ion Battery Materials, *Electrochemical Energy Reviews* (2018) 1-30.
- [145] Z. Hu, Z. Zhu, F. Cheng, K. Zhang, J. Wang, C. Chen, J. Chen, Pyrite FeS₂ for high-rate and long-life rechargeable sodium batteries, *Energy & Environmental Science* 8(4) (2015) 1309-1316.
- [146] F. Yang, S.M.A. Mousavie, T.K. Oh, T. Yang, Y. Lu, C. Farley, R.J. Bodnar, L. Niu, R. Qiao, Z. Li, Sodium–Sulfur Flow Battery for Low-Cost Electrical Storage, *Advanced Energy Materials* 8(11) (2018) 1701991.
- [147] G. Kear, A.A. Shah, F.C. Walsh, Development of the all-vanadium redox flow battery for energy storage: a review of technological, financial and policy aspects, *International Journal of Energy Research* 36(11) (2012) 1105-1120.
- [148] M. Skyllas-Kazacos, G. Kazacos, G. Poon, H. Verseema, Recent advances with UNSW vanadium-based redox flow batteries, *International Journal of Energy Research* 34(2) (2010) 182-189.
- [149] Y. Li, H. Dai, Recent advances in zinc–air batteries, *Chemical Society Reviews* 43(15) (2014) 5257-5275.
- [150] M. Chen, J. Liu, Y. He, R. Yuen, J. Wang, Study of the fire hazards of lithium-ion batteries at different pressures, *Applied Thermal Engineering* 125 (2017) 1061-1074.
- [151] N. Nitta, F. Wu, J.T. Lee, G. Yushin, Li-ion battery materials: present and future, *Materials Today* 18(5) (2015) 252-264.
- [152] K. Mizushima, P.C. Jones, P.J. Wiseman, J.B. Goodenough, Li_xCoO₂ (0 < x < 1): A new cathode material for batteries of high energy density, *Materials Research Bulletin* 15(6) (1980) 783-789.
- [153] A. Rougier, P. Gravereau, C. Delmas, Optimization of the Composition of the Li_{1-z} Ni_{1+z} O₂ Electrode Materials: Structural, Magnetic, and Electrochemical Studies, *Journal of The Electrochemical Society* 143(4) (1996) 1168-1175.
- [154] S.K. Martha, O. Haik, E. Zinigrad, I. Exnar, T. Drezen, J.H. Miners, D. Aurbach, On the Thermal Stability of Olivine Cathode Materials for Lithium-Ion Batteries, *Journal of The Electrochemical Society* 158(10) (2011) A1115-A1122.
- [155] A.R. Armstrong, P.G. Bruce, Synthesis of layered LiMnO₂ as an electrode for rechargeable lithium batteries, *Nature* 381 (1996) 499.
- [156] H. Zheng, Q. Sun, G. Liu, X. Song, V.S. Battaglia, Correlation between dissolution behavior and electrochemical cycling performance for LiNi_{1/3}Co_{1/3}Mn_{1/3}O₂-based cells, *Journal of Power Sources* 207 (2012) 134-140.
- [157] B. Dunn, H. Kamath, J.-M. Tarascon, Electrical Energy Storage for the Grid: A Battery of Choices, *Science* 334(6058) (2011) 928-935.
- [158] X. Rui, H. Tan, Q. Yan, Nanostructured metal sulfides for energy storage, *Nanoscale* 6(17) (2014) 9889-9924.
- [159] A. Manthiram, Materials Challenges and Opportunities of Lithium Ion Batteries, *The Journal of Physical Chemistry Letters* 2(3) (2011) 176-184.
- [160] S. Sil, A. Dey, S. Halder, J. Datta, P.P. Ray, Possibility to Use Hydrothermally Synthesized CuFeS₂ Nanocomposite as an Acceptor in Hybrid Solar Cell, *Journal of Materials Engineering and Performance* 27(6) (2018) 2649-2654.
- [161] J.W. Marple, High discharge capacity lithium battery, in: U.S. Patent (Ed.) Eveready battery Company Inc., United States, 2011.

- [162] X. Wu, Y. Zhao, C. Yang, G. He, PVP-assisted synthesis of shape-controlled CuFeS₂ nanocrystals for Li-ion batteries, *Journal of Materials Science* 50(12) (2015) 4250-4257.
- [163] L.Z. Pei, J.F. Wang, X.X. Tao, S.B. Wang, Y.P. Dong, C.G. Fan, Q.-F. Zhang, Synthesis of CuS and Cu_{1.1}Fe_{1.1}S₂ crystals and their electrochemical properties, *Materials Characterization* 62(3) (2011) 354-359.
- [164] D. Liang, R. Ma, S. Jiao, G. Pang, S. Feng, A facile synthetic approach for copper iron sulfide nanocrystals with enhanced thermoelectric performance, *Nanoscale* 4(20) (2012) 6265-6268.
- [165] Y.-H.A. Wang, N. Bao, A. Gupta, Shape-controlled synthesis of semiconducting CuFeS₂ nanocrystals, *Solid State Sciences* 12(3) (2010) 387-390.
- [166] M.X. Wang, L.S. Wang, G.H. Yue, X. Wang, P.X. Yan, D.L. Peng, Single crystal of CuFeS₂ nanowires synthesized through solventothermal process, *Materials Chemistry and Physics* 115(1) (2009) 147-150.
- [167] W. Ding, X. Wang, H. Peng, L. Hu, Electrochemical performance of the chalcopyrite CuFeS₂ as cathode for lithium ion battery, *Materials Chemistry and Physics* 137(3) (2013) 872-876.
- [168] Y. Wang, X. Li, Y. Zhang, X. He, J. Zhao, Ether based electrolyte improves the performance of CuFeS₂ spike-like nanorods as a novel anode for lithium storage, *Electrochimica Acta* 158 (2015) 368-373.
- [169] N. Eda, T. Fujii, H. Koshina, A. Morita, H. Ogawa, K.M. Murakami, Effects of an additive material, CuFeS₂, on Li/CuO battery performance, *Journal of Power Sources* 20(1) (1987) 119-126.
- [170] V. Srinivasan, J. Newman, Existence of Path-Dependence in the LiFePO₄ Electrode, *Electrochemical and Solid-State Letters* 9(3) (2006) A110-A114.
- [171] S.-Y. Chung, J.T. Bloking, Y.-M. Chiang, Electronically conductive phospho-olivines as lithium storage electrodes, *Nature Materials* 1 (2002) 123.
- [172] J.P. Zheng, J. Huang, T.R. Jow, The Limitations of Energy Density for Electrochemical Capacitors, *Journal of The Electrochemical Society* 144(6) (1997) 2026-2031.
- [173] B.E. Conway, *Electrochemical Supercapacitors Scientific fundamentals and technological applications*, Kluwer Academic / Plenum Publishers, New York, 1999.
- [174] Y.-G. Guo, J.-S. Hu, L.-J. Wan, Nanostructured Materials for Electrochemical Energy Conversion and Storage Devices, *Advanced Materials* 20(15) (2008) 2878-2887.
- [175] P.G. Bruce, B. Scrosati, J.M. Tarascon, Nanomaterials for rechargeable lithium batteries, *Angewandte Chemie International Edition* 47(16) (2008) 2930-2946.
- [176] P. Simon, Y. Gogotsi, *Materials for electrochemical capacitors*, *Nanoscience and Technology*, pp. 320-329.
- [177] D.N. Futaba, K. Hata, T. Yamada, T. Hiraoka, Y. Hayamizu, Y. Kakudate, O. Tanaike, H. Hatori, M. Yumura, S. Iijima, Shape-engineerable and highly densely packed single-walled carbon nanotubes and their application as super-capacitor electrodes, *Nature Materials* 5 (2006) 987.
- [178] C. Portet, J. Chmiola, Y. Gogotsi, S. Park, K. Lian, Electrochemical characterizations of carbon nanomaterials by the cavity microelectrode technique, *Electrochimica Acta* 53(26) (2008) 7675-7680.

- [179] C.-M. Yang, Y.-J. Kim, M. Endo, H. Kanoh, M. Yudasaka, S. Iijima, K. Kaneko, Nanowindow-Regulated Specific Capacitance of Supercapacitor Electrodes of Single-Wall Carbon Nanohorns, *Journal of the American Chemical Society* 129(1) (2007) 20-21.
- [180] W. Raza, F. Ali, N. Raza, Y. Luo, K.-H. Kim, J. Yang, S. Kumar, A. Mehmood, E.E. Kwon, Recent advancements in supercapacitor technology, *Nano Energy* 52 (2018) 441-473.
- [181] T. Nguyen, R.F. Savinell, Flow Batteries, *The Electrochemical Society Interface* 19(3) (2010) 54-56.
- [182] T. Oshima, M. Kajita, A. Okuno, Development of Sodium-Sulfur Batteries, *International Journal of Applied Ceramic Technology* 1(3) (2004) 269-276.
- [183] K.B. Hatzell, M. Boota, E.C. Kumbur, Y. Gogotsi, Flowable conducting particle networks in redox-active electrolytes for grid energy storage, *Journal of The Electrochemical Society* 162(5) (2015) A5007-A5012.
- [184] M. Dubarry, B.Y. Liaw, Identify capacity fading mechanism in a commercial LiFePO₄ cell, *Journal of Power Sources* 194(1) (2009) 541-549.
- [185] A. Pandolfo, A. Hollenkamp, Carbon properties and their role in supercapacitors, *Journal of power sources* 157(1) (2006) 11-27.
- [186] M. Yu, W. Wang, C. Li, T. Zhai, X. Lu, Y. Tong, Scalable self-growth of Ni@NiO core-shell electrode with ultrahigh capacitance and super-long cyclic stability for supercapacitors, *Npg Asia Materials* 6 (2014) e129.
- [187] S. Haladkar, P. Alegaonkar, Preparation and performance evaluation of Carbon-Nano-Sphere for electrode double layer capacitor, *Applied Surface Science* 449 (2018) 500-506.
- [188] D. Wang, Y. Wang, H. Liu, W. Xu, L. Xu, Unusual carbon nanomesh constructed by interconnected carbon nanocages for ionic liquid-based supercapacitor with superior rate capability, *Chemical Engineering Journal* 342 (2018) 474-483.
- [189] D. Wang, G. Fang, T. Xue, J. Ma, G. Geng, A melt route for the synthesis of activated carbon derived from carton box for high performance symmetric supercapacitor applications, *Journal of Power Sources* 307 (2016) 401-409.
- [190] H. Inoue, T. Morimoto, S. Nohara, Electrochemical Characterization of a Hybrid Capacitor with Zn and Activated Carbon Electrodes, *Electrochemical and Solid-State Letters* 10(12) (2007) A261-A263.
- [191] H.B. Li, M.H. Yu, F.X. Wang, P. Liu, Y. Liang, J. Xiao, C.X. Wang, Y.X. Tong, G.W. Yang, Amorphous nickel hydroxide nanospheres with ultrahigh capacitance and energy density as electrochemical pseudocapacitor materials, *Nature Communications* 4 (2013) 1894.
- [192] Z. Qiu, D. He, Y. Wang, X. Zhao, W. Zhao, H. Wu, High performance asymmetric supercapacitors with ultrahigh energy density based on hierarchical carbon nanotubes@NiO core-shell nanosheets and defect-introduced graphene sheets with hole structure, *RSC Advances* 7(13) (2017) 7843-7856.
- [193] F. Li, H. Chen, X.Y. Liu, S.J. Zhu, J.Q. Jia, C.H. Xu, F. Dong, Z.Q. Wen, Y.X. Zhang, Low-cost high-performance asymmetric supercapacitors based on Co₂AlO₄@MnO₂ nanosheets and Fe₃O₄ nanoflakes, *Journal of Materials Chemistry A* 4(6) (2016) 2096-2104.
- [194] Y. Hou, L. Chen, P. Liu, J. Kang, T. Fujita, M. Chen, Nanoporous metal based flexible asymmetric pseudocapacitors, *Journal of Materials Chemistry A* 2(28) (2014) 10910-10916.
- [195] T. Brousse, D. Bélanger, A hybrid Fe₃O₄ MnO₂ capacitor in mild aqueous electrolyte, *Electrochemical and Solid-State Letters* 6(11) (2003) A244-A248.

- [196] K.M. Deen, E. Asselin, A Hybrid Mineral Battery: Energy Storage and Dissolution Behavior of CuFeS_2 in a Fixed Bed Flow Cell, *ChemSusChem* 11(9) (2018) 1533-1548.
- [197] D.A. Shirley, High-Resolution X-Ray Photoemission Spectrum of the Valence Bands of Gold, *Physical Review B* 5(12) (1972) 4709-4714.
- [198] J.A. Mielczarski, J.M. Cases, M. Alnot, J.J. Ehrhardt, XPS Characterization of Chalcopyrite, Tetrahedrite, and Tennantite Surface Products after Different Conditioning. 1. Aqueous Solution at pH 10, *Langmuir* 12(10) (1996) 2519-2530.
- [199] J.J. McCarron, G.W. Walker, A.N. Buckley, An X-ray photoelectron spectroscopic investigation of chalcopyrite and pyrite surfaces after conditioning in sodium sulfide solutions, *International Journal of Mineral Processing* 30(1) (1990) 1-16.
- [200] J.M. Casas, F. Alvarez, L. Cifuentes, Aqueous speciation of sulfuric acid–cupric sulfate solutions, *Chemical Engineering Science* 55(24) (2000) 6223-6234.
- [201] B.E. Conway, W.G. Pell, Power limitations of supercapacitor operation associated with resistance and capacitance distribution in porous electrode devices, *Journal of Power Sources* 105(2) (2002) 169-81.
- [202] E. Frackowiak, F. Beguin, Carbon materials for the electrochemical storage of energy in capacitors, *Carbon* 39(6) (2001) 937-950.
- [203] W.G. Pell, B.E. Conway, N. Marincic, Analysis of non-uniform charge/discharge and rate effects in porous carbon capacitors containing sub-optimal electrolyte concentrations, *Journal of Electroanalytical Chemistry* 491(1) (2000) 9-21.
- [204] K. Jurewicz, E. Frackowiak, F. Beguin, Enhancement of reversible hydrogen capacity into activated carbon through water electrolysis, *Electrochemical and Solid-State Letters* 4(3) (2001) A27-A29.
- [205] H. Paul, D. Mohanta, Hydrazine reduced exfoliated graphene/graphene oxide layers and magnetoconductance measurements of Ge-supported graphene layers, *Applied Physics A* 103(2) (2011) 395-402.
- [206] E. Fuente, J.A. Menéndez, M.A. Díez, D. Suárez, M.A. Montes-Morán, Infrared Spectroscopy of Carbon Materials: A Quantum Chemical Study of Model Compounds, *The Journal of Physical Chemistry B* 107(26) (2003) 6350-6359.
- [207] Y.J. Oh, J.J. Yoo, Y.I. Kim, J.K. Yoon, H.N. Yoon, J.-H. Kim, S.B. Park, Oxygen functional groups and electrochemical capacitive behavior of incompletely reduced graphene oxides as a thin-film electrode of supercapacitor, *Electrochimica Acta* 116 (2014) 118-128.
- [208] C. Moreno-Castilla, M.V. López-Ramón, F. Carrasco-Marín, Changes in surface chemistry of activated carbons by wet oxidation, *Carbon* 38(14) (2000) 1995-2001.
- [209] M. Seredych, D. Hulicova-Jurcakova, G.Q. Lu, T.J. Bandosz, Surface functional groups of carbons and the effects of their chemical character, density and accessibility to ions on electrochemical performance, *Carbon* 46(11) (2008) 1475-1488.
- [210] M.A. Montes-Morán, D. Suárez, J.A. Menéndez, E. Fuente, On the nature of basic sites on carbon surfaces: an overview, *Carbon* 42(7) (2004) 1219-1225.
- [211] H.A. Andreas, B.E. Conway, Examination of the double-layer capacitance of an high specific-area C-cloth electrode as titrated from acidic to alkaline pHs, *Electrochimica Acta* 51(28) (2006) 6510-6520.
- [212] B.E. Conway, J.C.H. Ku, F.C. Ho, The electrochemical surface reactivity of iron sulfide, FeS_2 , *Journal of Colloid and Interface Science* 75(2) (1980) 357-372.

- [213] W.G. Pell, B.E. Conway, Analysis of power limitations at porous supercapacitor electrodes under cyclic voltammetry modulation and dc charge, *Journal of Power Sources* 96(1) (2001) 57-67.
- [214] B. Conway, V. Birss, J. Wojtowicz, The role and utilization of pseudocapacitance for energy storage by supercapacitors, *Journal of Power Sources* 66(1-2) (1997) 1-14.
- [215] O.J. Solís-Marcial, G.T. Lapidus, Study of the Dissolution of Chalcopyrite in Sulfuric Acid Solutions Containing Alcohols and Organic Acids, *Electrochimica Acta* 140 (2014) 434-437.
- [216] R. de Levie, On porous electrodes in electrolyte solutions—IV, *Electrochimica Acta* 9(9) (1964) 1231-1245.
- [217] B.E. Conway, W.G. Pell, Double-layer and pseudocapacitance types of electrochemical capacitors and their applications to the development of hybrid devices, *Journal of Solid State Electrochemistry* 7(9) (2003) 637-644.
- [218] G. Jerkiewicz, Electrochemical Hydrogen Adsorption and Absorption. Part 1: Underpotential Deposition of Hydrogen, *Electrocatalysis* 1(4) (2010) 179-199.
- [219] J.R.M. Evgenij Barsoukov, *Impedance Spectroscopy Theory, Experiment, and Applications*, 2 ed., John Wiley & Sons, Inc, New Jersey, 2005.
- [220] I.A. Blech, J. Kruger, Further Evidence for Monoatomic Hydrogen as a Darkening Agent in Chemography, *Journal of The Electrochemical Society* 131(10) (1984) 2455-2456.
- [221] G. Girishkumar, M. Rettker, R. Underhile, D. Binz, K. Vinodgopal, P. McGinn, P. Kamat, Single-Wall Carbon Nanotube-Based Proton Exchange Membrane Assembly for Hydrogen Fuel Cells, *Langmuir* 21(18) (2005) 8487-8494.
- [222] D. Meissner, R. Memming, Analysis of current—potential characteristics of n- and p-type semiconductor electrodes, *Electrochimica Acta* 37(5) (1992) 799-809.
- [223] V.S. Bagotsky, *Fundamentals of Electrochemistry*, 2 ed., John Wiley & Sons, Inc., New Jersey, 2006.
- [224] D. Zhao, Y.-l. Feng, Y.-g. Wang, Y.-y. Xia, Electrochemical performance comparison of LiFePO₄ supported by various carbon materials, *Electrochimica Acta* 88 (2013) 632-638.
- [225] K.M. Deen, E. Asselin, Differentiation of the non-faradaic and pseudocapacitive electrochemical response of graphite felt/CuFeS₂ composite electrodes, *Electrochimica Acta* 212 (2016) 979-991.
- [226] K. Sing, The use of nitrogen adsorption for the characterisation of porous materials, *Colloids and Surfaces A: Physicochemical and Engineering Aspects* 187-188 (2001) 3-9.
- [227] M. Al-Harashseh, S. Kingman, F. Rutten, D. Briggs, ToF-SIMS and SEM study on the preferential oxidation of chalcopyrite, *International Journal of Mineral Processing* 80(2) (2006) 205-214.
- [228] O.G. Olvera, M. Rebolledo, E. Asselin, Atmospheric ferric sulfate leaching of chalcopyrite: Thermodynamics, kinetics and electrochemistry, *Hydrometallurgy* 165 (2016) 148-158.
- [229] J.N. Soderberg, A.C. Co, A.H.C. Sirk, V.I. Birss, Impact of Porous Electrode Properties on the Electrochemical Transfer Coefficient, *The Journal of Physical Chemistry B* 110(21) (2006) 10401-10410.
- [230] D. Nava, I. González, Electrochemical characterization of chemical species formed during the electrochemical treatment of chalcopyrite in sulfuric acid, *Electrochimica Acta* 51(25) (2006) 5295-5303.

- [231] F.H. Yang, R.T. Yang, Ab initio molecular orbital study of adsorption of atomic hydrogen on graphite:: Insight into hydrogen storage in carbon nanotubes, *Carbon* 40(3) (2002) 437-444.
- [232] E.M. Arce, I. González, A comparative study of electrochemical behavior of chalcopyrite, chalcocite and bornite in sulfuric acid solution, *International Journal of Mineral Processing* 67(1) (2002) 17-28.
- [233] K.F. Blurton, An electrochemical investigation of graphite surfaces, *Electrochimica Acta* 18(11) (1973) 869-875.
- [234] G. Senanayake, A review of chloride assisted copper sulfide leaching by oxygenated sulfuric acid and mechanistic considerations, *Hydrometallurgy* 98(1) (2009) 21-32.
- [235] G.A. Mabbott, An introduction to cyclic voltammetry, *Journal of Chemical Education* 60(9) (1983) 697.
- [236] W. Zhang, D.M. Muir, P. Singh, Iron(II) oxidation by SO₂/O₂ in acidic media: Part II. Effect of copper, *Hydrometallurgy* 58(2) (2000) 117-125.
- [237] S. Biniak, M. Pakuła, G.S. Szymański, A. Świątkowski, Effect of Activated Carbon Surface Oxygen- and/or Nitrogen-Containing Groups on Adsorption of Copper(II) Ions from Aqueous Solution, *Langmuir* 15(18) (1999) 6117-6122.
- [238] M.C. Ruiz, O. Jerez, R. Padilla, Kinetics of the cupric catalyzed oxidation of FeII by oxygen at high temperature and high pressure, *Mineral Processing and Extractive Metallurgy Review* 37(3) (2016) 160-167.
- [239] D.B. Dreisinger, E. Peters, The oxidation of ferrous sulphate by molecular oxygen under zinc pressure-leach conditions, *Hydrometallurgy* 22(1) (1989) 101-119.
- [240] M. González-Cuenca, W. Zipprich, B.A. Boukamp, G. Pudmich, F. Tietz, Impedance Studies on Chromite-Titanate Porous Electrodes under Reducing Conditions, *Fuel Cells* 1(3-4) (2001) 256-264.
- [241] M. Pakuła, S. Biniak, A. Świątkowski, Chemical and Electrochemical Studies of Interactions between Iron(III) Ions and an Activated Carbon Surface, *Langmuir* 14(11) (1998) 3082-3089.
- [242] A. Singh, A. Chandra, Significant Performance Enhancement in Asymmetric Supercapacitors based on Metal Oxides, Carbon nanotubes and Neutral Aqueous Electrolyte, *Scientific Reports* 5 (2015) 15551.
- [243] L.-Q. Mai, A. Minhas-Khan, X. Tian, K.M. Hercule, Y.-L. Zhao, X. Lin, X. Xu, Synergistic interaction between redox-active electrolyte and binder-free functionalized carbon for ultrahigh supercapacitor performance, *Nature Communications* 4 (2013) 2923.
- [244] R.I. Holliday, W.R. Richmond, An electrochemical study of the oxidation of chalcopyrite in acidic solution, *Journal of Electroanalytical Chemistry and Interfacial Electrochemistry* 288(1) (1990) 83-98.
- [245] C. Klauber, Fracture-induced reconstruction of a chalcopyrite (CuFeS₂) surface, *Surface and Interface Analysis* 35(5) (2003) 415-428.
- [246] H.-b. Zhao, M.-h. Hu, Y.-n. Li, S. Zhu, W.-q. Qin, G.-z. Qiu, J. Wang, Comparison of electrochemical dissolution of chalcopyrite and bornite in acid culture medium, *Transactions of Nonferrous Metals Society of China* 25(1) (2015) 303-313.
- [247] I. Nakai, Y. Sugitani, K. Nagashima, Y. Niwa, X-ray photoelectron spectroscopic study of copper minerals, *Journal of Inorganic and Nuclear Chemistry* 40(5) (1978) 789-791.

- [248] M. Sauber, D.G. Dixon, Electrochemical study of leached chalcopyrite using solid paraffin-based carbon paste electrodes, *Hydrometallurgy* 110(1) (2011) 1-12.
- [249] J. Gerlach, E. Küzeci, Application of carbon paste electrodes to elucidate hydrometallurgical dissolution processes with special regard to chalcocite and covellite, *Hydrometallurgy* 11(3) (1983) 345-361.
- [250] C. Gómez, M. Figueroa, J. Muñoz, M.L. Blázquez, A. Ballester, Electrochemistry of chalcopyrite, *Hydrometallurgy* 43(1) (1996) 331-344.
- [251] R. Bye, L. Engvik, W. Lund, Thiourea as a complexing agent for reduction of copper interference in the determination of selenium by hydride generation/atomic absorption spectrometry, *Analytical Chemistry* 55(14) (1983) 2457-2458.
- [252] E. Laviron, The use of polarography and cyclic voltammetry for the study of redox systems with adsorption of the reactants. Heterogeneous vs. surface path, *Journal of Electroanalytical Chemistry* 382(1) (1995) 111-127.
- [253] R. Klingler, J. Kochi, Electron-transfer kinetics from cyclic voltammetry. Quantitative description of electrochemical reversibility, *The Journal of Physical Chemistry* 85(12) (1981) 1731-1741.
- [254] R.S. Nicholson, Theory and application of cyclic voltammetry for measurement of electrode reaction kinetics, *Analytical chemistry* 37(11) (1965) 1351-1355.
- [255] E. Laviron, General expression of the linear potential sweep voltammogram in the case of diffusionless electrochemical systems, *Journal of Electroanalytical Chemistry and Interfacial Electrochemistry* 101(1) (1979) 19-28.
- [256] R.G. Compton, C.E. Banks, *Understanding voltammetry*, World Scientific 2011.
- [257] M.H. Bridge, E. Williams, M.E.G. Lyons, K.F. Tipton, W. Linert, Electrochemical investigation into the redox activity of Fe(II)/Fe(III) in the presence of nicotine and possible relations to neurodegenerative diseases, *Biochimica et Biophysica Acta (BBA) - Molecular Basis of Disease* 1690(1) (2004) 77-84.
- [258] L.R.F. Allen J. Bard, *Electrochemical Method: Fundamentals and Applications*, 2 ed., John Wiley & Sons, Inc, New York, 1980.
- [259] A.L. Eckermann, D.J. Feld, J.A. Shaw, T.J. Meade, Electrochemistry of redox-active self-assembled monolayers, *Coordination Chemistry Reviews* 254(15) (2010) 1769-1802.
- [260] R.A.S. Luz, A.R. Pereira, J.C.P. de Souza, F.C.P.F. Sales, F.N. Crespilho, Enzyme Biofuel Cells: Thermodynamics, Kinetics and Challenges in Applicability, *ChemElectroChem* 1(11) (2014) 1751-1777.
- [261] J. Friedl, U. Stimming, Determining Electron Transfer Kinetics at Porous Electrodes, *Electrochimica Acta* 227 (2017) 235-245.
- [262] R. Salazar, E. Brillas, I. Sirés, Finding the best Fe²⁺/Cu²⁺ combination for the solar photoelectro-Fenton treatment of simulated wastewater containing the industrial textile dye Disperse Blue 3, *Applied Catalysis B: Environmental* 115-116 (2012) 107-116.
- [263] H. Matsuda, Y. Ayabe, Electrolytic Preparation of Titanium from Fused Salts, *Electrochemistry* 59 (1955) 494.
- [264] G.H. Kelsall, Q. Yin, D.J. Vaughan, K.E.R. England, N.P. Brandon, Electrochemical oxidation of pyrite (FeS₂) in aqueous electrolytes, *Journal of Electroanalytical Chemistry* 471(2) (1999) 116-125.

- [265] D. Zhang, J.P. Tu, J.Y. Xiang, Y.Q. Qiao, X.H. Xia, X.L. Wang, C.D. Gu, Influence of particle size on electrochemical performances of pyrite FeS₂ for Li-ion batteries, *Electrochimica Acta* 56(27) (2011) 9980-9985.
- [266] S.S. Zhang, D.T. Tran, Mechanism and Solution for the Capacity Fading of Li/FeS₂ Battery, *Journal of The Electrochemical Society* 163(5) (2016) A792-A797.
- [267] R. Fong, J.R. Dahn, C.H.W. Jones, Electrochemistry of Pyrite-Based Cathodes for Ambient Temperature Lithium Batteries, *Journal of The Electrochemical Society* 136(11) (1989) 3206-3210.
- [268] L.A. Montoro, J.M. Rosolen, J.H. Shin, S. Passerini, Investigations of natural pyrite in solvent-free polymer electrolyte, lithium metal batteries, *Electrochimica Acta* 49(20) (2004) 3419-3427.
- [269] J.-W. Choi, G. Cheruvally, H.-J. Ahn, K.-W. Kim, J.-H. Ahn, Electrochemical characteristics of room temperature Li/FeS₂ batteries with natural pyrite cathode, *Journal of Power Sources* 163(1) (2006) 158-165.
- [270] A.P. Karcz, A.J. Damø, J.B. Illerup, S. Rocks, K. Dam-Johansen, D. Chaiko, Surface characterization of activated chalcopyrite particles via the FLSmidth ROL process. Part 1: Electron microscope investigations, *Materials Science and Technology* 2016, 2016.
- [271] M. Wang, F. Xie, W. Li, M. Chen, Y. Zhao, Preparation of various kinds of copper sulfides in a facile way and the enhanced catalytic activity by visible light, *Journal of Materials Chemistry A* 1(30) (2013) 8616-8621.
- [272] C.I. Pearce, R.A.D. Pattrick, D.J. Vaughan, C.M.B. Henderson, G. van der Laan, Copper oxidation state in chalcopyrite: Mixed Cu d⁹ and d¹⁰ characteristics, *Geochimica et Cosmochimica Acta* 70(18) (2006) 4635-4642.
- [273] P. Velásquez, D. Leinen, J. Pascual, J.R. Ramos-Barrado, P. Grez, H. Gómez, R. Schrebler, R. Del Río, R. Córdova, A chemical, morphological, and electrochemical (XPS, SEM/EDX, CV, and EIS) analysis of electrochemically modified electrode surfaces of natural chalcopyrite (CuFeS₂) and pyrite (FeS₂) in alkaline solutions, *The Journal of Physical Chemistry B* 109(11) (2005) 4977-4988.
- [274] V.V. Klekovkina, R.R. Gainov, F.G. Vagizov, A.V. Dooglav, V.A. Golovanevskiy, I.N. Pen'kov, Oxidation and magnetic states of chalcopyrite CuFeS₂: A first principles calculation, *Optics and Spectroscopy* 116(6) (2014) 885-888.
- [275] S.W. Goh, A.N. Buckley, R.N. Lamb, R.A. Rosenberg, D. Moran, The oxidation states of copper and iron in mineral sulfides, and the oxides formed on initial exposure of chalcopyrite and bornite to air, *Geochimica et Cosmochimica Acta* 70(9) (2006) 2210-2228.
- [276] K.M. Deen, E. Asselin, On the use of a naturally-sourced CuFeS₂ mineral concentrate for energy storage, *Electrochimica Acta* (2018).
- [277] D. Miller, M. Biesinger, N. McIntyre, Interactions of CO₂ and CO at fractional atmosphere pressures with iron and iron oxide surfaces: one possible mechanism for surface contamination?, *Surface and Interface Analysis: An International Journal devoted to the development and application of techniques for the analysis of surfaces, interfaces and thin films* 33(4) (2002) 299-305.
- [278] A. Ghahremaninezhad, D. Dixon, E. Asselin, Electrochemical and XPS analysis of chalcopyrite (CuFeS₂) dissolution in sulfuric acid solution, *Electrochimica Acta* 87 (2013) 97-112.

- [279] M. Yin, C.-K. Wu, Y. Lou, C. Burda, J.T. Koberstein, Y. Zhu, S. O'Brien, Copper Oxide Nanocrystals, *Journal of the American Chemical Society* 127(26) (2005) 9506-9511.
- [280] M. Thommes, K. Kaneko, A.V. Neimark, J.P. Olivier, F. Rodriguez-Reinoso, J. Rouquerol, K.S. Sing, Physisorption of gases, with special reference to the evaluation of surface area and pore size distribution (IUPAC Technical Report), *Pure and Applied Chemistry* 87(9-10) (2015) 1051-1069.
- [281] K. Jurewicz, E. Frackowiak, F. Béguin, Towards the mechanism of electrochemical hydrogen storage in nanostructured carbon materials, *Applied Physics A* 78(7) (2004) 981-987.
- [282] L. Wei, G. Yushin, Nanostructured activated carbons from natural precursors for electrical double layer capacitors, *Nano Energy* 1(4) (2012) 552-565.
- [283] V. Garten, D. Weiss, The Quinone-Hydroquinone character of activated carbon and carbon black, *Australian Journal of Chemistry* 8(1) (1955) 68-95.
- [284] M. Lamache, D. Bauer, Anodic oxidation of cuprous sulfide and the preparation of nonstoichiometric copper sulfide, *Analytical Chemistry* 51(8) (1979) 1320-1322.
- [285] G.P. Rajarathnam, M. Schneider, X. Sun, A.M. Vassallo, The Influence of Supporting Electrolytes on Zinc Half-Cell Performance in Zinc/Bromine Flow Batteries, *Journal of The Electrochemical Society* 163(1) (2016) A5112-A5117.
- [286] A. Gomes, M.I. da Silva Pereira, Zn electrodeposition in the presence of surfactants: Part I. Voltammetric and structural studies, *Electrochimica Acta* 52(3) (2006) 863-871.
- [287] S. Shivakumara, U. Manohar, Y. Arthoba Naik, T.V. Venkatesha, Influence of additives on electrodeposition of bright Zn-Ni alloy on mild steel from acid sulphate bath, *Bulletin of Materials Science* 30(5) (2007) 455-462.
- [288] V. Shukla, M. Singh, Synthesis of in-situ luminescent ZnS nanoparticles facile with CTAB micelles and their properties study, AIP conference proceedings, AIP Publishing, 2016, p. 020126.
- [289] J. Zhu, Y. Zhou, C. Gao, Influence of surfactants on electrochemical behavior of zinc electrodes in alkaline solution, *Journal of Power Sources* 72(2) (1998) 231-235.
- [290] S. Afifi, A. Ebaid, M. Hegazy, A. Barakat, The effect of additives on zinc deposited from zinc sulfate solutions, *JoM* 44(1) (1992) 32-34.
- [291] A. Gomes, M.I. da Silva Pereira, Pulsed electrodeposition of Zn in the presence of surfactants, *Electrochimica Acta* 51(7) (2006) 1342-1350.
- [292] K.O. Nayana, T.V. Venkatesha, Bright zinc electrodeposition and study of influence of synergistic interaction of additives on coating properties, *Journal of Industrial and Engineering Chemistry* 26 (2015) 107-115.
- [293] K. Jurewicz, Influence of charging parameters on the effectiveness of electrochemical hydrogen storage in activated carbon, *International Journal of Hydrogen Energy* 34(23) (2009) 9431-9435.
- [294] K. Babel, D. Janasiak, K. Jurewicz, Electrochemical hydrogen storage in activated carbons with different pore structures derived from certain lignocellulose materials, *Carbon* 50(14) (2012) 5017-5026.
- [295] R. Wan, J. Miller, J. Foley, S. Pons, Electrochemical Features of the Ferric Sulfate Leaching of CuFeS₂/C Aggregates, UTAH UNIV SALT LAKE CITY DEPT OF CHEMISTRY, 1984.

- [296] N. Elgrishi, K.J. Rountree, B.D. McCarthy, E.S. Rountree, T.T. Eisenhart, J.L. Dempsey, A Practical Beginner's Guide to Cyclic Voltammetry, *Journal of Chemical Education* 95(2) (2018) 197-206.
- [297] A. Ghahremaninezhad, E. Asselin, D.G. Dixon, Electrochemical evaluation of the surface of chalcopyrite during dissolution in sulfuric acid solution, *Electrochimica Acta* 55(18) (2010) 5041-5056.
- [298] H. Koshima, H. Onishi, Adsorption of metal ions on activated carbon from aqueous solutions at pH 1–13, *Talanta* 33(5) (1986) 391-395.
- [299] B.E. Conway, V. Birss, J. Wojtowicz, The role and utilization of pseudocapacitance for energy storage by supercapacitors, *Journal of Power Sources* 66(1) (1997) 1-14.
- [300] F. Zhang, T. Zhang, X. Yang, L. Zhang, K. Leng, Y. Huang, Y. Chen, A high-performance supercapacitor-battery hybrid energy storage device based on graphene-enhanced electrode materials with ultrahigh energy density, *Energy & Environmental Science* 6(5) (2013) 1623-1632.
- [301] W. Zuo, R. Li, C. Zhou, Y. Li, J. Xia, J. Liu, Battery-Supercapacitor Hybrid Devices: Recent Progress and Future Prospects, *Advanced Science* 4(7) (2017) 1600539.
- [302] T. Biegler, D. Swift, Anodic electrochemistry of chalcopyrite, *Journal of Applied Electrochemistry* 9(5) (1979) 545-554.
- [303] S. Koter, M. Kultys, B. Gilewicz-Lukasik, I. Koter, Modeling the transport of sulfuric acid and its sulfates (MgSO₄, ZnSO₄, Na₂SO₄) through an anion-exchange membrane, *Desalination* 342 (2014) 75-84.
- [304] S. Koter, M. Kultys, Modeling the electric transport of sulfuric and phosphoric acids through anion-exchange membranes, *Separation and Purification Technology* 73(2) (2010) 219-229.
- [305] Y. Lorrain, G. Pourcelly, C. Gavach, Transport mechanism of sulfuric acid through an anion exchange membrane, *Desalination* 109(3) (1997) 231-239.
- [306] S. Koter, M. Kultys, Electric transport of sulfuric acid through anion-exchange membranes in aqueous solutions, *Journal of Membrane Science* 318(1-2) (2008) 467-476.
- [307] M. Martí-Calatayud, D.C. Buzzi, M. García-Gabaldón, E. Ortega, A. Bernardes, J.A.S. Tenorio, V. Pérez-Herranz, Sulfuric acid recovery from acid mine drainage by means of electro dialysis, *Desalination* 343 (2014) 120-127.
- [308] V.V. Nikonenko, N.D. Pismenskaya, E.I. Belova, P. Sistat, P. Huguet, G. Pourcelly, C. Larchet, Intensive current transfer in membrane systems: Modelling, mechanisms and application in electro dialysis, *Advances in colloid and interface science* 160(1-2) (2010) 101-123.
- [309] T. Luo, S. Abdu, M. Wessling, Selectivity of ion exchange membranes: A review, *Journal of Membrane Science* (2018).
- [310] E. Guerra, M. Bestetti, Physicochemical properties of ZnSO₄- H₂SO₄- H₂O electrolytes of relevance to zinc electrowinning, *Journal of Chemical & Engineering Data* 51(5) (2006) 1491-1497.
- [311] W.M. Haynes, *CRC handbook of chemistry and physics*, CRC press 2014.
- [312] D.L. Parkhurst, C. Appelo, Description of input and examples for PHREEQC version 3: a computer program for speciation, batch-reaction, one-dimensional transport, and inverse geochemical calculations, US Geological Survey, 2013.

[313] T. Javed, M. Xie, E. Asselin, Factors affecting hematite precipitation and characterization of the product from simulated sulphate-chloride solutions at 150 °C, *Hydrometallurgy* 179 (2018) 8-19.

[314] M. Park, X. Zhang, M. Chung, G.B. Less, A.M. Sastry, A review of conduction phenomena in Li-ion batteries, *Journal of Power Sources* 195(24) (2010) 7904-7929.

Appendices

Appendix A

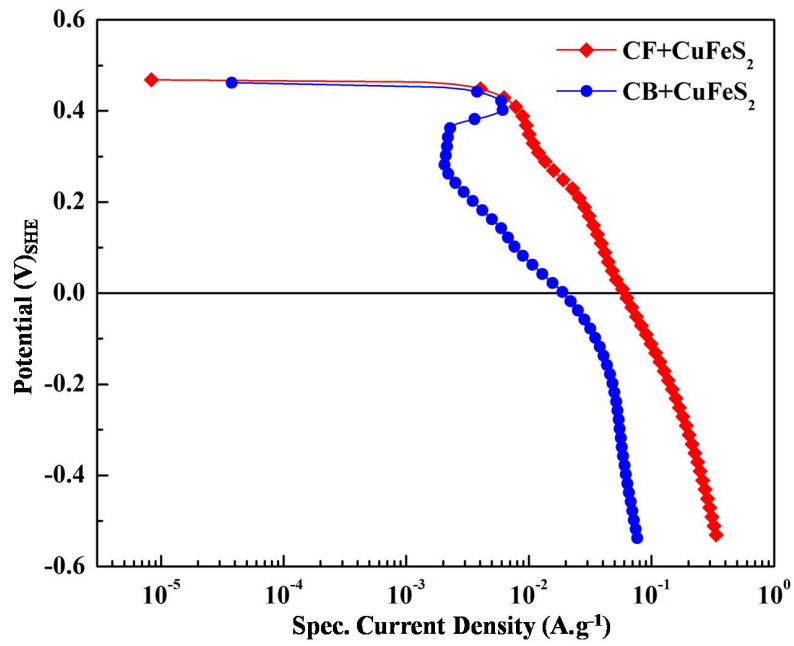


Figure A-1 Cathodic potentiodynamic polarization of composite (CF+CuFeS₂), with CuFeS₂ + black carbon paste electrode deposited on a Pt foil (CB+CuFeS₂) (Note: The current is normalized by the weight of CuFeS₂)

Table A-1 Parameters obtained by fitting the experimental spectra of the (a) CF and (b) Composite electrode to the EEC (the goodness of fit was assured by individual adjustment of the values of each individual element in the EEC and the residual impedance errors were within $\pm 100 \text{ m}\Omega$ of the experimental impedance)

(a)

$E_{ap} \text{ (V)} \eta \text{ (V)}$	R_s	Φ_{dl}	n_1	R_f	Φ_p	n_2	R_p	Goodness of Fit
	(Ω)	mS s^{n_1}		(Ω)	mS s^{n_2}		($\text{k}\Omega$)	
0.68 0.0	10.14	2.09	0.63	1.59	95.86	0.83	22770.00	9.90E-04
0.58 -0.1	10.07	2.70	0.65	1.55	106.10	0.83	1698.00	7.62E-04
0.48 -0.2	8.86	2.40	0.69	1.42	110.90	0.83	904.70	9.67E-04
0.38 -0.3	9.41	1.85	0.76	0.94	110.20	0.83	259.70	1.75E-03
0.28 -0.4	9.55	1.79	0.76	0.93	102.00	0.83	5.46	1.57E-03
0.18 -0.5	9.50	0.47	0.89	1.18	99.50	0.83	2.13	1.78E-03
0.08 -0.6	9.30	6.76	0.82	0.94	78.91	0.86	0.73	2.66E-03
-0.02 -0.7	9.33	10.60	0.80	1.31	65.47	0.88	0.54	2.26E-03
-0.12 -0.8	9.35	3.24	0.83	0.92	63.95	0.87	0.44	1.95E-03
-0.22 -0.9	9.66	2.92	0.77	1.22	57.27	0.87	0.30	1.30E-03

(b)

$E_{ap} \text{ (V)} \eta \text{ (V)}$	R_s	Φ_{dl}	n_1	R_f	Φ_p	n_2	R_p	Goodness of Fit
	(Ω)	mS s^{n_1}		(Ω)	mS s^{n_2}		($\text{k}\Omega$)	
0.47 0.0	7.81	3.62	0.46	2.85	42.10	0.87	2994.00	3.91E-04
0.37 -0.1	8.32	4.92	0.52	2.44	38.42	0.91	6.64	4.72E-04
0.27 -0.2	7.90	4.12	0.48	2.56	39.76	0.91	3.84	2.80E-04
0.17 -0.3	7.94	4.34	0.51	2.36	39.64	0.91	1.29	3.86E-04
0.07 -0.4	7.91	4.58	0.52	2.35	38.49	0.91	1.17	2.96E-04
-0.03 -0.5	7.62	2.80	0.46	2.64	39.82	0.90	1.23	2.26E-04
-0.13 -0.6	7.97	3.32	0.56	2.21	35.36	0.91	0.82	1.89E-04
-0.23 -0.7	7.74	2.63	0.53	2.27	33.10	0.90	0.67	2.17E-04
-0.33 -0.8	7.78	2.69	0.50	2.50	30.19	0.91	0.57	3.74E-04
-0.43 -0.9	8.18	2.87	0.54	2.36	28.17	0.91	0.45	4.91E-04